

Laboratoire des sciences de l'ingénieur, de l'informatique et de l'imagerie

ICube CNRS UMR 7357

École doctorale mathématiques, sciences de l'information et de l'ingénieur

THÈSE

présentée pour obtenir le grade de

Docteur de l'Université de Strasbourg

Mention: Informatique

par

Vasyl Mykhalchuk

Correspondance de maillages dynamiques basée sur les caractéristiques

Soutenu publiquement le **9 Avril 2015**

Members of the jury:

M. Florent Dupont.....*Rapporteur*

Professeur, Université Claude Bernard Lyon 1, France

M. Hervé Delingette.....*Rapporteur*

Directeur de Recherche, INRIA Sophia-Antipolis, France

M. Edmond Boyer.....*Examineur*

Directeur de Recherche, INRIA Grenoble Rhône-Alpes, France

M. Adrian Hilton.....*Examineur*

Professor , University of Surrey, UK

M. Christian Heinrich.....*Examineur*

Professeur, Université de Strasbourg, France

Mme. Hyewon Seo.....*Directrice de thèse*

CNRS Chargé de recherche, Université de Strasbourg, France

Acknowledgements

I wish to express sincere gratitude to my advisors, Hyewon Seo and Frederic Cordier, for their guidance over the past three years. Their support was invaluable.

Many people have influenced me in this journey. One of the most valuable aspects has been the friendships I've formed within the IGG graphics group. It was a great experience to work with my office mate and colleague over the years Guoliang Luo. Many thanks to Kenneth Vanhoey and Lionel Untereiner for helping me to settle down in Strasbourg and sharing their great experience and knowledge. I am also very grateful to Dominique Bechmann for providing such an enjoyable and stimulating working environment.

I acknowledge Robert Walker Sumner for providing triangle correspondences of the horse and camel models. I also thank Frederic Larue and Olivier Génevaux for their assistance with the facial motion capture.

A very special thanks to my dearest friends Dima Krasikov and Slava Tarabukhina for brightening every single day, motivating and uncovering the most important values in life. Finally, I would like to thank my family for supporting me throughout this process. My mom, my father and my brother Dima provide a foundation in my life on which I know I can always depend.

This work has been supported by the French national project SHARED (Shape Analysis and Registration of People Using Dynamic Data, No.10-CHEX-014-01).

Strasbourg, le 19 mai 2015

Abstract

3D geometry modelling tools and 3D scanners become more enhanced and to a greater degree affordable today. Thus, development of the new algorithms in geometry processing, shape analysis and shape correspondence gather momentum in computer graphics. Those algorithms steadily extend and increasingly replace prevailing methods based on images and videos. Non-rigid shape correspondence or deformable shape matching has been a long-studied subject in computer graphics and related research fields. Not to forget, shape correspondence is of wide use in many applications such as statistical shape analysis, motion cloning, texture transfer, medical applications and many more. However, robust and efficient non-rigid shape correspondence still remains a challenging task due to fundamental variations between individual subjects, acquisition noise and the number of degrees of freedom involved in correspondence search. Although dynamic 2D/3D **intra**-subject shape correspondence problem has been addressed in the rich set of previous methods, dynamic **inter**-subject shape correspondence received much less attention.

The primary purpose of our research is to develop a novel, efficient, robust deforming shape analysis and correspondence framework for animated meshes based on their dynamic and motion properties. We elaborate our method by exploiting a profitable set of motion data exhibited by deforming meshes with time-varying embedding. Our approach is based on an observation that a dynamic, deforming shape of a given subject contains much more information rather than a single static posture of it. That is different from the existing methods that rely on static shape information for shape correspondence and analysis.

Our framework of deforming shape analysis and correspondence of animated meshes is comprised of several major contributions: a new dynamic feature detection technique based on multi-scale animated mesh's deformation characteristics, novel dynamic feature descriptor, and an adaptation of a robust graph-based feature correspondence approach followed by the fine matching of the animated meshes.

First, we present the way to extract valuable inter-frame deformation characteristics from animated mesh's surface. Those deformation characteristics effectively capture non-rigid strain deformation values and curvature change of a discrete animated mesh's surface. We further propose a spatio-temporal multi-scale surface deformation representation in the animation and a novel spatio-temporal Difference-of-Gaussian feature detection algorithm. In scope of the work on animated mesh feature detection, a particular emphasis has been put on robustness and consistency of extracted features. Consequently our method shows robust and consistent feature detection results on animated meshes of drastically different body shapes.

Second, in order to integrate dynamic feature points into a framework for animated mesh correspondence, we introduce a new dynamic feature descriptor. Motivated by capturing as much as possible of local deformation and motion properties in the animated mesh, we elaborate a new dynamic feature descriptor composed of normalized displacement, deformation characteristic curves and Animated Mesh Histogram-of-Gradients. Given dynamic descriptors for all features on the source and target animations, we further employ a dual decomposition graph matching approach for establishing reliable feature correspondences between distinct animated meshes. We demonstrate robustness and effectiveness of dynamic feature matching on a number of examples.

Finally we use dynamic feature correspondences on the source and target to guide an iterative fine matching of animated meshes in spherical parameterization. Spherical parameterization aids to reduce significantly the number of degrees of freedom and consequently the computational cost. We demonstrate advantages of our methods on a range of different animated meshes of varying subjects, movements, complexities and details.

Our correspondence framework is also applicable in the case of animated meshes with time-varying mesh connectivity. That is possible due to our new efficient landmark transfer algorithm that can be used for inter-frame matching. The method produces a smooth correspondence map in polynomial time for moderately non-isometric meshes. To precisely locate any vertex on the source mesh we employ a minimum number geometric features and their spatial-geodesic relationship. Thus, a mapping of only a small number of feature points between the source and target meshes allows us to accurately compute arbitrary vertex correspondence. The new developments are demonstrated on a number of examples.

Keywords

Keywords Animated mesh; Feature detection; ·Feature descriptor;· Scale-space theory; Difference of Gaussians; Shape correspondence

Résumé

Correspondance de forme est un problème fondamental dans de nombreuses disciplines de recherche, tels que la géométrie algorithmique, vision par ordinateur et l'infographie. Communément définie comme un problème de trouver injective/ multivaluée correspondance entre une source et une cible, il constitue une tâche centrale dans de nombreuses applications y compris le transfert de attributes, récupération des formes etc. Dans récupération des formes, on peut d'abord calculer la correspondance entre la forme de requête et les formes dans une base de données, puis obtenir le meilleure correspondance en utilisant une mesure de qualité de correspondance prédéfini. Il est également particulièrement avantageuse dans les applications basées sur la modélisation statistique des formes. En encapsulant les propriétés statistiques de l'anatomie du sujet dans le model de forme, comme variations géométriques, des variations de densité, etc., il est utile non seulement pour l'analyse des structures anatomiques telles que des organes ou des os et leur variations valides, mais aussi pour apprendre les modèle de déformation de la classe d'objets.

Dans cette thèse, nous nous intéressons à une enquête sur une nouvelle méthode d'appariement de forme qui exploite grande redondance de l'information à partir des ensembles de données dynamiques, variables dans le temps. Récemment, une grande quantité de recherches ont été effectuées en infographie sur l'établissement de correspondances entre les mailles statiques (Anguelov, Srinivasan et al. 2005, Aiger, Mitra et al. 2008, Castellani, Cristani et al. 2008). Ces méthodes reposent sur les caractéristiques géométriques ou les propriétés extrinsèques/intrinsèques des surfaces statiques (Lipman et Funkhouser 2009, Sun, Ovsjanikov et al. 2009, Ovsjanikov, Mérigot et al. 2010, Kim, Lipman et al., 2011) pour élaguer efficacement les paires. Bien que l'utilisation de la caractéristique géométrique est encore un standard d'or, les méthodes reposant uniquement sur l'information statique de formes peuvent générer dans les résultats de correspondance grossièrement trompeurs lorsque les formes sont radicalement différentes ou ne contiennent pas suffisamment de caractéristiques géométriques.

Nous soutenons qu'en considérant les objets qui subissent une déformation nous pouvons étendre la capacité limitée des informations de géométrie statique et obtenir correspondances plus fiables et de haute qualité entre les formes. L'observation clé est qu'un maillage d'animation contient beaucoup plus d'information que son homologue statique. Fait encourageant, les ensembles de données de maillage animées deviennent plus populaire et abordable aujourd'hui en raison de l'avancement du développements de capteurs optiques et des dispositifs de capture de mouvement (Dobrian et Bevilacqua 2003, Vlastic, Adelsberger et al. 2007, Camplani et Salgado 2012, Webb et Ashley 2012), des performances capture (Valgaerts, Wu et al. 2012, Cao, Weng et al. 2013), des algorithmes de post-traitement (Weise, Li et al. 2009, Weise, Bouaziz et al., 2011), et des techniques d'animation et reciblage (Sumner et Popović 2004, Li, Weise et al., 2010).

Intrigué par l'idée d'utiliser des propriétés de déformation dynamique de mailles pour l'amélioration de l'appariement de formes, nous étudions une nouvelle méthode de correspondance de forme qui tire parti d'un vaste ensemble d'informations supplémentaires à partir des données de mouvement dynamique des formes.

Comme cela a été discuté, l'emploi des caractéristiques de déformation dynamiques de formes est un investissement raisonnable qui peut faire une différence significative dans la capacité d'appariement de formes. La principale contribution que nous apportons dans cette thèse est un nouveau méthode qui traite les caractéristiques de déplacement et de déformation de la surface de sujets - nous élaborons une nouvelle méthode d'ap-

pariement de formes qui rend l'utilisation de ce riche ensemble d'informations de mouvement qui assure l'appariement de formes fiable et efficace. Au meilleur de notre connaissance, il n'y a pas de travail existant qui examine propriétés de déformation ou de mouvement de formes variables dans le temps pour correspondance des forms.

Pour atteindre l'objectif susmentionné, nous nous concentrons sur la façon de représenter efficacement les données de mouvement et la façon de coder les données de mouvement en vue de trouver une appariement de formes fiable. Nous reprenons les principales phases d'approches typiques de recherche d'appariement en incorporant les données dynamiques dans le pipeline de correspondance des formes. Nous développons un algorithme dynamique d'extraction de caractéristiques multi-échelles, un appariement clairsemé parmi les caractéristiques en utilisant des signatures de caractéristiques dynamiques, et un fine correspondance de formes. Dans le chapitre 3, nous développons un méthode de détection de caractéristiques spatio-temporel sur des maillages animés basés sur les approches spatiales à grande échelle. Pour un ensemble donné de caractéristiques dynamiques sur chacune des formes source et cible, l'objectif est d'estimer efficacement l'appariement en mettant des points avec signatures similaires de caractéristiques dynamiques en correspondance. Cette tâche exigeait l'élaboration de mesures de similarité entre des points caractéristiques dynamiques, ce qui est détaillé au chapitre 4. Les caractéristiques dynamiques ainsi que les caractéristiques géométriques basé sur la forme sont ensuite utilisés pour guider l'appariement dense pour l'appariement optimal (chapitre 4).

1.1 Détection de caractéristiques pour les maillages animés

L'extraction de points caractéristiques est un sujet longtemps étudié en vision par ordinateur, traitement de l'image et l'infographie. Traditionnellement, les caractéristiques sont souvent extraites de différentes modalités et entités graphiques tels que des images 2D / 3D, des vidéos, des maillages polygonaux et des nuages de points. Par conséquent, il est particulièrement regrettable que le problème de la détection de points caractéristiques sur des maillages animés reste peu étudiée. Bien que les points caractéristiques classiques sont directement liés à voisinage local statique et à la géométrie, nous proposons une nouvelle technique de détection de caractéristiques basée sur le comportement dynamique de la forme et de ses caractéristiques de déformation.

Dans cette thèse, nous développons d'abord un cadre de détection de caractéristiques spatio-temporel sur des maillages animés basés sur les approches spatiales à grande échelle. Notre système de détection de caractéristiques est ensuite utilisée pour la correspondance de forme dynamique clairsemée et dense. Notre algorithme étend les détecteurs spatiales de points d'intérêts sur des maillages statiques (Pauly, Keiser et al. 2003, Castellani, Cristani et al. 2008, Zaharescu, Boyer et al. 2009, Darom et Keller 2012) de manière à détecter des points caractéristiques spatio-temporel sur des maillages animés. Basé sur des caractéristiques de déformation calculées à chaque sommet dans chaque trame, nous construisons l'espace d'échelle en calculant différentes versions lissée des données d'animation. Au cœur de notre algorithme est une nouvelle opérateur spatio-temporal Différence de Gaussiennes (DoG), ce qui se rapproche de la, Laplace échelle normalisée spatio-temporelle. En calculant les extrema locaux du nouvel opérateur dans l'espace-temps et de l'échelle, on obtient des ensembles reproductibles de points caractéristiques spatio-temporelles sur différentes surfaces déformées modélisées sous forme d'animations de triangle de maillage. Nous validons l'algorithme proposé dans sa robustesse et la cohérence de détection de caractéristiques. Pour le meilleur de nos connaissances, notre travail est le premier qui aborde le détection de caractéristiques spatio-temporelle en maillages animés.

Les caractéristique que nous voulons extraire sont les blobs, qui sont situées dans des régions qui présentent une forte variation de la déformation spatialement et temporellement. Nous définissons d'abord des attributs de déformation locales sur le maillage d'animation, à partir de laquelle nous construisons une représentation

multi-échelle de celui-ci. L'une des principales motivations pour fonder notre méthode sur la déformation de la surface locale peut être expliqué par le fait que (1) la déformation locale sur une surface peut être efficacement mesurée par certains principes bien définis, et que (2) la dimension intrinsèque du domaine est de $2D + \text{temps}$ (plutôt que $3D + \text{temps}$) avec une hypothèse raisonnable sur les données.

Nous proposons d'utiliser des tensions de triangle locaux comme une caractéristique de déformation de surface. Par définition tension triangle porte de mesure pure pour de déformation non rigide. Nous améliorer encore les caractéristiques de déformation par fusion robustesse tension de triangle avec la variation de courbure moyenne. La dernière nous permet de capturer des déformations presque isométriques telles que la flexion. De telles caractéristiques de déformation, comme nous le montrons dans l'évaluation du procédé, sont cohérent avec la perception de maillages déformés par l'oeil humain. Deuxièmement, nous aimerions que le point caractéristique dynamique porte les informations à propos de l'étendue spatiale et temporelle de la déformation exposée dans un lieu de détection de caractéristiques. En outre, nous avons prouvé être correct à utiliser des outils mathématiques de la théorie de l'espace échelle linéaire afin de répondre fonctionnalité représentation multi-échelle. La théorie de l'espace à l'échelle linéaire est un sous-ensemble des cadres de l'espace à l'échelle développés dans la communauté de visions par ordinateur dans les années 1980. Au cours de la dernière décennie, il a attiré l'attention dans l'analyse de surface polygonale. Dans cette thèse, nous définissons des mécanismes spatiaux à grande échelle pour l'extraction de points caractéristiques de maillages animés. Certains des résultats de détection de caractéristique de notre procédé sont représentées sur la Figure 1-1.

1.2 Correspondance entre maillages animés

Si nous voulons élaborer des techniques de correspondance de formes, capables d'exploiter des ensembles de données conséquents sur des images dynamiques, il nous faut mettre en perspective le pipeline traditionnel des méthodes de correspondance de formes en essayant de comprendre où et comment la mobilité peut être encapsulée. Pour ce faire, nous nous efforcerons de répondre aux questions suivantes: - Comment représenter efficacement le mouvement sur des images dynamiques aux différentes étapes de la correspondance de formes? - Comment interpréter les données de mouvement pour trouver des correspondances fiables?

Dans cette thèse nous détaillerons de nouvelles méthodes de correspondances entre différents maillages animés. Notre méthode se distingue de celles existantes dans son utilisation des propriétés dynamiques des maillages animés plutôt que dans l'utilisation des ses propriétés géométriques. Dans le cadre de cette thèse nous avons élaboré un nouveau descripteur de points dynamiques faisant office de signature robuste des caractéristiques dynamiques. Étant donné la mesure de similarité entre ces descripteurs de points dynamiques, nous appréhendons la correspondance de maillages animés en calculant en premier lieu les correspondances des caractéristiques dynamiques puis en établissant ensuite la correspondance complète entre chaque sommet des animations cibles et des animations sources.

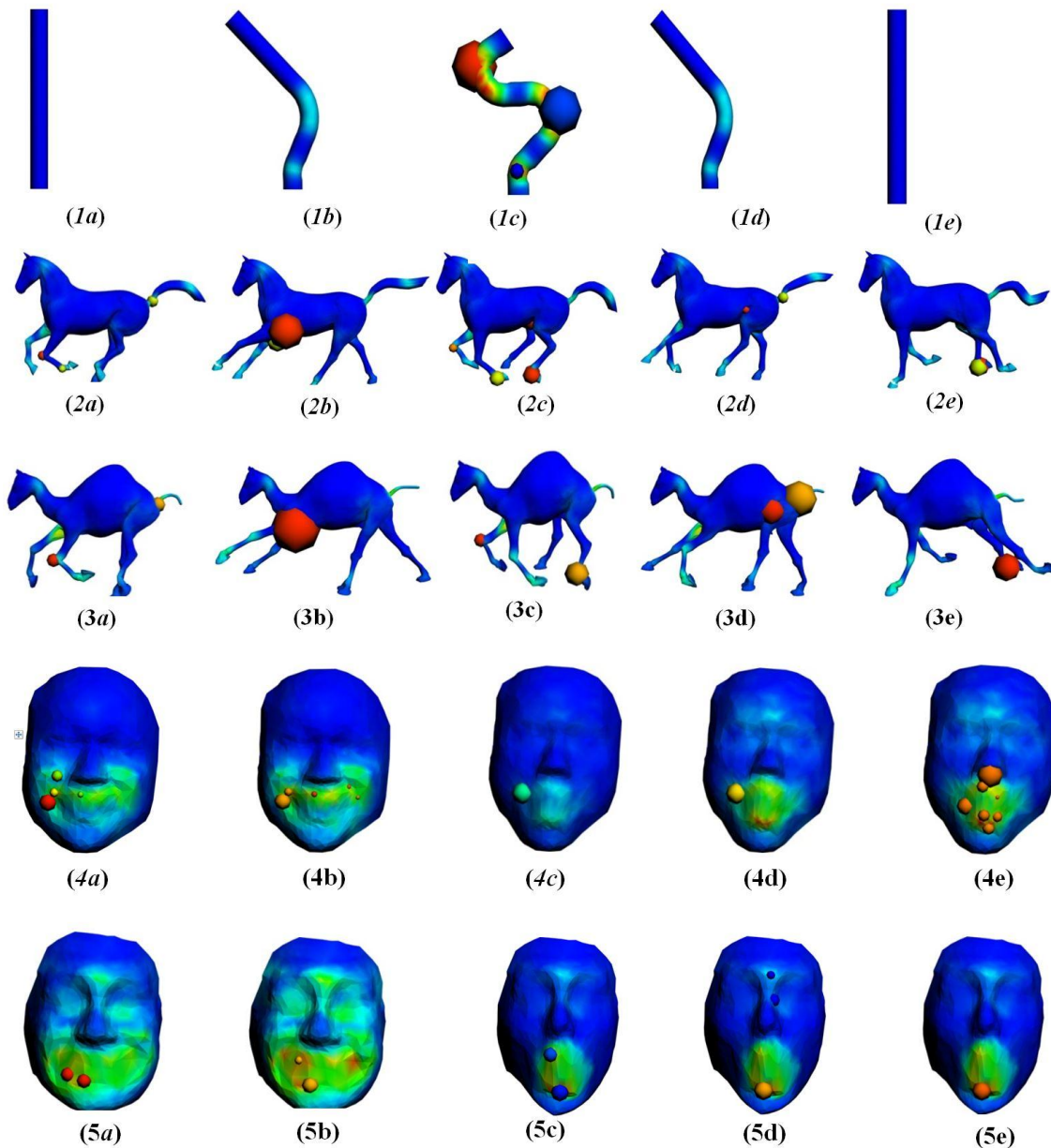


Figure 1-1. points caractéristiques dynamiques détectées par notre cadre sont illustrés sur un certain nombre d'images sélectionnées de maillages animés. La couleur d'une sphère représente l'échelle temporelle (du bleu au rouge) du point caractéristique, et le rayon de la sphère indique l'échelle spatiale.

La technique proposée se décompose en plusieurs sous-étapes majeures. La première étape (Figure 1-2(1)) d'extractions des caractéristiques dynamiques d'un maillage animé est décrite dans le chapitre 3. Ensuite, chaque caractéristique de la source et de la cible est liée avec le descripteur de points caractéristiques dynamiques (Figure 1-2(2)), et mis en correspondance avec les caractéristiques généraux (Figure 1-2(3)) puis avec le maillage complet (Figure 1-2(4)). Nous avons conçu notre nouvelle signature de points caractéristiques de sorte à ce qu'elle permette, non seulement d'acquérir de façon robuste les propriétés de mouvement, mais aussi une correspondance de caractéristiques efficace. En se basant sur ces descripteurs de point caractéristiques, notre approche consiste ensuite à calculer les correspondances initiales des points caractéristiques dynamiques en utilisant la technique de correspondance de graphe de décomposition duale (Torresani, Kolmogorov et al. 2008).

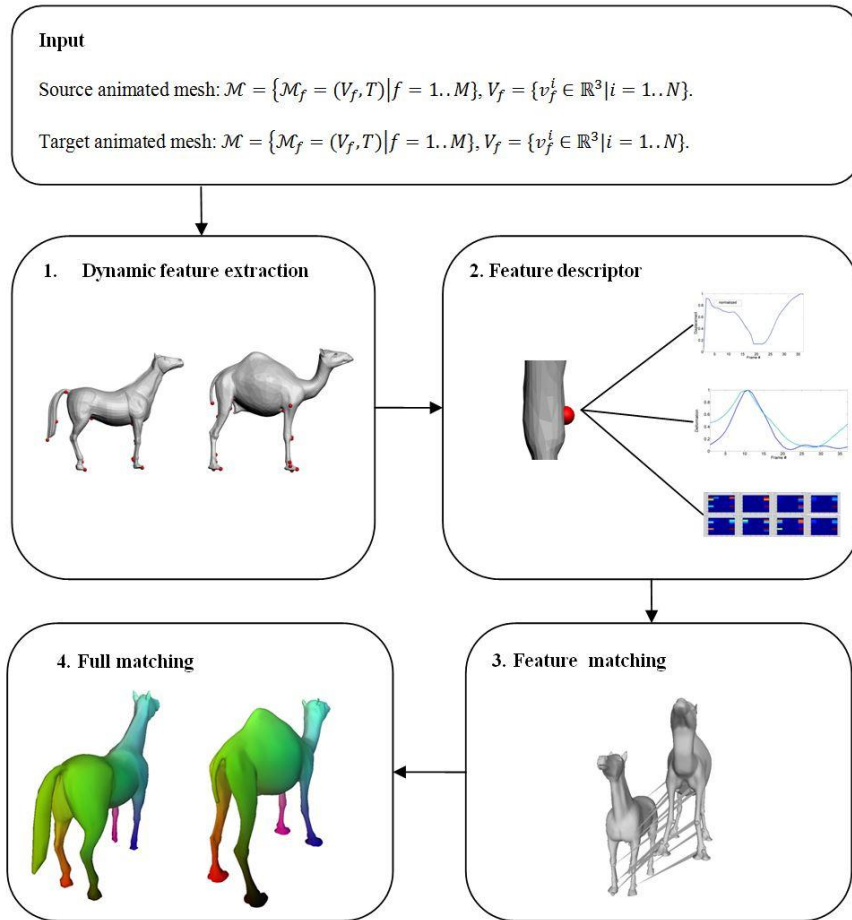


Figure 1-2. Pipeline proposée pour établir la correspondance de maillages dynamiques. (1) Détection de caractéristiques dynamiques. (2) Descripteur de caractéristiques dynamiques. (3) Correspondances des caractéristiques. (4). Correspondance forte.

Enfin, nous avons conçu une nouvelle approche pour la correspondance forte entre des maillages sources et cibles en projection sphérique. Une correspondance complète en paramétrisation sphérique se formule en tant que séquence de distorsion en domaine sphérique qui aligne de façon optimale les correspondances des caractéristiques dynamiques (Figure 1-3). Un exemple d'une telle correspondance entre deux maillage animés est présenté en Figure 1-4.

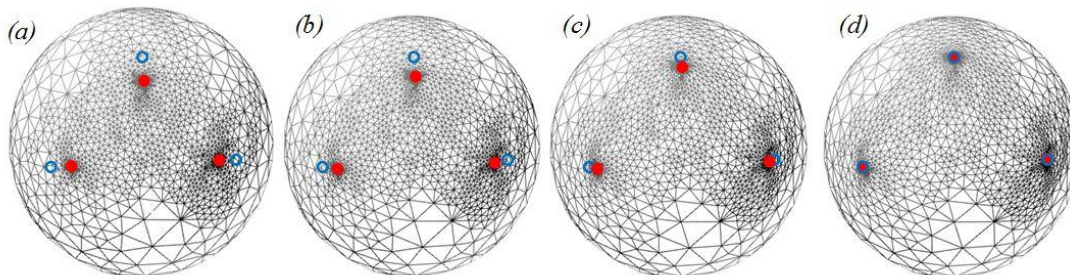


Figure 1-3 Distorsion des sommets du maillage pour déplacé les points caractéristiques (en bleu) jusqu'à leurs positions cibles (en rouge). Les Figures (a) et (b) sont le maillage sphérique avant et après leur distorsions respectives. Les Figures (b) et (c) sont étapes intermédiaire de cette distorsion.

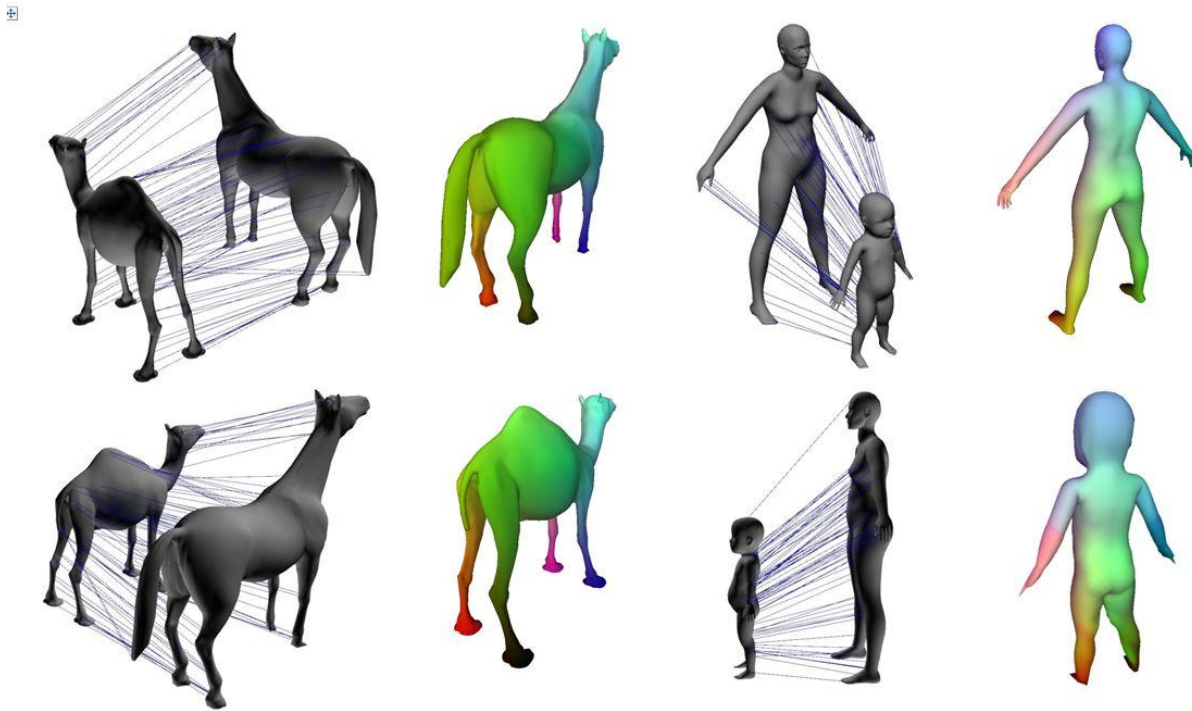


Figure 1-4. Exemple de correspondance forte. La couleur désigne la correspondance des sommets.

1.3 Cas des maillages animés avec changement de connectivité

Comme établi dans les chapitres 3 et 4, notre framework de détection/description de la caractéristique dynamique et la correspondance de la forme basé sur les caractéristiques est conçu pour le domaine des maillages animés. Par définition, un maillage animé est une séquence ordonnée de maillages avec une connectivité de maillage fixée et des correspondances de sommets entre-frames connues au préalable. Cependant, ceci est une hypothèse relativement forte qui n'est pas nécessairement maintenue pour des grandes variations de la géométrie dynamique disponible, en particulier, dans la géométrie obtenue par l'acquisition des données réelles.

Dan le cadre de notre travail, nous abordons le problème du traitement des déformations des maillages qui changent la connectivité au cours du temps. Nous proposons une technique rapide et efficace, qui peut être utilisée potentiellement pour établir les correspondances entre-frames dans les maillages qui se déforment au cours du temps, ce qui lui permet d'être applicable aux algorithmes d'analyse de formes et de correspondance présentés dans les chapitres 3 et 4.

Notre première observation est que quelques caractéristiques géométriques sont souvent persistantes à travers les changements et les mouvements des sujets. Ces caractéristiques qui persistent nous permettent de définir un système de coordonnées géodésiques pour localiser n'importe quel point sur la donnée en entrée et son correspondant sur le maillage cible. Nous développons notre méthode uniquement pour n'importe quel sommet indiqué sur la forme, ce qui n'est pas nécessairement significatif géométriquement. L'un des plus principaux avantages de notre méthode en comparant aux algorithmes de correspondance de forme existants est son temps de calcul rapide. Ceci est possible car notre méthode est développée de façon optimale pour utiliser le minimum d'information pour identifier la localisation des points. La méthode a été initialement développée pour une correspondance rapide et fine et une correspondance grossière de "marqueur". Il est à

noter que notre méthode de correspondance non rigide est générale et n'est pas limitée uniquement aux correspondances des déformations de maillage entre frame. La méthode peut être utilisée dans plusieurs cas de correspondance de formes non rigides avec des contraintes isométriques raisonnables. Nous avons montré une performance robuste de notre méthode pour les correspondances de forme non rigide.

Les différentes étapes de notre algorithme sont illustrées dans la Figure 1-5.

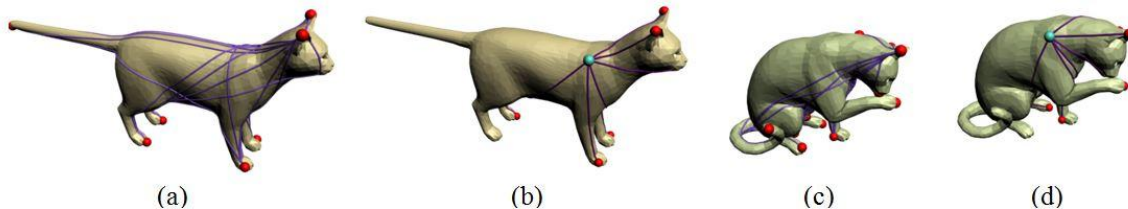


Figure 1-5. Vue d'ensemble de notre approche. Les points caractéristiques de la géométrie extraits sont marqués avec des sphères rouges, et les marqueurs bleus. (a) Les points caractéristiques de la géométrie sont extraits sur le maillage d'entrée, à partir duquel le graphe complet est calculé (b) Des marqueurs fournis sur le maillage d'entrée, le graphe minimal pour les marqueurs est construit (c) Similairement au maillage d'entrée, les points caractéristiques de la géométrie sont extraits, et le graphe complet est calculé sur le maillage cible. (d) Un point correspondant est calculé sur le maillage cible par l'utilisation d'une correspondance partielle des graphes complets.

Malheureusement, les maillages sont approximativement isométriques et une telle méthode peut échouer pour estimer efficacement la localisation des marqueurs, notamment lorsque la déformation entre les deux maillages est grande. Nous résolvons ce problème en interpolant les distances géodésiques sur le maillage cible afin de compenser les changements des distances qui ont été induits en raison de la déformation non isométrique.

1.4 Conclusion

Dans le cadre de nos recherches, nous nous sommes intéressés à l'analyse de forme pour de la géométrie variable dans le temps (*ie.* maillages animés) et avons présenté de nouveaux algorithmes pour la détection de caractéristiques dynamiques, la description de ces caractéristiques sur des maillages animés ainsi que leur application à de la mise en correspondance de formes. Nous nous sommes particulièrement attachés à utiliser au maximum les propriétés dynamiques de mouvement dans des séquences de maillages animés pour l'extraction et la description de points caractéristiques dynamiques.

1.4.1 Contributions

Les travaux présentés dans ce manuscrit s'inscrivent dans la réalisation d'un pipeline de mise en correspondance de maillages animés en exploitant des caractéristiques liées à la déformation de leurs surfaces. Nos contributions sont les suivantes:

- Nous avons d'abord présenté une nouvelle technique de détection de points caractéristiques pour des séquences de maillages animés. Nous avons commencé par une approche basée sur des caractéristiques de déformation locale de la surface. Nous avons ensuite développé le coeur de notre technique d'extraction de caractéristiques dynamiques, basée sur la théorie des espaces d'échelles linéaires appliquée aux caractéristiques de déformation d'une animation. Nos contributions sont l'introduction d'une nouvelle représentation d'échelle spatio-temporelle de la déformation des surfaces animées et une extension du filtre DoG classique (différence de Gaussiennes) au cas spatio-temporel des maillages animés. Notre méthode est capable d'extraire de manière robuste et répétable des ensembles

cohérents de points caractéristiques entre les surfaces de différents maillages déformables. Les résultats de nos expérimentations sur différents types de jeux de données montrent une extraction de points caractéristiques cohérente pour des animations similaires d'un point de vue cinématique et sémantique.

- La principale contribution de nos travaux est un pipeline robuste de mise en correspondance de maillages animés, introduisant un nouveau descripteur de caractéristiques dynamiques. Celui-ci vient consolider nos nouvelles détection et description de caractéristiques dynamiques, et l'appariement épar/dense point à point. La nouvelle signature de points dynamiques que nous proposons se compose de différentes modalités de mouvement et propriétés de déformation des maillages animés. Elle nous a permis de faire un appariement *grossier* efficace et précis suivi d'un appariement *fin* robuste entre différents maillages animés.
- Enfin, dans le but de trouver des correspondances inter-frame pour des maillages animés disposant d'une connectivité évoluant dans le temps, nous avons développé une méthode d'appariement robuste et efficace pour des objets déformables quasi-isométriques. L'idée première est d'utiliser un minimum d'information pour localiser précisément un point en coordonnées géodésiques sur la surface du maillage source et de reconstruire sa position sur le maillage cible. L'intérêt majeur de la méthode est le faible coût en temps de calcul de l'appariement, étant donné que seul un nombre de points réduit a besoin d'être mis en correspondance. Nos tests confirment que cette approche présente des performances comparables aux algorithmes tirés de l'état de l'art.

1.4.2 Perspectives

Les méthodes étudiées dans ce manuscrit ouvrent la voie à de nouvelles directions prometteuses de recherche et d'intéressantes applications en rapport avec l'analyse de modèles animées. Voici quelques perspectives possibles pour ces travaux.

- En considérant les développements réalisés dans le cadre de cette thèse, une direction intéressante serait l'analyse statistique de maillages animés. Une manière de faire serait de mettre au point un modèle statistique qui capturerait à la fois les variations de la forme et la déformation résultant des mouvements d'instances distinctes d'animations provenant d'une base de données. De plus, des méthodes d'apprentissage pourraient être appliquées aux modèles statistiques pour améliorer les techniques de modélisation et d'animation d'humains virtuels.
- Nous envisageons également d'améliorer les algorithmes de mise en correspondance en capturant davantage de propriétés mécaniques des surfaces déformées. Dans la réalité, les lois de la physique gouvernent les mouvements et la déformation des objets, ce qui pourrait devenir un composant du pipeline de mise en correspondance de formes: les propriétés physiques telle que la tension des surfaces, ou les directions des tenseurs de déformation (jusqu'à présent nous n'avons employé que les magnitudes de ces tenseurs) pourraient en effet y être incorporées. Ces propriétés pourraient également être introduites dans le descripteur de points caractéristiques dynamiques. Une possibilité serait d'extraire les propriétés physiques des régions d'intérêt de la source et de comparer les directions du champ tensoriel de déformation extrait de celles estimées sur le maillage de destination. La mise en correspondance de formes pourrait alors être exprimée comme une optimisation globale comparant et alignant les champs tensoriels de déformation des surfaces source et destination.

Enfin, notre détection de points caractéristiques dynamiques peut être employée pour de nombreuses applications en animation par ordinateur, comme la simplification de surfaces animées, la sélection d'un cadrage optimal, l'alignement ou la recherche de similarités entre différentes animations.

- *Simplifications de surfaces animées.* Notre algorithme pourrait être utilisé dans ce but étant donné qu'il détecte des points caractéristiques se trouvant précisément dans les régions déformées. Leur échelle spatiale peut être utilisée pour définir des régions dans lesquelles le maillage doit conserver un échantillonnage plus dense lors de la simplification. L'échelle temporelle peut également être utilisée pour déterminer dynamiquement le coût d'un triangle situé près d'un point caractéristique. Une très petite échelle temporelle implique une animation soit très courte, soit très rapide, ce qui requerrait d'assigner au point caractéristique une priorité basse. À l'inverse, les régions situées autour de points caractéristiques dotés de grandes échelles temporelles recevraient une priorité plus haute.
- *Sélection d'un cadrage optimal.* Il peut être très commode de disposer d'un outil de sélection automatique de cadrage pour la génération d'aperçus dans des bases de données d'animations. L'idée est de permettre à l'utilisateur de parcourir l'animation aux points qui maximisent la visibilité des déformations du maillage. Avec une telle sélection de points de vue, l'utilisateur bénéficie d'une meilleure perception de l'animation. Une manière tout aussi pratique et simple de sélectionner automatiquement un point de vue optimal est de calculer celui qui maximise le nombre de points caractéristiques visibles durant l'optimisation. On peut noter que nos points caractéristiques spatio-temporels peuvent simplifier la sélection d'un ou de plusieurs bons points de vue. Par exemple, la qualité d'un point de vue pourrait être définie comme une fonction de la visibilité de ces points caractéristiques, en termes de nombre total, de variabilité temporelle, de concavité des régions caractéristiques projetées (définies par les échelles spatiales et temporelles), etc.

Mots-clés

Keywords Animated mesh; Feature detection; ·Feature descriptor;· Scale-space theory; Difference of Gaussians; Shape correspondence

Contents

Acknowledgements	ii
Abstract	iii
Keywords	iv
Résumé	1
Mots-clés	1
List of notations	13
List of Figures	14
List of Tables	18
Chapter 1 Introduction	20
1.1 Context.....	20
1.2 Contributions.....	22
1.3 List of publications	23
Chapter 2 Related work: Non-rigid correspondence and matching methods	24
2.1 Feature based methods	25
2.2 Tree- or graph- based matching (combinatorial search)	25
2.3 Iterative improvement	27
2.4 Voting and clustering	28
2.5 Random sampling	30
2.6 Embedding-based shape correspondence.....	31
2.7 Use of prior-knowledge	36
Chapter 3 Feature detection for animated meshes	38
3.1 Introduction.....	38
3.2 Related work: Feature point detection based on scale-space theory	40
3.2.1 Feature detection on static meshes	40
3.2.2 Feature detection on time varying geometry	43
3.3 Animated mesh	45
3.4 Deformation characteristics	46

3.5	Basics of linear scale-space theory	47
3.6	Scale-space of surface deformation characteristics.....	49
3.6.1	Relationship between box filter and Gaussian filter widths.	50
3.7	Spatio-temporal DoG operator.....	52
3.8	Feature point detection for animated meshes.....	53
3.9	Experiments	55
3.9.1	Consistency.....	58
3.9.2	Comparison to the manually selected feature points	60
3.10	Conclusion	61
Chapter 4	Correspondence between animated meshes	62
4.1	Introduction.....	62
4.2	Related work : Feature point descriptors	63
4.2.1	Spatial feature descriptors for surface matching.....	64
4.2.2	Spatio-temporal feature descriptors.....	69
4.3	Feature point signature.....	72
4.3.1	Normalized displacement curves.....	73
4.3.2	Spatio-temporal scales σ, τ	75
4.3.3	Deformation characteristics curves.....	77
4.3.4	Animated meshes Histogram-of-Gradients (AnimMeshHoG).....	78
4.3.5	Composite descriptor	83
4.4	Displacement feature points.....	84
4.5	Feature correspondence via graph matching.....	86
4.5.1	Graph matching formulation.....	86
4.5.2	Dual decomposition.....	89
4.5.3	Improving geodesic distortion term.....	92
4.5.4	Experiments	94
4.6	Full matching	96
4.6.1	Spherical embedding	96
4.6.2	Iterative warping.....	98
4.7	Conclusion	101
Chapter 5	Case of animated meshes with changing mesh connectivity	102
5.1	Introduction.....	102
5.2	Outline of the method	103
5.3	Graph construction on the source mesh	104

5.3.1	Geodesic distance computation	104
5.3.2	Feature point extraction	104
5.3.3	Construction of the full graph on the source mesh	105
5.3.4	Minimal graph construction.....	105
5.4	Landmark transfer via graph matching	109
5.4.1	Construction of the full graph GF on the target mesh	109
5.4.2	Matching the minimal graph to the full graph	109
5.4.3	Landmark transfer.....	109
5.5	Results.....	113
5.5.1	Timing	113
5.5.2	Robustness	114
5.5.3	Inverse distance weighting scheme	118
5.5.4	Comparison with existing methods	119
5.5.5	Limitations.....	120
5.6	Conclusion	121
Chapter 6	Conclusion	123
6.1	Contributions.....	123
6.2	Future directions	124
Chapter 7	Appendices	127
7.1	Appendix A. MOCAP Data Acquisition Process	127
7.2	Appendix B : Subgraph matching using Ullmann's Algorithm	129
References	130

List of notations

Operators

$f * g$	convolution operator
\times	cross product
∇^2	Laplacian operator
Δ_M	Laplace-Beltrami operator over a manifold M
\propto	proportional to

Animated mesh

$c_d^{\mathbf{p}}$	normalized deformation characteristic curve at a feature point \mathbf{p} in an animated mesh
$\Delta^{\mathbf{p}}$	normalized displacement curve at a feature point \mathbf{p} in an animated mesh
$d(v)$	local surface deformation characteristics at a vertex v of an animated mesh \mathcal{M}
$D_{\Delta^{\mathbf{p}}}$	distance metric between normalized displacement curves
$D_{c_d^{\mathbf{p}}}$	distance metric between normalized deformation characteristic curves
$D_{H^{\mathbf{p}}}$	distance metric between Animated Mesh Histograms-of-Gradients
$D_{\mathcal{H}}$	distance metric between composite dynamic feature descriptors
$G(\mathbf{x}, \sigma)$	Gaussian function with standard deviation σ
$\Gamma_{\mathbf{p}, \mathbf{q}}^M$	geodesic path from a point \mathbf{p} to point \mathbf{q} on a mesh M
$H^{\mathbf{p}}$	Animated Mesh Histograms-of-Gradients at a feature point \mathbf{p} of an animated mesh
\mathcal{H}	a composite dynamic feature point signature
\mathcal{M}	an animated mesh
$N_s^1(\mathbf{p})$	1-ring spatial neighbourhood of a point \mathbf{p} of a mesh
$N_s^k(\mathbf{p})$	k -ring spatial neighbourhood of a point \mathbf{p} of a mesh
$N_t^1(\mathbf{p})$	1-ring temporal neighbourhood of a point \mathbf{p} of an animated mesh
$N_{st}(\mathbf{p})$	a spatio-temporal neighbourhood of a point \mathbf{p} in an animated mesh \mathcal{M}
$N_{\sigma\tau}$	a set of eight direct neighbours in a spatio-temporal scale space
$\vec{\mathbf{n}}_v$	a normal vector at vertex v of a mesh
\mathbf{p}	a dynamic feature point extracted from an animated mesh \mathcal{M}
P	a set of dynamic feature points extracted from an animated mesh \mathcal{M}
$s(v)$	average strain values of adjacent triangles of a vertex v
$V(\mathbf{p})$	a spatio-temporal volume around a feature point \mathbf{p}

List of Figures

Figure 1-1. The overview of the animated mesh correspondence pipeline.....	21
Figure 2-1. Hierarchical matching approach	26
Figure 2-2. Refinement of a hierarchical solution.....	26
Figure 2-3. The two-phases deformation of a template via energy minimization...	28
Figure 2-4. Articulated shape matching	29
Figure 2-5. Electors voting scheme.....	30
Figure 2-6. Matching isometric shapes by embedding them into a lowdimensional Euclidian space	31
Figure 2-7. Isometric matching with Uniformization of surfaces	32
Figure 2-8. The pipeline of the Möbius voting algorithm.....	32
Figure 2-9. Blended Intrinsic Maps.	33
Figure 2-10. Heat Kernel Signature matching	34
Figure 2-11. Heat Kernel Signature correspondence pairs	34
Figure 2-12. Matching results between voxelized articulated shapes.	35
Figure 2-13. Alignment of the shapes in spectral domain.....	36
Figure 3-1. Mesh saliency.	41
Figure 3-2. Feature detection from photometric scalar field and mean curvature ..	42
Figure 3-3. The neighbourhood of the vertex in scale space of mean curvature ...	42
Figure 3-4. Features computed on armadillo model with Harris operator	43
Figure 3-5. Features on models at different Levels of Details	43
Figure 3-6. Saliencies based on mean curvature, velocity, and acceleration	44
Figure 3-7. Animated mesh examples.....	45
Figure 3-8. Rest shapes for defining the deformation characteristics.	47
Figure 3-9. Local deformation characteristics.....	48
Figure 3-10. The smallest possible spatio-temporal neighborhood	49
Figure 3-11. Scale space of an input animated mesh.	50
Figure 3-12. Multi-scale deformation characteristics on an animated mesh.....	50
Figure 3-13. The DoG response function evaluation	51
Figure 3-14. A 2D illustration of our feature detection method.....	54
Figure 3-15. The consistent behavior of our feature detector	57
Figure 3-16. Dynamic feature points detected by AniM-DoG.....	58

Figure 3-17. Inter-subject consistency of feature points	59
Figure 3-18. The matching error plots of feature points	60
Figure 3-19. Comparison of the manually and automatically selected features	61
Figure 4-1. Proposed pipeline for animated mesh matching.....	63
Figure 4-2. Spin image shape descriptor.....	64
Figure 4-3. 1-D Curvature maps of Gaussian and Mean curvature.....	65
Figure 4-4. Illustration of geodesic fans.	65
Figure 4-5. 2D analogy of the Integral Volume descriptor	66
Figure 4-6. Clockwise spiral path around a feature point	67
Figure 4-7. Spherical histogram used to compute local histograms.....	67
Figure 4-8. Heat Kernel Signatures for the dragon model	68
Figure 4-9. Three isocurves of the Intrinsic wave descriptor.....	68
Figure 4-10. IWD descriptor can capture local and global shape properties.	69
Figure 4-11. 2D SIFT image descriptor	69
Figure 4-12. 3D SIFT descriptor.....	71
Figure 4-13. The computation pipeline of the HOG3D descriptor.	71
Figure 4-14. Similarities between drastically different meshes	72
Figure 4-15. Normalized and not normalized displacement curves.....	74
Figure 4-16. Normalized displacement curves.....	74
Figure 4-17. Interpolated displacement curves	75
Figure 4-18. The amplitude of first order normalized derivatives	76
Figure 4-19. Semantically different features of similar characteristic scales.....	76
Figure 4-20. Deformation functions of the corresponding features	78
Figure 4-21. The steps of AnimMeshHoG computation pipeline	79
Figure 4-22. Consistent normals directions with respect to a feature's normal	79
Figure 4-23. Spatio-temporal volume centered around dynamic feature	80
Figure 4-24. Scattered deformation characteristics.....	81
Figure 4-25. Deformation characteristics inside spatio-temporal volume.	81
Figure 4-26. Interpolation of AnimMeshHoG histograms	82
Figure 4-27. Displacement feature points	85
Figure 4-28. Geodesic distortion in assignments	88
Figure 4-29. Relationship between the primal and dual optimization problems.....	89
Figure 4-30. Problem decomposition of the dual optimization problem.	90
Figure 4-31. Local subproblem decomposition.....	91

Figure 4-32. Average geodesic distance maps.....	92
Figure 4-33. Change of average geodesic distance along the paths.....	93
Figure 4-34. Edge weights before and after the average geodesic distance prior ...	94
Figure 4-35. Matching result between feature of the cylinders.....	95
Figure 4-36. Feature matching result between the horse and camel	95
Figure 4-37. Inter-subject matching of the dynamic features	95
Figure 4-38. The bijective mapping using spherical parameterization	97
Figure 4-39. A feature point pair drive the iterative warping steps.	97
Figure 4-40. Warping of the mesh vertices	98
Figure 4-41. Fine matching between different animated mesh models	100
Figure 5-1. Mesh connectivity is dissimilar in different postures of the subject ..	102
Figure.5-2. Overview of landmark transfer approach.....	103
Figure. 5-3. Convexity and geometric feature points on the mesh.....	105
Figure. 5-4. Construction of the minimal graph.....	107
Figure. 5-5. Enclose-by-nodes of the landmark location.	107
Figure. 5-6. Influence of pose change on the geodesic path	110
Figure. 5-7: Histograms of the corresponding point on the source and target	111
Figure. 5-8: The length variation of corresponding geodesic paths	112
Figure 5-9. The models used have different number mesh structures.....	113
Figure. 5-10. Impact of the landmark location on the quality of transfer	114
Figure 5-11. Results obtained from our landmark transfer technique.....	115
Figure. 5-12. Quality of landmark transfer with respect to the ground truth	117
Figure. 5-13. Performance of LTMG method on a genus-one plate model	118
Figure. 5-14: Quality of landmark transfer without and with the IDW.	118
Figure. 5-15. Error plots from the BIM, MOB, LTMG techniques	119
Figure. 5-16. Quality of transferred landmark	122
Figure 7-1. Vicon system installation	127
Figure 7-2. Data acquisition in MOCAP session	128

List of Tables

_Toc413763516

Table 3-1. The animated meshes used in the experiments.....	55
Table 4-1. Time complexity, storage complexity of the feature point signature.	84
Table 4-2. Dynamic feature matching results.	94
Table 5-1: Average computation time.of the landmark trasnfer.	114

Chapter 2 Introduction

2.1 Context

Shape matching is a fundamental problem in many research disciplines, such as computational geometry, computer vision, and computer graphics. Commonly defined as a problem of finding one-to-one/one-to-many/many-to-many point-based mappings between a source and a target, it constitutes a central task in numerous applications including attribute transfer, shape retrieval and analysis. For example, it allows an automatic re-usage of attributes, such as texture information or other surface characteristics, from the source object to a number of targets. In shape retrieval, one can first compute the correspondence between query shape and the shapes in a database, then obtain the best match by using some predefined matching quality metric. It is also particularly advantageous in applications based on statistical shape modeling. By encapsulating the statistical properties of the anatomy of the subject in the shape model, such as inter- and intra-subject geometrical variations, density variations etc., it is helpful not only for the analysis of anatomical structures such as organs or bones and their valid variations, but also for learning the deformation models of the given class of objects.

However, finding a reliable, efficient matching is an inherently challenging task, at least due to two reasons: First, typically large size of data sets increases combinatorially the time complexity of the matching algorithms. Given two shapes discretized as polygonal meshes of M and N vertices respectively, the exhaustive (brute force) search for point-to-point correspondence is comprised of $\binom{M \cdot N}{N} = \frac{(M \cdot N)!}{N!(M \cdot N - N)!}$ evaluations. In order to avoid impractically expensive brute force search, heuristics are often used for computing the shape correspondence. Note, that size of time-varying data sets we consider in this dissertation is even higher, which makes it even more difficult to work with. In this thesis, we first extract feature points using dynamic properties of the animated mesh, and solve for a sparse matching among the feature points. We then propagate the matching results to a full matching so that the similarity of dynamic properties is locally maximized. Second difficulty of shape matching comes from the input data, which can be incomplete or cluttered with geometric/topological noise. Therefore, in order to keep a realistic trade of between the two main shape matching complexities, in this thesis we focus on processed data sets in a form of animated meshes with a fixed mesh connectivity over time, rather than directly working on a raw data.

In this thesis, we are interested in investigating a novel shape matching method that exploits large redundancy of information from *dynamic, time-varying* datasets. Recently, a large amount of research has been done in computer graphics on establishing correspondences between static meshes (Angelov, Srinivasan et al. 2005, Aiger, Mitra et al. 2008, Castellani, Cristani et al. 2008). These methods rely on the geometric features or extrinsic/intrinsic properties of static surfaces (Lipman and Funkhouser 2009, Sun, Ovsjanikov et al. 2009, Ovsjanikov, M erigot et al. 2010, Kim, Lipman et al. 2011) to efficiently prune matching pairs. Although the use of geometric feature is still a golden standard, methods relying solely on the static information of shapes can generate in grossly misleading correspondence results when the shapes are drastically different or do not contain enough geometric features.

We argue that by considering objects that undergo deformation we can extend the limited capability of static geometry information and obtain more reliable, high quality correspondence computation between shapes. The

key observation is that an animated mesh contains significantly more information rather than its static counterpart. Encouragingly, animated mesh data sets become more popular and affordable today due to advancing developments of optical sensors and motion capture devices (Dobrian and Bevilacqua 2003, Vlastic, Adelsberger et al. 2007, Camplani and Salgado 2012, Webb and Ashley 2012), performance capture schemes (Valgaerts, Wu et al. 2012, Cao, Weng et al. 2013), post processing algorithms (Weise, Li et al. 2009, Weise, Bouaziz et al. 2011), and animation techniques and retargeting (Sumner and Popović 2004, Li, Weise et al. 2010).

Intrigued by the idea of using dynamic deformation properties of meshes for the improved shape matching, we investigate a novel shape correspondence method that takes advantage of a large set of supplementary information from shape’s dynamic motion data. As have discussed, employment of shape’s dynamic deformation characteristics is a reasonable investment that can make a significant difference in the capability of shape correspondence. The main contribution we bring in this thesis is a novel scheme that processes subjects’ movement and surface deformation characteristics – we devise a new shape matching method that makes use of this rich bundle of motion information that ensures reliable and efficient shape correspondence. To the best of our knowledge, there is no existing work that examines deformation or motion properties of time-varying shapes in shape matching, despite their increasing availability and relevance.

To reach the aforementioned objective, we focus on how to efficiently represent the motion data and how to encode the movement data towards finding reliable shape correspondence. We reconsider the main phases of typical correspondence search approaches by incorporating the dynamic data into the shape-matching pipeline. We develop a dynamic multi-scale feature extraction algorithm, a sparse correspondence among features using dynamic feature signatures, and a follow-up dense shape correspondence. The overall outline for the proposed work is depicted in Figure 2-1.

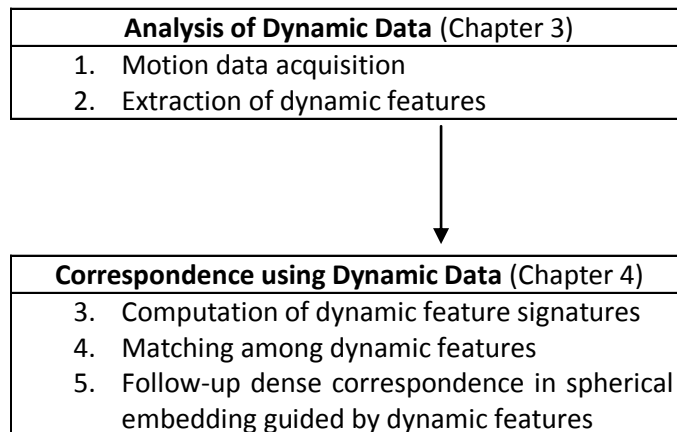


Figure 2-1. The overview of the proposed animated mesh motion-based correspondence pipeline. Each item represents a sub-task of the method presented in the thesis.

In Chapter 3, we develop a spatio-temporal feature detection framework on animated meshes based on the scale space approaches. For a given set of dynamic features on each of the source and target shapes, the goal is to efficiently estimate the correspondence by putting points with similar dynamic feature signatures into correspondence. This task specifically required developing similarity measures between dynamic feature points, which is detailed in Chapter 4. The dynamic features along with shape-based geometric features are then used to guide the dense correspondence for the optimal match (Chapter 4). In Chapter 6 we present a shape corre-

spondence method for approximately isometric¹ deforming meshes that correspond to the majority of human, animal and articulated object motions. The method shows high quality intra-subject matching results and can be potentially used to compute inter-frame correspondence in animated meshes with changing mesh graph structures.

2.2 Contributions

Our shape correspondence approach for animated meshes brings several contributions: multi-scale surface deformation characteristics, multi-scale dynamic feature point detector and descriptor. All of these items finally formed a solid basis of our sparse and dense matching scheme for animated meshes.

Our first contribution is a new feature detection technique on animated mesh sequences. In the core of the proposed technique the principles of the linear scale-space theory are encapsulated. Our sub-contributions here include: introduction of a new spatio-temporal scale representation of animated meshes surface deformation, extension of classical DoG (Difference of Gaussians) filter to spatio-temporal case of animated meshes. Our method is able to robustly extract repeatable sets of feature points over different deforming surfaces modelled as triangle mesh animations. Validations and experiments on various types of data sets show consistent feature extraction results, as well as robustness to spatial and temporal sampling of mesh animation.

The second contribution of our work is a dynamic feature descriptor. We developed a complex dynamic feature descriptor for animated meshes that can effectively capture most of the motion properties such as vertex displacement functions, vertex deformation characteristics (local strain and curvature change) and spatio-temporal Histogram of Oriented Gradients for animated meshes. The combination of those motion properties results in the robust dynamic descriptor that can distinctively match feature points from the source to target animation.

We further devised a dense correspondence method between animated meshes that is effectively guided by matched pairs of dynamic feature points with respect to their dynamic signatures. Our shape correspondence method can help to cope with intrinsic symmetries that might be present in the animated mesh. For example, the confusion of vertices with respect to the two main sagittal and coronal symmetry planes of the human body can be recovered by considering dynamic properties of the body motions performing a certain action. Of course, the matching result might not be improved if the motions are also symmetric with respect to the body symmetry planes. However, that is exceptionally infrequent in the real world.

Finally, in case of complex animated meshes with time-varying mesh connectivity we propose an algorithm to efficiently and robustly establish inter-frame vertex correspondence in the animated mesh (Chapter 5). This landmark-based matching method is especially effective for the correspondence of nearly isometric shapes, which is commonly observed in inter-frame relationship of widespread variations of articulated motions of humans or animals.

In summary, the overall purpose of our research is to devise methods that can supply advanced shape analysis in computer graphics with significant contributions in multiscale deformable shape motion studies and time-varying surface correspondence. Our novel solution to the new demand for the analysis of dynamic shapes and correspondence adopts valuable dynamic information obtained from shape surface's motion data. That results in a new set of methods for shape analysis and shape matching, shading a light on even more interesting applications such as animation matching, spatio-temporal animation alignment, etc.

¹Isometry is bending and twisting of a surface without extra tension, compression or shear

2.3 List of publications stemming from this thesis

International journal publications

Mykhalchuk V., Seo H., and Cordier F., On Spatio-Temporal Feature Point Detection for Animated Meshes, extension/revision of an article presented at CGI 2014 ("AniM-DoG: A Spatio-Temporal Feature Point Detector for Animated Mesh"), to appear, *The Visual Computer*, Springer.

Mykhalchuk V., Cordier F., Seo H., Landmark Transfer with Minimal Graph, Vol. 37, Num. 5, pp. 539–552, *Computers & Graphics* (Elsevier), 2013.

International conferences

Mykhalchuk V., Seo H., and Cordier F., AniM-DoG: A Spatio-Temporal Feature Point Detector for Animated Mesh, full paper, the 31st Computer Graphics International (CGI), June 2014, Sydney, Australia.

Chapter 3 Related work: Non-rigid correspondence and matching methods

Correspondence problems abound in both 2-dimensional and 3-dimensional cases. In some cases they span over both dimension domains, such as 2D/3D registration (Blanz and Vetter 1999, Gilles, Reveret et al. 2010) – three-dimensional information is inferred from 2D images in which either the camera or the objects in the scene have moved. In this thesis we will concentrate on the correspondence and the registration problems on 3D surfaces. Fortunately, with the advent of improved sensor capability and fast computing power, it has become more and more common to acquire 3D images with, for example, laser range scanners (Allen, Curless et al. 2003, Seo and Magnenat-Thalmann 2003, Anguelov, Springivasan et al. 2005), multi-view image sequences (Plänkner, Apuzzo et al. 1999, Starck and Hilton 2007, de Aguiar, Stoll et al. 2008), and the latest 3D modalities (Williem, Yu-Wing et al. 2014).

Until about two decades ago, most of the boundary registration algorithms have focused on **rigid problems**, i.e., when the motion between the source and target is assumed to be rigid. Commonly used algorithms are Iterative Closest Point (ICP) (Besl 1992) and its variants. ICP alternates between computing correspondences between the source and target and performing a rigid transformation in response to these correspondences. The correspondences could be as simple as closest points, but also used are manually placed landmarks, or local shape descriptors. The transformation from source to target is accomplished by minimizing a cost function based on discrepancy metrics between source-to-target correspondences. The problem of **non-rigid correspondences/registrations** is more complex, as surface deformation must be accounted for in the transformation. In this case, computed geometric features are not necessarily persistent across shapes, and the correspondences finding can be unreliable. Thus, the only way to ensure successful matching is either to assume that the source and target surfaces are very close, to rely on features that are invariant to the assumed deformation (i.e. isometry, partwise rigid, etc.), or to benefit shape priors about the objects being registered (i.e., operating only on human faces, bodies, or brain surfaces). Here we limit our discussion to the correspondence/registration of 3D surfaces under non-rigid transformation.

Formally, the problem is to find the optimal correspondence or alignment by minimizing a combination of a feature term and a distortion term, as given by:

$$\min_M \alpha \cdot \text{dist}_{\text{lin}}(M) + \beta \cdot \text{dist}_{\text{quad}}(M \times M). \quad (3-1)$$

The M above is a set of geometric transformations for each element on the source surface so as to align the source shape to the target, in case of registration. In a discrete setting, the mappings are constrained to be one-to-one and M is the bijective correspondence. The first term $\text{dist}_{\text{lin}}(M)$ measures the dissimilarity between the descriptors of the two shapes. The second term measures the global consistency or regularization, such as geodesic² distance or smoothness. Measuring the consistency in global structures of the two shapes serves as a constraint that can be used to guide the algorithms more effectively to a correct solution, by pruning the poten-

² A geodesic distance between points x and y on a surface is a shortest within surface path between x and y .

tial correspondence. One commonly used constraint is the approximately isometric deformation (where geodesic distances are nearly invariant) between the source and the target, which can be observed in many real-world deformations such as skeleton driven deformation. Many of robust correspondences have been demonstrated using this constraint, as we will review in this subchapter. The regularization is typically done in the registration setting, by penalizing large deformations. Typically, transformations of neighboring vertices are similar (transformation smoothness).

In this section, we classify existing methods of non-rigid correspondence according to their computational paradigms: feature based methods (3.1), tree- or graph-based matching (3.2), iterative improvement (3.3), voting (3.4) and random sampling (3.5), use of embeddings (3.6), and prior-knowledge (3.7).

3.1 Feature based methods

The most common approach is to first compute a set of discriminative feature points on both shapes along with a local, isometry invariant descriptor and then try to find a matching of these features such that the pairwise geodesic distances between all corresponding pairs of feature points are preserved. We refer to Section 5.2 for the feature descriptors and those who rely heavily on the descriptors for the matching.

3.2 Tree- or graph- based matching (combinatorial search)

An alternative formulation of is to find matching or correspondence without actually aligning the shapes. The correspondence is denoted by a mapping $C: X \times Y \rightarrow \{0,1\}$ such that

$$C(x,y) = \begin{cases} 1, & x \in X \text{ corresponds to } y \in Y, \\ 0, & \text{otherwise.} \end{cases}$$

The dimensionality of the problem allows us to handle only up to several dozens of points. Let S and T have n and m vertices, respectively. The number of possible correspondence between S and T is nm , and thus, the dimension of the quadratic problem is $nm \times nm$. Even for a small number of points, e.g. 30, the problem becomes almost infeasible.

To avoid exponential complexity, many previous methods concentrate on the problem of sparse correspondence, using global and structural shape descriptors such as skeleton graphs (Sundar, Silver et al. 2003, Au, Tai et al. 2010) or reeb graphs (Biasotti, Marini et al. 2006, Tierny, Vandeborre et al. 2009). Each graph node corresponds to a semantic part of the shape or a feature point, and is assigned a geometric attributes for graph matching. When the goal is to find sparse matching (among feature points, for example), combinatorial matching methods can be adopted to be used in practice (Sahillioğlu and Yemez 2012). The found matching is then propagated, to expand the set of correspondence until all samples are assigned.

Graph-based matching. It is also natural to look at the correspondence problem as that of matching two graphs. The feature points on a shape or skeleton can be seen as the nodes of a graph, where every or selected pair of nodes is connected with an edge whose weight is proportional to some metric (e.g. geodesic distance between the nodes). Since it is NP-complete, heuristics have been proposed to address this problem. In case of partial matching, the problem becomes *subgraph isomorphism*. Later in Chapter 5, we also formulate a subgraph isomorphism for the problem of part matching.

Another commonly adopted formulation in correspondence finding is *bipartite graph matching*. (Ruggeri and Saupe 2008) construct geodesic distance matrix, where each row yields a histogram of its elements. The dissimilarity between two point set surfaces is computed by matching the corresponding sets of histograms with bipartite graph matching, which had been solved by Edmonds' blossom algorithm.

In many other works, correspondence problem is formulated as a *binary labeling* of a graph, where a node represents a mapping from X to Y and an edge represents the global compatibility between the two mappings. (Wang, Bronstein et al. 2011) formulate the minimum-distortion correspondence problem as a binary labeling problem with uniqueness constraints in a graph. They adopt the graph matching algorithm based on dual-decomposition (Torresani, Kolmogorov et al. 2013) to perform their optimization. The key idea of Torresani et al.'s work is, instead of minimizing directly the energy of the original problem, to maximize a lower bound on it by solving the dual to the linear programming relaxation of the integer problem. The original problem, which is too complex to solve directly, is decomposed into a series of sub-problems that are smaller and solvable. After solving each the sub-problems, the solutions are combined using a projected-subgradient scheme to obtain the solution of the original problem.

Hierarchical matching methods (Wang, Bronstein et al. 2011, Torresani, Kolmogorov et al. 2013, Raviv, Dubrovina et al. 2012) reduce the high dimensionality of the problem using an iterative scheme. At the lowest resolution they start with a few number of points and solve the exact correspondence problem. Then the information is propagated to higher resolutions, thus refining the solution. (Wang, Bronstein et al. 2011) iteratively increase the number of points to be matched. At each level $k + 1$, new points are inserted for matching, which is solved by using the matching from the previous level k along with the neighborhood restriction – Correspondence candidates are restricted for neighbor points around previously matched points, i.e. matching between a neighboring point around x to one around y only is considered, given $(x, y) \in C_k$ (Figure 3-1). For the graph labeling at each level they use the dual-decomposition approach proposed by (Torresani, Kolmogorov et al. 2013). Similar approach has been employed by (Raviv, Dubrovina et al. 2012), who at each iteration add new points to find matching, but they also refine the solution as they iterate along the hierarchy. The matching from the previous level is locally improved by looking at the neighborhood of the match: At each iteration, for each previously found match $(x, y=c(x))$, x and neighborhood of $c(x)$ constitute candidate correspondences and $c(x)$ is replaced by one of its neighbor (Figure 3-2). As well, new points are inserted. At each iteration we add points x and y , evaluate the neighborhood of the new points, reevaluate the neighborhood of the old points, and continue until convergence.

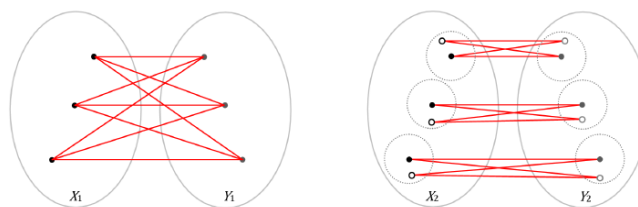


Figure 3-1. At each iteration, a set of new points and their potential correspondences are generated (right) around the neighborhood of the previously found matching point set (left) (Wang, Bronstein et al. 2011).

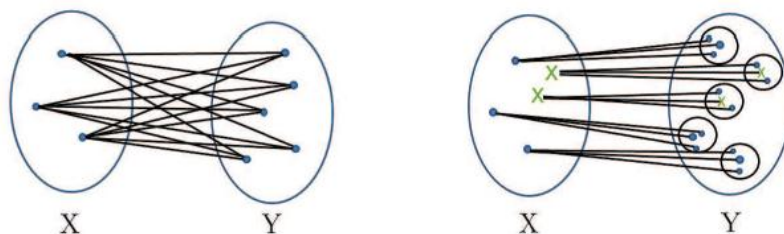


Figure 3-2. An example of hierarchical matching (Raviv, Dubrovina et al. 2012). A quadratic correspondence matrix from all points in X into all points in Y has been constructed (left). In each iteration the matches are locally improved by searching for possible matches between points in X from the previous iteration (blue circle) and new sampled points in X (green X) and their corresponding neighborhoods (black circles) in Y .

Tree-based matching. One group of methods in discrete optimization make use of branch-and-bound search techniques on combinatorial trees to explore the solution space (Funkhouser and Shilane 2006, Zhang, Sheffer et al. 2008, Au, Tai et al. 2010). Every tree node contains a possible matching pair (correspondence), except for the root which is an auxiliary node representing an empty set. Each node represents a partial solution, comprising all correspondences along the path from that node to the root. A node is expanded (branch) to other nodes that represent new partial solutions only if the new correspondence set including the new node passes a cascade of pruning tests, otherwise the subtree rooted at that node is pruned (bound). Although these tests differ from one method to another, the goal is to efficiently filter out incorrect correspondences. On the completion of the search, a complete solution is retrieved by following the path from the root of the tree to one of its leaves. However, in general, the inherent highly complexity of these approaches have limited them to match only a small number of points.

3.3 Iterative improvement

Some methods solve for non-rigid registration as continuous optimization one, where the goal is to search for the transformation (displacement) of each source vertex that optimally aligns the shapes. Due to the high-dimensional nature of the solution space, these problems are typically solved with a form of repetitive local or approximate search, iteratively improving the quality of matching until some criteria are met. Heuristic solutions are often adopted, such as alternating between the correspondence computation and the deformation optimization (Huang, Adams et al. 2008), adjusting the weights for each error term at different phases of the optimization (Allen, Curless et al. 2003) or gradually increasing the granularity over the optimization (Allen, Curless et al. 2003, Seo and Magnenat-Thalmann 2003). In both cases, manually labeled feature points have been used. However, the quality of the matching will depend on the initial guess.

Use of skeletons. In their work on the whole-body modeler based on 3D scan examples, (Seo and Magnenat-Thalmann 2003) bring approximately 100 scans of different bodies into full correspondence. They start with a template model and find the error- and energy- minimizing deformation of the template model onto each scan geometry. A two-phase deformation devoted to the human body shape has been proposed (see Figure 3-3): First, an optimal set of joint transformations are found, which, when applied to the skin mesh through the skinning, will determine the linear approximation of the body. Then the residual vertex displacements are found by an iterative improvement that alternates between the closest point match (data error) and the smoothness error, with feature vertices constrained to their respective target positions. Note that by adopting deformation models that are well suited for the pose dependent shape change (e.g. skeleton driven models) (Allen, Curless et al. 2002, Seo and Magnenat-Thalmann 2003), the initial solution is found by using a relatively small number of degree of freedom of joint transformations. Then the final solution is found by finding affine transformation of each vertex in the template surface, so as to maximize the similarity measure between the source and the target and to minimize the distortion energy of the template mesh.

(Allen, Curless et al. 2003) use the L-BFGS-B (Zhu, Byrd et al. 1997), a quasi-Newton solver, to find the transformation of each geometric element on the surface by taking into account all the error terms simultaneously. As in (Seo and Magnenat-Thalmann 2003), manually labeled feature points have been used:

$$E = \alpha E_d + \beta E_S + \gamma E_m.$$

In order to, they first run the optimization on the low resolution and upsample to the high-resolution to complete the optimization at full resolution. The weights are varied as well: At the beginning γ is set to a high value so that the marker error mainly drives the optimization, quickly approaching the global solution. Then it terminates with a high α value, allowing the data error to dominate.

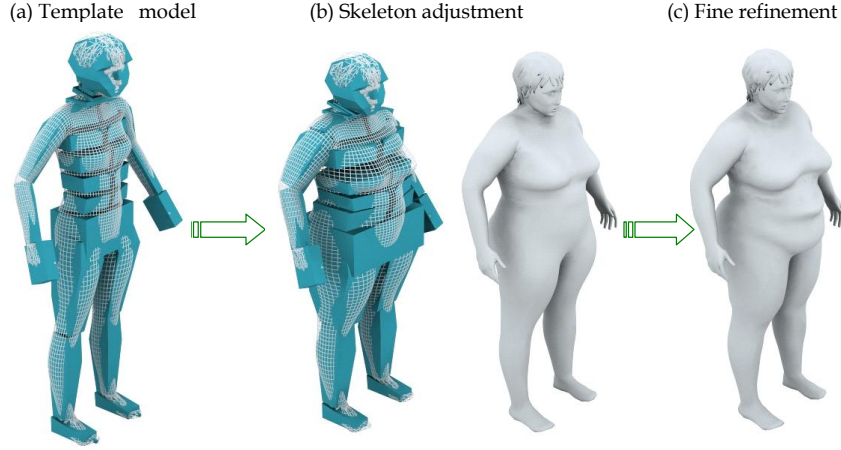


Figure 3-3. The two-phases of the deformation of the template (Seo and Magnenat-Thalmann 2003).

(Huang, Adams et al. 2008) have developed an iterative two-step procedure that makes use of both correspondence computation (first step) and deformation optimization (second step). After downsampling the source and target point clouds and computing neighborhoods, they compute reliable correspondences by adopting a variant of ICP (i.e. closet point match) combined with local improvements using a feature match, which they prune by finding the largest subset of correspondences that are consistent in a geodesic sense by using the spectral clustering (Leordeanu and Hebert 2005). The affinity between the matching i and matching j are defines as:

$$c_{ij} = \min \left\{ \frac{d_g(s_i, s_j)}{d_g(t_i, t_j)}, \frac{d_g(t_i, t_j)}{d_g(s_i, s_j)} \right\}, \text{ with } c_{ij} \leq 1.$$

Full correspondence is obtained by propagating the consistent correspondences using the geodesic consistency criterion. With the newly found correspondence, they cluster groups of sample points who share a same rigid transformation, and compute the deformation field so that the sample source points are best aligned with their corresponding target points while minimizing local non-rigid deformations.

3.4 Voting and clustering

The main objective of voting or clustering techniques is to achieve collective consistency. In the context of optimal point matching of 2D images, (Leordeanu and Hebert 2005) adopt spectral techniques to prune potential correspondences efficiently. Spectral methods have been commonly used for finding the main clusters of a graph, in tasks such as segmentation (Shi and Malik 2000) and grouping (Scott and Longuet-Higgins 1990, Mahamud, Williams et al. 2003). They start by building the adjacency matrix M of an assignment graph where a node $a = (i, i')$, $i \in S, i' \in T$ represents a potential correspondence and the weight on an edge $M(a, b) = M(b, a)$ represents pairwise agreement between two potential correspondences a and b . In that work they developed an inverse function of pairwise Euclidian distance, which can be replaced to a geodesic distance in case of 3D surface (Huang, Adams et al. 2008). In order to maintain only a small fraction of all possible correspondence, and therefore to avoid unpractical computation time for the eigenanalysis of a very large matrix M ($nm \times nm$, where $n=|S|$ and $m=|T|$), use of discriminative feature descriptors is desirable. The method is based on the following speculation : Correct assignments tend to establish links (edges with positive weights) among each other and thus form a strongly connected cluster with a high association score, while the wrong assignments will be weakly connected to other assignments and not form strong clusters. In this setting, the correspondence problem is posed as one of finding the main cluster C of M associated with the graph that maximizes the inter-cluster score:

$$S = \sum_{a,b \in C} M(a, b) = x^T M x.$$

The optimal solution x^* is the binary vector that maximizes the score:

$$x^* = \operatorname{argmax}(x^T M x).$$

By relaxing the constraints on x , such that its elements can take real values in $[0,1]$, they can find the solution analytically, which is the principal eigenvector of M (by the Raleigh's ratio theorem). The eigenvector value corresponding to a particular assignment a is interpreted as the confidence that a is a correct assignment. They develop an iterative algorithm that binarizes the eigenvector by accepting assignments in an order of confidence.

(Chang and Zwicker 2008) concentrate on the problem of finding the correspondence between two poses of an articulated object, which they cast as that of choosing a set of optimal transformations among a set of predetermined transformations that describe the partwise motion between the two poses. For each subsampled point in the source shape, they find a set of potentially corresponding points in the target by computing the similarity score based on the spin image (Johnson 1997). Then for each correspondence candidate (p,u) , a rigid transformation from p to u is computed by combining the precomputed, per-vertex coordinate frames. They cluster the computed set of transformations by using the mean-shift (Tuzel, Subbarao et al. 2005), from which they obtain a pruned set of transformations (see Figure 3-4). Finally, the problem resorts to labeling each point in the source with one of the selected transformations such that the feature similarity as well as smoothness is maximized, which they solve by using the graph cuts algorithm (Boykov, Veksler et al. 2001). However, such piecewise rigid motion assumption is not appropriate for deformable objects (i.e. human faces) or for different instances of an object class (i.e. different horses) or even objects from different classes (horse and camel), related by highly non-linear mappings.

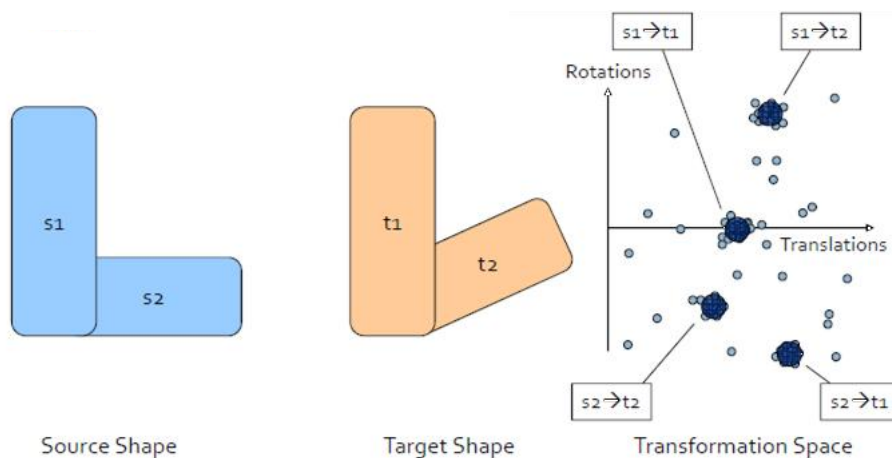


Figure 3-4. (Chang and Zwicker 2008) cast the problem as that of choosing a set of optimal transformations via clustering.

Electors voting by (Au, Tai et al. 2010) finds sparse, semantic correspondence between the skeletons of two models that are possibly geometrically very different. The electors (a large set of pruned correspondences) are first selected via a combinatorial search with pruning tests designed to quickly prune out a majority of bad correspondence. In order to maintain a reasonable size of the combinatorial solution space, they have used a skeleton structure composed of terminal (extremity) nodes and junction nodes (joints). On the completion of the search, each node in the combinatorial tree represents an elector, which contains a series of correspondences along the path from the root to that node. Each elector then casts one vote for each of its constituent matching pair to establish the final correspondence. (Figure 3-5)

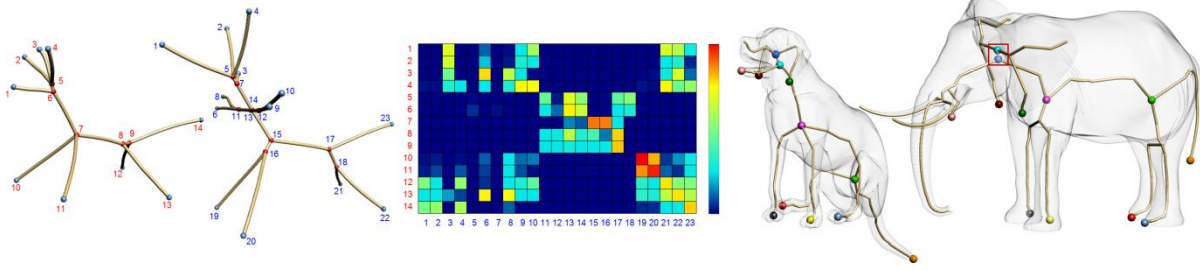


Figure 3-5. Electors voting scheme by (Au, Tai et al. 2010).

3.5 Random sampling

Since the concept of *hypothesis-and-check* has been introduced by (Fischler and Bolles 1987) to fit a model to observed data, several correspondence estimation algorithms based on RANSAC (Ransom sample consensus) have been presented on image (Torr and Zisserman 2000) and surface (Memoli and Sapiro 2004, Tevs, Bokeloh et al. 2009, Tevs, Berner et al. 2011) data. The RANSAC algorithm is a hypothesis and verify algorithm. It proceeds by repeatedly generating solutions estimated from minimal sets of correspondences and then testing each solution for support from the complete set of putative correspondences. Memoli and Sapiro's randomized matching algorithm (Memoli and Sapiro 2004) compares two manifold surfaces using an iterative farthest point sampling (FPS) algorithm, which computes an optimized coverings (collection of sets whose union contains the initial point set) of the given surface by minimizing an approximate Gromov-Hausdorff-Distance.

(Tevs, Bokeloh et al. 2009) have been applied RANSAC techniques to intrinsic surface matching. They first randomly sample an initial set of correspondence. Starting at random source points, corresponding target points are chosen with probability proportional to the likelihood that the match is correct, e.g.:

$$P_{\text{descr}}(x, y) \sim \exp(-0.5\sigma_d^{-2}|D_x - D_y|),$$

where $(x, y) \in M_S \times M_T$ is a matching candidate and D_g is a feature descriptor and σ_d^{-2} a user-defined parameter. Then additional correspondence is added randomly, with probability proportional to the likelihood that the match is correct according to the isometric matching criterion, given k previous correspondences:

$$P_{\text{dist}}(x, y | x_1, y_1, \dots, x_k, y_k) \sim \prod_{i=1}^k \exp(-0.5\sigma_g^{-2}|d_{M_S}(x, x_i) - d_{M_T}(y, y_i)|).$$

The final sampling probability is obtained by multiplying P_{descr} with P_{dist} . The algorithm continues the sampling until no more matching pairs are found that do not exceed the maximum error, or until all points are matched. The matching results are then evaluated by measuring the error introduced by the isometry represented by the solution set, in order to determine whether the algorithm will terminate or to repeat the steps with a new set of random selection.

(Tevs, Berner et al. 2011) extend the idea by carefully planning on how to choose optimized sample points on the source shape that maximize the information gained (and therefore minimize the cost for guessing the correspondence) (PLANSAC, Planned Sample Consensus). More specifically, starting from an empty *plan set*, they incrementally add points that minimize the entropy of the posterior distribution of potential matches. They begin by choosing a most discriminative point that leads to minimal entropy of P_{descr} when compared to all other points. Having selected the first point, they add points with most information content with respect to both descriptor matching and distances to previous points, e.g. a point with a discriminative descriptor and can be uniquely defined to all points that are in the plan set. Finally, they stop building the *plan* if all remaining points are fixed in their position and can be located uniquely by their intrinsic distance to all points in the plan. As a

by-product, these methods remove the need for keypoint extraction as a preprocessing step to the matching. This is the case on some models who do not have characteristic points that the feature detectors rely on. However, the computational efficiency remains as a drawback of techniques based on random sampling. Their verification phase requires testing each solution, which demands high computational cost.

3.6 Embedding-based shape correspondence

In computer graphics, the problem of isometric shape correspondence is often solved in embedded domain. Embedding of a shape gives an intrinsic representation of the surface, which is invariant to bending or more general isometries. Most frequently intrinsic spectral embedding of a shape is done from geodesic affinities matrices which are computed by collecting geodesic distances between all pairs of surface points. The key idea of embedding based methods is that the intrinsic geometry of the shape is modeled as its extrinsic geometry in the new embedding space.

(Elad and Kimmel 2003) suggested a method for matching isometric shapes by embedding them into a low-dimensional Euclidian space (Figure 3-6) using multidimensional scaling (MDS) (Borg and Groenen 1997), thus obtaining isometry invariant representations, followed by rigid shape matching in that space. (Bronstein A., Bronstein M. et al. 2006) proposed an MDS-like algorithm named as generalized MDS (GMDS) for the computation of the Gromov-Hausdorff distance and deformation invariant correspondence between shapes. This framework has been extended in (Bronstein A., Bronstein M. et al. 2010) using diffusion geometry instead of the geodesic one.

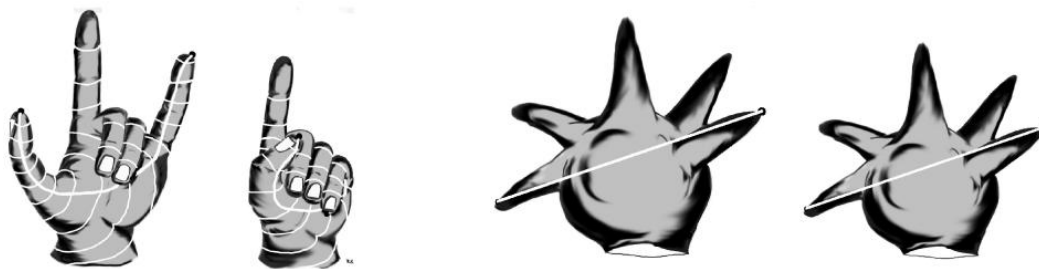


Figure 3-6. (left) Two different configurations of a hand on which a matching is to be computed (Elad and Kimmel 2003). A geodesic path connecting two surface points is drawn in a thick white curve, while equal geodesic distance contours are drawn as thinner curves. (right) MDS generates bending invariant surfaces (signatures). With geodesic distances transformed into Euclidean ones, the minimal geodesic curve on the hand becomes a straight line connecting the two corresponding points.

The low dimensional embedding can be obtained with the recent techniques such as (Lipman and Funkhouser 2009) and (Kim, Lipman et al. 2011). In the work of (Lipman and Funkhouser 2009) the authors propose an efficient algorithm for computing intrinsic surface correspondence relying on conformal embedding and Möbius transformation. Given two input meshes of spherical or disk topology M_1 and M_2 that are approximately or partially isometric, the algorithm produces a discrete sparse pairs of correspondences between the meshes. The approach is based on two fundamental concepts. First, as postulated by the Poincaré’s Uniformization Theorem (Bartolini 2006) for any genus-zero³ surface exist a conformal (angle preserving) map to a unit sphere \mathbb{S}^2 . Thus the problem of establishing one to one correspondences between isometric genus zero surfaces can be formulated as finding a conformal map from a unit sphere to itself $f: \mathbb{S}^2 \rightarrow \mathbb{S}^2$ (Figure 3-7).

³ Genus zero surface could be intuitively think of as a surface without holes. Genus zero surface without a boundary is topologically equivalent to a sphere; in case if a genus zero surface has a boundary then the surface is topologically a disk.

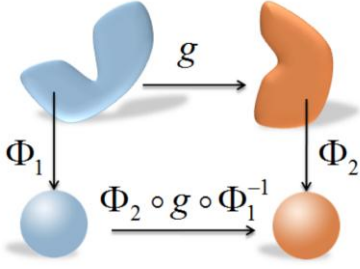


Figure 3-7. Isometric matching with Uniformization of surfaces: correspondence of two genus zero surfaces can be regarded as conformal transformation of a unit sphere to itself (Lipman and Funkhouser 2009).

On the other hand, the group of all one to one conformal transformations $m: \mathbb{S}^2 \rightarrow \mathbb{S}^2$ forms Möbius group $M(2)$ which is well studied in geometry (Carne 2006). Since the Möbius group has six degrees of freedom, it is sufficient to establish three unique correspondences in order to define the Möbius transformation m (MT). The main implication of these observations is that establishing the entire map between isometric surfaces can be done with just three point correspondences. More precisely, the algorithm proceeds as follows. Iteratively select three distinct point pairs on the source and target. Compute Möbius transformation based on those point correspondences. Use the obtained MT to transform all other points on the meshes. Then (Lipman and Funkhouser 2009) measure the deformation error between mapped points as deviation from isometry. The deformation errors are accumulated in correspondence matrix C . Finally, based on confidence scores (the voting scores that indicate the quality of correspondence) from the matrix C , the matching solution is extracted (Figure 3-8). The algorithm performs the isometric shape matching in polynomial time $O(N^3)$ with respect to number of vertices.

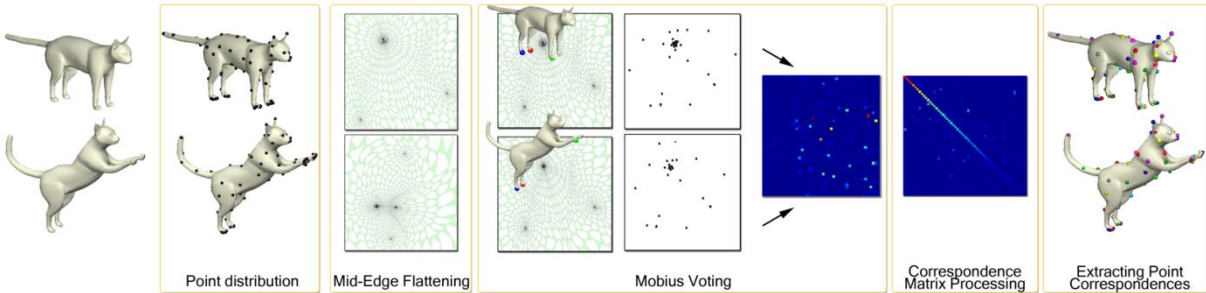


Figure 3-8. The pipeline of the Möbius voting algorithm (Lipman and Funkhouser 2009). Deformation errors of Möbius transformations for the different triplets of initial correspondences are accumulated into correspondence matrix.

The follow up method of (Kim, Lipman et al. 2011) mends matching distortion of the conformal embedding algorithm (Lipman and Funkhouser 2009) and establish reliable correspondences between not necessary isometric surfaces. The key idea is to use a weighted combination of low-dimensional conformal correspondence maps of Möbius voting in order to produce a so-called blended map which minimizes the mapping distortion originating from violations of isometry.

Given the source M_1 and target M_2 surfaces with number of samples P_1 and P_2 correspondingly, the authors compute first a set of candidate conformal maps $\{m_i: M_1 \rightarrow M_2 \mid i = 1..K\}$, $K = \binom{|P_1|}{3} \cdot \binom{|P_2|}{3}$. Then for each point $p \in M_1$ on the source its correspondence $f(p)$ is computed as a blended map that minimizes distortion across the entire surface

$$f(p) = \min_{q \in M_2} \sum_{i=1}^K b_i(p) \cdot d_{M_2}(q, m_i(p))^2, \quad (3-1)$$

where b_i are so-called blended weights.

The authors consider distortion of the mapping to be the deviation from isometry, even though other definitions are possible. Smooth blending weights b_i are defined in a way that they are proportional to the area preservation of the map at every point (isometry), and incorporate global similarities between different conformal maps m_i (consistency among maps).

The authors optimize blending weights b_i separately for the isometry preservation and consistency of the maps. Finally, given optimal weights b_i the blended map effectively minimize the isometry distortion (Figure 3-9).

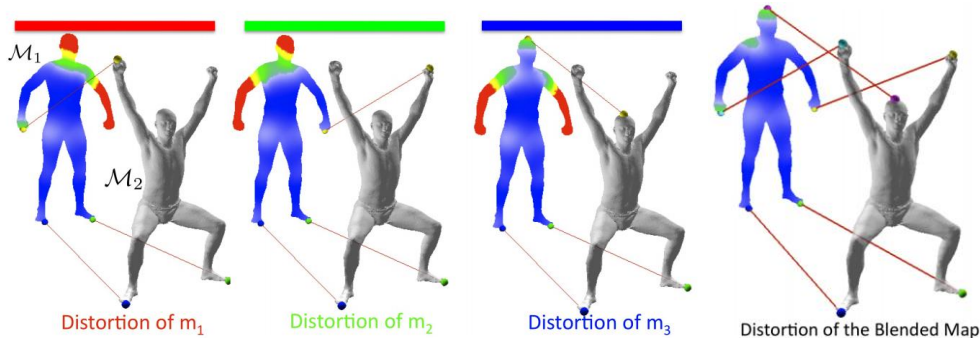


Figure 3-9. Blending weights b_i effectively minimize distortion of the maps m_1, m_2, m_3 (Kim, Lipman et al. 2011).

The other methods explore intrinsic shape matching of the space of isometric surfaces by modeling heat diffusion process (Sun, Ovsjanikov et al. 2009, Ovsjanikov, M erigot et al. 2010). In the work of (Sun, Ovsjanikov et al. 2009) the authors present an interesting concept of *Heat Kernel Signature (HKS)* and show its suitability for shape matching. The *HKS* relies on heat diffusion process over manifold that approximates a discrete shape surface. For each point x on the manifold M , *Heat Kernel Signature* is defined in the following way as a function over time t

$$HKS(x, t) = k_t(x, x)$$

where $k_t(x, x)$ is a heat kernel function (Sun, Ovsjanikov et al. 2009). Intuitively, the *HKS* can be interpreted as a measure of the amount of heat transferred in time t between two points in infinity small neighborhood of x .

As reported in (Sun, Ovsjanikov et al. 2009) *HKS* can be efficiently used for the shape matching. The *HKS* is distinctive enough so that the matching of a point x on the source can be established by associating x with the nearest point y on the target in the *HKS* space (i.e. in terms of distance metric between $HKS(x, t)$ and $HKS(y, t)$) (Figure 3-10).

Nice properties of heat diffusion are further exploited in the work of (Ovsjanikov, M erigot et al. 2010). The authors present an intrinsic shape matching algorithm that can recover full isometric shape mapping out of a single correspondence pair. The key idea behind their technique is that the full correspondence map that keeps invariant the heat kernel of at least one matching pair is an isometry map. Hence without exhaustive search it is possible to efficiently check if a potential correspondence pair between the source and target could be extended to the full correspondence. Given two manifolds M and N with a known correct correspondence pair (p, q) , $p \in M, f(p) \in N$, the *Heat Kernel Map* is constructed for every other point $x \in M, y \in N$ on the manifolds

$$\Phi_p^M(x) = k_t^M(p, x), \quad \Phi_q^N(y) = k_t^N(q, y),$$

where k_t^M and k_t^N are heat kernel functions (Sun, Ovsjanikov et al. 2009) on the source M and target N manifolds.

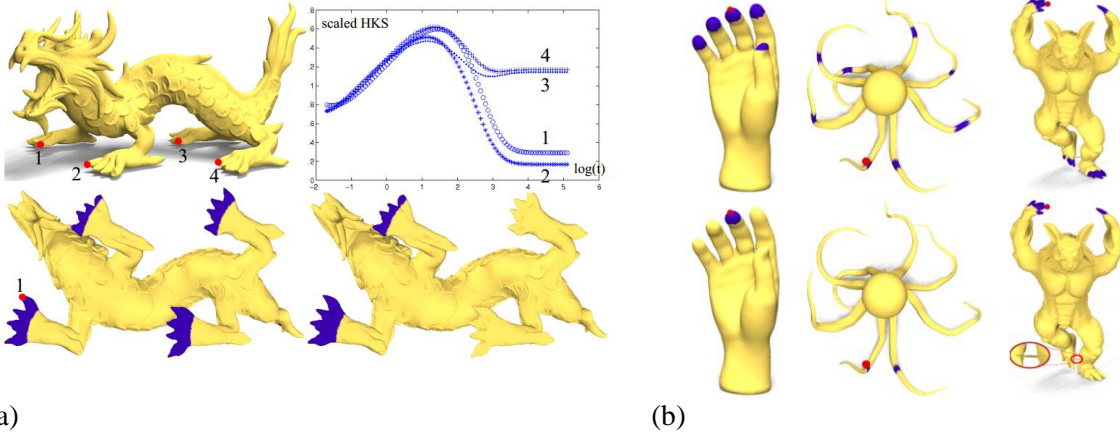


Figure 3-10. (a) heat kernel signature for the points 1-4 of the dragon model (b) matching (marked in purple) of the point on the tip of the hand (marked in red) based on the HKS (Sun, Ovsjanikov et al. 2009).

The authors formally prove that *Heat Kernel Maps* are injective and are invariant under isometric mappings $f: M \rightarrow N$. This means that for an isometric map f between the source M and target N manifolds the following holds: $\forall x \in M \Phi_p^M(x) = \Phi_{f(p)}^N(f(x)) \wedge \exists z \in N \Phi_{f(p)}^N(f(x)) = \Phi_{f(p)}^N(z)$. Therefore for every point $x \in M$ on the source, it is possible to find a unique correspondence $y \in N$ on the target such that their *Heat Kernel Maps* coincide. In practice, the correspondence f can be computed as the nearest neighbor with respect to Heat Kernel Maps

$$f(x) = \underset{y \in N}{\operatorname{argmin}} \|\Phi_p^M(x) - \Phi_q^N(y)\|, \text{ where } x \in M \text{ and } y \in N \text{ (Figure 3-11).}$$

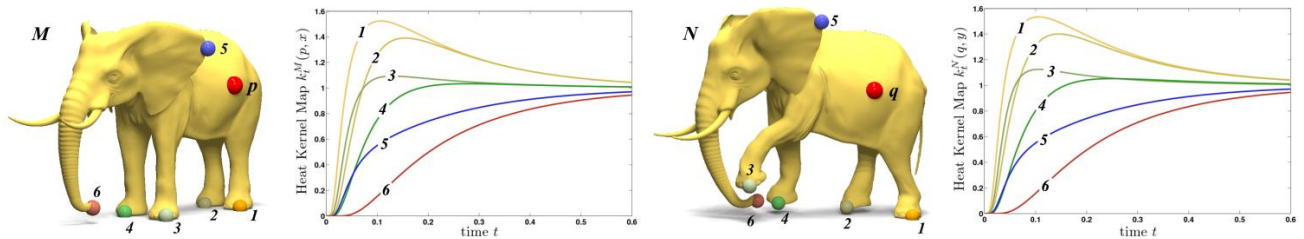


Figure 3-11. Given initial correspondence pair (p, q) between the source M and target N shapes, each point on the source is associated with the closest point on the target in terms of Heat Kernel Map similarities. Points 1-6 from the source are put into correspondence with point 1-6 on the target (Sun, Ovsjanikov et al. 2009).

The other class of the methods rely on spectral embedding (Jain, Zhang et al. 2007), (Mateus, Horaud et al. 2008), (Sahilliođu and Yemez 2010). Instead of solving shape correspondence directly in Euclidean space, the solution (or initial solution) is obtained in the intrinsic spectral domain.

(Jain, Zhang et al. 2007) develop an algorithm for correspondence computation in spectral embedding between non-rigid meshes. The key observation for the method is that in spectral embedding it is possible to automatically remove the effects of rigid-body transformations, uniform scaling and bending. Taking this into account, the authors first propose to perform non-rigid alignment of shapes in spectral domain and then follow it by fine matching with thin plate splines (TSP). Given the source M and target N meshes, the method establishes vertex-to-vertex correspondences in the following way. First, pair-wise vertex affinity matrices A, B are computed for the source and target, where the affinity between vertex i and j is estimated as the mesh path length from i to j (i.e. the sum of edge length). Then spectral embeddings \hat{A}_k and \hat{B}_k are established by projecting affinity matrices A and B on their first k principal eigenvectors. These embedded matrices represent the coordinates of all vertices from M and N in k -dimensional spectral domain. In order to handle reflections caused by eigenvector switching and sign flips, the authors heuristically enforce consistent eigenvector ordering and signs. Finally the

k -dimensional spectral embeddings \hat{A}_k and \hat{B}_k are registered via non-rigid ICP based on TSP (Chui and Rangarajan, 2003). The advantage of TSP algorithm is that it allows handling the presence of non-rigid deformations in the spectral domain.

Another spectral based technique of (Mateus, Horaud et al. 2008) addresses the problem of voxel-based articulated shape matching. The main characteristic of the method is a combination of Laplacian embedding and probabilistic point matching. Another relevant contribution of the technique includes eigenfunction histogram. Similarly to the Laplace–Beltrami operator, the eigenvalues and the eigenfunctions are defined by the intrinsic geometry of the manifold, and thus remain invariant under its isometric transformations. First, from the input source and target voxel sets X and Y , l -nearest neighborhood graphs G_x, G_y are built and equipped with normalized graph Laplacian matrices L_x and L_y . The normalized Laplacian matrices are analogous to normalized graph adjacency matrices. Given G_x, G_y and the Laplacian matrices L_x, L_y , the articulated shape matching is then formulated as an instance of maximal subgraph isomorphism. The later problem is approached in a spectral graph matching way. To put it simply, alignment of L_x and L_y is equivalent to alignment of their eigenspaces (*Umeyama's theorem* (Umeyama, 1988)). Similarly to the Laplacian eigenmaps scheme (Belkin and Niyogi, 2003), the authors perform a generalized eigendecomposition of matrix L and rely only on k smallest eigenvalues with their associate eigenspace. In order to make the method invariant to the order of eigenfunctions, the authors propose an interesting technique of computing histograms of eigenfunctions. Histograms of eigenfunctions of the articulated source and target sets show strong similarities and the problem of optimal assignment of the eigenfunctions can be effectively solved with the Hungarian algorithm. Finally, the matching between the matching of the source and target point sets in k -dimensional eigenspaces is computed via EM algorithm (Dempster et al, 1977). Some of the matching results of (Mateus, Horaud et al. 2008) are demonstrated in Figure 3-12.

In the work (Sahilliođu and Yemez 2010) the coarse correspondence between isometric shapes is obtained in spectral embedding based on vertex geodesic affinity. More precisely, given k leading eigenvectors of geodesic affinity matrix⁴, sparse vertex samples on the source and target meshes are embedded into k -dimensional spectral domain. Thus geodesic distances between vertices in Euclidean space approximately correspond to L2 distances in k -dimensional spectral domain. The sparse vertex samples in the source are then aligned purely in spectral domain to the nearest neighbors on the target (Figure 3-13).

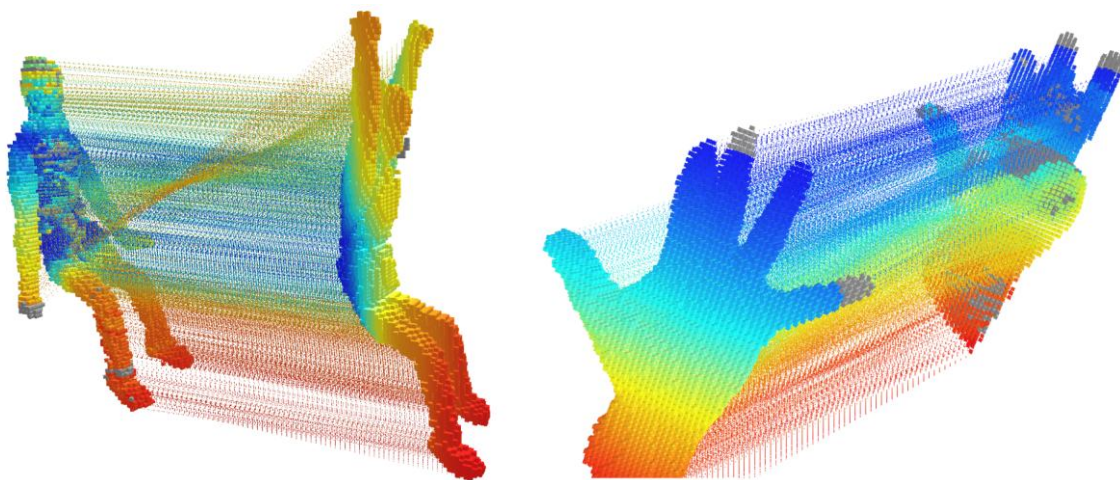


Figure 3-12. Matching results between voxelized articulated shapes. Unmatched voxels are marked in grey (Mateus, Horaud et al. 2008).

⁴ Geodesic affinity matrix is composed of pair-wise geodesic distances between all the vertices of a mesh.

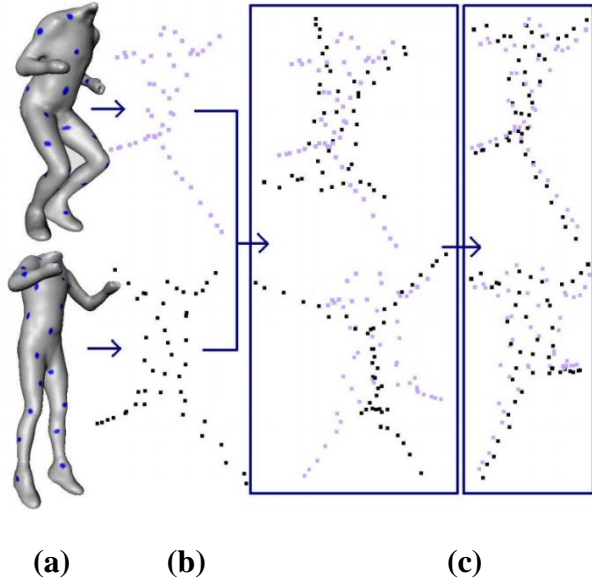


Figure 3-13. (a) The source and target shapes, (b) spectral embedding of the sparse vertex samples, (c) alignment of the samples in spectral domain to the nearest neighbors (Sahilliođu and Yemez 2010).

3.7 Use of prior-knowledge

One promising way to registration is to base on statistical analysis. Statistical properties of the density and geometric variations in the target shape (typically human face or body) are extracted and encoded into a statistical atlas. A number of methods have been shown to use statistical atlas to exploit the prior knowledge (probable shape range, correlated shape change, for instance) to guide the registration process (Blanz and Vetter 1999, Allen, Curless et al. 2003, Seo, Yeo et al. 2006, Anguelov, Springivasan et al. 2005). These methods typically have an additional advantage of reduced size of the solution space, at the cost of preprocessing that brings a set of shape instances into correspondence. Initially shown in the registration of medical images (Chen, Kanade et al. 2000), this technique has been first demonstrated to the computer graphics community by (Blanz and Vetter 1999). They use the term *morphable model* to present the idea of manipulating a single surface representation that can be deformed to represent all other faces. They build their morphable model from a collection of individual models that are placed in correspondence, which has been found by using a modified version of 2D optical flow on the cylindrical parameterization of the head scan. Once the correspondence has been established, a face is represented with a shape-vector $\mathbf{S}=(x_1, y_1, z_1, x_2, \dots, y_n, z_n)^T \in \mathbb{R}^{3n}$ and a texture-vector $\mathbf{T}=(r_1, g_1, b_1, r_2, \dots, g_n, b_n)^T \in \mathbb{R}^{3n}$, which contains coordinates and color values of its n vertices, respectively. From the m exemplar faces that are put in correspondence, principal component analysis (PCA) is applied to m shape vectors and m texture vectors. PCA performs a basis transformation to an orthogonal coordinate system (often called eigenspace) formed by the eigenvectors of the covariance matrices. A face shape is then described as a weighted sum of the orthogonal basis of 3D shapes called principal components.

$$\mathbf{S}(\vec{\alpha}) = \bar{\mathbf{S}} + \sum_{i=1}^{m-1} \alpha_i \cdot \mathbf{s}_i, \quad \mathbf{T}(\vec{\beta}) = \bar{\mathbf{T}} + \sum_{i=1}^{m-1} \beta_i \cdot \mathbf{t}_i$$

where \mathbf{s}_i and \mathbf{t}_i are eigenvectors of the covariance matrices in descending order according to their eigenvalues. Thus, the morphable model is parameterized by the coefficients; i.e., arbitrary new faces can be generated by varying the parameters $\vec{\alpha}$ and $\vec{\beta}$ that control the shape and texture.

When matching the morphable model to image input (2D-3D registration), they take a bootstrapping approach to find the error-minimizing PC coefficients of the 3D model in the linear space of reduced size. The optimal

coefficients of the 3D model along with a set of rendering parameters are found such that they produce an image as close as possible to the input image. In their *analysis-by-synthesis* loop, the algorithm creates a texture mapped 3D face from the current model parameters, renders an image, and updates the parameters according to the residual difference. It starts with the average head and with rendering parameters roughly estimated by the user. Similarly, when matching the morphable model to a 3D scan (3D-3D registration), they search for optimal coefficients that minimize the color error between the corresponding points.

Later, similar approach has been demonstrated by (Allen, Curless et al. 2003) (markerless matching) and (Seo, Yeo et al. 2006) (image guided reconstruction of human body shapes). Given a set of example body shapes represented as vectors, they apply PCA to them to obtain linear shape spaces. As has been the case with the morphable face model, such shape space allows not only to systematically observe the diversity and individuality of shapes, but also to generate a new, plausible individual shape in an easier and simpler manner. When computing for the optimal set of coefficients, a new error term indicating the likelihood of a particular set of PCA coefficients is introduced:

$$E_p = \sum_{i=1}^{k'} (p_i/\sigma_i)^2.$$

The SCAPE approach of (Anguelov, Springivasan et al. 2005) propose combined models that learn both static (identity-dependent) and dynamic (movement-dependent) shape variation have been suggested, allowing to generate shapes of any identity in any pose. SCAPE learns pose-deformation as completely separate phenomenon from the PCA-based identify variation model, and then combines the two modalities when a new shape is synthesized. Though very powerful, it cannot capture the correlation between the two modalities. For example, when a muscular person bends his/her arm, the shape change will be the same as when a very thin person bends the arm. Vlastic et al's multilinear models (Vlastic, Brand et al. 2005) has shown how multilinear algebra could be adopted to extend latent variable techniques to handle multiple modalities, such as identity, expression, and viseme of a face. Later, (Allen, Curless et al. 2006) propose to capture both identity-dependent and pose-dependent shape variation in a correlated fashion. By incorporating the two entities that have previously handled separately into a single model, the model is potentially more expressive and realistic for synthesizing and editing animated characters.

Chapter 4 Feature detection for animated meshes

4.1 Introduction

In this chapter we present a novel technique of dynamic feature detection for animated meshes. Since such data has considerably large sizes, it often becomes indispensable to be able to select distinctive features from it, so as to maintain efficiency in its representation and in the process applied to it. Consequently, the need for robust, repeatable, and consistent detection of meaningful features from animation data cannot be overemphasized. However, the feature detection in animated mesh remains as much less explored domain, despite the proliferation of feature detectors developed by many researchers in computer graphics and computer vision. As we explained in Chapter 2, dynamic feature points have a potential to bring a particularly remarkable value to time-varying animated mesh correspondence. Being able to extract repeatable coherent sets of dynamic features and to establish reliable correspondences between them (as detailed in Chapter 5), facilitates significantly dynamic shape matching.

Feature point extraction has been a long-studied subject in computer vision, image processing and computer graphics. Traditionally, features are often extracted from different modalities and graphical entities such as 2d/3d images, videos, polygonal meshes and point clouds. Therefore it is especially unfortunate that a problem of feature point detection on animated meshes remains unstudied. While classical feature points are directly related to static local neighbourhood and geometry, we proposed a novel feature detection technique based on dynamic behaviour of the shape and its deformation characteristics.

Chapter 4 details a new feature extraction method on animated meshes in the following way:

1. We survey related works on feature extraction for (static) meshes and videos, which are the most closely related to our work (Section 4.2)
2. Describe the deformation characteristics and how they are captured (Section 4.4)
3. Outline the basics of linear scale-space theory (Section 4.5)
4. Establish a novel spatio-temporal Difference of Gaussians (DoG) operator (Section 4.7)
5. Show results of proposed feature point extraction algorithm and evaluate robustness of the method (Sections 4.8, 4.9)

In scope of this dissertation, we first develop a spatio-temporal feature detection framework on animated meshes (an ordered sequence of static mesh frames with fixed number of vertices and connectivity), based on the scale space approaches. Our feature detection scheme is then used for the sparse and dense dynamic shape correspondence (Chapter 5). The algorithm, which we call AniM-DoG, extends the spatial interest point (IP) detectors on static meshes (Pauly, Keiser et al. 2003, Castellani, Cristani et al. 2008, Zaharescu, Boyer et al. 2009, Darom and Keller 2012) so as to detect spatio-temporal feature points on animated meshes. Based on deformation characteristics computed at each vertex in each frame, we build the scale space by computing various smoothed versions of the given animation data. At the heart of our algorithm is a new space-time Difference of Gaussian (DoG) operator, which approximates the spatio-temporal, scale-normalized Laplacian.

By computing local extrema of the new operator in space-time and scale, we obtain repeatable sets of spatio-temporal feature points over different deforming surfaces modelled as triangle mesh animations. We then validate the proposed AniM-DoG algorithm for its robustness and consistency. To the best of our knowledge, our work is the first that addresses the spatio-temporal feature detector in animated meshes.

Our goal in this chapter is to develop a feature detector on animated mesh based on space-time DoG, which has been reported to be efficient approximation of robust Laplacian blob detector in space domain. Note that animated meshes that we are dealing with are assumed to have no clutters or holes, and maintain fixed topology over time, without tearing or changing genus. The spatial samplings can vary from one mesh to another, but it is desirable to have uniform sampling across one surface. The temporal sampling rate can also vary (~30Hz in our experiments), depending on how the animation has been obtained. In any case, the temporal sampling is considered uniform.

The features we want to extract are the corners/blob-like structures, which are located in regions that exhibit a high variation of deformation spatially and temporally. We first define local deformation attributes on the animated mesh, from which we build a multi-scale representation of it. One of the main motivations to base our method on local surface deformation can be explained by the fact that (1) local deformation on a surface can be effectively measured by some well-defined principles, and that (2) the domain has intrinsic dimension of 2D+time (rather than 3D+time) with some reasonable assumption on the data, i.e. differentiable compact 2-manifold with time-varying embedding.

Since feature extraction in animated meshes is a relatively unexplored area we had some freedom to define the approach to the problem. The goal is to build a powerful dynamic feature extraction framework that satisfies a set of highly desirable requirements:

1. Capture animation deforming characteristics (Section 4.4)
2. Multiscale i.e. representing deforming structures at different scales (Section 4.6)
3. Robust to noise and geometry variations (Section 4.9)
4. Consistent and repeatable over semantically similar mesh animations (Section 4.9.1)
5. Meaningful for human perception (Section 4.9.2)

We addressed those requirements within a scope of different applied mathematical fields: mechanics, differential geometry, linear scale space theory and signal processing. First, the items 1, 4, 5 require to analyze and numerically measure the deformation of the animated mesh shape. Inter frame vertex displacement i.e. velocity or acceleration can be used to quantify the motion (Bulbul, Koca et al. 2010). However it can over-emphasize the saliency of rigidly moving animated mesh parts, which is undesirable. We propose to use local triangle strains as a surface deformation characteristic. By definition triangle strain carries only pure non-rigid deformation measure. We further improve the deformation characteristics robustness by fusing triangle strain with the mean curvature change. The later allows us to quantitatively capture approximately isometric deformations such as bending. Such deformation characteristics, as we show in evaluation of the method, also coherent with human eye perception of deforming mesh. Second, we would like the dynamic feature point to carry the information about spatio and temporal extents of deformation exhibited in a place of feature detection. Further we proved being correct to use math tools from linear scale space theory in order to address feature multiscale representation (Section 4.6). Linear scale space theory is a subset of scale space frameworks developed in Computer Vision community in 1980s. During the past decade it attracted attention in point-sampled and polygonal surface analysis. In this thesis we define scale space mechanisms for feature point extraction from animated meshes.

In this chapter we propose new deformation characteristics on animated meshes (Section 4.4), spatio-temporal Difference of Gaussians feature response operator (Section 4.7), robust dynamic feature point extraction framework for animated meshes (Section 4.9).

4.2 Related work: Feature point detection based on scale-space theory

4.2.1 Feature detection on static meshes

Feature extraction is essential in different domains of computer graphics and is frequently used for numerous tasks including registration, object query, object recognition etc. Scale-space representation has been widely used for feature extraction in image, video and triangle mesh data sets (Lindeberg 1998). However, almost no research has been done on the feature extraction of deforming surfaces, such as animated meshes.

One of the main contributions of this dissertation is dynamic feature detection and description on animated meshes. Feature point detection is a long-studied subject in computer vision, computer graphics and medical imaging. There is an extensive amount of existing works on feature detection, therefore we focus here only on the techniques most relevant and closely related to our method. We recapitulate previous works in feature detection for static and deforming shapes. (Pauly, Keiser et al. 2003, Lee, Varshney et al. 2005, Zaharescu, Boyer et al. 2009, Maes, Fabry et al. 2010, Sipiran and Bustos 2011, Darom and Keller 2012).

Feature detection from static geometry. (Pauly, Keiser et al. 2003) propose a technique for extracting features from point-sampled geometry. Given an input point cloud and an interest point p , the method first computes a surface variation using principal component analysis of the point local neighborhoods. The surface variation is closely related to the curvature and intuitively can be seen as surface’s deviation of being flat. The authors emphasize that the size of the neighborhood of the sample point p can be used as discrete scale parameter and therefore the concepts of scale-space theory (Lindeberg 1993) can be applied for the feature identification. Increasing the size of local neighborhood is essentially similar to applying a smoothing filter of larger scale. The features are determined as local maxima of surface variation across the scale axis. Instead of relying on just a single maximum for feature detection the authors propose to measure the saliency of a point by counting the number of times the surface variation exceeds a certain threshold. In that sense the approach favors scale-persistent feature points.

In the work of (Lee, Varshney et al. 2005) the mesh saliency is introduced as a measure of local regional importance of the mesh surface. First, the authors compute surface mean curvature map $\mathcal{C}(v)$ over vertices v of the mesh. However, curvature alone is insufficient for assessing saliency since it does not decently consider the local context. Therefore the following technique is proposed. Gaussian weighted combination $G(\mathcal{C}(v), \sigma)$ of mean curvature is computed over local neighborhood $N(v, \sigma)$ i.e. the set of points within a distance σ . Then the saliency $J(v)$ in vertex v is estimated as an absolute difference between the Gaussian-weighted averages (Difference-of-Gaussians (Hildreth and Marr 1980) at fine σ and coarse 2σ scales: $J(v) = |G(\mathcal{C}(v), \sigma) - G(\mathcal{C}(v), 2\sigma)|$. The mesh saliency of (Lee, Varshney et al. 2005) is illustrated in Figure 4-1. The interesting property of the proposed saliency measure is that it can be computed at multiple scales. The saliency at multiple scales is obtained by varying the standard deviation σ_i of the Gaussian filter. Then the saliency at scale σ_i is defined as $J_i(v) = |G(\mathcal{C}(v), \sigma_i) - G(\mathcal{C}(v), 2\sigma_i)|$. The applications of the mesh saliency include salient-based simplification and viewpoint selection.

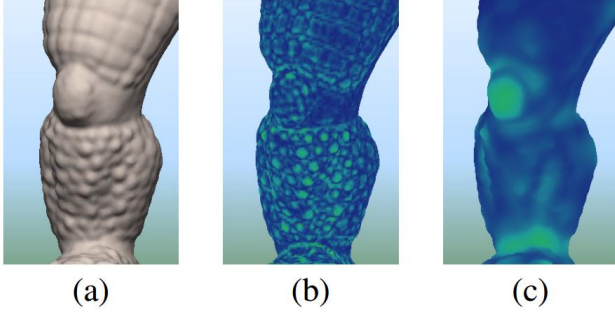


Figure 4-1. (a) The input mesh. (b) Magnitude of mean curvatures. (c) The mesh saliency values (Lee, Varshney et al. 2005).

Castellani and co-workers (Castellani, Cristani et al. 2008) present a framework for feature point detection and feature description applicable to incomplete noisy point clouds obtained from an optical scanning process. Given a mesh M , its representation at different levels of decimation is established via quadratic edge collapse remeshing technique (Garland and Heckbert 1997). Each level of decimation of a mesh the authors call an *octave* M^d . For the feature detection they propose the two-stage procedure: *intra-octave* and *inter-octave* phases. First, in *intra-octave* phase a multi-scale representation M_i^d of each M^d is established by applying n Gaussian filters $g(\sigma_i)$, $i=1..n$ on mesh vertex coordinates. On top of the multi-scale representation of the mesh, the Difference-of-Gaussians(DoG) operator is defined. Given a vertex $v \in M_i^d$, the DoG operator is computed as the Euclidean distance $\|n(v)(g(v, \sigma_i) - g(v, k\sigma_i))\|$ between vertex coordinates in the neighboring scales along the normal direction $n(v)$. Then feature points are extracted as local maxima of DoG operator. In the *inter-octave* phase, in order to improve robustness of the feature detection an inter-resolution validation is performed. Validation is carried out in a way that only feature points appearing in at least three distinct octaves are included in the final feature point set.

In the framework of a new matching method for photometric surfaces Zaharescu et al. (Zaharescu, Boyer et al. 2009) develop a new feature detector called MeshDoG. The proposed technique in some sense extends local feature detectors for 2D images to the case of scalar fields defined on 2D manifolds. Similarly to previous works (Pauly, Keiser et al. 2003, Lee, Varshney et al. 2005, Castellani, Cristani et al. 2008) the method of (Zaharescu, Boyer et al. 2009) is based on linear scale-space theory (Lindeberg 1993). Given a triangle mesh M that approximates a 2D manifold and a scalar function defined on the mesh $f: M \rightarrow \mathbb{R}$, the scale-space of f is computed progressively. Starting from $f_0 = f$, each next scale f_i is built by a convolution with Gaussian kernel $\{f_i = f_{i-1} * g_\sigma\}_{i=1}^k$ of standard deviation σ . The authors have chosen $k=93$ and $\sigma = \frac{7}{3}e_{avg}$, where e_{avg} is the average edge length in the mesh M . Then similarly to works (Lee, Varshney et al. 2005, Castellani, Cristani et al. 2008), the Difference of Gaussians operator is computed over the mesh. That differential operator the authors refer to as MeshDoG. However, in contrast to (Lee, Varshney et al. 2005) MeshDoG is built on scalar function scale-space rather than vertex coordinates. The MeshDoG is defined as a subtraction of neighbouring scales $\text{MeshDoG}_i = f_i - f_{i-1}$. The authors impose the following criteria for feature point extraction from MeshDoG response. The point $x \in M$ is marked as a feature if it satisfies (a) MeshDoG reaches maximum over scales and one-ring neighbourhood of the point x and (b) the value of MeshDoG at x is in top 5% of vertices of the mesh sorted by magnitude of MeshDoG. Lastly, unstable extrema are eliminated by retaining only features with high corner response of the Harris operator (Harris and Stephens 1988, Lowe 2004). Note that the method can work on photometric data of the mesh such as texture or vertex color but not limited to. Any scalar field defined over mesh surface (such as curvature maps for example) can be used in the algorithm.

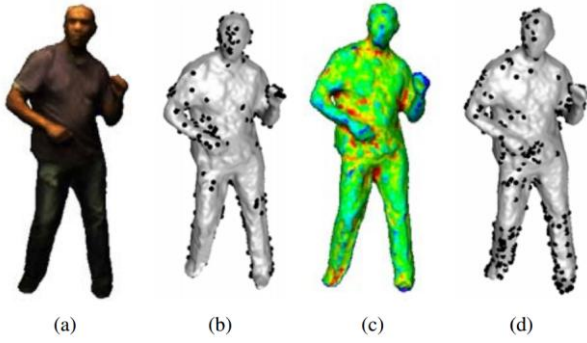


Figure 4-2. Feature detection from scalar field defined over 2D manifold (Zaharescu, Boyer et al. 2009). (a) input mesh with photometric scalar field. (b) features extracted from (a). (c) mean surface curvature. (d) features extracted from (c).

The work of (Sun, Ovsjanikov et al. 2009) propose not only robust *Heat Kernel Signature* (HKS) but also suggest feature extraction technique based on heat kernels. To identify the feature points the authors propose to search for local maxima of heat kernel $k_t(x, x)$ for large t . These maxima allow capturing most of the shape extremities and protrusions such as limb tips of people or humanoid models. The authors define a point x to be a feature if $k_t(x, x) > k_t(y, y)$ for all y in the 2-ring neighbourhood $y \in N_s^2(x)$ of x .

The method of (Maes, Fabry et al. 2010) performs reliable feature detection as extrema in the scale space of the mean curvature in each vertex on different smoothed versions of the input mesh. First a scale space is constructed by smoothing the input mesh via the approximation of Gaussian filter. For the detection of feature points the authors compute the mean curvature H for each vertex at each scale of the scale space. In contrast to (Castellani, Cristani et al. 2008) who defines Difference-of-Gaussians (DoG) on vertex displacements in scale space, (Maes, Fabry et al. 2010) define feature response DoG as differences in mean curvature between subsequent scales $DH_i = H_{i+1} - H_i$, where i corresponds to scale index. The feature points are defined as a scale-space extrema over the scale-space neighborhood of a vertex (Figure 4-3). In order to do, that for each vertex and each scale the value of DH_i is compared to its neighbors. The point is added to the feature point set only if DH_i is a local extremum with respect to all its neighbors.

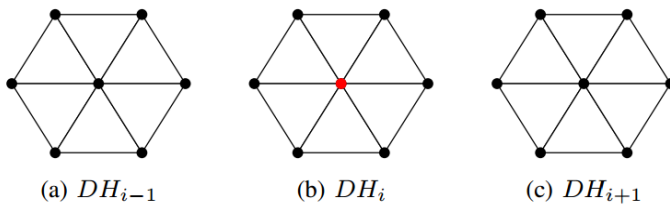


Figure 4-3. The neighbourhood of the vertex (red point) in scale space of mean curvature H (Maes, Fabry et al. 2010).

(Sipiran and Bustos 2011) present an effective interest point detector for 3D meshes. The method is established on the idea that extends the Harris operator (Harris and Stephens 1988) which is successfully used in Computer vision for feature point detection on images (Mikolajczyk and Schmid 2004, Mikolajczyk, Tuytelaars et al. 2005) and videos (Laptev 2005). The authors propose to consider a local surface patch around a vertex as an image, which makes it feasible to rely on the robust Harris operator. Briefly the algorithm proceeds as follows. First, the local neighborhood for each vertex is determined. Second, applying PCA on the neighborhood yields a canonical XY-plane. In such settings z -axis is aligned with a surface normal which corresponds to the eigenvector of the smallest magnitude. Then the authors fit a quadratic surface of the form $z = f(x, y)$ to the local surface patch in the new xyz coordinate system. This step is followed by the computation of derivatives on the fitted surface. In order to improve robustness to local geometry changes, Gaussian functions are used for smoothing the derivatives. Using the derivatives, the algorithm constructs the auto-correlation function for

evaluation of the Harris operator (Harris and Stephens 1988), Harris response is computed for each vertex. Finally, the method of (Sipiran and Bustos 2011) suggests several ways for extracting interest points relying on the vertex responses. Feature can be defined as a local maxima of responses with respect to 1-ring neighborhood, or as vertices with the response values over a user-defined threshold, or as cluster centers w.r.t. to the Harris response. Figure 4-4 depicts examples of feature extraction of (Sipiran and Bustos 2011). Note, that in contrast to (Sun, Ovsjanikov et al. 2009) this feature extraction technique is not invariant to bending and isometries. Another results of (Sipiran and Bustos 2011) are shown in Figure 4-5 where features are extracted at different levels of detail (LoD) of the same mesh. It can be clearly seen that changes in LoD directly affect the feature extraction results.

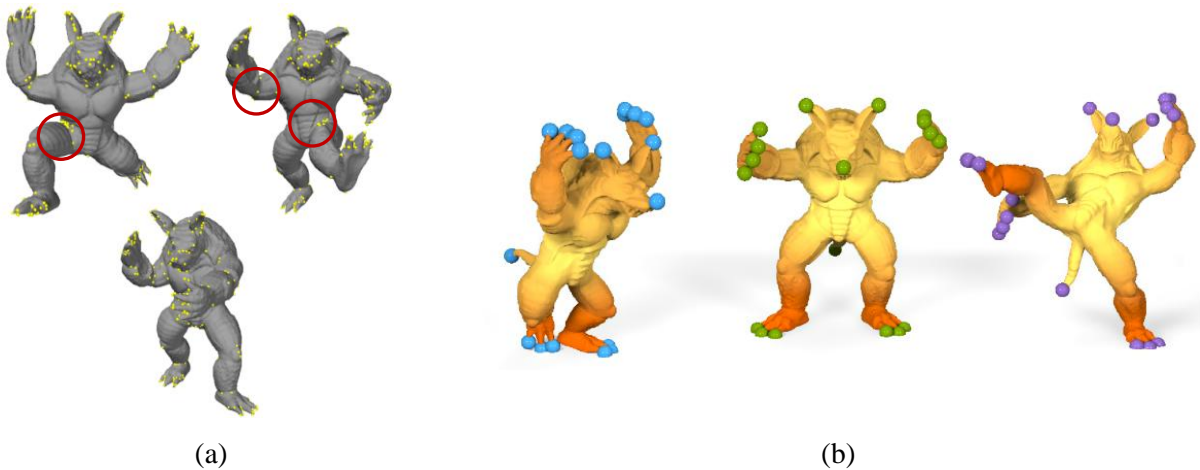


Figure 4-4. (a) Examples of features extracted by method of (Sipiran and Bustos 2011) from different postures of Armadillo model. Some of the discrepancies between extracted features (as for example in regions marked in red) are induced by bending of the model, which is in contrast to HKS feature extraction (Sun, Ovsjanikov et al. 2009). (b) Features extracted from Armadillo model by (Sun, Ovsjanikov et al. 2009).

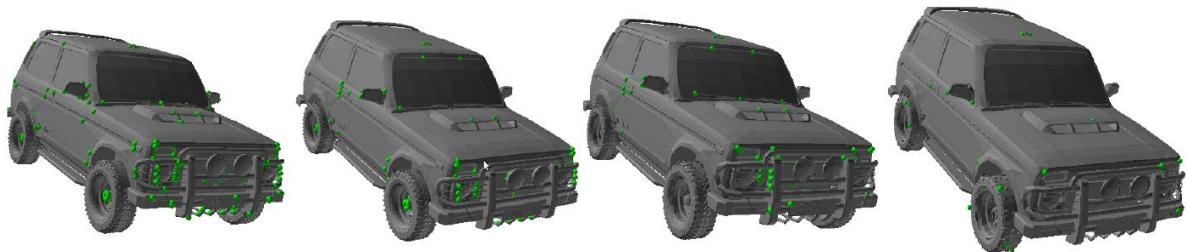


Figure 4-5. Features on models at different Levels of Details (Sipiran and Bustos 2011).

In the work (Darom and Keller 2012), the authors propose a framework for feature detection and description on 3D meshes. The method is closely related to works (Castellani, Cristani et al. 2008, Zaharescu, Boyer et al. 2009, Maes, Fabry et al. 2010). Similarly to (Castellani, Cristani et al. 2008) the authors apply Gaussian smoothing on mesh geometry. However as one of the contributions they add a regularization term to facilitate invariance of smoothing with respect to sampling density of meshes. As in (Castellani, Cristani et al. 2008), the local features are selected as local maxima both in scale-space and location.

4.2.2 Feature detection on time varying geometry

In contrast to feature detection on static shapes, feature detection on dynamic geometry has not received enough attention in the graphics community, which is unfortunate. To the best of our knowledge there is very limited amount of work that directly address the problem of the saliency of deforming shapes such as the work of Bulbul et al. (Bulbul, Koca et al. 2010).

In the work of (Bulbul, Koca et al. 2010) the authors address the problem of calculating saliency on animated meshes with material properties. The authors achieve an integrated approach to saliency computation by incorporating multiple modalities such as color, geometry and motion that can characterize the saliency of animated meshes. For each modality a separate feature map is computed and then combined in so-called master feature map. The geometry feature maps are computed in spirit of (Lee, Wang et al. 2006, Maes, Fabry et al. 2010) by estimating mean curvatures in each vertex and each frame. Given each point x of the animated mesh, the velocity feature map is obtained straightforwardly by computing displacements of x in all pairs of subsequent frames. Similarly, measuring of changes of pre-computed velocities in all vertices over all frames yields the acceleration feature map. The last feature maps are composed of color maps and luminance maps obtained directly from the photometric information of the input animated mesh. Then a saliency response D for each of the feature maps is computed with the Difference-of-Gaussians operator analogous to (Castellani, Cristani et al. 2008, Zaharescu, Boyer et al. 2009, Darom and Keller 2012). Different saliency response maps are depicted in Figure 4-6. The master saliency response is composed of a combination of all feature saliency responses. The authors also propose several useful applications of their technique including viewport selection, adaptive mesh simplification and dynamic level of detail.

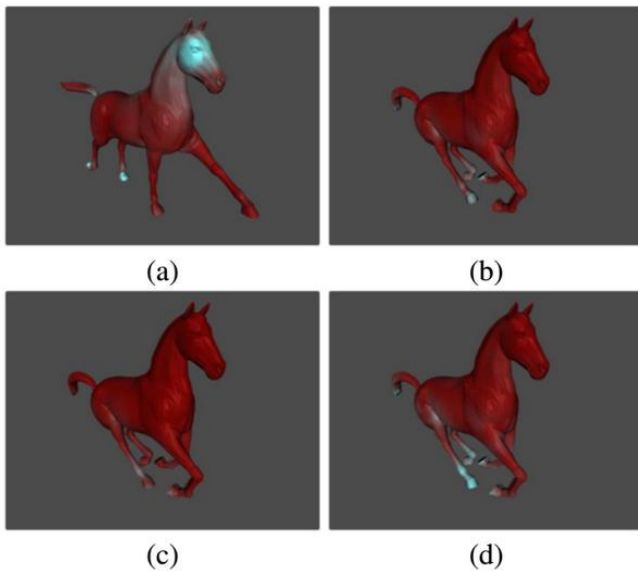


Figure 4-6. The calculated saliencies based on geometric mean curvature (a), velocity (b), and acceleration (c) in a horse model. The image in (d) shows the combined saliency map of the velocity and acceleration features (Bulbul, Koca et al. 2010).

4.3 Animated mesh

Here we provide a formal definition of an animated mesh. Note that we consider deforming mesh and animated mesh to be synonyms and therefore we use the terms interchangeably.

Definition 1. (Implicit) Animated mesh is a 2-manifold with time-varying embedding in Euclidean space.

Definition 2. (Explicit) Animated mesh is an ordered sequence of M triangle meshes with fixed number of vertices N and fixed triangulation T :

$$\mathcal{M} = \{\mathcal{M}_f = (V_f, T) \mid f = 1..M\}, V_f = (\{v_f^i \in \mathbb{R}^3 \mid i = 1..N\}, T).$$

Some examples of animated meshes we work with are depicted in Figure 4-7. Note that deforming meshes with artefacts (such as zero-sized triangles) or meshes that approximate invalid 2-manifolds as well as time-varying point-clouds are beyond the scope of this work. Note, that the case of animated meshes with changing mesh connectivity is addressed in Chapter 6.

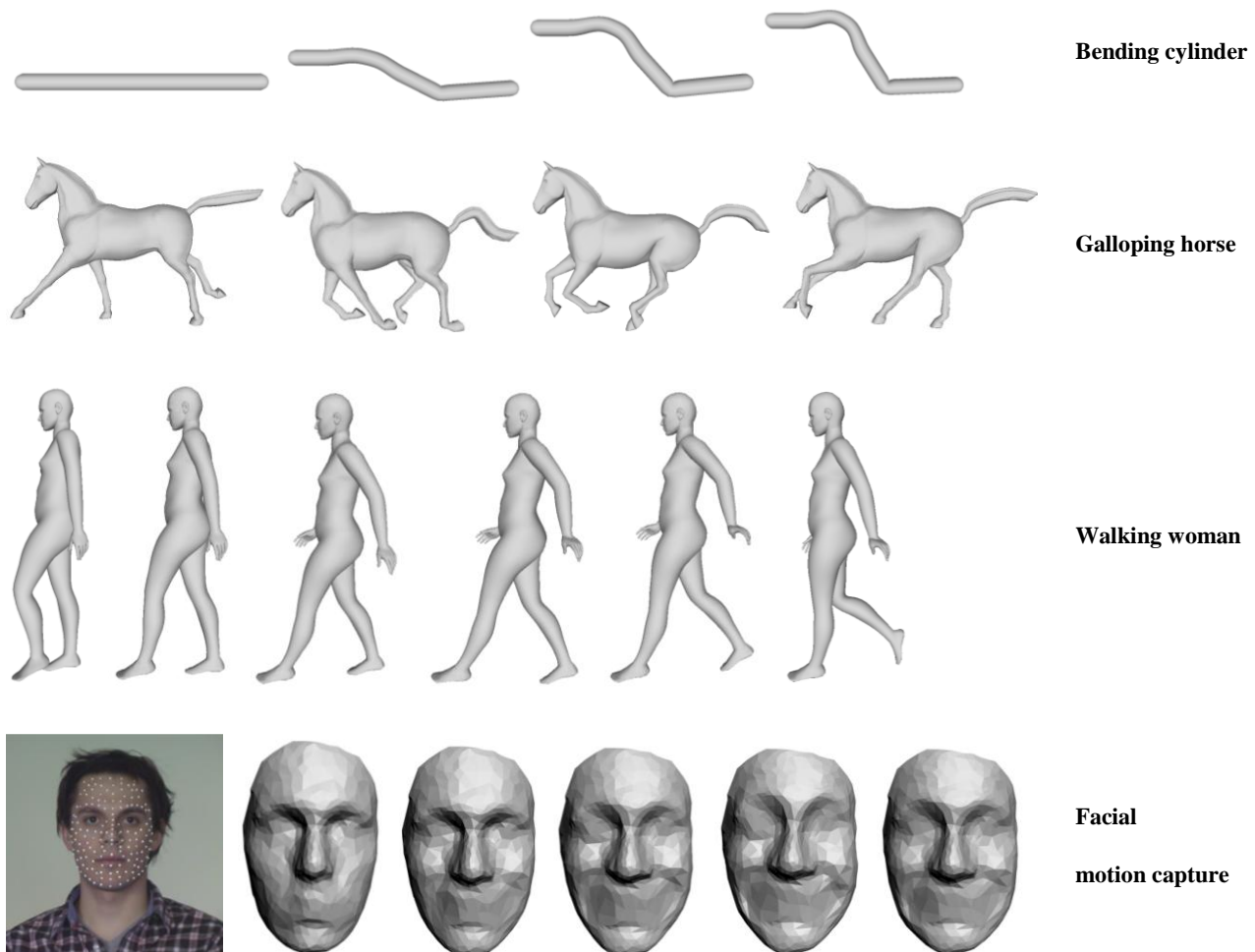


Figure 4-7. Animated mesh examples including synthetic data as well as animation originating from motion capture and real performance.

Typically animated meshes originate either from animation software (Autodesk Maya, 3ds Max), real-time optical sensor devices (Li, Weise et al. 2010, Cao, Weng et al. 2013) or from motion capture sessions. Refer to (Appendix A. MOCAP Data Acquisition Process) for the details on the motion capture technique we arranged in scope of this thesis.

4.4 Deformation characteristics

Our feature extraction method is based on capturing of local surface deformation characteristics in animated meshes. We are interested in quantities that are related to local deformation characteristics associated to each point of the mesh, at each frame. Thus, we base our algorithm on locally computed strain and curvature values computed as follows.

Strain computation. We first consider the degree of deformation associated to each triangle on the mesh at each frame. Our method requires to specify the reference pose, the rest shape of the mesh before deformation (Figure 4-8). In certain cases the reference pose can be found in one of the frames of the animation. If none of the given frames is appropriate as the rest pose, some prior works (Lian, Godil et al. 2013) could be adopted to compute a canonical mesh frame by taking the average of all frames.

Let \mathbf{v}_i and $\tilde{\mathbf{v}}_i$ be the vertices of a triangle before and after the deformation, respectively. A 3 by 3 affine matrix \mathbf{F} and displacement vector \mathbf{d} transforms \mathbf{v}_i into $\tilde{\mathbf{v}}_i$ as follows.

$$\mathbf{F} \cdot \mathbf{v}_i + \mathbf{d} = \tilde{\mathbf{v}}_i, i = 1, \dots, 3$$

Similarly to (Sumner and Popović 2004), we add a fourth vertex⁵ in the direction of the normal vector of the triangle and subtract the first equation from the others to eliminate \mathbf{d} . Then, we get $\mathbf{F} = \tilde{\mathbf{V}} \cdot \mathbf{V}^{-1}$ where

$$\mathbf{V} = [\mathbf{v}_2 - \mathbf{v}_1 \quad \mathbf{v}_3 - \mathbf{v}_1 \quad \mathbf{v}_4 - \mathbf{v}_1],$$

and

$$\tilde{\mathbf{V}} = [\tilde{\mathbf{v}}_2 - \tilde{\mathbf{v}}_1 \quad \tilde{\mathbf{v}}_3 - \tilde{\mathbf{v}}_1 \quad \tilde{\mathbf{v}}_4 - \tilde{\mathbf{v}}_1].$$

Non-translational component of \mathbf{F} encodes the change in orientation, scale, and skew induced by the deformation. Note that this representation specifies the deformation in per-triangle basis, so that it will be independent of the specific position and orientation of the mesh in world coordinates. Without loss of generality, we assume that the triangle is stretched first and then rotated. Then we have $\mathbf{F} = \mathbf{R}\mathbf{U}$, where \mathbf{R} denotes the rotation tensor and \mathbf{U} the stretch tensor. Since we want to describe the triangle only with its degree of stretch, we eliminate the rotation component of \mathbf{F} by computing the right Cauchy deformation tensor \mathbf{C} as defined by:

$$\mathbf{C} = \mathbf{F}^T \mathbf{F} = (\mathbf{R}\mathbf{U})^T (\mathbf{R}\mathbf{U}). \quad (4-1)$$

Because of the orthogonality property of the rotation matrix \mathbf{R} (Eq. (4-2))

$$\mathbf{R}^T \mathbf{R} = \mathbf{I}, \quad (4-2)$$

where \mathbf{I} is the identity matrix, the matrix \mathbf{C} (Eq. (4-1)) can be simplified to

$$\mathbf{C} = \mathbf{U}^T \mathbf{R}^T \mathbf{R} \mathbf{U} = \mathbf{U}^T \mathbf{U}. \quad (4-3)$$

It can be shown that \mathbf{C} is equal to the square of the right stretch tensor (refer to (Dill 2006) for in depth information on finite strain theory and properties of deformation tensors). We obtain principal stretches by the Eigen-analysis on \mathbf{C} , and use the largest eigenvalue λ_1 (maximum principal strain) as the in-plane deformation of

⁵ It is not necessary to add a fourth vertex if working in 2d coordinate frame (i.e. triangle's plane). The output strain values are invariant to computing in 2d or 3d.

the triangle. Intuitively, the principal strain measures quantitatively the degree of non-rigid deformation of a triangle (strain and shear).

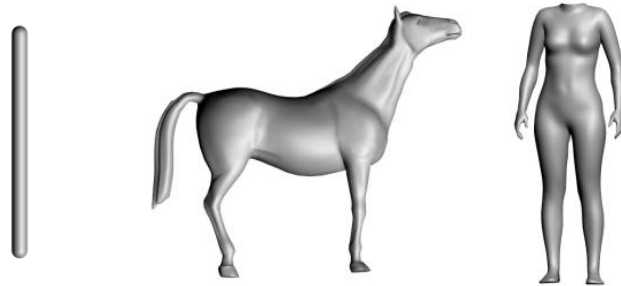


Figure 4-8. Rest shapes are chosen as the reference frame for defining the deformation characteristics.

Curvature computation. Computing the curvature at the vertices of a mesh is known to be non-trivial because of the piecewise-linear nature of meshes. One simple way of computing the curvature would be to compute the angle between two neighboring triangles along an edge. However, such curvature measurement is too sensitive to the noise on the surface of the mesh because its computation relies on two triangles only. Instead, we compute the curvature over a set of edges as described in (Alliez, Cohen-Steiner et al. 2003). Given a vertex v_i , we first compute the set of edges E_i whose two vertices are within a user-defined geodesic distance to v_i . Next we compute the curvature at each of the edges of E_i . The curvature at v_i is then calculated as the average of the curvatures at the edges of E_i .

Deformation measure. Let \mathcal{M} with M frames and N vertices be a given deforming mesh. For each vertex $v_i^f \in \mathcal{M}$ ($f = 1, \dots, M, i = 1, \dots, N$) on which we have computed strain $s(v_i^f)$ and curvature $\kappa(v_i^f)$, we define the deformation characteristics $d(v_i^f)$ as follows:

$$d(v_i^f) = s(v_i^f) + \alpha \cdot |\kappa(v_i^f) - \kappa(v_i^1)|.$$

The first term is obtained by transferring the above described per-triangle strain values to per-vertex ones, computed at each frame. At each vertex, we take the average strain values of its adjacent triangles as its strain.

The second term encodes the curvature change with respect to the initial, reference frame. Note that $d(v_i^f) \geq 0$ for $\forall v_i^f$, which we use later for the feature detection (Section 4.8). We set α typically to 7 in our experiments. This weighting parameter has been tuned specifically for improving consistency of deformation characteristics extracted from corresponding pairs of animated meshes (e.g. galloping horse and camel). Color coded deformation characteristics on a bending cylinder data is shown in Figure 4-9.

4.5 Basics of linear scale-space theory

At the heart of our algorithm is a scale-space representation of animated meshes. Here we briefly recapitulate some basic notions that have been previously studied. Later, we develop its extensions to animated mesh data, which are described in Sections 4.6-4.8.

Scale-space representations have been studied extensively in feature detection for images, and more recently, for videos. The basic idea is to represent an original image $f: \mathbb{R}^d \rightarrow \mathbb{R}$ at different scales as $L: \mathbb{R}^d \times \mathbb{R}_+ \rightarrow \mathbb{R}$ by convolution of f with a Gaussian kernel with variance σ :

$$L(\mathbf{x}; \sigma) = G(\mathbf{x}; \sigma) * f(\mathbf{x}), \tag{4-4}$$

where $G(\mathbf{x}; \sigma) = \frac{1}{(\sqrt{2\pi}\sigma)^d} \exp(-\frac{x_1^2 + \dots + x_d^2}{2\sigma^2})$.

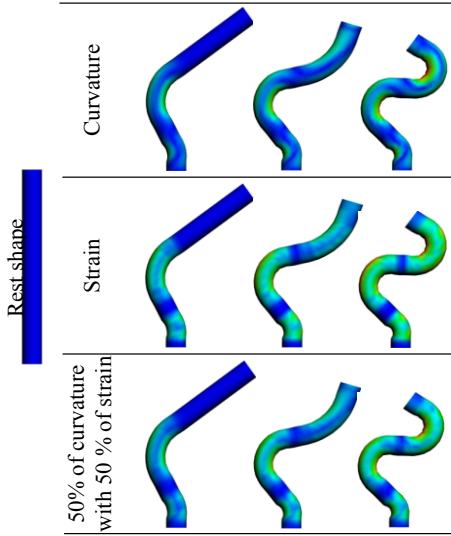


Figure 4-9. Local deformation characteristics are shown on a bending cylinder mesh.

One of the most successful feature detectors is based on DoG (Difference of Gaussians). To efficiently detect feature points in scale space, Lowe (Lowe 2004) proposed using convolution of the input image with the DoG functions. It is computed from the difference of two nearby scales:

$$D(\mathbf{x}; \sigma) = (G(\mathbf{x}; k\sigma) - G(\mathbf{x}; \sigma)) * f(\mathbf{x}) = L(\mathbf{x}; k\sigma) - L(\mathbf{x}; \sigma), \quad (4-5)$$

where k is a constant multiplicative factor separating the two nearby scales.

Note that DoG is particularly efficient to compute, as the smoothed images L need to be computed in any case for the scale space feature description, and D can therefore be computed simply by image subtraction.

The DoG provides a close approximation to the scale-normalized Laplacian of Gaussian (Lindeberg 1994), $\sigma^2 \nabla^2 G$, which has been proven to produce the most stable, scale-invariant image features (Mikolajczyk and Schmid 2001). The DoG and scale-normalized LoG are related through the heat-diffusion equation:

$$\frac{\partial G(\mathbf{x})}{\partial \sigma} = \sigma \nabla^2 G(\mathbf{x}), \quad (4-6)$$

where the Laplacian on the right side is taken only with respect to the \mathbf{x} variables. From this, we see that $\nabla^2 G(\mathbf{x})$ can be computed from the finite difference approximation to $\partial G(\mathbf{x})/\partial \sigma$, using the difference of nearby scales at $k\sigma$ and σ :

$$\frac{\partial G(\mathbf{x})}{\partial \sigma} = \lim_{k \rightarrow 1} \frac{G(\mathbf{x}; k\sigma) - G(\mathbf{x}; \sigma)}{k\sigma - \sigma} = \sigma \cdot \nabla^2 G(\mathbf{x}), \quad (4-7)$$

and therefore,

$$G(\mathbf{x}; k\sigma) - G(\mathbf{x}; \sigma) \approx (k - 1) \cdot \sigma^2 \cdot \nabla^2 G \quad (4-8)$$

4.6 Scale-space of surface deformation characteristics

Given the deformation measures d for all vertices of the input animated mesh M , we re-compute d at $K \cdot L$ different scale representations, obtaining octaves $O_{kl} (k \in \Sigma=0, \dots, K, l \in T=0, \dots, L)$ of deformation characteristics at different spatio-temporal resolutions. Theoretically, the octaves are obtained by applying an approximated Gaussian filter for meshes. In practice, the approximation consists of subsequent convolutions of the given mesh with a box (average) filter (Darom and Keller 2012). In our work, we define a spatio-temporal average filter on the deformation characteristics of the animated mesh and compute a set of filtered deformation scalar fields, which we call as anim-octaves. As shown in Figure 4-10, we define spatio-temporal neighborhood N_{st} of a vertex in animation as a union of its spacial and temporal neighborhoods. A spatio-temporal average smoothing over N_{st} is obtained by applying a local spatial filter followed by a local temporal one.

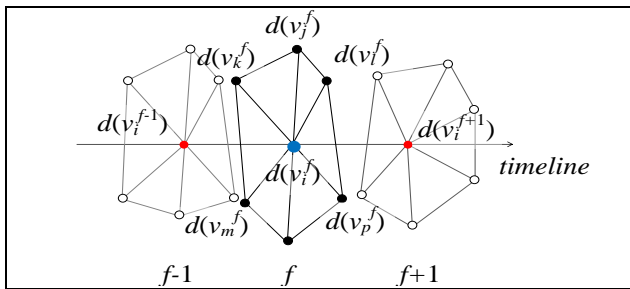


Figure 4-10. The smallest possible spatio-temporal neighborhood N_{st} of a vertex v_i^f (blue dot) is composed of 1-ring spatial neighbors in frame f (black vertices) and 1-ring temporal neighbors (red vertices). Note that considering the temporal neighbors implies considering their spatial neighbors (white vertices) as well.

More specifically, for each vertex v_i^f at an anim-octave of scale (σ_k, τ_l) , we compute deformation measures at next spatial octave (σ_{k+1}, τ_l) , by averaging deformation measurements in current vertex of current octave $d(v_i^f, \sigma_k, \tau_l)$ and its 1-ring's spatial neighborhood $d(N_s^1(v_i^f), \sigma_k, \tau_l)$ i.e. at adjacent vertices. For the next temporal octave (σ_k, τ_{l+1}) we repeat similar procedure but this time averaging deformation values in 1-ring temporal neighborhood $N_t^1(v_i^f)$ as in Fig. 3. And for the next spatio-temporal octave, we start from deformations in octave (σ_{k+1}, τ_l) and apply temporal average filter again in the way described above, which yields $d(v_i^f, \sigma_{k+1}, \tau_{l+1})$. We continue this procedure until we build the desired number of spatio-temporal octaves. Fig. 4 illustrates our anim-octaves structure. We denote an anim-octave as $O_{kl} = d(\mathcal{M}, \sigma_k, \tau_l)$, where $O_{00} = d(\mathcal{M})$. We note that although the term octave is widely used to refer to a discrete interval in the scale space, it may be misleading since in a strict sense, our octaves do not represent the interval of half or double the frequency. In Figure 4-10, we illustrate multi-scale deformation characteristics we computed on an animated mesh. The horizontal axis represent the spatial scale σ_k , and the vertical axis the temporal scale τ_l .

Widths of the average filters. We set the width of the spatial filter as the average edge length of the mesh taken at the initial frame, assuming that spatial sampling of the mesh is moderately regular, and that the edge lengths in the initial frame represent well those in other frames of animation. Note that it can be done in a per-vertex manner, by computing for each vertex the average distance to its 1-ring neighbors, as it has been proposed by (Darom and Keller 2012). However, since this will drastically increase the computation time for the octave construction stage, we have chosen to use the same filter width for all vertices.

Determining the width of the temporal filter is simpler than the spatial one, as almost all data have regular temporal sampling rate (fps) throughout the duration of animation. Similarly to the spatial case, the inter-frame time is used to set the width of the temporal filter. Instead of averaging over immediate neighbors, however, we

consider larger number of frame neighbors, in most cases. This is especially true when the animated mesh is densely sampled in time. The filter widths we used for each dataset are summarized in Table 4-1.

octave scale	σ_1	σ_2	...	σ_k
τ_1	O_{11}	O_{12}	...	O_{1k}
τ_2	O_{21}	O_{22}	...	O_{2k}
\vdots	\vdots	\vdots	\ddots	\vdots
τ_1	O_{11}	O_{12}	...	O_{1k}

Figure 4-11. Scale space is built by computing a set of octaves of an input animated mesh.

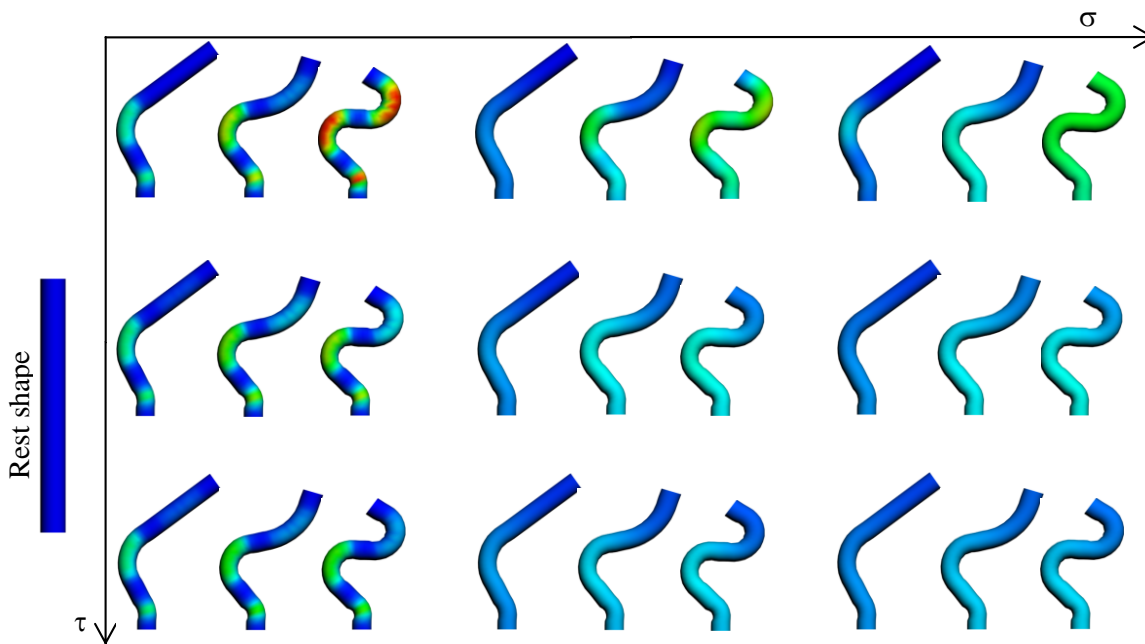


Figure 4-12. Multi-scale deformation characteristics on an animated mesh. From left to right, spatial scale σ_j increases, and from top to bottom, temporal scale τ_i increases.

4.6.1 Relationship between box filter and Gaussian filter widths.

To compute animation deformation multi-scale representation we use box-filtering that approximates Gaussian smoothing. As reported in (Salden, Romeny et al. 1998), average box filter applied n times is equivalent to Gaussian filter with standard deviation :

Maximum number of smoothings. Since an animated mesh can be highly redundant and heavy in size, the memory space occupied by the anim-octaves can be large as the number of scales increases. This becomes problematic in practice. With an insufficient number of smoothings, on the other hand, features of large characteristic scale will not be detected. Indeed, when the variance of the Gaussian filter is not sufficiently large, only boundary features will be extracted. Figure 4-13 illustrates the principle behind the characteristic scale and the

maximum required scale level. Given a spatio-temporal location on the mesh, we can evaluate the DoG response function and plot the resulting value as a function of the scale (number of smoothings). Here, the spatial scale has been chosen as a parameter for the simplicity. The characteristic scales of the chosen vertices are shown as vertical lines, which can be determined by searching for scale-space extrema of the response function. To detect the feature points on the bending region in the middle (v_1), for instance, the octaves should be built up to 12 level. This means the maximum number of smoothings must be carefully set in order to be able to extract feature points of all scales while maintaining moderate number of maximum smoothing.

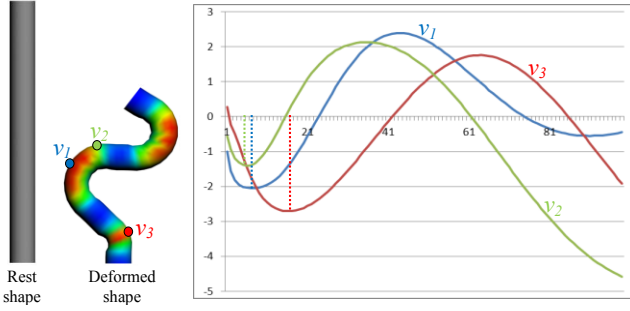


Figure 4-13. The DoG response function has been evaluated as a function of the spatial scale (number of smoothings). The characteristic scales of the chosen vertices are shown as vertical lines.

In order to make sure that the features representing blobs of large scale are detected, we start by an average filter. Multiple applications of a box (average) filter approximates a Gaussian filter (Andonie and Carai 1992). More precisely, n averagings with a box filter of width w produce overall filtering effect equivalent to the Gaussian filter with a standard deviation of:

$$\sigma = \sqrt{\frac{n(w^2 - 1)}{12}}. \quad (4-9)$$

When the Laplacian of Gaussian is used for detecting blob centers (rather than boundaries), the Laplacian achieves a maximum response with

$$\sigma = \frac{r}{\sqrt{2}} \quad (4-10)$$

where r is the radius of the blob we want to detect.

Now assuming that the maximum radius r_{\max} of the blob we want to detect is known, we can compute the required number of average smoothing that is sufficient to detect blob centers from Eq.(4-9) and Eq. (4-10):

$$r_{\max}^2 = \frac{n(w^2 - 1)}{6} \quad (4-11)$$

$$\Leftrightarrow n = \frac{6r^2}{w^2 - 1}. \quad (4-12)$$

The maximum number of application of box filter for each dataset is listed in Table 4-1.

Maximum radius of all possible blobs. Along the spatial scale space, we consider the average edge length of the initial shape as the width of the average filter w , as described above. For the maximum possible radius of a blob, we compare the axis-length change of the tight bounding box of the mesh during animation, with respect to its initial shape. The half of the largest change in axis-length is taken as r_{\max} .

Along the temporal scale space, we assume that the maximum radius r_{\max} of all possible blobs is the half of the total time of duration of animation. By fixing the maximum number of smoothing to some moderate value, we obtain the desirable box filter width from Eq.(4-11) or Eq.(4-12).

4.7 Spatio-temporal DoG operator

We extend the idea of scale representation in spatial domain to spatio-temporal domain and adopt it to the case of animated mesh. Next, we propose our feature point detector and discuss some of its implementation related issues.

Spatio-temporal scale space principles. Given time varying input signal $f(\mathbf{x}, t)$, $f: \mathbb{R}^d \times \mathbb{R} \rightarrow \mathbb{R}$, one could build its scale-space representation $L(\mathbf{x}, t; \sigma, \tau)$ by convoluting f with anisotropic Gaussian

$$L(\mathbf{x}, t; \sigma, \tau): \mathbb{R}^d \times \mathbb{R} \times \mathbb{R}_+^2 \rightarrow \mathbb{R}.$$

The motivation behind the introduction of separate scale parameters in space σ and time τ is that the space- and the time- extents of feature points are independent in general (Laptev and Lindeberg 2003).

Alternatively, another useful formulation of spatio-temporal scale space was reported in the work of (Salden, Romeny et al. 1998). The spatio-temporal scale space $L(\mathbf{x}, t; \sigma, \tau)$ for a signal $f(\mathbf{x}, t)$ could be defined as a solution of two diffusion equations

$$\frac{\partial L}{\partial \sigma} = \sum_i \frac{\partial^2 L}{\partial x^i \partial x^i}, \quad (4-13)$$

$$\frac{\partial L}{\partial \tau} = \frac{\partial^2 L}{\partial t^2}, \quad (4-14)$$

with an initial condition

$$\lim_{\sigma \rightarrow 0^+ \tau \rightarrow 0^+} L(\mathbf{x}, t; \sigma, \tau) = f(\mathbf{x}, t).$$

In our case, the input animated mesh M can be considered as 2-manifold with time-varying embedding, i.e. $m(u, v, t)$ in 3D Euclidean space. Measuring deformation scalar field $d(\mathcal{M})$ in 2-manifold over space and time yields a 3D input signal of the form $d(u, v, t)$, $d: \mathbb{R}^2 \times \mathbb{R} \rightarrow \mathbb{R}$, and its scale space of the form $L_d(u, v, t; \sigma, \tau): \mathbb{R}^2 \times \mathbb{R} \times \mathbb{R}_+^2 \rightarrow \mathbb{R}$. Given the scale space representation $L_d(\mathbf{x}, t; \sigma, \tau)$ of the input animated mesh, we proceed with the construction of the DoG feature response pyramid, which we as describe below.

Computing DoG pyramid. To achieve the invariance in both space and time, we introduce a spatio-temporal DoG operator, which is a new contribution. Our idea is to combine the spatial and the temporal parts of Laplacian and Difference-of-Gaussians. Given the property of DoG Eq.(4-8) and Eq.(4-13), Eq.(4-14), we obtain the following:

$$D(\mathbf{x}; \sigma) = L(\mathbf{x}; k\sigma) - L(\mathbf{x}; \sigma) = \sum_i \frac{\partial^2 L}{\partial x^i \partial x^i}, \quad (4-15)$$

$$D(t; \tau) = L(t; k\tau) - L(t; \tau) = \frac{\partial^2 L}{\partial t^2}. \quad (4-16)$$

Then we propose to define the spatio-temporal Laplacian by adding (4-15) and (4-16):

$$D(\mathbf{x}; \sigma) + D(t; \tau) = \sum_i \frac{\partial^2 L}{\partial x^i \partial x^i} + \frac{\partial^2 L}{\partial t^2} = \nabla^2 L. \quad (4-17)$$

The new spatio-temporal Laplacian operator is just a sum of DoG in space scale and DoG in time scale, which is computationally very efficient.

In order to be able to extract features of all scales correctly, we need to scale-normalize the DoG response function. Choosing the exponent coefficients for the spatial Eq.(4-15) (rightmost-hand term) and the temporal Eq.(4-16) (rightmost-hand term) parts of Laplacian (Laptev and Lindeberg 2003):

$$\nabla_{norm}^2 L = \sigma^2 \tau^{1/2} \sum_i \frac{\partial^2 L}{\partial x^i \partial x^i} + \sigma \tau^{3/2} \frac{\partial^2 L}{\partial t^2} \quad (4-18)$$

Therefore, to achieve scale-normalized approximation of Laplacian through DoG, we multiply both sides of Eq.(4-15) with $\sigma^2 \tau^{1/2}$ and both sides of Eq.(4-16) with $\sigma \tau^{3/2}$ obtaining

$$\sigma^2 \tau^{1/2} D(\mathbf{x}; \sigma) = \sigma^2 \tau^{1/2} \sum_i \frac{\partial^2 L}{\partial x^i \partial x^i}, \quad (4-19)$$

$$\sigma \tau^{3/2} D(t; \tau) = \sigma \tau^{3/2} \frac{\partial^2 L}{\partial t^2}. \quad (4-20)$$

And from Eq.(4-19), Eq.(4-20) we see that

$$\nabla_{norm}^2 L = \sigma^2 \tau^{1/2} D(\mathbf{x}; \sigma) + \sigma \tau^{3/2} D(t; \tau).$$

On the other hand, we can get a formulation of spatio-temporal DoG that approximates scale-normalized Laplacian

$$D_{st}(\mathbf{x}, t; \sigma, \tau) = \sigma^2 \tau^{1/2} D(\mathbf{x}; \sigma) + \sigma \tau^{3/2} D(t; \tau).$$

Thus, given the definition of spatio-temporal Difference of Gaussians we can compute feature response pyramid in the following way. For each vertex (u, v, t) in the animated mesh \mathcal{M} , and for every scale $(\sigma_k, \tau_l) \in \Sigma \times T$ of the surface deformation pyramid we compute $D_{st}(u, v, t; \sigma_k, \tau_l)$.

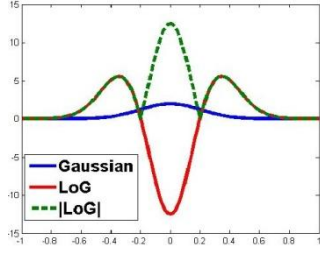
4.8 Feature point detection for animated meshes

Once the spatio-temporal DoG pyramid $\{D_{st}(u, v, t; \sigma_k, \tau_l) | (\sigma_k, \tau_l) \in \Sigma \times T\}$ is constructed, we extract feature points by identifying local extrema of the adjacent regions in the space, time, and scales. In contrast to (Mikolajczyk and Schmid 2001) who computes Harris and Laplacian operators, our method requires only DoG, which makes itself computationally efficient. This is particularly interesting for the animated mesh data which is generally much heavier than the image. Considering that our surface deformation function is always non-negative (and consequently its scale-space representation), it is worth mentioning that Laplacian of Gaussian and its DoG approximation reach local minima in centers of blobs. Such specific LoG behavior is illustrated in Figure 4-14.

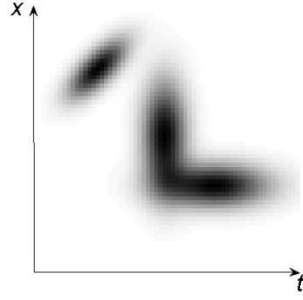
For each scale $(\sigma_k, \tau_l) \in \Sigma \times T$ of 2D DoG pyramid, we first detect vertices in animation that are local minima in DoG response over their spatio-temporal neighborhood N_{st} :

$$P_{kl} = \{p \in \mathcal{M} | \forall p_i \in N_{st}(p), D_{kl}(p) < D_{kl}(p_k) \text{ and } D_{kl}(p) < \varepsilon_{st}\},$$

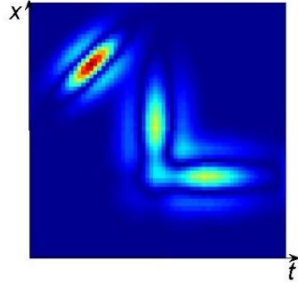
where $N_{st}(p)$ is a spatio-temporal neighborhood of vertex p in the animation \mathcal{M} (Figure 4-10).



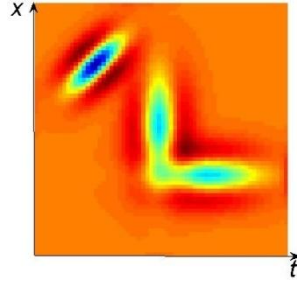
(a) Gaussian and LoG



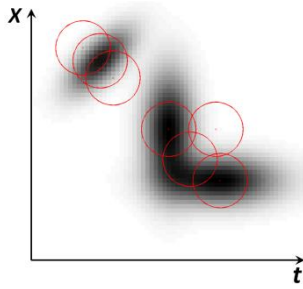
(b) Synthetic signal



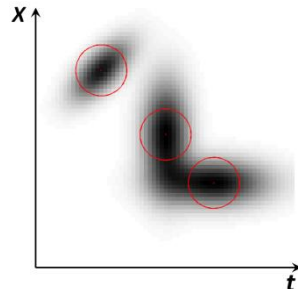
(c) LoG magnitude



(d) LoG



(e) Features as maxima of LoG magnitude response



(f) Features as minima of LoG response

Figure 4-14. A 2D illustration of our feature detection method. (a) LoG yields the valley in blob's center and peaks around the boundary, while the magnitude of LoG has peaks in both cases. (b) Synthetic input signal consisting of 3 Gaussian blobs in 2d. (c) Response of synthetic 2d signal as the absolute value of LoG. (d) Response of the 2d signal computed as LoG. (e) Working with LoG magnitude response we observe several false secondary blobs. (f) Features captured as the local minima of LoG response are reliable.

Next, out of preselected feature candidates P_{kl} , we retain only those vertices which are simultaneous minima over neighboring spatio-temporal scales of DoG pyramid :

$$P = \{p \in P_{kl} | \forall (i, j) \in N_{\sigma\tau}(k, l), D_{ij}(p) > D_{kl}(p) \text{ and } D_{kl}(p) < \varepsilon_{\sigma\tau}\},$$

where $N_{\sigma\tau}(k, l)$ is a set of eight neighboring scales $N_{\sigma\tau}(k, l) = \{D_{(k+1)l}, D_{(k+1)(l-1)}, D_{(k+1)(l+1)}, D_{k(l-1)},$

$$D_{k(l+1)}, D_{(k-1)l}, D_{(k-1)(l-1)}, D_{(k-1)(l+1)}\},$$

and ε_{st} , $\varepsilon_{\sigma\tau}$ are user-controlled thresholds. The spatial scale of a feature point corresponds to the size of the neighborhood where some distinctive deformation is exhibited. Similarly, the temporal scale corresponds to the duration (or speed) of the deformation.

Dealing with secondary (border) blobs. However, in case we consider local maxima of DoG (LoG) magnitude, we may detect artifacts. Undesirable secondary blobs are caused by the shape of Laplacian of Gaussian

which yields peaks around the border of real blob (Figure 4-14(a)). Consider a perfect Gaussian blob as an input signal. If we assume magnitude (i.e. absolute value) of LoG to be feature response, we get strong peak in the center of the blob and two other secondary peaks around edges, and that is troublesome. In contrast, dealing with signed LoG (not absolute) we observe valleys (local minima) in blob centers and peaks (local maxima) on borders. Hence searching for local minima of LoG, rather than local maxima of LoG magnitude, prevents from the detection of false secondary features Figure 4-14(b-f). The other way around could be to use LoG magnitude but discard local maxima which are not strong enough in initial signal, and therefore are false findings. Though, previous works in feature extraction on images/video/static meshes (Mikolajczyk and Schmid 2001, Laptev and Lindeberg 2003, Zaharescu, Boyer et al. 2009) often adopt Hessian detector, which does not detect secondary blobs. However, in contrast to DoG detector, estimation of Hessian on a mesh surface is significantly heavier. In the case of animated meshes estimation of Hessian matrix would be much more problematic and computationally costly.

Implementation notes. Often, animated meshes are rather heavy data. As we increase the number of anim-octaves in the pyramid, we can easily run out of memory, since each octave is essentially a full animation itself but at different scale. Consequently, we have to address that issue in the implementation stage. In order to minimize memory footprint, we compute pyramids and detect feature points progressively. We fully load into main memory only space scale dimension of Gaussian and DoG pyramids. As for time scale, we keep only two neighboring time octaves simultaneously, which are required for DoG computation. Then we construct the pyramid from bottom to top by iteratively increasing time scale. On each iteration of Gaussian/DoG pyramid movement along time scale, we apply our feature detection method to capture interest points (if any on current layer). We repeat the procedure until all pyramid scales have been processed.

4.9 Experiments

Deforming meshes used in our experiments include both synthetic animations and motion capture sequences, which are summarized in Table 3-1. We synthesized a simple deforming Cylinder animation by rigging and used it for initial tests. Also we captured two person’s facial expressions using Vicon system (Vicon) and then transferred the expressions to the scanned faces of the two persons Face1 and Face2.

Name	No.vertices/	No. frames	Filter widths (space/time)	Max. no. smoothings
Cylinder	587/1170	40	10.0/0.83	50/100
Face1(happy)	608/1174	139	8.96/8.45	118/113
Face1(surprise)	608/1174	169	9.39/13.2	96/107
Face2(happy)	662/1272	159	9.31/13.2	112/94
Face2(surprise)	662/1272	99	8.95/8.45	109/57
Horse	5000/9984	48	3.48/5.33	77/54
Camel	4999/10000	48	2.62/5.33	102/54
Woman1	4250/8476	100	5.12/5.2	72/150
Woman2	4250/8476	100	4.44/5.2	82/150
Woman3	4250/8476	100	4.54/5.2	99/150
Face3	5192/9999	71	5.18/3.65	90/114
Head	7966/15809	71	9.06/3.65	28/114

Table 4-1. The animated meshes used in our experiments.

Figure 4-15 shows selected frames of several animated meshes we used in our experiments. Spatio-temporal feature points we have extracted using our algorithm are illustrated as spheres. The demo video that is available

at <https://vimeo.com/120707827> shows the complete animation sequences along with the extracted dynamic feature points.

Face1 (happy), Face1 (surprise), Face2 (happy), Face2 (surprise) contain facial expressions of happiness and surprise of those scanned subjects. The horse and the camel were obtained from results of (Sumner and Popović 2004) work. Furthermore, we produced two mesh animations of seventy frames, Face3 and Head, by using nine facial expressions of the face and the head from (Sumner and Popović 2004). More specifically, given an ordered sequence of nine facial expressions, we smoothly morphed each mesh to the next one through a linear interpolation of their vertex coordinates. We also used skeletal animations of three women models performing “walk and whirl” motions. Those models share the same mesh connectivity and were obtained by deforming a template mesh onto three body scans of different subjects. Note that there is high semantic similarity between animation pairs of Face1/Face2, horse/camel, Face3/Head. It is also the case for three women models.

The color of a sphere represents the temporal scale (red color corresponds to more fast deformations) of the feature point, and radius of sphere indicates the spatial scale. Vertex color on surfaces corresponds to amount of deformation (strain and curvature change) observed in each of animation frame. During experiments we have discovered that our method captures spatio-temporal scales in a robust manner. For example, surface patches around joints of cylinder (Figure 4-16 1a-1e) exhibit different amount of deformation that occurs at different speed. The top joint is moving fast and consequently corresponding feature was detected at low temporal scale (red color). However, the mid-joint is deforming for a long time and we identify it at high temporal scale (blue color). Moreover large radii of deforming spheres for both joints make sense and indicate large deforming regions around the features, rather than very local deformation (Figure 4-16 1c). Second row in (Figure 4-16 2a-2e) depicts some of the feature points in the galloping Horse mesh animation, and third row (Figure 4-16 3a-3e) corresponds to the galloping Camel animation. Those two meshes deform in a coherent manner (Sumner and Popović 2004), and eventually we detect their spatio-temporal features quite consistently. In the last two rows (Figure 4-16 4a-4e, 5a-5e) we present feature points in mocap-driven face animations of two different subjects. Our subjects were asked to mimic of slightly exaggerated emotions during the mocap session. Notice that people normally use different set of muscles when they show up facial expressions, and therefore naturally we observe some variations in the way their skin deforms.

Our algorithm is implemented in C++. All our tests have been conducted on an Intel Core i7-2600 3.4 GHz machine, with 8GB of RAM. The computation time devoted to full pipeline of the algorithm is approximately 2 minutes for most of our example data.

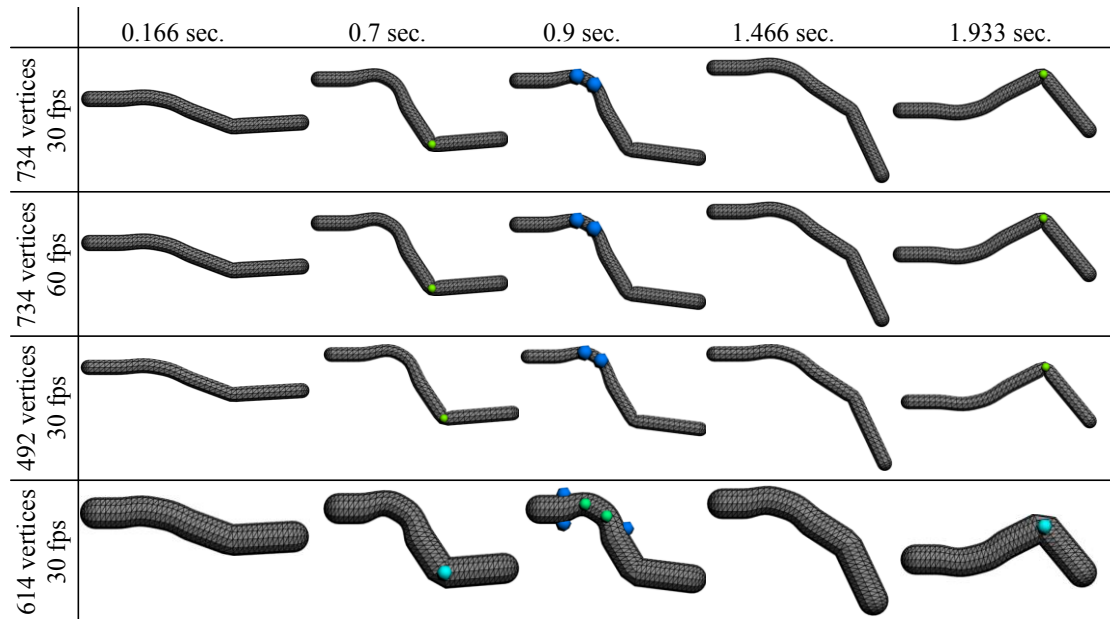


Figure 4-15. Results we obtained on varying datasets of bending cylinder animations demonstrate the consistent behavior of our feature detector. Size of features (drawn as spheres) reflects the spatial scale σ of the corresponding feature and the color corresponds to temporal scale τ .

Invariance to rotation and scale. Invariance of our detector to rotation as well as scale is evident from the definition of our deformation characteristics. Both the strain and the curvature measure we use are invariant to rotation and scale of the animated mesh.

Robustness to changes in spatial and temporal sampling. Robustness of our feature detector to changes in spatial sampling is obtained by the adaptive setting of the widths of the box filters. As described in Section 4.6 of this chapter, we set the width of the spatial filter as the average edge length of the mesh taken at the initial frame. In order to demonstrate the invariance to spatial density of the input mesh, we have conducted comparative experiments on two bending cylinders. These two cylinders have identical shape and deformation; they only differ by the number of vertices and the inter-vertex distance. As shown in the first and third rows of Figure 4-15, the features are extracted at the same spatio-temporal locations.

Robustness to changes in temporal sampling is obtained similarly to the above, i.e. by the adaptive setting of the widths of the box filters. Similar experiments have been conducted by using the two bending cylinders as shown in the 1st and 2nd rows of Figure 4-15. They are perfectly identical except that the temporal sampling of the first one is twice higher than that of the first one. Once again, the extracted feature points are identical in their locations in space and time.

We have further experimented with datasets of similar animations, but with different shape, spatial- and temporal- samplings (galloping animals and two face models in Figure 4-16. Although the extracted features show a good level consistency, they are not always identical. For example, feature points for the galloping horse and camel do not have the same properties (location, time, tau and sigma). Similar results have been observed for the “face” models. This can be explained by the following facts: Firstly, although the two meshes have deformations that are semantically identical, the level of deformation (curvature and strain) might differ greatly. Secondly, most of these models have irregular vertex sampling whereas in our computation of the spatial filter width, we assume that the vertex sampling is regular.

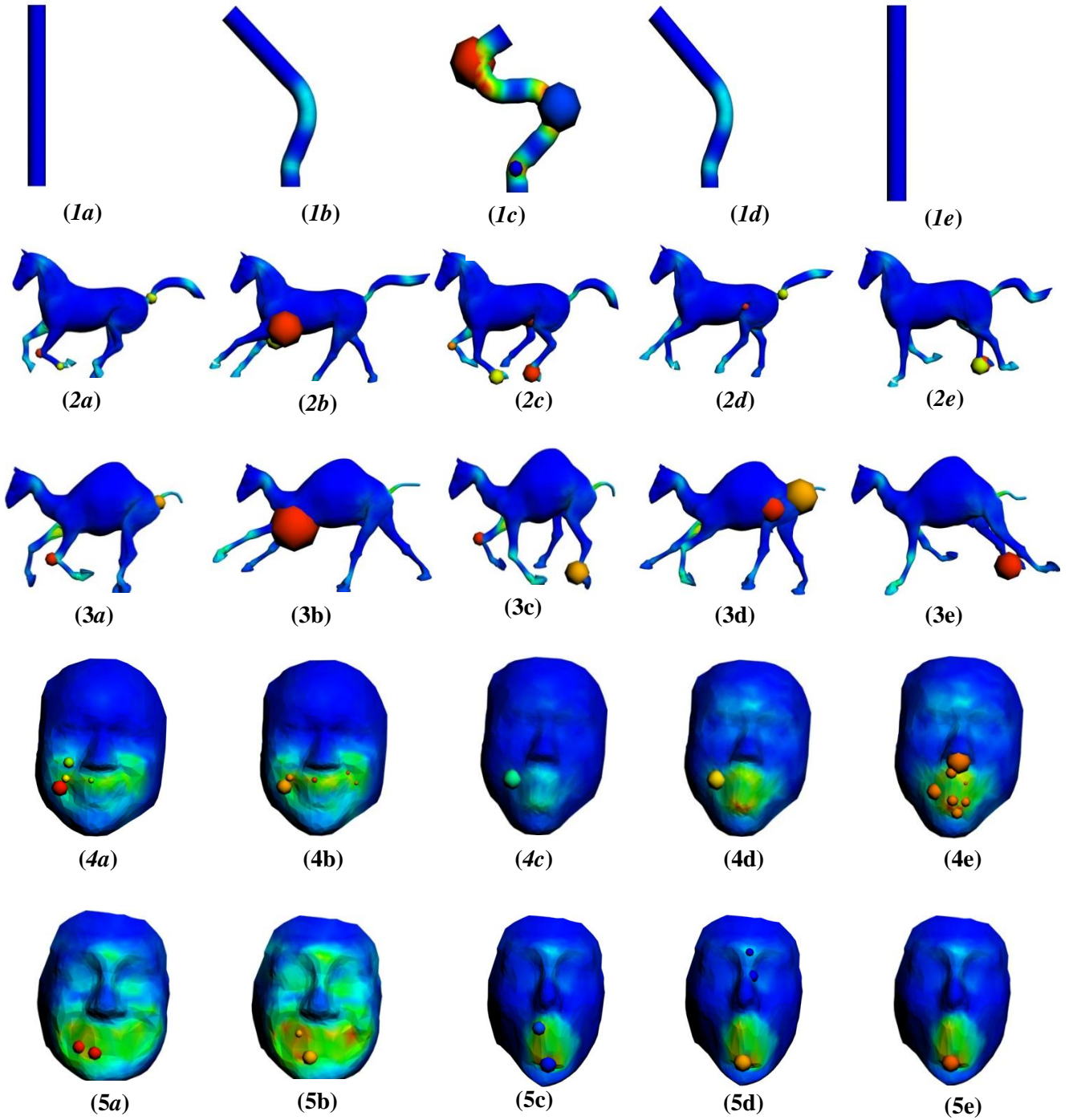


Figure 4-16. Dynamic feature points detected by our AniM-DoG framework are illustrated on a number of selected frames of animated meshes. The color of a sphere represents the temporal scale (from blue to red) of the feature point, and radius of sphere indicates the spacial scale.

4.9.1 Consistency

Since our method is based on deformation characteristics, it has an advantage of consistent feature point extraction across mesh animations with similar motions. To demonstrate mutual consistency among feature points in different animations, we used animation data that exhibit semantically similar motions. Our technique captures similarity of surface deformations and therefore ensures feature point detection consistency (Figure 4-17).

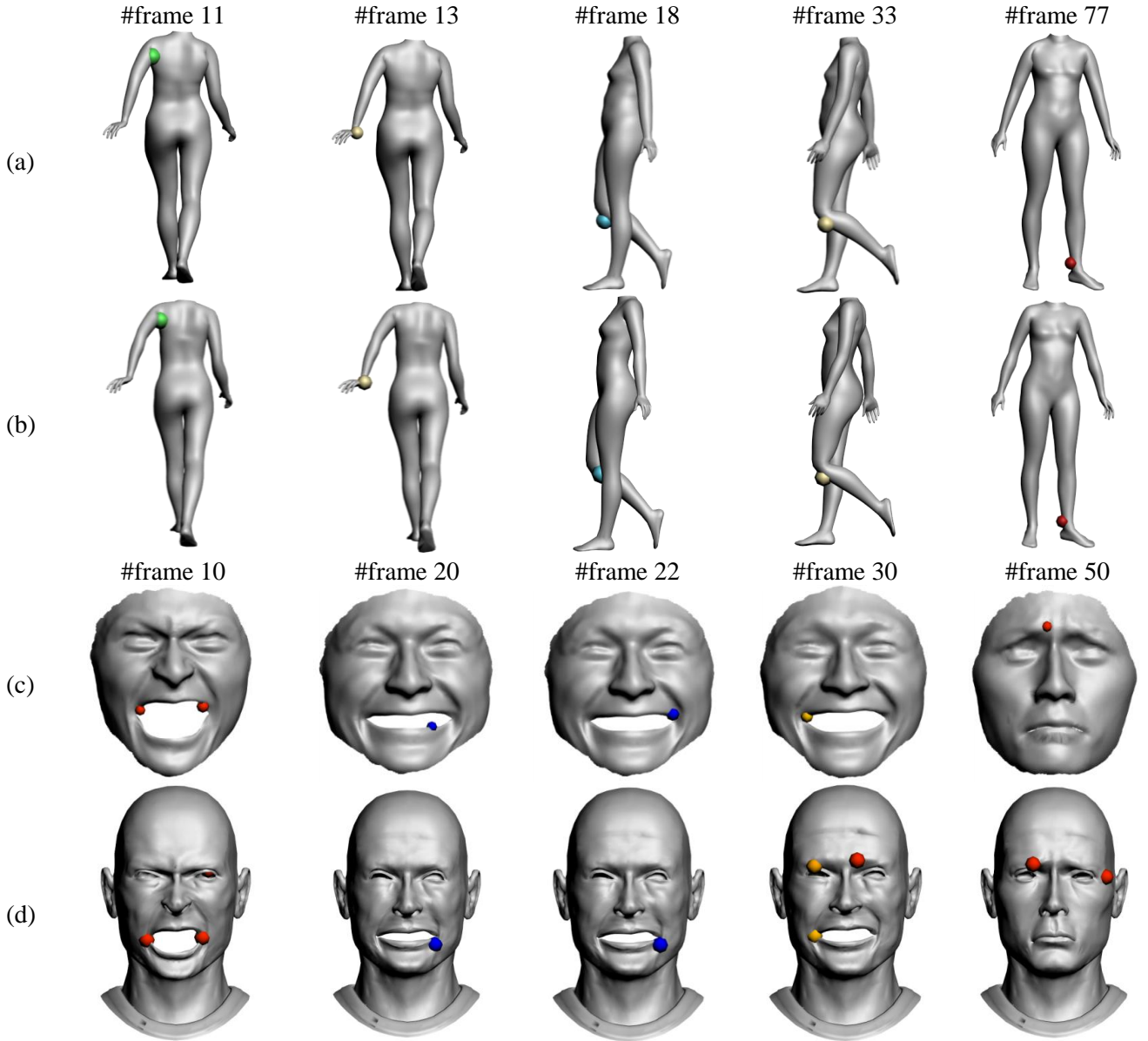


Figure 4-17. Inter-subject consistency of feature points extracted from semantically similar mesh animations. Rows (a-b) depict subset of feature points extracted from walking subject sequences (woman2/woman3 as in Table 4-1) and (c-d) from Face3/Head animations. Note that each column corresponds to identical frame of the animations.

In most cases our method demonstrates high coherency not only in space and time locations of extracted features but also in their space-time scales σ and τ . The only data sets for which we observed relatively lower consistency of feature detection are the two face mocap sequences. The reason for this lies in inherent difference of people’s facial expressions and underlying muscle anatomy.

Additionally, we have performed the quantitative evaluation of the feature extraction consistency as follows. For all feature points we consider only their spatial locations disregarding the time coordinates. Then a pair of similarly deforming meshes \mathcal{M}_S and \mathcal{M}_T whose full correspondence $f: \mathcal{M}_S \rightarrow \mathcal{M}_T$ is known, we find the matching between their feature points P_S and P_T based on the spatial proximity. More precisely, for each feature point $p_S^i \in P_S$, the feature point $p_T^j \in P_T$ that minimizes $\delta_T^i = \|f(p_S^i) - p_T^j\|$ is considered to be the matching one. The distance δ_T^i is what we call feature matching error. Histogram plots of feature matching errors are depicted in Figure 4-18. Obtaining the full correspondence for walking women models was straightforward because they

share the same mesh connectivity. For horse/camel, we obtained a full per-triangle correspondence from (Sumner and Popović 2004), which we converted to a per-vertex correspondence.

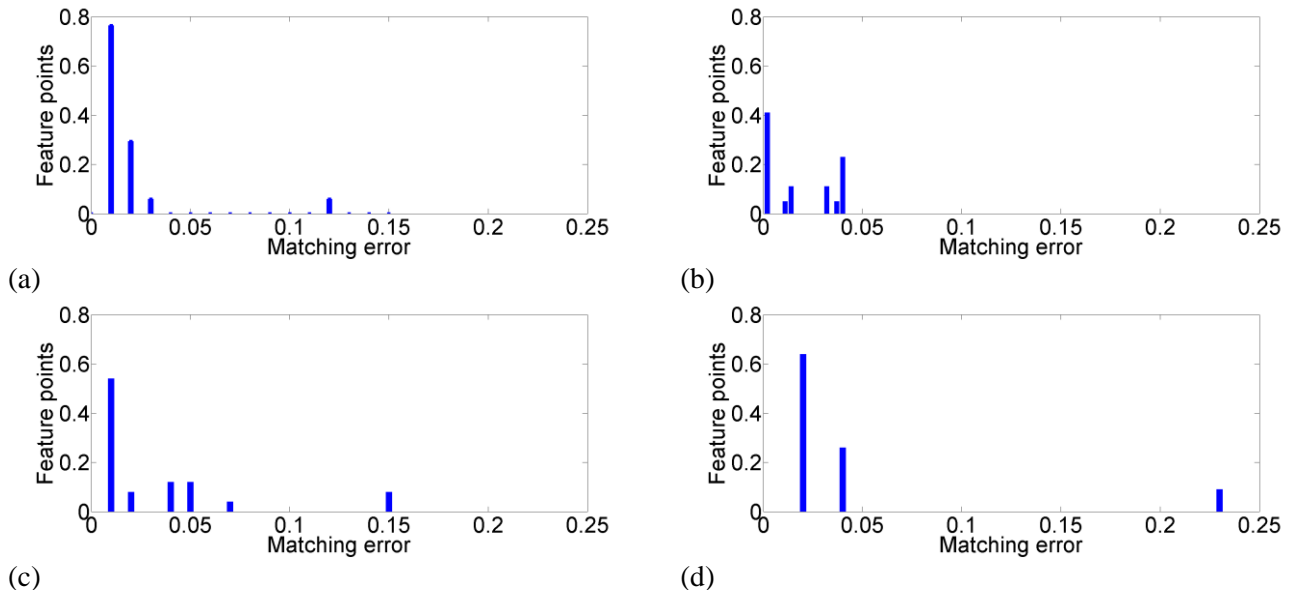


Figure 4-18. The error plots of feature points for pairs (a) Woman1-Woman2, (b) Woman1 – Woman3, (c) Woman2 - Woman3, Camel-Horse (d). We depict the feature matching error on the x-axis as the error (percentage of the error with respect to the diagonal length of the mesh bounding box). The percentage of features with prescribed matching error is depicted on the y-axis. For all four pairs of animations, more than 90% of features have a matching error less than 0.05.

4.9.2 Comparison to the manually selected feature points

We have validated our method by comparing the feature points to the manually defined features. We asked six volunteers to paint feature regions on the animated meshes using an interactive visualization tool. The task was to mark locations at which salient surface deformation behavior can be observed from the user point of view. Each of them could play and pause the animation at any moment and mark feature regions by a color. To simplify the task, the time duration of each feature region was not considered. Since the per-vertex selection can be error-prone, we deliberately allow users to select a region on the surface instead of a single vertex. By aggregating the feature regions from all volunteers, we generated a color map of feature regions. More specifically, for each vertex we summed up and averaged the number of times it has been included in the user-selected regions. The aggregated ground truth was then converted into a surface color map, as depicted in Figure 4-19(a, c). Note, that eyes do not belong to feature regions of face animations, since the user’s task was to define features based on the surface deformation rather than geometric saliency or naturally eye-catching regions.

To compare our results with respect to the user-selected features, we compute for every feature point p its feature region of neighbouring vertices q such that $\mathcal{L} = \{q : d_{\mathcal{M}}(q, p) < \sigma_k\}$, where $d_{\mathcal{M}}(\cdot, \cdot)$ is a within-surface geodesic distance and σ_k is the corresponding scale value at which the feature was detected. Similarly, in the sets of manually selected feature points on a animated mesh, for each vertex we count the number of occurrences in feature regions during the animation, and convert the numbers to the surface color map as shown in Figure 4-19(b, d). We observe a good level of positive correlation between the computed feature regions and the ground truth.

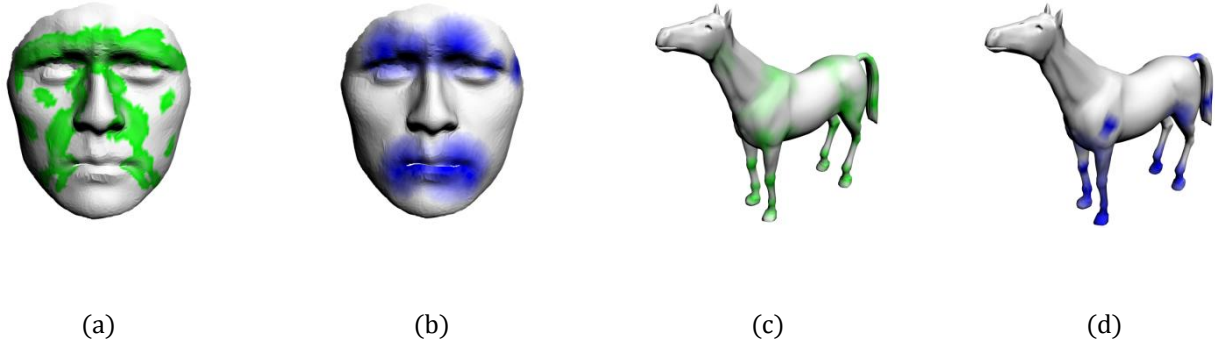


Figure 4-19. Comparison of the manually selected feature points (a, c) to the feature regions computed by our method (b, d). For each vertex, color intensity depicts the accumulative number of its appearances during the animation. Green and blue colors were used for the manually selected features and our computed feature regions respectively.

4.10 Conclusion

We introduced a new dynamic feature point extraction framework for animated meshes. The proposed algorithms robustly extract repeatable sets of features from multi-scale representation of surface deformation characteristics (Section 4.4) by the novel spatio-temporal Difference of Gaussians response operator (Section 4.7). We demonstrate effectiveness of the method on a number of examples and compare extracted features to the ground truth (Section 4.9). Most importantly, feature point sets that are coherent over similarly deforming animated meshes result in development of a new feature descriptor (Section 5.3), which plays a crucial role in the pipeline of animated mesh correspondence search (Figure 2-1). We provide in-depth explanation of the novel feature point signature as well as coarse and fine matching algorithms for animated meshes in scope of the next Chapter 5. Results of our dynamic feature extraction method could be also extended and applied to a number of useful applications. We describe some of the ideas below while leaving their developments as future works (Chapter 7).

Chapter 5 Correspondence between animated meshes

5.1 Introduction

In Chapter 4 we presented a novel method for a dynamic feature point extraction which is initial and very important stage in scope of our shape correspondence framework for animated meshes. In Chapter 5 we focus on how dynamic feature points can be incorporated in a complete animated shape correspondence framework.

If we want to move towards shape correspondence techniques capable of exploiting rich set of information on dynamic images, we have to put an entirely new perspective on the traditional shape correspondence pipeline, trying to understand where and how the mobility can be encapsulated. To reach this objective, we will focus on the following questions: - How to efficiently represent the movement data from the dynamic images, and at different stages of shape correspondence? - How to interpret the movement data towards finding reliable correspondence?

This chapter details the new method of animated mesh matching. The main difference of our method to existing approaches is that it makes use of dynamic properties of animated mesh rather than on its static geometry. In scope of this chapter we develop a novel dynamic point descriptor that serves as a robust signature for the dynamic features. Given the similarity measure between the dynamic feature point descriptors, we approach the animated mesh matching by first computing sparse matching of dynamic features followed by full matching of every vertex of the source and target animations.

The pipeline of the proposed technique consists of several major substeps. The initial step (Figure 5-1(1)) of dynamic feature extraction from an animated mesh is detailed in Chapter 4. Then each feature on the source and target is supplied with the dynamic feature point descriptor (Figure 5-1(2)), and followed by sparse feature correspondence (Figure 5-1(3)) and dense full mesh correspondence (Figure 5-1(4)). This chapter is organized as follows. First, we detail our new feature point signature that is able to not only robustly capture dynamic motion properties of features, but also effectively used for feature matching. Based on these feature point descriptors we propose to compute initial sparse correspondences of dynamic feature points using dual decomposition graph matching technique (Torresani, Kolmogorov et al. 2008). Then we overview the core aspects of our graph matching approach and show its robustness in feature matching.

Finally, we develop a new dense correspondence (full matching) approach between the source and the target meshes in spherical embedding. Full matching in spherical parameterization is formulated as a sequence of warping in spherical domain that optimally align initial sparse correspondences of dynamic features.

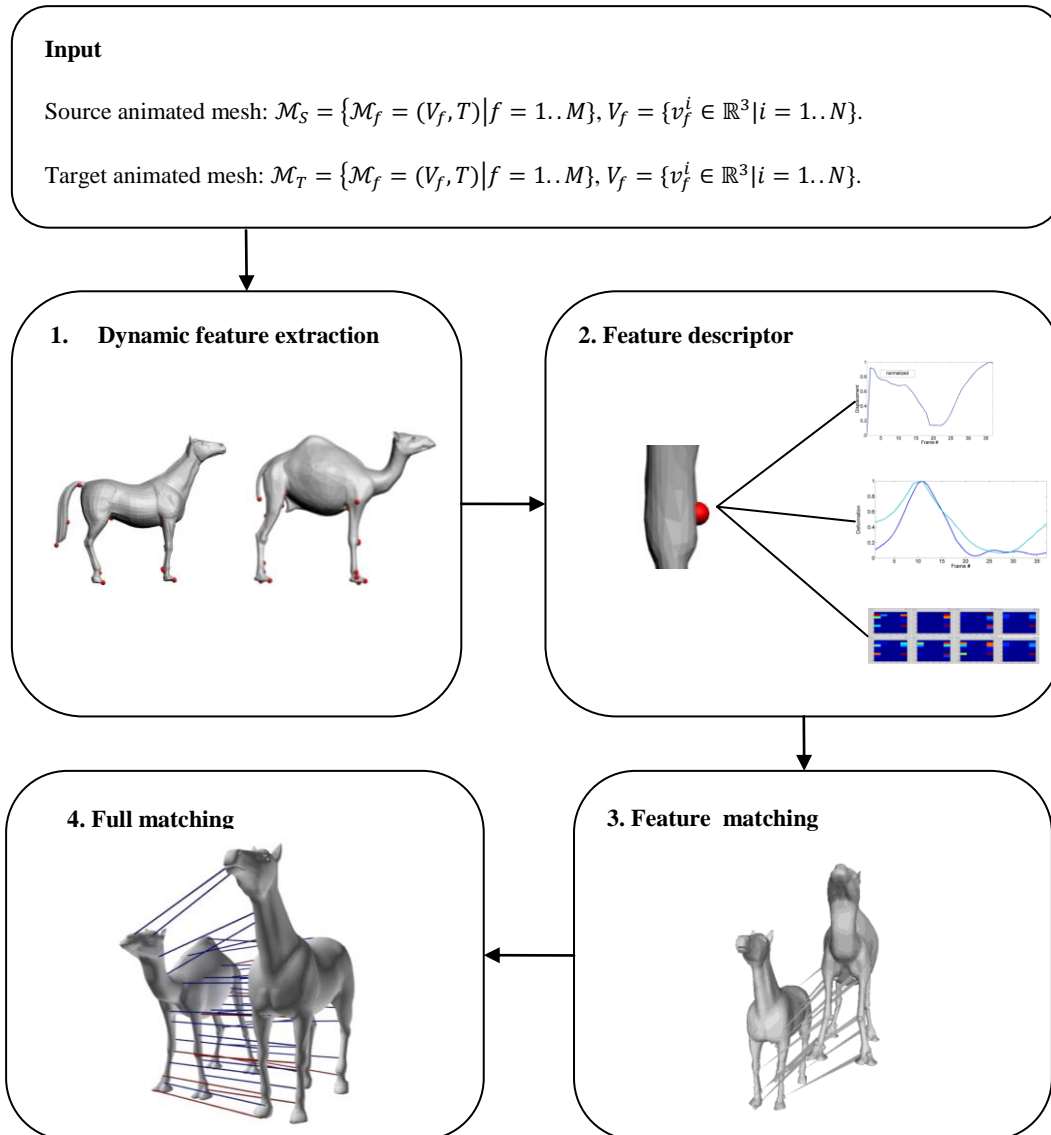


Figure 5-1. Proposed pipeline for animated mesh matching.

5.2 Related work : Feature point descriptors

Here we recapitulate point signatures which are the most substantial and the most related to our new dynamic feature point descriptors. We review existing feature descriptor methods in this section and not in Chapter 3 because the feature descriptors are the most specific to Chapter 5 rather than to a generic shape correspondence problem. Here we recapitulate not only local shape descriptors but also relevant local descriptors for images and videos, which are closely related to our work. We organize this section as follows. First we overview the most important feature descriptors on static geometry in subsection Section 4.2.1 Then, due to limited availability of existing works on point signatures for time varying geometry, we address the spatio-temporal point descriptors on videos in subsection Section 4.2.2 that are relevant to our dynamic descriptor presented in section 5.3.

5.2.1 Spatial feature descriptors for surface matching

A vast variety of point signatures and feature descriptors has been proposed in the literature for the 3d geometry (Johnson 1997, Gatzke, Grimm et al. 2005, Gelfand, Mitra et al. 2005, Castellani, Cristani et al. 2008, Sun, Ovsjanikov et al. 2009, Zaharescu, Boyer et al. 2009, Tevs, Berner et al. 2011, Darom and Keller 2012). Here we describe each of the most important shape descriptors. Note that we focus on the local shape descriptors since the global descriptors are not directly relevant to our work. Most of the common low dimensional shape descriptors rely on differential quantities of the shape that makes them sensitive to noise in the input data. Therefore in order to make differential shape descriptors useful for the shape correspondence, in most of the cases data smoothing has to be performed.

Spin image is one of the first surface shape descriptors originally proposed by (Johnson 1997). The spin image surface representation technique is often used for surface matching and object recognition in 3-D scenes. Spin images essentially encode the global properties of a given surface in an object-oriented coordinate system. Spin image (or spin map) is a 2d histogram of point locations accumulated in cylindrical coordinates (aligned as the point's normal) over the surface's locale support region. Each point within the local support region is projected into corresponding bin depending on its cylindrical coordinates. The procedure is repeated for all vertices within the support region of the spin image. The resulting accumulation spin map can be thought of as a 2D image $S: \mathbb{R}^3 \rightarrow \mathbb{R}^2$ (Figure 5-2).

Scale-invariant spin image (SISI). Scale-invariant spin image (SISI) descriptor for meshes (Darom and Keller 2012) extends classical spin image shape descriptor (Johnson 1997). The computation of the original spin image descriptor (Johnson 1997) relies on a constant predefined support in a neighborhood of a point, hence it is rather global in nature. Therefore in a recent work of (Darom and Keller 2012) the authors propose to compute the scale-invariant version of spin image (SISI) by computing the descriptor over the adaptive local scale σ that corresponds to the scale at which a feature was detected (Darom and Keller 2012).

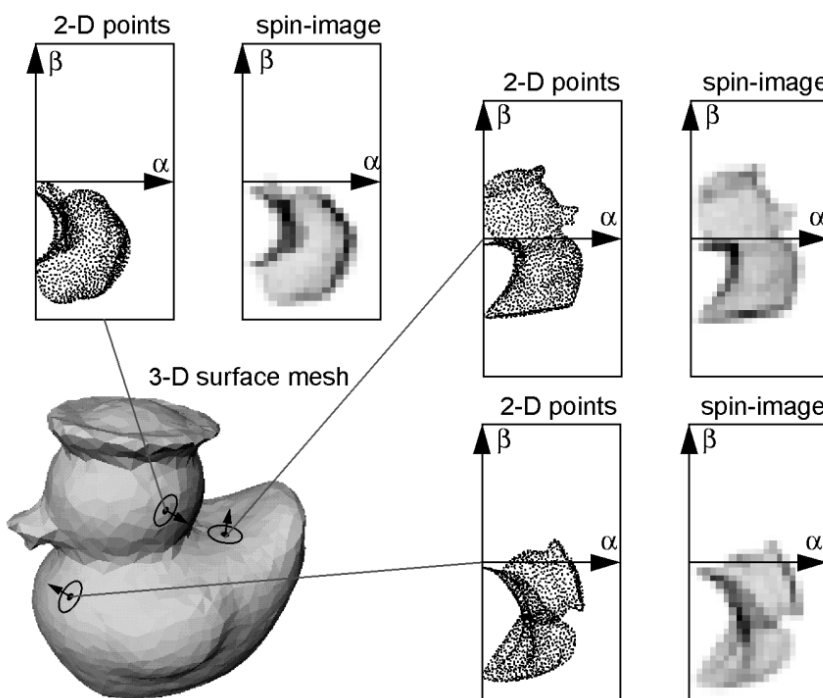


Figure 5-2. Spin image shape descriptor (Johnson 1997). Dark areas in the image correspond to bins that contain many accumulated points.

3D Shape context (Körtgen, Park et al. 2003). 3D shape contexts are a natural extension of 2D shape contexts introduced by Belongie et al. (Belongie, Malik et al. 2000). for 2D image recognition (Belongie, Malik et al. 2000). Kortgen et al. (Körtgen, Park et al. 2003) try to apply 3D shape contexts for 3D shape retrieval and matching. 3D shape contexts are semi-local descriptions of object shape centered at points on the surface of the object. The shape context of a point is defined as a coarse histogram of the relative coordinates of the remaining surface points. The bins of the histogram are constructed by the overlay of concentric shells around the centroid of the model and sectors emerging from the centroid.

Curvature maps (Gatzke, Grimm et al. 2005). In that work two curvature maps are proposed that exploit surface curvature information in the local region of a point. The method is based on curvature computation, which is an intrinsic property of a surface. However curvature is a very local surface characteristic, which does not capture the information about surface region around the point. Given a point v on the mesh, curvature map of 0-D is defined as a curvature at v . 1-D curvature map accumulates information from M -ring neighborhood region around v . More precisely, 1-D curvature map is a set of maps that associate each ring with the corresponding average Gaussian or average mean curvature over the ring (Figure 5-3).

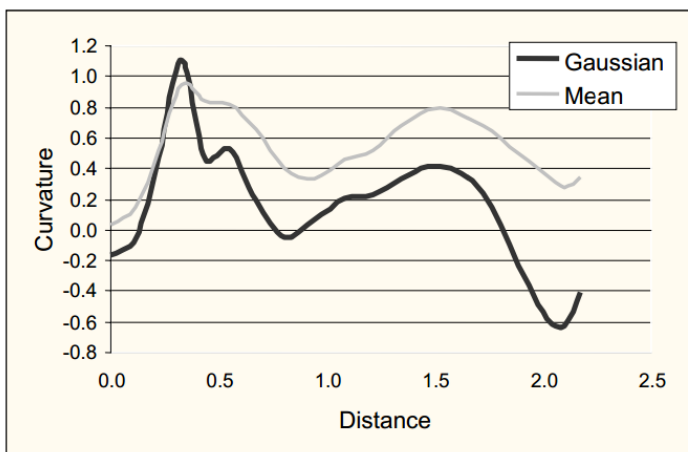


Figure 5-3. 1-D Curvature maps of Gaussian and Mean curvature as a function of distance from the point (Gatzke, Grimm et al. 2005).

An alternative way of computing curvature maps is established through Geodesic Fans (Zelinka and Garland 2004) that provide a uniform neighbourhood structure around a vertex. A geodesic fan consists of a set of spokes and a set of samples on each spoke. Samples equally spaced along each spoke form a local geodesic polar map around the vertex (Figure 5-4).

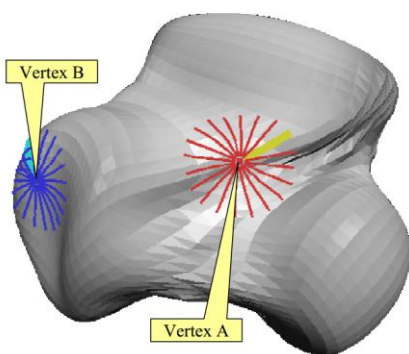


Figure 5-4. Illustration of geodesic fans at two given vertices A and B (Gatzke, Grimm et al. 2005).

Given a geodesic fan computed around vertex v , instead of ring-based 1-D Curvature map it is possible to define a fan-based curvature map. For that, each spoke of the fan is associated with a function of Gaussian/mean curvature as a function of distance from the point v . 2-D curvature map is defined similarly to 1-D map, except that angular information (i.e. angle between normals of sample points) is kept along the spoke of the fan. Additionally (Gatzke, Grimm et al. 2005) show that curvature maps are robust to mesh resolution and regularity.

Integral descriptor (Gelfand, Mitra et al. 2005). Gelfand et al. proposed an Integral Volume local shape descriptor. The descriptor is robust to geometric noise and is invariant under rigid transformations, which makes it useful for shape correspondence algorithms. The Integral Volume descriptor is defined at each point \mathbf{p} of the shape as $V_r(\mathbf{p}) = \int_{B_r(\mathbf{p}) \cap S} dx$. Where the integral kernel $B_r(\mathbf{p})$ corresponds to the ball of the radius r centered at \mathbf{p} , and S is the interior of the surface at \mathbf{p} (Figure 5-5). In practice the integral $\int_{B_r(\mathbf{p}) \cap S} dx$ is computed over discrete voxel grid as depicted in Figure 5-5 (b). The authors demonstrate the Integral Volume descriptor V_r is closely related to the mean curvature H of the surface, but in contrast to H much more robust to the noise.

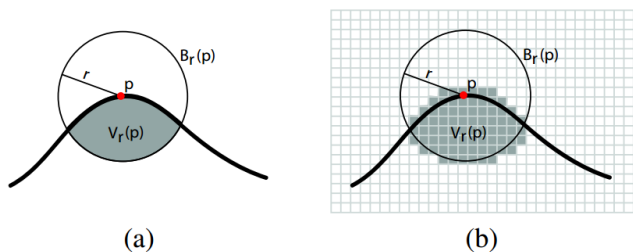


Figure 5-5. 2D analogy of the Integral Volume descriptor (Gelfand, Mitra et al. 2005). (a) The Integral Volume descriptor measures the volume of the ball of radius r centered at point \mathbf{p} defined by the local interior of the shape. (b) $V_r(\mathbf{p})$ is computed in discrete voxel grid.

Statistical descriptor. In the work of (Castellani, Cristani et al. 2008), the authors propose a feature descriptor that relies on statistical Hidden Markov Model (Rabiner 1989) to collect the information related the feature point and its neighborhood. Given a feature point \mathbf{p} , a clockwise spiral path is constructed on the surface around \mathbf{p} until a fixed geodesic radius is reached (Figure 5-6). Along the spiral the following five entities are sampled: local point information (Petitjean 2002), saliency level (Castellani, Cristani et al. 2008), maximal curvature, minimal curvature, normal displacement between local point and the feature \mathbf{p} . These repeatedly occurring 5-dimensional entries can be modeled as a stochastic process by discrete HMM (Rabiner 1989). In such a way, HMM descriptor gives a statistical encoding of the interest point and its neighborhood. For measuring similarities between HMM descriptors of different features a classical HMM similarity measure (Smyth 1997) can be successfully used. The matching of features based on HMM descriptor shows robust and accurate results for the rigid partially incomplete shapes (Castellani, Cristani et al. 2008).

MeshHoG (Mesh Histogram of Oriented Gradients). (Zaharescu, Boyer et al. 2009) propose an extension of the Histogram of Oriented Gradients method of (Dalal and Triggs 2005) from the image domain to the domain of 3D meshes. Given vertex p , the descriptor relies on the information gathered within support region $N_r(p)$ of size r around p . The size of the support region is chosen adaptively depending on a given mesh in a way that r is proportional to the square root of the mesh area $r \propto \sqrt{A}$ and inversely proportional to the average edge length $r \propto (e_{avg})^{-1}$. More precisely, given the user parameter $\alpha_r \in (0,1)$, the value of r is computed as following $r = \left\lfloor \frac{1}{e_{avg}} \sqrt{\frac{\alpha_r \cdot A}{\pi}} \right\rfloor$. Then 3D discrete gradients of the photometric data of the mesh in the neighborhood $N_r(p)$ are pooled into a polar histogram \mathcal{H} . Given the dominant orientation \mathbf{a}_p in the histogram \mathcal{H} and normal vector \mathbf{n}_p

at vertex p , a new local coordinate system is defined as $\{\mathbf{a}_p, \mathbf{n}_p, \mathbf{a}_p \times \mathbf{n}_p\}$. The new local coordinate system generates three orthonormal planes (Figure 5-7 (b)).

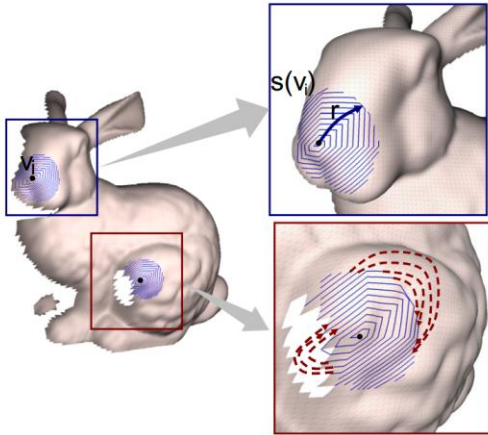


Figure 5-6. Clockwise spiral path around a feature point (Castellani, Cristani et al. 2008).

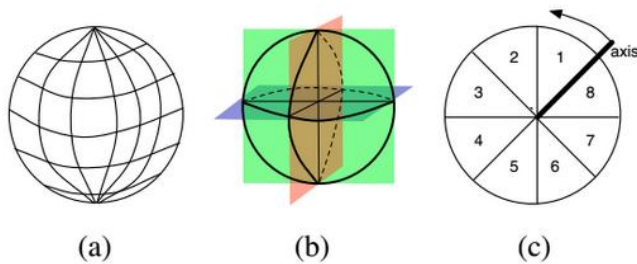


Figure 5-7. (a) Spherical histogram used to compute local histograms \mathcal{H} . (b) Three orthonormal planes generated by the new local coordinate system. (c) Binning of 2D projected gradients into polar coordinate system (Zaharescu, Boyer et al. 2009).

The final descriptor is obtained by concatenating the orientation histograms of the 2D gradients projected on the orthonormal planes.

HKS (Sun, Ovsjanikov et al. 2009). Sun et al. proposed an elegant Heat Kernel point signature using diffusion geometry of the shape. Heat kernel signature (HKS) is based on the fundamental solutions of the heat equation (heat kernels). Given a Heat diffusion equation over a manifold M ,

$$\Delta_M u(x, t) = -\frac{\partial u(x, t)}{\partial t},$$

and initial heat distribution $f: M \rightarrow \mathbb{R}$ over the manifold M , the solution of Heat equation can be represented as $\int_M k_t(x, y)f(y)dy$, where $k_t(x, x)$ is a heat kernel function (Sun, Ovsjanikov et al. 2009). Heat Kernel function has a nice property of being isometry invariant which makes it a good candidate for a isometric shape point signature. Given a point $x \in M$, Heat Kernel Signature is defined by considering heat kernel function only over temporal domain t

$$HKS(x, t) = k_t(x, x).$$

In that way, the HKS assesses the amount of heat transferred in infinity small neighborhood of x in time t . Examples of Heat Kernel Signatures for a few points on the dragon model are depicted in Figure 5-8.

HKS provides a multi-scale representation of the surface and can be used for shape matching (Dey, Li et al. 2010, Ovsjanikov, M erigot et al. 2010) and shape retrieval (Bronstein and Kokkinos 2010, Spagnuolo, Bronstein et al. 2012) applications

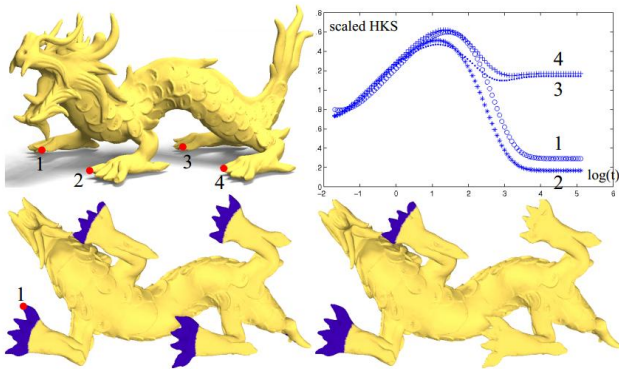


Figure 5-8. Heat Kernel Signatures for the four tips of the limbs of the dragon model (1-4). Note that due to local symmetry of the limbs the HKS starts to be informative and distinctive with high values of t (Sun, Ovsjanikov et al. 2009).

Intrinsic wave descriptor (IWD). Tevs et al. (Tevs, Berner et al. 2011) develop a simple approximation of the Heat Kernel Signature (Sun, Ovsjanikov et al. 2009). Given a 2-manifold M and a point \mathbf{x} , let $C(\mathbf{x}, r) = \{\mathbf{y} \in M \mid d(\mathbf{x}, \mathbf{y}) = r\}$ be an intrinsic isocurve of radius r around the point \mathbf{x} . Starting from a given point \mathbf{x} , the authors compute all isocurves of distance $r = (r_0, r_1, \dots, r_m)$ and measure the isocurve lengths $l = (l_0, l_1, \dots, l_m)$ (Figure 5-9). Then, the descriptor for each point \mathbf{x} is the function that maps radius r to the normalized length of the corresponding isocurve $D(r_i) = l_i/2\pi r_i$. The authors refer to the descriptor as intrinsic wave descriptor. In their implementation, the authors fix 16 values at constant intervals constitute $r = (r_0, r_1, \dots, r_{16})$. In the majority of the experiments (Tevs, Berner et al. 2011) the maximum distance r_m is set to 0.05 of the largest length of the bounding box of M .

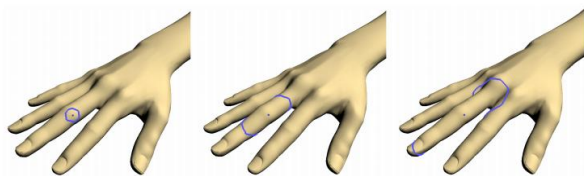


Figure 5-9. Three isocurves of the Intrinsic wave descriptor corresponding to a point on a finger of an example model (Tevs, Berner et al. 2011).

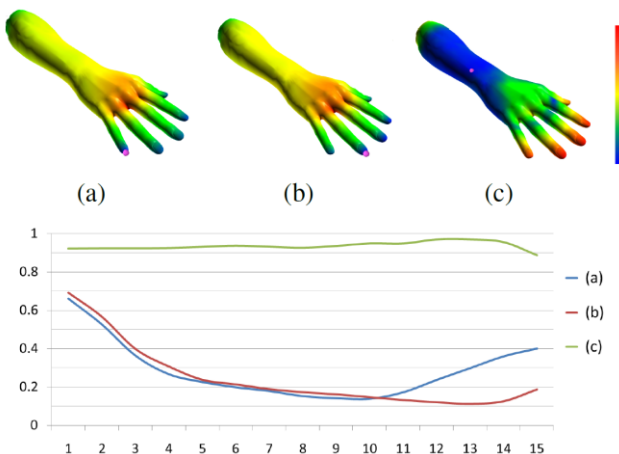


Figure 5-10. By changing the radius of IWD from low to high values the descriptor captures more local and more global shape properties correspondingly. The curves depict Intrinsic Wave descriptors as functions of r for the two distinct fingertips (a-b) and a point on a forearm (c). The difference between descriptors (a) and (b) appears only in high values of radius r .

The authors further show analogy of the Intrinsic Wave Descriptor and Heat Kernel Signature (Sun, Ovsjanikov et al. 2009). IWD and HKS are similar in a way that small values of radius r in IWD and small values of scale t in HKS capture local properties of the surface. Correspondingly, the large values capture more global object properties. The illustration of this behavior is illustrated in Figure 5-10.

LD-SIFT. Inspired by popular state-of-the-art feature detector/descriptor Scale-Invariant Feature Transform (SIFT) (Lowe 2004), Darom et al. (Darom and Keller 2012) propose to adopt similar technique for the case of 3D meshes. The classical SIFT descriptor is computed as a set of radial-angular histograms of image gradients (Figure 5-11). Scale invariance of the descriptor is imposed by computing SIFT over adaptive support neighborhood correlated to the feature scale. Rotation invariance is achieved by aligning the feature’s support neighborhood with the dominant orientation in SIFT descriptor’s histogram.

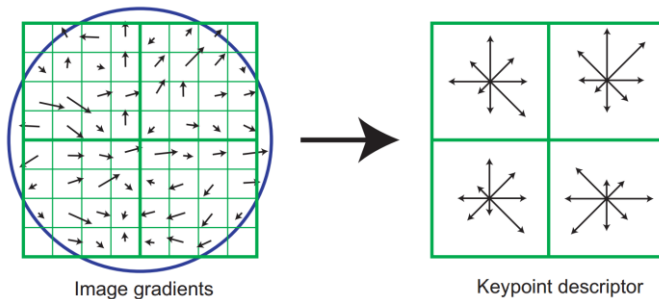


Figure 5-11. SIFT image descriptor (Lowe 2004).

Similarly to (Mian, Bennamoun et al. 2010), Darom and Keller propose the following technique to generalize image SIFT to the mesh descriptor called Local Depth SIFT (LD-SIFT). First, given a feature point p of a scale σ , the local support N_p proportional to the scale ($N_p \propto \sigma$) is used to fit a plane P by using two leading eigenvectors of PCA analysis over N_p . Then the local depth map is computed by evaluating distances from points in N_p to the plane P . Finally, the SIFT descriptor (Lowe 2004) is applied over the LD map.

5.2.2 Spatio-temporal feature descriptors

To the best of our knowledge the problem of computing point signature on animated meshes has not been directly addressed in computer graphics. However, there several indirectly related methods in mesh segmentation sub-domain and Computer Vision field that relies on dynamic spatio-temporal properties of the input graphical entity (i.e. animated meshes/videos). Bridging the gap between our dynamic feature signature and existing spatio-temporal descriptor approaches, we first briefly overview animated mesh dynamic properties that are used in segmentation methods and then review the signatures in videos.

Note, that even though in the works the motion properties of meshes are treated just as input signal, those properties can be also viewed as animated mesh signatures. Some of the segmentation methods rely on per-vertex signatures, other work on per-face signatures (Lee, Wang et al. 2006).

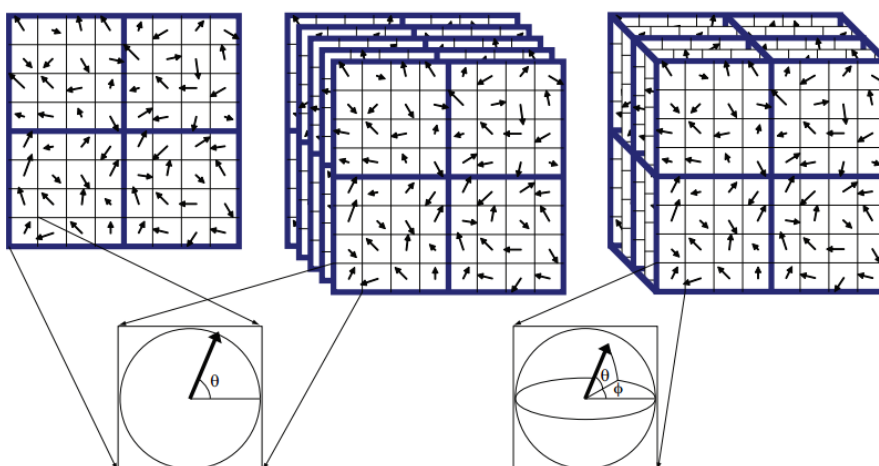
The method presented in (Sattler, Sarlette et al. 2005) analyzes vertex trajectories $(v_i^1, v_i^2, \dots, v_i^F)$ which are further used for the animated mesh segmentation. Similarly, animated mesh segmentation algorithm of (De Aguiar, Theobalt et al. 2008) utilizes vertex trajectories as local descriptor too. Lee et al. 2006 (Lee, Wang et al. 2006) propose a segmentation framework for animated meshes that relies on per-triangle deformation gradients computed over subsequent frames of an animation. The deformation gradients are computed in each frame

in spirit of (Sumner and Popović 2004). Those deformation gradients essentially encode rotation and scale/shear components of the local surface deformation. The authors (Lee, Wang et al. 2006) further use a Frobenius norm of deformation gradients to design their animated mesh segmentation algorithm. The animated mesh segmentation approach of (Mamou, Zaharia et al. 2006) use vertex Affine transformations in homogeneous coordinates in order to capture the surface movement characteristic. In the recent works (Arcila, Buddha et al. 2010, Arcila, Cagniard et al. 2013) the authors propose use vertex displacement signature to compute the segmentation of animated meshes.

Now we further recapitulate existing approaches of video descriptors, which are relevant to our animated mesh dynamic feature descriptor.

Cuboids descriptors (Dollár, Rabaud et al. 2005). In scope of their work Dollár and co-authors propose cuboid descriptor technique for videos. Given a set of features extracted from scale-space video representation, at each feature point a cuboid (i.e. a spatio-temporal set of pixels bounded by a rectangular parallelepiped) is extracted proportional to the feature’s characteristic ⁶scale . The authors propose first to transform pixels inside cuboids to a set of alternative modalities, and then on top of them compute the transformed and flattened feature vector descriptor. After normalization of the pixel intensities inside a cuboid, at each spatio-temporal location (x, y, t) the two new modalities are computed: brightness gradients (G_x, G_y, G_t) and image flow vectors (V_x, V_y) . Image flow vectors are computed between frames using optical flow method of (Lucas and Kanade 1981). Finally the gradients and image flow orientations are binned into 1D and 2D feature vectors. The authors perform an evaluation of the proposed variations of the descriptor and show that each option can be used alternatively depending on the task and desired balance between the descriptor distinctiveness and efficiency.

3D SIFT (Scovanner, Ali et al. 2007). In the work of Scovanner et al. the new 3D SIFT descriptor is introduced. Motivated by the robust state of the art 2D SIFT image descriptor, the authors propose to extend it to the 3D domain of video sequences. Similarly to the 2D SIFT, the 3D SIFT is based on the histograms of the gradient orientations in the local neighbourhood of a feature point. In contrast to the 2D SIFT, the temporal dimension is introduced for the gradient computation and the orientation binning. The pipeline of the 3D SIFT algorithm consists of several steps: (1) estimation the gradients inside the spatio-temporal characteristics volume, (2) sub-division of the volume into eight octets, (3) computation of the histograms of the gradients orientations, (4) normalization of the histogram bins by the corresponding solid angle of the bin. The illustration of 3D SIFT approach is schematically depicted in (Figure 5-12, right).



⁶ Characteristic scale reflect a length of a corresponding structure in the data (Lindeberg, 1998).

Figure 5-12. Classical 2D SIFT (left). Straightforward extension to the spatio-temporal domain without modification of the original 2D SIFT (middle). 3D SIFT approach with the gradients computed over spatio-temporal volume (Scovanner, Ali et al. 2007).

HOG3D (Klaser and Marszalek 2008). Histogram of Oriented Gradients (HOG) (Dalal and Triggs 2005) are feature descriptors used in computer vision and image processing for the purpose of object detection. The technique counts occurrences of gradient orientation in localized portions of an image. This method is similar to scale-invariant feature transform (Scovanner, Ali et al. 2007) descriptors, and shape contexts (Körtgen, Park et al. 2003), but differs in that it is computed on a dense grid of uniformly spaced cells and uses overlapping local contrast normalization for improved accuracy. (Klaser and Marszalek 2008) propose a new descriptor for video sequences based on orientations of spatio-temporal 3D gradients. First, the spatio-temporal gradients are efficiently computed in the volume of interest in the video. Extending analogy from 2D, where n-bin histogram can be seen as an approximation of a circle, the authors quantize the 3D gradient histogram in regular n-sided polyhedron. Then the HOG3D descriptor is computed by pooling the spatio-temporal gradient orientations in 3D histogram over the polyhedron (Figure 5-13).

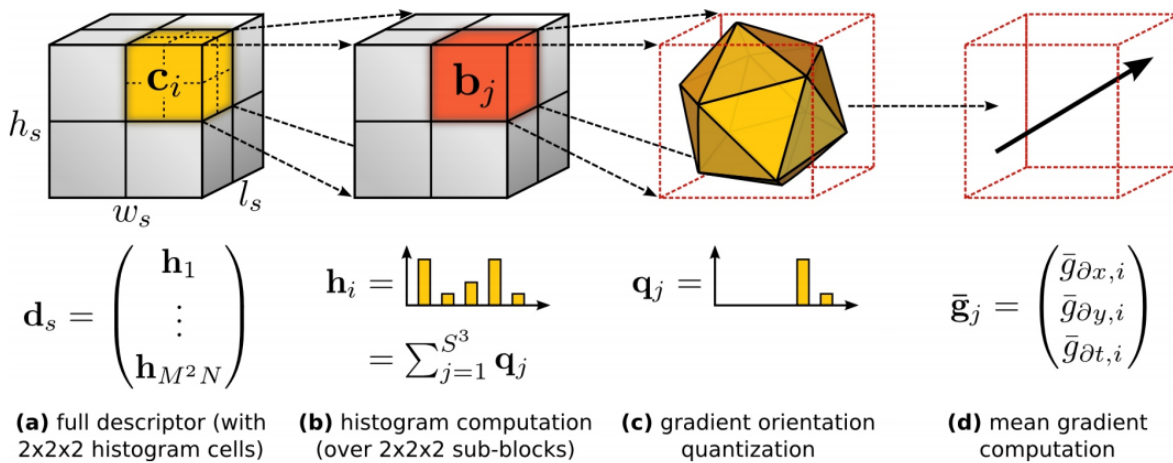


Figure 5-13. The computation pipeline of the HOG3D descriptor (Klaser and Marszalek 2008).

HoG/HoF. HoF descriptor stands for Histogram of Oriented Optical Flow and also known in the literature as Internal Motion Histograms (Dalal, Triggs et al. 2006, Laptev, Marszalek et al. 2008). Dalal et al. (Dalal, Triggs et al. 2006) apply HoG/HoF detectors/descriptors to the problem of human detection in films and videos. Essentially the proposed technique involves the combination of regular HOG descriptors on individual video frames with the new HoF(IMH) descriptors on pairs of subsequent video frames. The Internal Motion Histograms (IMH) uses the gradient magnitudes from optical flow fields obtained from two consecutive frames. The gradient magnitudes of the optical flow are then used in the same manner as those produced from static image data within the HoG descriptor approach.

Extended SURF (3D SURF). Willems et al. (Willems, Tuytelaars et al. 2008) introduce an extension of the state-of-the-art Speed Up Robust Features (SURF) (Bay, Tuytelaars et al. 2006) image feature descriptor to the 3D domain. The SURF descriptor gained a reputation of a robust scale- and rotation-invariant feature detector/descriptor for images, therefore it is interesting to consider similar solution in more general spatio-temporal video domain. In order to describe a point of interest with spatio-temporal characteristic scales, a rectangular volume of dimensions proportional to characteristic scales is established around the feature point. Analogously to the previous methods (Scovanner, Ali et al. 2007, Klaser and Marszalek 2008), the volume is furthermore split into sub-volumes. The key idea of the proposed feature description is based on the classical SURF descriptor (Bay, Tuytelaars et al. 2006). Extended SURF uses Wavelet responses in horizontal and vertical spatial di-

rection and orthogonal temporal direction. Technically, for each sub-volume responses of axis-aligned Haar-wavelets are accumulated into vector $v = (\sum d_x, \sum d_y, \sum d_t)$. In contrast to the original SURF (Bay, Tuytelaars et al. 2006), the sums of absolute values of wavelet responses are dismissed. The set of vectors v for each of the sub-volumes form the output descriptor. For efficiency reasons, in spirit of (Bay, Tuytelaars et al. 2006), the integral volume structure is employed that extends integral images technique.

5.3 Feature point signature

In this section we address the problem of dynamic feature description (Figure 5-1(2)) which plays a crucial role in our animated mesh matching pipeline. It would be almost impossible to compute reliable correspondences between feature points on the source and target animations without a robust dynamic feature point signature. However, feature signature for animated mesh is relatively new problem that does not have a standard solution in the computer graphics community.

Probably the most straightforward approach to the dynamic feature descriptor is to adopt one of the existing state-of-the-art signatures for static meshes and observe how the signature changes over a frame sequence. Alternatively, in scope of this thesis we try to avoid strict assumption on geometric similarities of animated meshes to be registered. We rather assume semantic similarity of mesh movement's i.e. similarity of dynamic behaviors. Therefore we develop signatures based on static geometry of the dynamic behavior of mesh surface.

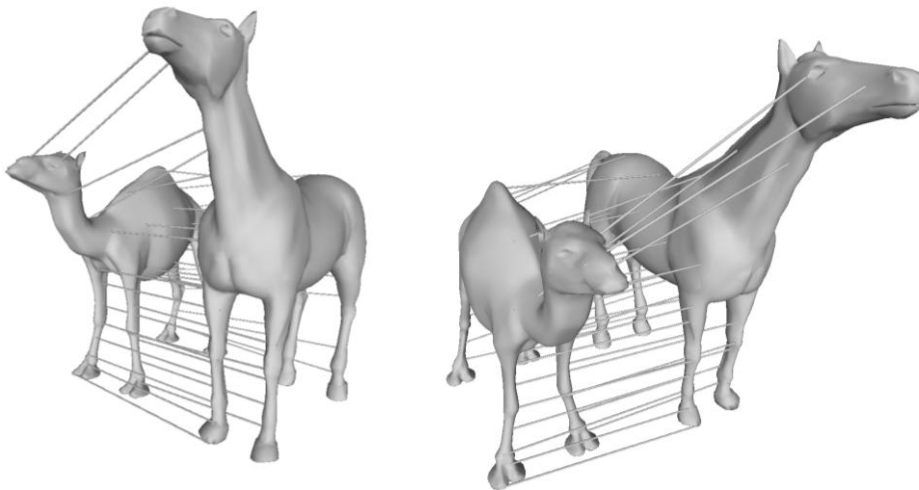


Figure 5-14. Similarities between drastically different meshes are captured from their dynamic behavior.

To the best of our knowledge there is no existing descriptor for animated meshes available today that can be used for feature matching. There are just a few existing works that address animated mesh saliency (Bulbul et al., 2010) and intra-animation vertex signature (Tung and Matsuyama, 2013). But the results of these works are not directly applicable to inter subject feature similarities and the dynamic feature matching between animated meshes.

In this thesis we consider several alternatives for the dynamic feature point signature of animated meshes:

- A. Displacement function. Represented as a normalized map of per-frame feature point displacements over animated mesh.
- B. Spatio-temporal characteristic scales. The signature composed of the pair of characteristic scales at which a signature was detected.

C. Histogram-of-Gradients for animated mesh

D. Deformation signature. The signature that captures deformation characteristics at a feature point over frames in animation.

For each of the feature signature candidates we further develop the signature distance metric so that they can be used for feature matching (5.5.1).

Hence we find it advantageous to largely exploit dynamic properties of animated meshes for the new feature descriptor.

In the following sections we formally define each of these alternatives (sections 5.3.1-5.3.4). We evaluate their time and storage complexities and formulate our final composite dynamic feature point signature in section 5.3.5.

5.3.1 Normalized displacement curves

In a recent work focusing on vertex saliency of animated meshes (Bulbul et al., 2010), Bulbul et al. present a simple yet efficient method that identifies salient regions in animation meshes. The velocity saliency of a vertex is calculated by taking the positional difference of a vertex in consecutive frames divided by the length of the main diagonal of the mesh bounding box. Though Bulbul et al. refer as velocity to such saliency measure, one can easily see that it is frame rate independent and therefore measures absolute displacements rather than velocity. Given a feature point $\mathbf{p} \in P$ from the extracted dynamic feature point set P , one can calculate the magnitude of inter-frame displacement of a feature point \mathbf{p} with respect to the previous frame in world coordinate system. In Definition 3 we give a formal description of the displacement curve signature.

Definition 3. The displacement signature of a feature point \mathbf{p} is defined as a function $\Delta_p: [1, M] \rightarrow \mathbb{R}$ that maps all the frames from animated mesh to the corresponding Euclidean displacement values

$$\Delta_p(f) = \|\mathbf{p}^{f+1} - \mathbf{p}^f\|, f \in [1, M],$$

where \mathbf{p}^f is the global coordinate of the feature point \mathbf{p} in the frame f and M is the number of frames in the animation.

However displacement curve Δ_p captures values of absolute vertex movement, which is not desirable for a point signature. Typically, the displacement curve is directly proportional to the isotropic scale of animated mesh (Figure 5-15).

We note that it is more advantageous to define the displacement curve that is invariant to the mesh scale. The main function of the scale invariant signature is to compensate differences in absolute motion between source and target meshes due to their scales i.e. absolute size. To this end we compare the relative movement of each vertex between two consecutive frames by dividing Δ_p by the global maximum displacement in the given animation \mathcal{M} . The *normalized displacement curve* signature that is invariant to absolute vertex movement defined as

$$\Delta_p(f) = \frac{\Delta_p(f)}{\Delta_{\max}},$$

(5-1)

where $\Delta_{\max} = \max_{v_i \in \mathcal{M}} \Delta_{v_i}$.

In Figure 5-15 we plot of the displacement curve and normalized displacement curve signatures for the feature point of the walking woman animation. In Figure 5-16 a comparison of normalized displacement curves is depicted for the corresponding features in the walking woman and walking baby animations.

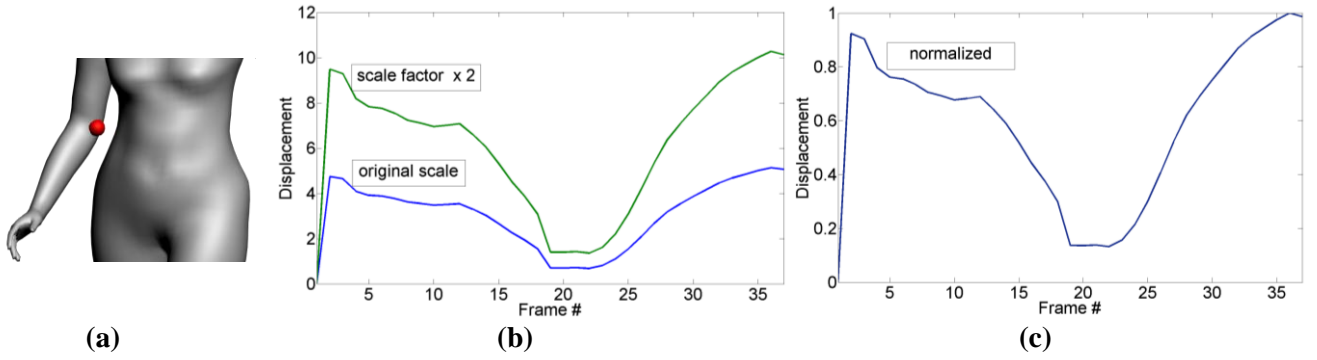


Figure 5-15. Left: the displacement curve Δ_p of the feature point on the right elbow of the walking woman (a). Displacement curves corresponding to the feature point on the elbow of the original animated mesh and walking woman animation that was isotropically enlarged by a scale factor of 2 (b). Normalized version of the displacement curve.

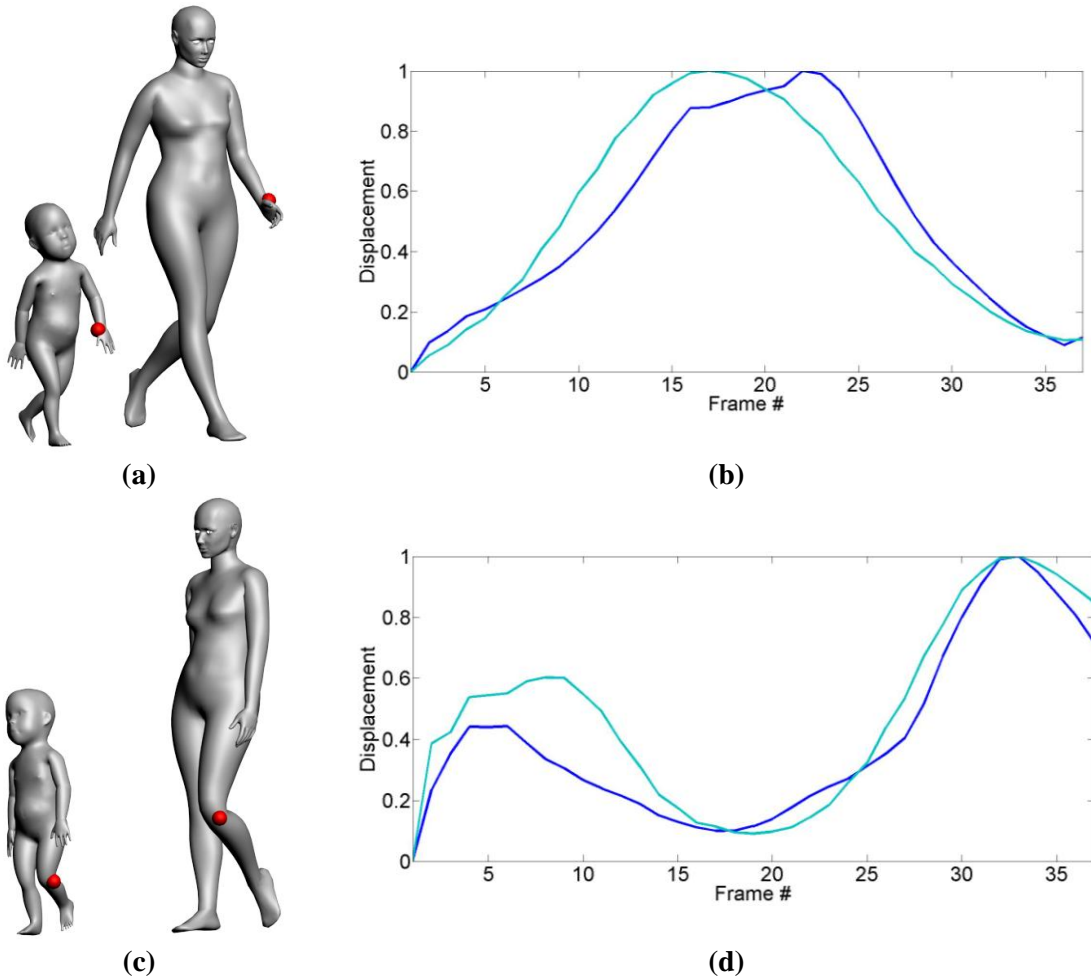


Figure 5-16. Normalized displacement curves for the walking woman and baby animations. Given consistently extracted feature points on the wrist (a) and the knee (c), the corresponding normalized displacement curves are depicted in (b) and (d). Displacement curves of the woman are shown in blue, while displacement curves of the baby are shown in cyan.

Distance metric. Given feature point from the source p and feature point p' from the target, the distance between two normalized displacement curve signatures is defined as l_2 -norm of the difference between the two curves:

$$D_{\Delta^p} = \|\Delta_p - \Delta_{p'}\|_2 = \sum_{f=1}^M (\Delta_p(f) - \Delta_{p'}(f))^2 \quad (5-2)$$

In order to make (5-2) valid for the case when the source and target come with different number of frames, we develop a more general variation of the displacement curve Δ_p . For the animations \mathcal{M} and \mathcal{M}' with the number of frames M and M' respectively, $M \neq M'$, we proceed as follows. First, we estimate the least common multiple $\bar{M} = \text{LCM}(M, M')$ of the source and target number of frames M and M' . Out of the least common multiple \bar{M} we construct a new common uniform domain of frames for both the source and target displacement curves. Then the source displacement sampling is originally known in frames $\{\frac{\bar{M}}{M}i \mid i = 1..M\}$. And for the target correspondingly in frames $\{\frac{\bar{M}}{M'}i \mid i = 1..M'\}$. Then cubic spline interpolation (De Boor, 1978) of predefined displacement samplings yields displacement curves for the source and target on the full frame domain \bar{M} (Figure 5-17).

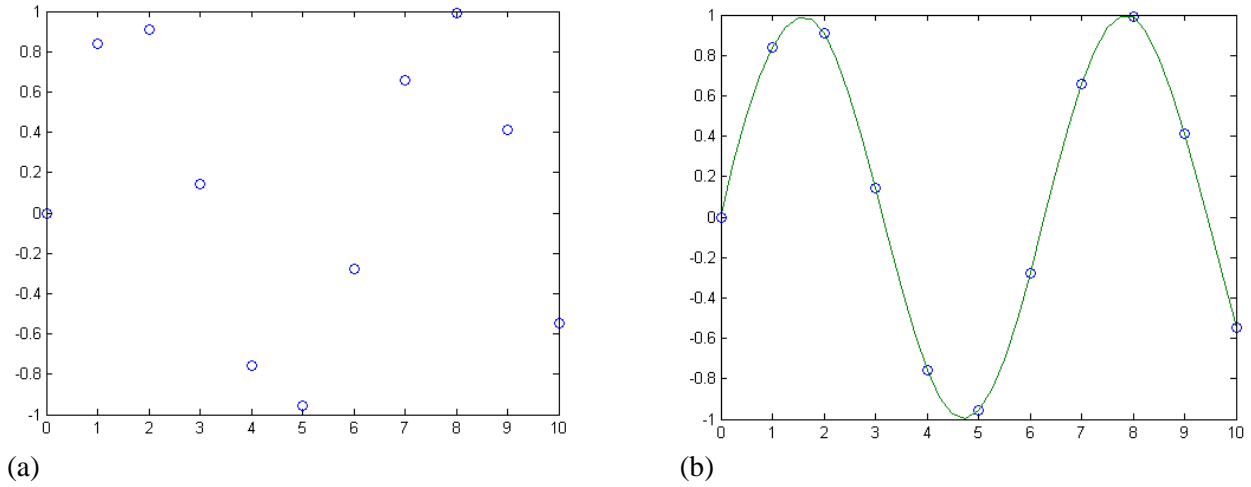


Figure 5-17. Interpolated displacement curves. A new frame domain with displacements known in the subset of frames from the initial animation (a). Interpolated displacements in all frames of the new frame domain of the animation (b).

We further evaluate displacement curve signature and form a composite descriptor with the use of other dynamic signatures (sections 5.3.3, 5.3.4) in section 5.3.5.

5.3.2 Spatio-temporal scales σ, τ

In this section we address the possibility of using spatio-temporal characteristic scales to define a signature of feature points. It would be natural to think of a feature point signature that is defined as a pair of a feature's characteristic scales σ, τ (section 4.8). For example, in a feature point corresponding to the large deforming region we expect to observe a large spatial characteristics scale, and for those corresponding to small deforming regions the characteristic scale is smaller. Hence the characteristic scale can possibly help to differentiate the large and small types of features.

However, at the same time characteristic scales of a feature point are not a part of any state-of-the-art descriptor in computer vision and graphics, such as SIFT (Lowe, 2004), SURF (Bay et al., 2006), Salient features (Castellani et al., 2008), MeshHoG (Zaharescu et al., 2009), SI-HKS (Bronstein and Kokkinos, 2010), Harris 3D (Sipiran and Bustos, 2011), SISI (Darom and Keller, 2012), LD-SIFT (Darom and Keller, 2012).

Now we discuss why the inviting idea of σ, τ feature signature cannot be reliable in practise. The characteristic scales originate from physics and they essentially represent the size/length of corresponding signal (image) structures. Lindeberg(1998) defines the characteristic scale as a scale value at which some possibly non-linear

combination of normalized derivatives assumes a local maximum over multi-scale representation of input data. This definition induces the following properties:

1. The scale value at which a scale-normalized feature response operator reaches extremum is inversely proportional to square of input signal frequency. It implies that given scaled structures in the input data, the feature points are identified at coarser (larger) scales.
2. Presence of unique structure of given characteristic scales within a signal cannot be guaranteed. In particular, for the case of animated mesh, it is possible that different feature points (i.e. in different spatio-temporal locations) are extracted at similar characteristic scales. This is illustrated in (Figure 5-19). Similarly, semantically identical feature points can be extracted at different characteristic scales.

In Figure 5-18, we make a plain illustration of the property (1). For simplicity we can consider a sinusoidal input signal in one dimension, $f(x) = \sin \omega_0 x$, of a frequency ω_0 . Consider a scale space $L(\cdot, s)$ of the signal f , where s denotes a Gaussian kernel width. As Lindeberg (1998) shows, the maximum value $\max_s L_{\xi, m}(s) = m/\omega_0^2$ of the m th order scale-normalized derivative response operator $L_{\xi, m}(s)$ over $L(\cdot, s)$ is independent of the frequency ω_0 . However, the argument of the maximum $\operatorname{argmax}_s L_{\xi, m}(s) = m/\omega_0^2$ is inversely proportional to the square of the frequency ω_0 (Figure 5-18).

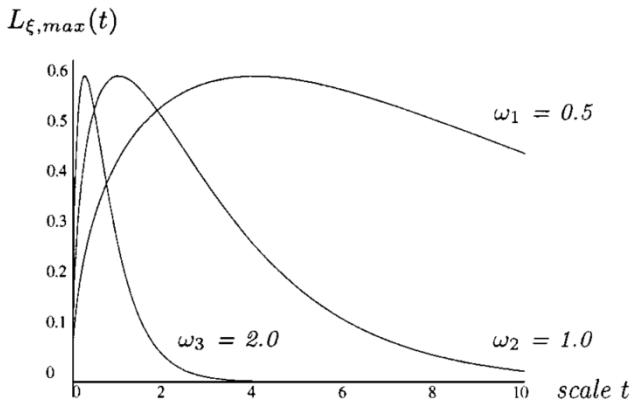


Figure 5-18. The amplitude of first order normalized derivatives as function of scale for sinusoidal input signals of different frequency ($\omega_1 = 0.5$, $\omega_2 = 1.0$ and $\omega_3 = 2.0$) (Lindeberg, 1998). Although $\max L_{\xi, 1}(s)$ is independent of the signal frequency ω_0 , the scale argument of the maximum $\operatorname{argmax}_s L_{\xi, 1}(s)$ inversely proportional to the square the signal frequency ω_0 .

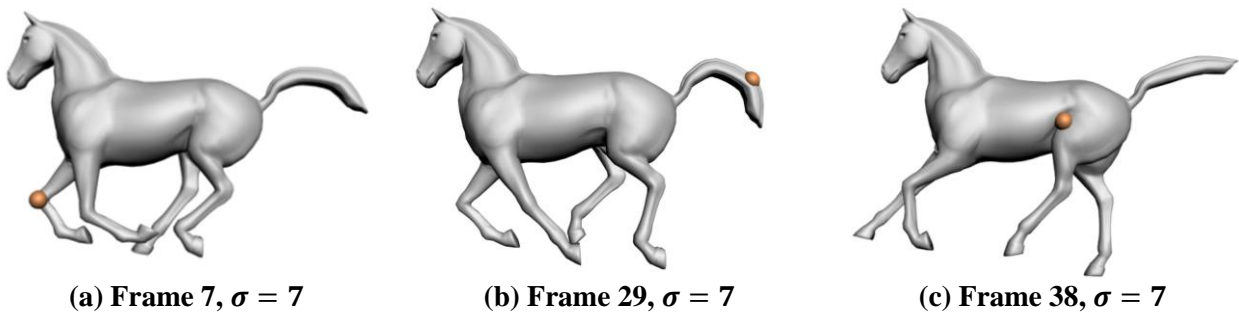


Figure 5-19. Semantically different feature points are extracted at similar characteristic scales at different spatial and temporal locations (a-c). In such a case the characteristic scales cannot help to differentiate between given feature points. The characteristic scales represent the size of the deforming shape areas rather than the way the shapes actually deforms.

In our case of deformation characteristics signal originating from the animated mesh, properties (1-2) of characteristic scales have the following direct consequences:

- Characteristic scale intrinsically reflects the body shape undergoing the deformation in animated mesh. For example, thickness of the legs of the horse and camel induces different characteristic scales of the feature points on the limbs in these two animated meshes. And that is not desirable for the feature signature since we cannot robustly capture similarities of the motion because of dissimilar body shapes.
- A point signature that relies purely on characteristic scales cannot help avoiding confusion in matching of feature points, due to frequent presence of multiple structures of similar scales in animated mesh data sets.

In conclusion on the characteristic scale approach to feature signature, first, characteristic scales descriptor cannot be completely reliable for establishment correspondences between feature points. Second, it is often desirable for a descriptor to be scale-invariant, i.e. invariant to characteristic scales. For instance, as in recent works on scale-invariant descriptors on triangle meshes SI-HKS (Bronstein and Kokkinos, 2010), SISI (Darom and Keller, 2012), LD-SIFT (Darom and Keller, 2012). For this two reasons in this thesis we do not consider including feature characteristic scales in a signature definition.

5.3.3 Normalized deformation characteristics curves

We now examine an alternative way of dynamic feature signature definition using surface deformation characteristics. Consider animated mesh $\mathcal{M} = \{(V^f) | f = 1..M\}$ with constant triangulation T , where V^f denotes vertex coordinates at frame $f: V^f = \{v_i^f | i = 1..N\}$. As described in Section 4.4, mesh surface deformation characteristics are defined as a weighted combination of strain and curvature change components:

$$d(v_i^f) = s(v_i^f) + \alpha \cdot |\kappa(v_i^f) - \kappa(v_i^1)|.$$

We exploit information obtained from mesh deformation characteristics to design a new feature point signature (Definition 4).

Definition 4. *Deformation signature* of a feature point \mathbf{p} is defined as a real-valued function on indices of animation frames

$$\begin{aligned} c_d^{\mathbf{p}}: [1, M] &\rightarrow \mathbb{R} \\ \text{s.t. } \forall f \in [1, M] \quad c_d^{\mathbf{p}}(f) &= d(\mathbf{p}^f). \end{aligned}$$

The primary purpose of the signature which we try to design here is to assist in estimation of inter-subject dynamic feature similarities or dissimilarities that can reliably guide feature matching. Hence we strive to make the descriptor invariant to absolute values of deformation characteristics in animated mesh, and consider relative characteristics values. For this reason we normalize deformation function by the global maximum of deformation characteristics in the animated mesh.

Definition 5. *Normalized deformation characteristics curve* $c_d^{\mathbf{p}}$ at a point \mathbf{p} is defined as follows

$$\begin{aligned} c_d^{\mathbf{p}}: [1, M] &\rightarrow \mathbb{R} \\ \text{s.t. } c_d^{\mathbf{p}}(f) &= d(\mathbf{p}^f) / d_{\max}, \text{ where } d_{\max} = \max_{v \in \mathcal{M}} d(v). \end{aligned}$$

Distance metric. We consider a distance metric in a Euclidean sense to compute dissimilarities between feature points on the source and target meshes. Given a deformation characteristics curve $c_d^{\mathbf{p}}$ for a feature point \mathbf{p} on the source and another $c_d^{\mathbf{p}'}$ for a feature point \mathbf{p}' on the target, the metric is defined as l_2 -norm of the difference between the two curves, as given by:

$$D_{c_d^{\mathbf{p}}}(\mathbf{p}, \mathbf{p}') = \sum_{f=1}^M (c_d^{\mathbf{p}}(f) - c_d^{\mathbf{p}'}(f))^2. \quad (5-3)$$

In order to cope with the case of different number of frames M and M' ($M \neq M'$) in the source and target animations \mathcal{M} and \mathcal{M}' we apply a similar sub-sampling interpolation algorithm as described in Section 5.3.1.

In Figure 5-20 we show plots of deformation characteristics curves for feature points in the walking woman and baby animations. Note that despite notable differences between the shapes and motions of the woman and baby models, our deformation characteristics curve shows similar behaviour for the corresponding feature points. Further evaluation of deformation function signature and its contribution to the composite dynamic feature descriptor is detailed in section 5.3.5.

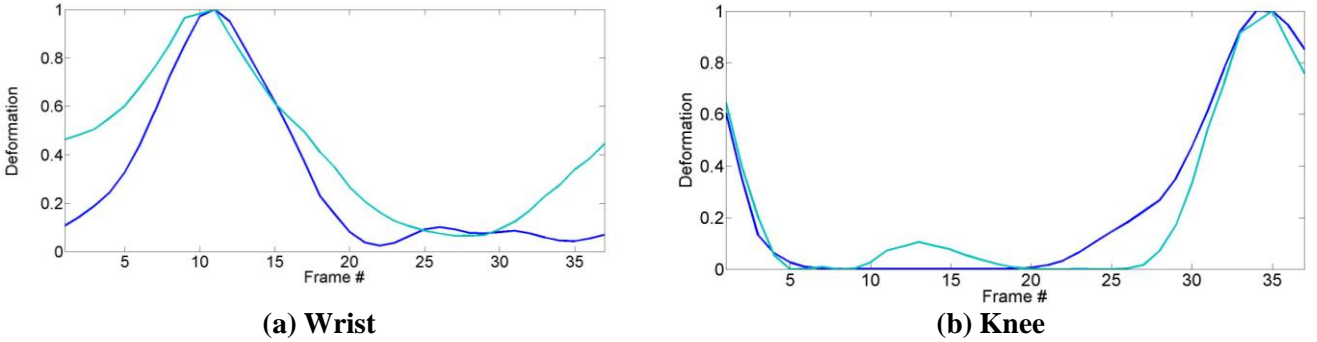


Figure 5-20. Deformation functions of the corresponding features for the walking woman (blue) and baby (turquoise) animations. Similarly to Figure 5-16 (a-c), deformation functions are captured for the wrist (a) and knee (b) feature points. Note the difference between behavior of the corresponding displacement curves and deformation functions.

5.3.4 Animated meshes Histogram-of-Gradients (AnimMeshHoG)

The third option for the dynamic feature signature we propose is named AnimMeshHoG. Similar in spirit to MeshHoG descriptor (Zaharescu et al., 2009) as well as 3D SIFT descriptor (Scovanner et al., 2007), we formulate our own new dynamic feature signature for animated meshes. The key idea is to characterize a signature as a histogram of oriented strain gradients in a local spatio-temporal neighborhood of a dynamic feature point. The algorithm of AnimMeshHoG signature computation is detailed below.

The algorithm for the computation of AnimMeshHoG signature is comprised of a sequence of intermediate computational steps.

Flattening the spatial neighborhood. First, around a feature point \mathbf{p} we define spatial neighborhood $N_s^k(\mathbf{p})$ (k -rings) proportionally to the feature's characteristic scale in space (Figure 5-21 (a)). Then we apply isomap (Tenenbaum et al., 2000) to flatten the surface patch $N_s^k(\mathbf{p})$ in a quasi isometric way (Figure 5-21 (b)). Note that in certain cases of high k values we can obtain cylindrical spatial neighbourhood around the feature point. In such case isomap will result in incorrect flat patch output. In order to cope with the issue, when constructing $N_s^k(\mathbf{p})$ we keep only those neighboring vertices whose normal vectors are consistent with normal vector \mathbf{n}_p at feature point \mathbf{p} (see Figure 5-22). In particular:

$$\tilde{N}_s^k(\mathbf{p}) = \{v \in N_s^k(\mathbf{p}) : \angle(\mathbf{n}_v, \mathbf{n}_p) < \frac{\pi}{2}\}$$

In the final patch $\tilde{N}_s^k(\mathbf{p})$ we additionally remove vertices that are disconnected from \mathbf{p} .

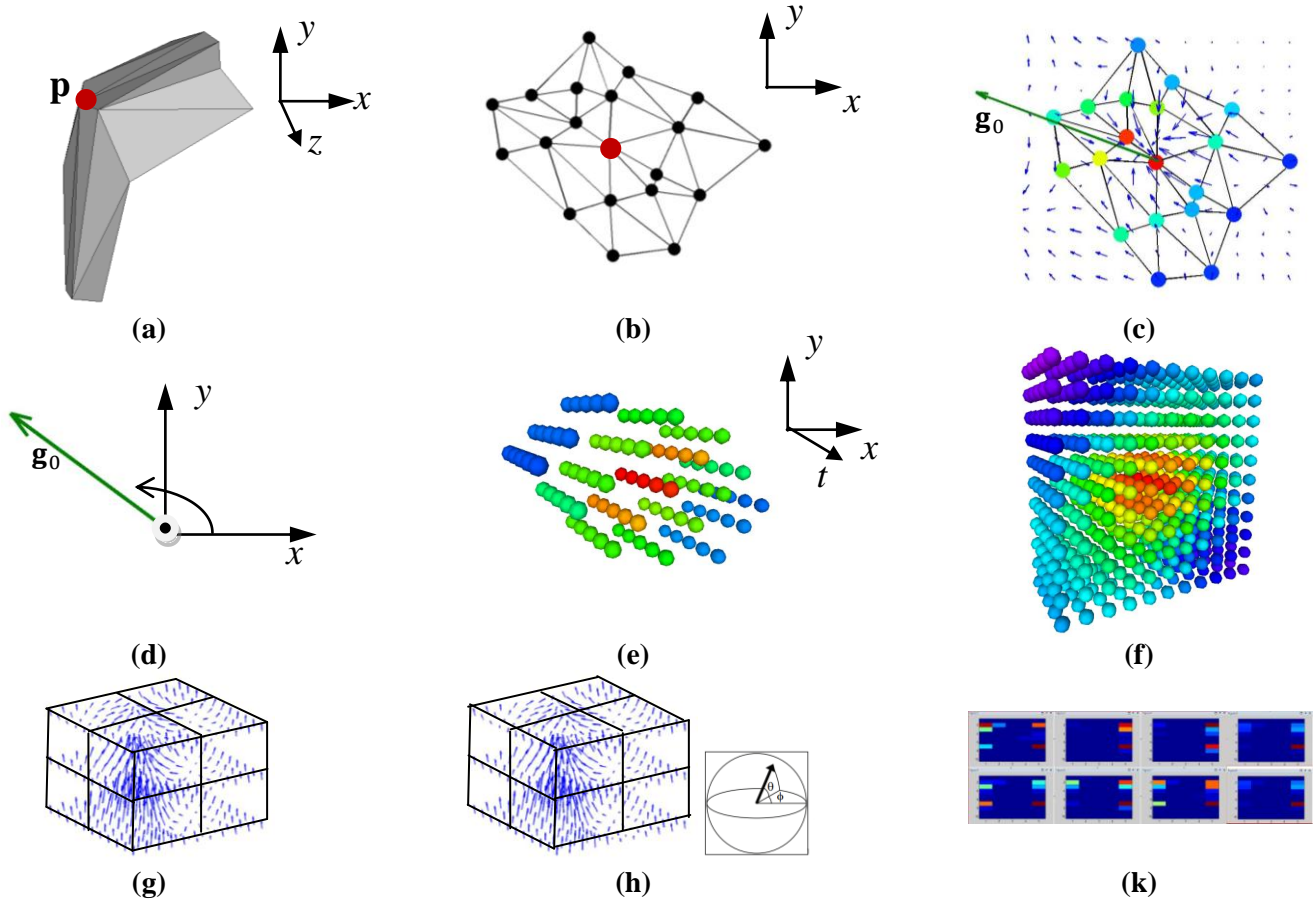


Figure 5-21. The steps of AnimMeshHoG computation pipeline ordered from (a) to (k).

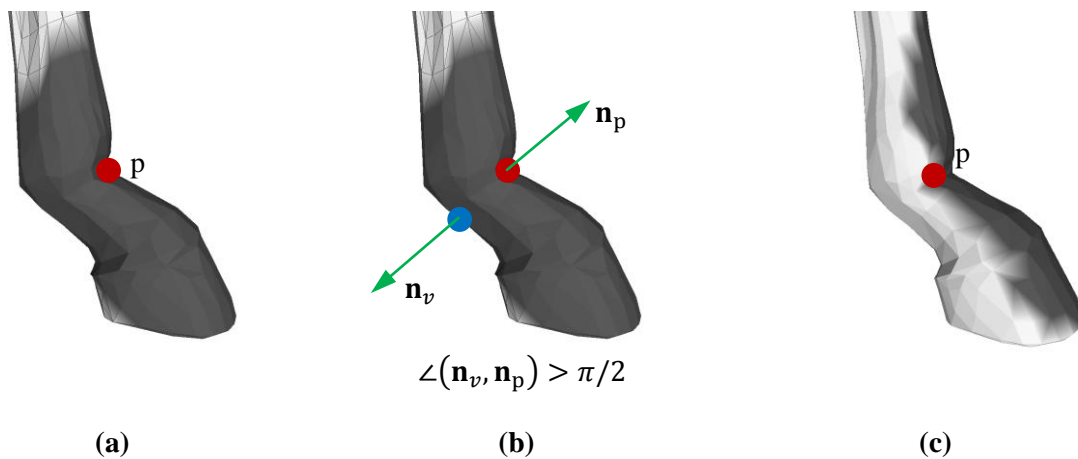


Figure 5-22. Cylindrical local neighborhood $N_s^k(p)$ of p is shown in dark color (a); by considering the angles between surface normals (b) neighborhood $N_s^k(p)$ is enforced to have a disk topology (c).

Gradient vectors computation. Flattening step is then followed by computing gradient vector field of the patch's vertex deformation characteristics and the global gradient dominant direction in the patch (Figure 5-21 (c)). Dominant gradient direction g_0 within $\tilde{N}_s^k(p)$ can be estimated by binning into a polar histogram all strain gradients orientations in the flattened patch. After that, the angle corresponding to a polar bin of the global maxima in the histogram is taken as the dominant gradient direction g_0 . Then we first translate the p to the origin of the global coordinate system. Second, given the vector g_0 , the patch is rotated in a way that g_0 be-

comes aligned with the x axis of the world coordinate system (Figure 5-21 (d)). Alignment of the patch with the world coordinates system is introduced to ensure consistency across coordinate frames of corresponding features from the source and target.

Volume construction with temporal neighborhood. Furthermore, in the next step of the pipeline, we define a temporal neighborhood $N_t(\mathbf{p})$ proportional to the feature's characteristic scale τ . Given the time t^* (i.e. frame number) at which the feature was detected, $N_t(\mathbf{p})$ is defined as

$$N_t(\mathbf{p}) = \{t^* + \iota\Delta t \mid \iota \in [-\tau, \dots, \tau]\},$$

where Δt is a pre-defined temporal distance between consequent frames.

Temporal distance can be assumed as an inverse value of the fps in a given animation. However, we set it equal to the average edge length in the animated mesh which makes homogenous sampling in the spatial and temporal domains.

We also consider two boundary conditions for the temporal neighborhood when the feature \mathbf{p} was detected either in the very beginning or in the end of the animation:

$$N_t(\mathbf{p}) = \begin{cases} t^* + \iota\Delta t : \iota \in [0, \dots, \tau], & \text{if } t^* < \tau, \\ t^* + \iota\Delta t : \iota \in [-\tau, \dots, |M - t^*|], & \text{if } |M - t^*| < \tau. \end{cases}$$

A combination of spatial $N_s^k(\mathbf{p})$ and temporal $N_t(\mathbf{p})$ neighborhoods define a feature's spatio-temporal volume $V(\mathbf{p})$:

$$V(\mathbf{p}) = \{(\mathbf{x}, t) \mid \mathbf{x} \in N_s^k(\mathbf{p}), t \in N_t(\mathbf{p})\}.$$

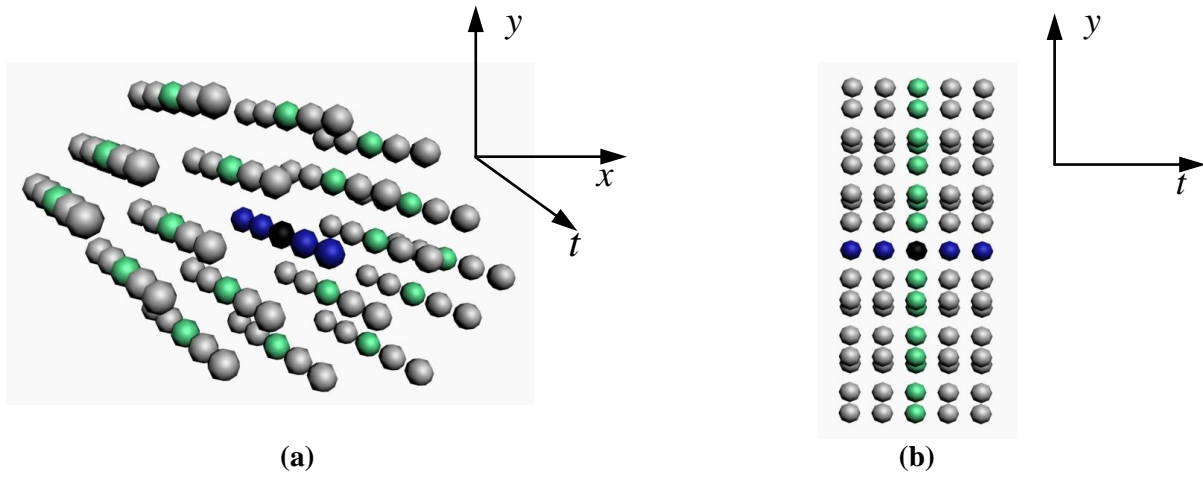


Figure 5-23. Spatio-temporal volume centered around dynamic feature point marked in black (a). View of the spatio-temporal volume in x-axis direction.

The volume $V(\mathbf{p})$ can be intuitively interpreted as a stack of patches from feature's spatio temporal neighborhood with fixed spatial coordinates and with identical intervals Δt in time (see Figure 5-23). Each vertex inside the spatio-temporal volume $V(\mathbf{p})$ is supplied with a corresponding deformation characteristic value $d(\mathbf{p}^t)$. Note that alignment of the dominant gradient direction \mathbf{g}_0 of the spatial neighborhood around the feature with the x-axis makes construction of characteristic volume invariant to the feature point absolute coordinates. The time axis t is orthogonal to xy -plane and is chosen according to the right-hand rule with respect to x and y axes.

Scattered strain interpolation. Our main idea behind AnimMeshHoG is to treat histograms of spatio-temporal gradients in $V(\mathbf{p})$ as the point signature. However, spatio-temporal volume $V(\mathbf{p})$ is supplied with deformation characteristics values only in relatively small and number of scattered locations (Figure 5-21(e)), which is problematic for the gradient vector field computation in the volume $V(\mathbf{p})$. Of course, the numerical gradient computation in the volume $V(\mathbf{p})$ can be approximated similarly to Zaharescu, Boyer et al., 2009, but we found it advantageous to densely interpolate the input deformation characteristics scalar field in order to decrease possible gradient field inaccuracy.

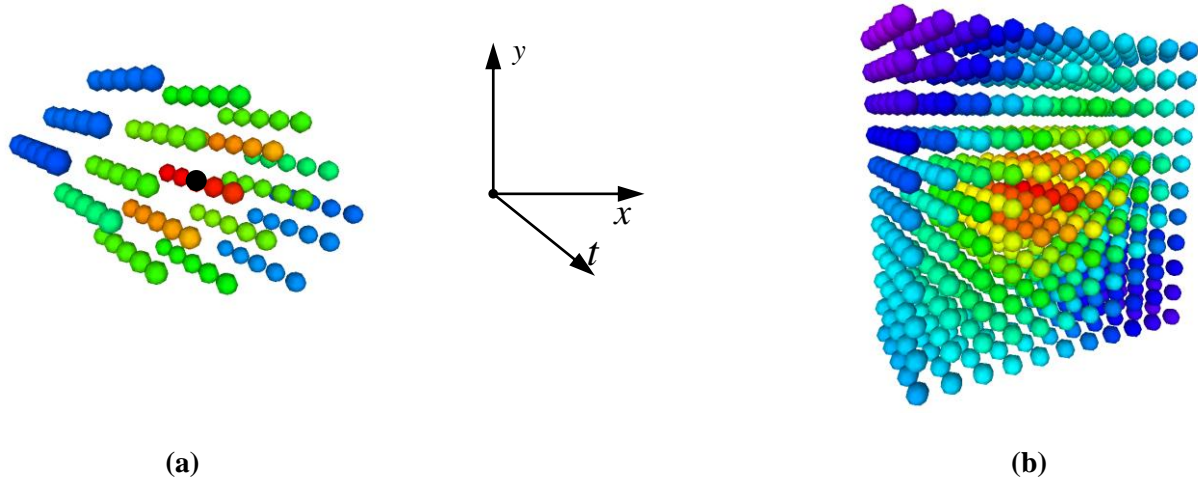


Figure 5-24. Scattered deformation characteristic values inside spatio-temporal volume of a feature point (a) and the corresponding densely interpolated deformation values (b).

In order to deal with the problem of sparse vertex locations, we densely and regularly sub-sample the volume, and interpolate strain values in all sub-sampled locations given input sparse values. For that we use RBF interpolation with Gaussian radial basis. The interpolation procedure yields a characteristic volume with strains in dense spatio-temporal grid (Figure 5-24).

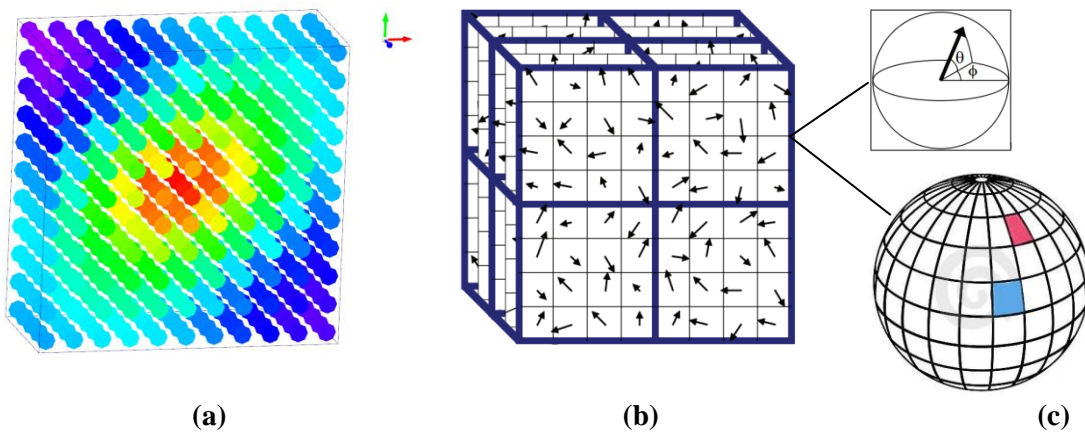


Figure 5-25. Values of deformation characteristics inside spatio-temporal volume around a feature point (a). Gradients of the deformation characteristics scalar field (b). Histogram bins of the gradient field are normalized by a corresponding solid angle in spherical coordinates (c).

Descriptor definition. Given dense interpolated strain data inside the volume $V(\mathbf{p})$ computed in the previous stage, we continue with a numerical computation (Faires and Burden, 1998) of strain gradients. Computed gradient directions in the characteristic volume of an interest point are depicted in Figure 5-25.

Then, the descriptor is obtained by computing gradients orientation histograms $H_p = \{H_p^i | i = 1, \dots, 8\}$ in each of the octet of characteristic volume (Figure 5-21 (g-h)). Each of H_p^i , $i = 1, \dots, 8$ is essentially a 2d histogram

computed by binning gradient directions in spherical coordinate system (φ, θ) as in Figure 5-24. Note that azimuth $\varphi \in [0, 2\pi]$, and elevation $\theta \in [0, \pi]$ i.e. the range of azimuth is twice larger than elevation. The number of bins is a configurable parameter. Initially we implemented descriptor with 18/9 bins per φ/θ . However, during evaluation experiments, in order to reduce aliasing in the histograms we decided to reduce the number of bins to a smaller number. After reducing the φ/θ to 8/4 we notice more robust performance of the descriptor in the application of feature matching (Section 5.5).

Similarly to 3D SIFT (Scovanner, Ali et al., 2007) we further normalize the values added to each radial bin in H_p by the area of corresponding bin's solid angle Ω . Solid angle normalization compensates the fact that bins near sphere equator tend to be significantly larger than bins around sphere poles. It can be shown (Scovanner, Ali et al., 2007) that the area Ω of a solid angle equals to

$$\Omega = \Delta\varphi(\cos \theta - \cos(\theta + \Delta\theta)),$$

where $\Delta\varphi, \Delta\theta$ are angular dimensions of the spherical bin, and θ is the elevation of the bin (a parallel at which the bin is located). Finally, in order to vastly improve anti-aliasing in the histograms, we applied fast 2d histogram smoothing technique of (Eilers and Goeman, 2004) (Figure 5-26). Reducing aliasing in the histograms helps to make the signature more robust on the feature matching stage.

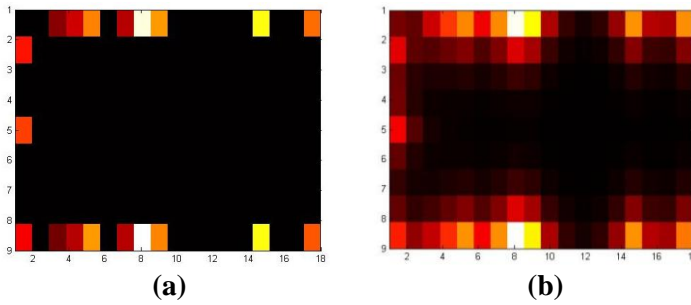


Figure 5-26. Left - original histograms from the Cylinder's feature point (aliased); right - interpolated histograms.

Distance metric. In order to finalize the HoG signature it must be supplied with a distance metric. Given interest points \mathbf{p}, \mathbf{p}' with signatures $H_p = \{H_p^i \mid i = 1, \dots, 8\}$ and $H_{p'} = \{H_{p'}^i \mid i = 1, \dots, 8\}$, distance between their signatures can be defined as follows:

$$D_{H^p}(\mathbf{p}, \mathbf{p}') = \sum_{i=1}^8 \left\| H_p^i - H_{p'}^i \right\|_H, \quad (5-4)$$

where $\|\cdot\|_H$ is a histogram earth mover's distance also known as Wasserstein metric (Rubner, Guibas et al. 1997, Ling and Okada 2007). Generally, given two signatures $\{(x_i, w_{x_i})\}_{i=1}^n$ and $\{(y_j, w_{y_j})\}_{j=1}^m$ (where x_i and y_j are points in some metric space, and w_{x_i}, w_{y_j} are the corresponding weights of the points) the earth mover's distance is defined as

$$\min_{C=\{C_{ij}\}} \frac{\sum_{i,j} C_{ij} \|x_i - y_j\|}{\sum_{i,j} C_{ij}}, \quad (5-5)$$

where $C = \{C_{ij}\}$ is the flow which minimizes the cost function and the value of this flow.

In our case x_i is an Euclidean distance between histogram bins. Eq.(5-5 is the transportation problem and is solved by the efficient algorithm (Rubner, Guibas et al. 1997). The AnimHoG signature is further used to build a composite dynamic feature descriptor section 5.3.5.

5.3.5 Composite descriptor

In this section we propose a composite feature signature based on dynamic descriptors described in sections 5.3.1-5.3.4. We define the dynamic descriptor at a given feature \mathbf{p} as a triple composed of the corresponding displacement curve, deformation characteristics curve and AnimMeshHoG descriptors:

$$\mathcal{H} = (\Delta^{\mathbf{p}}, c_d^{\mathbf{p}}, H^{\mathbf{p}})$$

Proposed descriptor maximizes the amount of information about distinctive deformation and dynamic properties gained around spatial and temporal extents around a feature point. Given the composite descriptor \mathcal{H} , the distance metric between feature point signatures is defined as

$$D_{\mathcal{H}}(\mathbf{p}, \mathbf{p}') = w_1 D_{\Delta^{\mathbf{p}}}(\mathbf{p}, \mathbf{p}') + w_2 D_{c_d^{\mathbf{p}}}(\mathbf{p}, \mathbf{p}') + w_3 D_{H^{\mathbf{p}}}(\mathbf{p}, \mathbf{p}'),$$

where $w_i, i=1..3$ are the positive weights that control the influence of each of the signatures. In our settings we usually set equally $w_i=1$. Proposed dynamic feature point descriptor \mathcal{H} is effectively used for the feature point matching as detailed in Section 5.5. Evaluation of distinctiveness of each of these signatures is under development at the time of writing this document.

Complexity analysis. Now we consider two important properties for the signature: time and storage complexities. We present a comparative evaluation of time and storage complexities of the signatures in Table 5-1. Each entry in the triple $\mathcal{H} = (\Delta^{\mathbf{p}}, c_d^{\mathbf{p}}, H^{\mathbf{p}})$ of the composite feature signature has its advantages and its disadvantages. Both the displacement and deformation characteristics curves have a light linear time and storage complexity of $O(M)$, where M is the number of frames in an animation. However, deformation characteristics curve can be sensitive to the triangulation of animated meshes. In certain cases when deformation characteristic computation fails the deformation function signature fails as well. For example it can happen when animated mesh contains degenerated zero-area triangles or when the source and target animations contain extremely different number of triangles $|T| \gg |T'|$ or $|T| \ll |T'|$. The main limitation of the dynamic signature based solely on vertex displacement curve is that it is not invariant to rigid transformations. Consequently, features in bending and at the same time rigidly moving parts of a mesh (such as the knees of the horse) can exhibit much larger displacements comparing to features with purely non-rigid neighbourhood (groin of the horse). Such highly rigidly moving features can suppress the rest of displacement curves of other feature points during normalization of the signatures.

The AnimMesh HoG descriptor possesses an advantageous constant $O(1)$ storage complexity, but at the same time a heavy time complexity. As described in section 5.3.4, the algorithm of HoG computation is comprised of the following major routines of corresponding time complexities. Given the number of points in the spatial $|N_s^k(\mathbf{p})|$, temporal $|N_t^k(\mathbf{p})|$, and spatio-temporal $|N_{st}^k(\mathbf{p})|$ neighborhoods of a feature point \mathbf{p} , the computational time for each step of AnimMesh HoG descriptor can be estimated as follows:

1. ISOMAP: $O(|N_s^k(\mathbf{p})|) + O(|N_s^k(\mathbf{p})| \cdot \log(|N_s^k(\mathbf{p})|)) + O(|N_s^k(\mathbf{p})|^2)$
2. Normal orientation check: linear $O(|N_s^k(\mathbf{p})|)$
3. RBF interpolation: $O(|N_{st}(\mathbf{p})| \cdot \log(|N_{st}(\mathbf{p})|))$, where $|N_{st}(\mathbf{p})| = |N_s^k(\mathbf{p})| |N_t^k(\mathbf{p})|$ is the total number of points in the spatio-temporal volume $V(\mathbf{p})$ of the feature point \mathbf{p} .
4. Histogram binning: $O(|N_{st}(\mathbf{p})|)$

The overall time complexity of AnimMesh HoG, according the big O summation rule, is given in Table 5-1. In practice the computation of the animation HoG is the most heavy dynamic descriptor. Note that all the anima-

tions in our data set have less than one hundred number of frames, which results in practically negligible average storage complexity of the displacement and deformation characteristics curve descriptors.

Signature	Time Complexity	Storage Complexity
Displacement curve	$O(M)$	$O(M)$
AnimMeshHoG	$O(N_s^k(\mathbf{p}) ^2 + O(N_{st}(\mathbf{p}) \cdot \log(N_{st}(\mathbf{p}))))$	$O(1)$
Deformation function	$O(M)$	$O(M)$

Table 5-1. Time complexity, storage complexity of the components of the feature point signature \mathcal{H} . M denotes the number of frames in the animation. The terms $|N_s^k(\mathbf{p})|$ and $|N_t^k(\mathbf{p})|$ denote the number of points in the spatial and temporal neighborhoods of a feature point \mathbf{p} . And the term $|N_{st}(\mathbf{p})| = |N_s^k(\mathbf{p})| |N_t^k(\mathbf{p})|$ is the total number of points in the spatio-temporal volume $V(\mathbf{p})$ of the feature point.

5.4 Displacement feature points

Since our full matching optimization algorithm is guided by the feature matching, it is important to have sufficient number of feature points, on which we can establish reliable correspondences. The more regions of the shape are supplied with feature points with distinct correspondence, the better effectiveness and quality of full matching can be obtained. To this end we extend dynamic feature point sets by detecting additional feature points in highly mobile regions which will supplement the dynamic feature point set (section 4.8). Typically, these points represent end-effectors or extremity points of animated characters. In order to differentiate from the dynamic feature points, we refer to the new type of features as *displacement features*.

Consider displacement function Δ_v (section 5.3.1) for a given vertex $v \in \mathcal{M}$ in animated mesh \mathcal{M} , then the sum of vertex displacements over all frames yields the total length of the vertex trajectory in the animation, as given by

$$\Delta_v = \sum_{f=1}^M \Delta_v(f).$$

Then displacement feature point is defined as a local maxima of the trajectory length subject to a threshold (Definition 6).

Definition 6. Vertex $v \in \mathcal{M}$ is a displacement feature point if and only if

$$\forall u \in N_s(v): (\Delta_v > \Delta_u) \wedge (\Delta_v > h^\Delta),$$

where threshold h^Δ controls the minimum allowed trajectory length of the displacement feature points. In our experiments we usually set h^Δ to 0.1 of global maximum in trajectory length.

From now on we refer to a full set P of dynamic feature points of animated mesh as a union of deformation feature points and displacement ones $P = P_d \cup P_\Delta$. In Figure 5-27 we present some of displacement feature points that we extracted from our data sets. As expected, displacement features correspond to the tips of limbs in most cases of the skeleton-driven deformations such as animals and humans. For the horse and camel, for instance, we detect displacement features on the tips of the legs and the tip of the tail.

In general, the displacement feature points depend on the type of skeletal animation. The same static mesh that undergoes two distinct skeletal animations can yield accordingly two different sets of the displacement feature points. Moreover, in case of animated meshes with no skeleton (such as faces), there is no general pattern of the place of the displacement feature extraction. Depending on the facial expressions and head motions the dis-

placement features can be extracted at different locations. However, as long as we consider pairs of semantically similar deforming shapes displacement feature points will be extracted coherently.

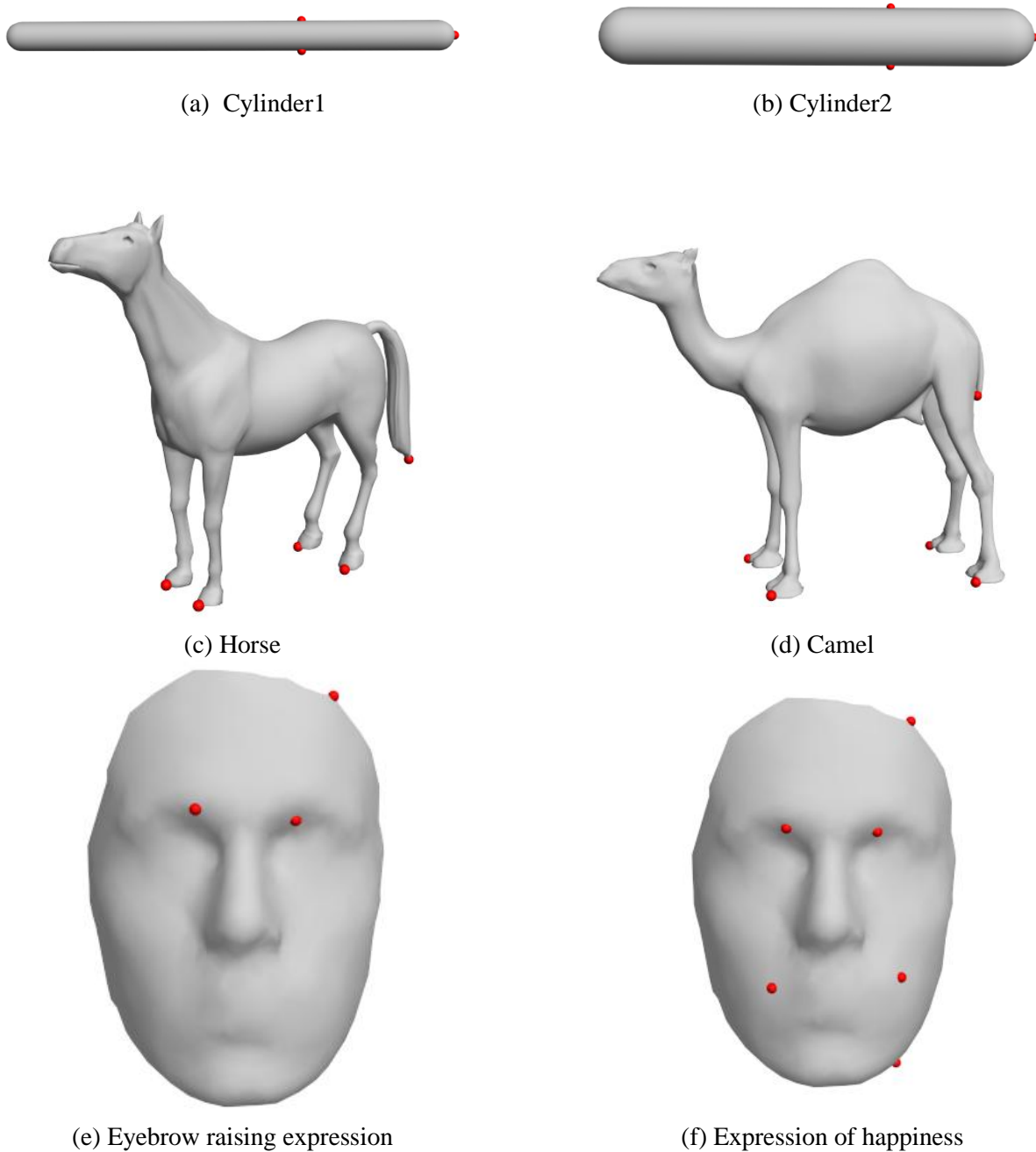


Figure 5-27. Displacement feature points: (a) bending cylinder1, (b) bending cylinder2, (c) galloping horse, (d) galloping camel, (e) facial expression1 (“eyebrow raising”), (f) facial expression2 (“happiness”).

Distance metric. After extending the full feature point set P with displacement features P_{Δ} we face an issue of comparing the signatures of the dynamic feature points with the signatures of the displacement feature points. As defined in Section 5.3.5 the dynamic feature signature is composed of a triple $\mathcal{H}=(\Delta^P, c_d^P, H^P)$ with the distance metric

$$D_{\mathcal{H}}(\mathbf{p}, \mathbf{p}') = w_1 D_{\Delta^P}(\mathbf{p}, \mathbf{p}') + w_2 D_{c_d^P}(\mathbf{p}, \mathbf{p}') + w_3 D_{H^P}(\mathbf{p}, \mathbf{p}').$$

Nevertheless it is important to note, that for obvious reasons, among all proposed dynamic feature signatures we can rely only on displacement function for the measuring the similarity between displacement feature points during matching. Moreover the same is true when comparing displacement to dynamic feature points. Therefore we define the distance metric as

$$D_{\mathcal{F}}(\mathbf{p}, \mathbf{q}) = D_{\Delta^P}(\mathbf{p}, \mathbf{q}),$$

where \mathbf{p} is a displacement feature and \mathbf{q} is either displacement or dynamic feature point.

5.5 Feature correspondence via graph matching

Robust feature correspondence based on the dynamic feature point signature developed in section 5.3 is a first and very important building block in the animated mesh matching pipeline (Figure 5-1). Naturally and similarly to the majority of existing shape matching techniques, we cannot rely solely on the feature signatures to establish reliable correspondences between them. Therefore we take into account not only the signature of feature points but also their relative spatial relationship. One of the most powerful mathematical tools that can provide an accurate matching between two set of points based both on point signatures and relative spatial arrangement is inexact graph isomorphism (inexact graph matching). Note, that in Chapter 6 we use a simpler Ullman’s graph matching method for isometric shape correspondence, because the features involved in matching in Chapter 6 are usually highly consistent. Here we propose to use the graph matching technique based on the work of (Torresani, Kolmogorov et al., 2008, Torresani, Kolmogorov et al. 2013).

Unfortunately, inexact graph matching is a NP-hard problem (Gallagher, 2006). We have chosen to use the graph matching via dual decomposition by (Torresani, Kolmogorov et al., 2008, Torresani, Kolmogorov et al. 2013) due to our several practical requirements for the feature matching technique:

1. Fast. The method should have a low computational complexity.
2. Inexact. We would like to adopt attributed subgraph matching which allows us to perform as best as possible in matching between inconsistent feature point sets.
3. Robust. The method should produce stable and correct matching results in most of the cases. Even though we assume similarities of the source and target animated meshes, their motions are not perfectly the same in practice. This results in a fair amount of differences between the signatures of corresponding features from the source and target animations in certain cases. Therefore graph matching algorithm should allow to robustly handle variations of the point signatures of corresponding feature points.

In the work of (Torresani, Kolmogorov et al. 2013) the authors compare Dual Decomposition graph matching optimization to other state-of-the-art graph matching techniques (Cour et al., 2007, Elidan et al., 2007, Lempitsky et al., 2007) and demonstrate that their technique outperforms significantly existing graph matching algorithms. We adopt a similar technique in our graph matching solution, however with important differences that make it suitable for animated mesh dynamic feature matching. More specifically, we provide a way to the graph matching algorithm to strongly penalize matches that are incompatible in geodesic sense on the source and target meshes (Section 4.5.3).

5.5.1 Graph matching formulation

In this section, we show how we adapt the DD technique of (Torresani et al. 2008, Torresani, Kolmogorov et al. 2013) to our problem of feature matching for animated meshes. Given a set of feature points $P = \{(\mathbf{p}, t)\}$, $P' = \{(\mathbf{p}', t')\}$, extracted from the source \mathcal{M} and target \mathcal{M}' animations respectively, we propose to construct feature graphs in the following way. First we discard the time coordinate by projecting the feature point sets on

the space domain: $P = \{(\mathbf{p}, t)\} \rightarrow \{\mathbf{p}(\mathbf{p})\}$, $P' = \{(\mathbf{p}', t')\} \rightarrow \{\mathbf{p}'\}$. Note, that we do not lose the temporal information regarding a feature point since we compensate it in some of the feature point signatures (e.g. displacement and deformation characteristics curves). It means that two features (\mathbf{p}, t_1) and (\mathbf{p}, t_2) detected at the same spatial location \mathbf{p} and different time are considered to be a same feature.

Then we define a set of possible assignments $A \subseteq P \times P'$ between feature points from the source and target. The set A represents potential matching pairs. Each assignment $a = (\mathbf{p}, \mathbf{p}') \in A$ is supplied with a cost θ_a equal to the distance (section 5.3.5) $D_{\mathcal{H}}(\mathbf{p}, \mathbf{p}')$ between corresponding feature descriptors. Instead of considering the complete set of all possible assignments $P \times P'$, each feature point $\mathbf{p} \in P$ is associated only with l features $P'_l(\mathbf{p}) \subset P'$ on the target that are closest in terms of feature signature. We further populate the set of assignments by including matching pairs of features on target and l features on the source $P_l(\mathbf{p}') \subset P$ with the most similar signatures. The algorithm of assignment set construction is summarized in Algorithm 5-1. We typically set l to 4 throughout our experiments in this thesis.

Algorithm 5-1. The construction of assignment set.
Input: Feature points sets on the source and target P, P'
Output: Possible assignment set $A \subseteq P \times P'$
begin
 $A = \emptyset$
 for each $\mathbf{p} \in P$
 $A = A \cup P'_l(\mathbf{p})$
 for each $\mathbf{p}' \in P'$
 $A = A \cup P_l(\mathbf{p}')$
end

Considering all feature point assignments to be the nodes of complete graph, we now can formulate our objective function to be minimized as a weighted sum of energy terms:

$$\operatorname{argmax}_{\mathbf{x}} E(\mathbf{x}) = \operatorname{argmax}_{\mathbf{x}} (E(\mathbf{x}) = \lambda^{dscr} E^{dscr}(\mathbf{x}) + \lambda^{geod} E^{geod}(\mathbf{x}) + \lambda^{unmat} E^{unmat}(\mathbf{x}) + \lambda^{coh} E^{coh}(\mathbf{x})), \quad (5-6)$$

where \mathbf{x} is a binary-valued vector $\mathbf{x} \in \{0,1\}^A$ representing a feature matching solution. Each value x_a in \mathbf{x} is associated with an assignment a . If $x_a = 1$ then the assignment a is included in feature matching solution (i.e. assignment a is active), and it is not included if $x_a = 0$ (a is inactive). E^{dscr} energy term estimates nodes dissimilarities (distance $D_{\mathcal{H}}$ in section 5.3.5), E^{geod} describes edge dissimilarities and E^{unmat} , E^{coh} are stabilizing terms enforcing valid graph matching results. We detail each of the energy terms below.

Descriptor energy term. Descriptor energy term measures similarities between feature point signatures involved in active assignments

$$E^{dscr}(\mathbf{x}) = \sum_{a \in A} \theta_a x_a,$$

with θ_a defined as the distance (section 5.3.5) between feature points $D_{\mathcal{H}}(\mathbf{p}, \mathbf{p}')$ involved in assignment $a = (\mathbf{p}, \mathbf{p}')$. The term E^{dscr} favours matching solutions of features with similar signatures (descriptors).

Geodesic distortion term. We further define an important geodesic distortion term E^{geod} that measures how much the relative geodesic distance between feature points \mathbf{p}, \mathbf{q} on the source is preserved between their correspondences \mathbf{p}', \mathbf{q}' on the target.

Let \mathcal{N} be a set of neighbouring correspondence pairs (Torresani, Kolmogorov et al. 2008)
 $\mathcal{N} = \{((\mathbf{p}, \mathbf{p}'), (\mathbf{q}, \mathbf{q}')) \in A \times A \mid \mathbf{p} \in N_s^k(\mathbf{q}) \vee \mathbf{q} \in N_s^k(\mathbf{p}) \vee \mathbf{p}' \in N_s^k(\mathbf{q}') \vee \mathbf{q}' \in N_s^k(\mathbf{p}')\}$

where $N_s^k(\mathbf{p})$ is a set of $k \in \mathbb{N}^+$ nearest neighbours of feature point \mathbf{p} . For our matching experiments we used constant k from interval $[3,6]$.

Then we further propose additional definitions Definition 7, Definition 8.

Definition 7. Let $\Gamma_{\mathbf{p},\mathbf{q}}^M$ be a Dijkstra's shortest path approximating discrete geodesic path between vertices \mathbf{p} and \mathbf{q} on mesh M .

Definition 8. $|\Gamma_{\mathbf{p},\mathbf{q}}^M| = \sum_{i=1}^k \|\mathbf{v}_{i-1} - \mathbf{v}_i\|$ is the length of Dijkstra's shortest path $\Gamma_{\mathbf{p},\mathbf{q}}^M = \langle \mathbf{v}_0, \mathbf{v}_1, \dots, \mathbf{v}_k \rangle$, $\mathbf{v}_0 = \mathbf{p}$, $\mathbf{v}_k = \mathbf{q}$ between vertices \mathbf{p} and \mathbf{q} on triangle mesh M .

We finally define the geodesic distortion energy term over the pairs of active assignments in set \mathcal{N} as

$$E^{geod}(\mathbf{x}) = \sum_{(a,b) \in \mathcal{N}} \theta_{ab}^{geod} x_a x_b,$$

where $\theta_{ab}^{geod} = \text{abs}(|\Gamma_{\mathbf{p},\mathbf{q}}^M| - |\Gamma_{\mathbf{p}',\mathbf{q}'}^{M'}|)$, $a = (\mathbf{p}, \mathbf{p}') \in A$, $b = (\mathbf{q}, \mathbf{q}') \in A$ (see Figure 5-28).

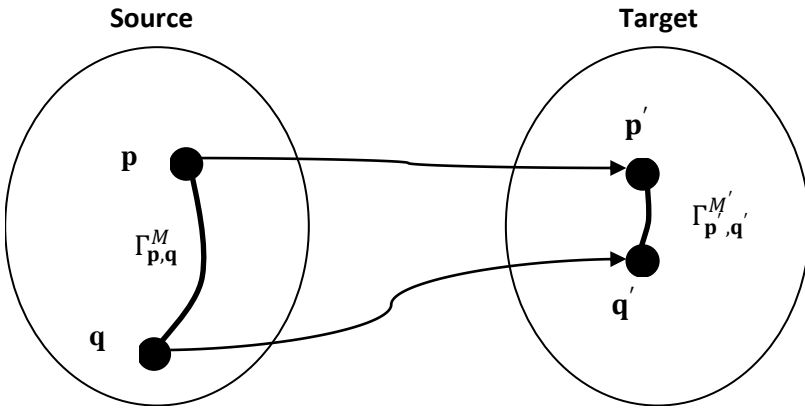


Figure 5-28. Geodesic distortion in assignments $a = (\mathbf{p}, \mathbf{p}') \in A$, $b = (\mathbf{q}, \mathbf{q}') \in A$ is equal to the absolute geodesic path length change $\theta_{ab}^{geod} = \text{abs}(|\Gamma_{\mathbf{p},\mathbf{q}}^M| - |\Gamma_{\mathbf{p}',\mathbf{q}'}^{M'}|)$.

Penalty term for unmatched feature pairs. The goal of $E^{unmat}(\mathbf{x})$ energy term is to impose a penalty on the number of unmatched features. The penalty can be effectively defined as a ratio of unmatched features in the smaller set among P and P' . More precisely the unmatched ratio is defined as

$$E^{unmat}(\mathbf{x}) = 1 - \frac{1}{\min\{|P|, |P'|\}} \sum_{a \in A} x_a.$$

Without losing generality we can assume that the number of source features is less than the number target features i.e. $\min\{|P|, |P'|\} = |P|$. Then $E^{unmat}(\mathbf{x}) = 0$ is minimal when all features from P are matched, and $E^{unmat}(\mathbf{x}) = 1$ is maximal when none of features is matched. Note that $E^{unmat}(\mathbf{x})$ is a specifically useful term in inexact graph matching, since it balances with the proportion of discrepancies in feature point sets that the matching can tolerate.

Coherency term. The last energy term measures coherency in neighborhoods of matched regions. The coherency term favors the feature matching solution \mathbf{x} that preserves spatial proximity of matched features. Intuitively the term is interpreted as a proportion of neighboring features \mathbf{p} , \mathbf{q} with different matched/unmatched status.

More precisely, given neighboring features \mathbf{p} (involved in assignment x_a) and \mathbf{q} (involved in assignment x_b), the matching status $V_{\mathbf{p},\mathbf{q}}$ is computed as

$$V_{\mathbf{p},\mathbf{q}} = \begin{cases} 0, & x_a = 1 \wedge x_b = 1 \\ 0, & x_a = 0 \wedge x_b = 0 \\ 1, & \text{otherwise} \end{cases}$$

The matching term $V_{\mathbf{p},\mathbf{q}}$ is equal to zero when both features \mathbf{p}, \mathbf{q} are matched or unmatched and equal to one otherwise. Now, formally the consistency term is defined as a fraction of all neighboring features with different matched/unmatched status

$$E^{coh}(\mathbf{x}) = \frac{1}{|N_{\mathbf{p},\mathbf{q}}|} \sum_{(\mathbf{p},\mathbf{q}) \in \mathcal{N}} V_{\mathbf{p},\mathbf{q}}(\mathbf{x}),$$

where $N_{\mathbf{p},\mathbf{q}}$ is a set of neighbouring features $N_{\mathbf{p},\mathbf{q}} = \{(\mathbf{p}, \mathbf{q}) \in (P \times P) \cup (P' \times P') : \mathbf{p} \in N_s^k(\mathbf{q}) \vee \mathbf{q} \in N_s^k(\mathbf{p})\}$.

Uniqueness constraint. Similarly to matching of 2D image features of (Torresani, Kolmogorov et al. 2008, Torresani, Kolmogorov et al. 2013), we are interested in finding feature matching solution \mathbf{x} so that each of the features on the source has no more than one correspondence on the target and vice versa. Given a union of features $\bar{P} = P \cup P'$ and a set of assignments $A(\mathbf{p})$ involving \mathbf{p} , the constraint is formulated as:

$$\Lambda = \{\mathbf{x} \in \{0,1\}^A \mid \sum_{a \in A(\mathbf{p})} x_a \leq 1 \ \forall \mathbf{p} \in \bar{P}\}$$

5.5.2 Dual decomposition

In this section we briefly review the dual decomposition (DD) technique, which we adopted in spirit of (Torresani, Kolmogorov et al. 2008, Torresani, Kolmogorov et al. 2013) in order to solve the optimization problem Eq. (5-6) with the uniqueness constraint.

In discrete optimisation, duality refers to the relationship between a primal problem (P) and its dual (D). We want to solve the primal problem which is the minimization of the energy function $E(\mathbf{x})$ (Eq. (5-6)). However it is often much more efficient to solve heuristically the dual optimization problem. In contrast to the primal which is the minimization problem, the dual is formulated as a maximization problem. These problems are related in a way that the minimal value for (P) is always higher or equal to the maximal value for (D) (Figure 5-29). We denote as $\Phi(\theta)$ a dual function (i.e. a lower bound) of the primal function $E(\mathbf{x}|\theta)$:

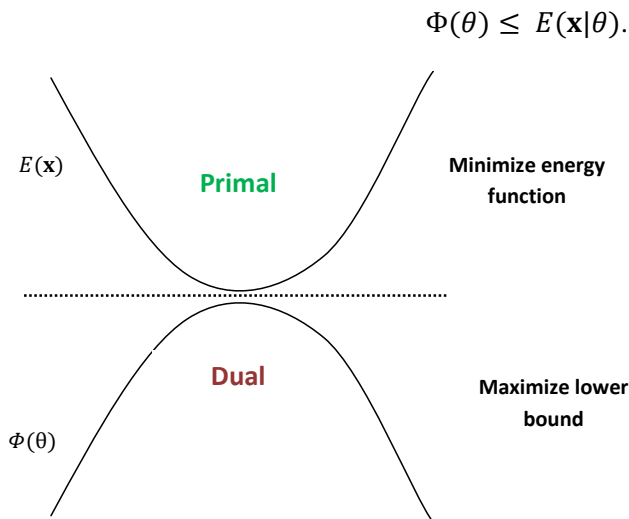


Figure 5-29. Relationship between the primal and dual optimization problems.

By choosing the dual approach we do not attempt to accurately minimize the energy function $E(\mathbf{x}|\theta)$ directly. Instead, the lower bound $\Phi(\theta)$ of the energy function is maximized. Based on resulting lower bound, a solution to the primal problem is extracted. We detail the lower bound $\Phi(\theta)$ later in this section.

The second core idea behind the technique is problem decomposition: given a difficult or large problem, we decompose it into several smaller, solvable subproblems and then extract a solution by cleverly combining the solutions from these subproblems (Chardaire and Sutter 1995, Komodakis, Paragios et al. 2007, Torresani, Kolmogorov et al. 2008). Although simple as a concept, decomposition is extremely general and powerful, and has been used extensively in the research literature for solving optimization problems. In the scope of this work we decompose the dual problem rather than primal, therefore the approach is referred as dual decomposition (Figure 5-30).

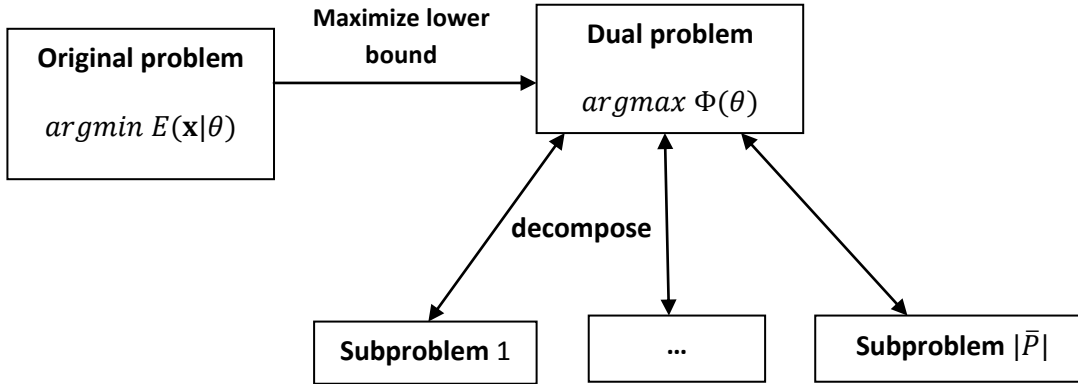


Figure 5-30. Problem decomposition of the dual optimization problem.

In order to solve the DD problem, the lower bound maximization is decomposed into a set of sufficiently small local subproblems, and then followed by the combination of the solutions from these subproblems. We decompose the lower bound maximization into $|\bar{P}|$ subproblems for each point $\mathbf{p} \in \bar{P} = P \cup P'$. Given a set of k nearest neighbours $N_{\mathbf{p}}$ for each point $\mathbf{p} \in \bar{P}$, consider a subproblem with a set of assignments $A(N_{\mathbf{p}}) = \{(\mathbf{q}, \mathbf{q}') \in A | \mathbf{q} \in N_{\mathbf{p}} \vee \mathbf{q}' \in N_{\mathbf{p}}\}$ (Figure 5-31). With respect to these assignments from the set $A(N_{\mathbf{p}})$, we set the values of the graph matching terms $\theta^{\mathbf{p}}$ for the local subproblem \mathbf{p} :

$$\theta_a^{\mathbf{p}} = 0 \text{ if } a \notin A(N_{\mathbf{p}}),$$

$$\theta_{ab}^{\mathbf{p}} = 0 \text{ if } a \notin A(N_{\mathbf{p}}) \text{ or } b \notin A(N_{\mathbf{p}}).$$

Intuitively, for the local subproblem of the point \mathbf{p} , we consider only assignments to its k nearest neighbourhood $N_{\mathbf{p}}$. Hence the afore-defined assignment set $A(N_{\mathbf{p}})$ and corresponding terms $\theta^{\mathbf{p}}$ define a local graph matching problem over the local neighbourhood $N_{\mathbf{p}}$.

As demonstrated in the work of (Torresani, Kolmogorov et al. 2008), the sum of the solutions to all local subproblems $\sum_{\zeta \in I} \min_{\mathbf{x}} E(\mathbf{x} | \theta^{\zeta})$ can serve as a lower bound optimization function $\Phi(\boldsymbol{\theta})$ (Figure 5-29) as defined:

$$\Phi(\boldsymbol{\theta}) = \sum_{\zeta \in I} \min_{\mathbf{x}} E(\mathbf{x} | \theta^{\zeta}) \leq \min_{\mathbf{x}} E(\mathbf{x} | \boldsymbol{\theta}),$$

where I is the set of subproblem indexes. The global minimum for each subproblem is computed by exhaustive search $\min_{\mathbf{x}} E(\mathbf{x} | \theta^{\mathbf{p}})$ (Torresani, Kolmogorov et al., 2008). The solution search is repeated for all local subproblems defined by full set of points $\mathbf{p} \in \bar{P}$.

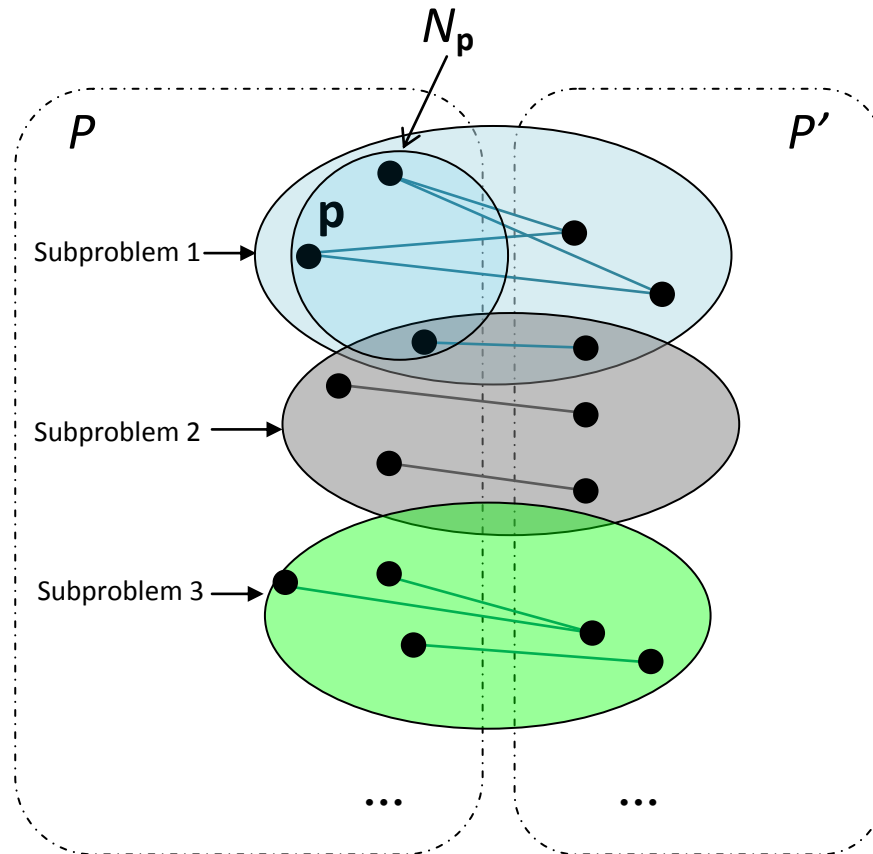


Figure 5-31. Local subproblem decomposition. For each point p , local subproblem involves only assignments within the local neighbourhood N_p .

Then, given the solutions for all local subproblems, the lower bound $\Phi(\theta) = \sum_{\zeta \in I} \min_{\mathbf{x}} E(\mathbf{x} | \theta^\zeta)$ is **maximized** via classical optimization subgradient method as presented in (Shor 1985, Chardaire and Sutter 1995, Bertsekas 1999, Komodakis, Paragios et al. 2007, Schlesinger and Giginyak 2007, Torresani, Kolmogorov et al. 2008). The subgradient maximization of Φ recomputes subproblem solutions on each iteration until the value of lower bound change between the next and previous iterations is less than a user threshold (Torresani, Kolmogorov et al. 2008). Finally in order to obtain solution \mathbf{x} we follow the technique of (Torresani, Kolmogorov et al. 2008) so that at each iteration the solution is obtained in the way detailed in Algorithm 5-2.

Algorithm 5-2. Combining solutions of local subproblems into a global solution
Input: solutions $x^\zeta, \zeta \in I$ of all local subproblems
Output: output matching global solution \mathbf{x}
begin
$\mathbf{x}=0$
foreach subproblem $\zeta \in I$
foreach assignment x_a^ζ
if $x_a^\zeta = 1$ // if assignment is active in a subproblem
$x_a = 1$ // then activate it the global solution
end
end
end
end

The solution with the smallest energy is kept on each iteration which yields final output result when the maximization of the lower bound converges.

5.5.3 Improving geodesic distortion term

In this section we further ameliorate the positive influence of geodesic distortion term on the feature matching accuracy. What we intend to do is to strongly penalize the matching of a pair of features that belong to one semantic part of the source mesh to a pair of features that belong to the different semantic parts of the target mesh (and vice versa). In order to differentiate distinct body parts we propose to observe how the average geodesic distances to all other vertices change along geodesic paths between feature points.

Definition 9. $|\Gamma_{\mathbf{p}_1}^M| = \frac{1}{N} \sum_{\mathbf{p} \in M} |\Gamma_{\mathbf{p}_1, \mathbf{p}}^M|$ is an average geodesic distance from vertex \mathbf{p}_1 to all other vertices of the mesh M , where N is the total number of vertices in M .

Our idea is based on an observation that the values of average geodesic distances to all others vertices reach global minimum in near the center of an object and reach global maximum near the “tips”(Figure 5-32).

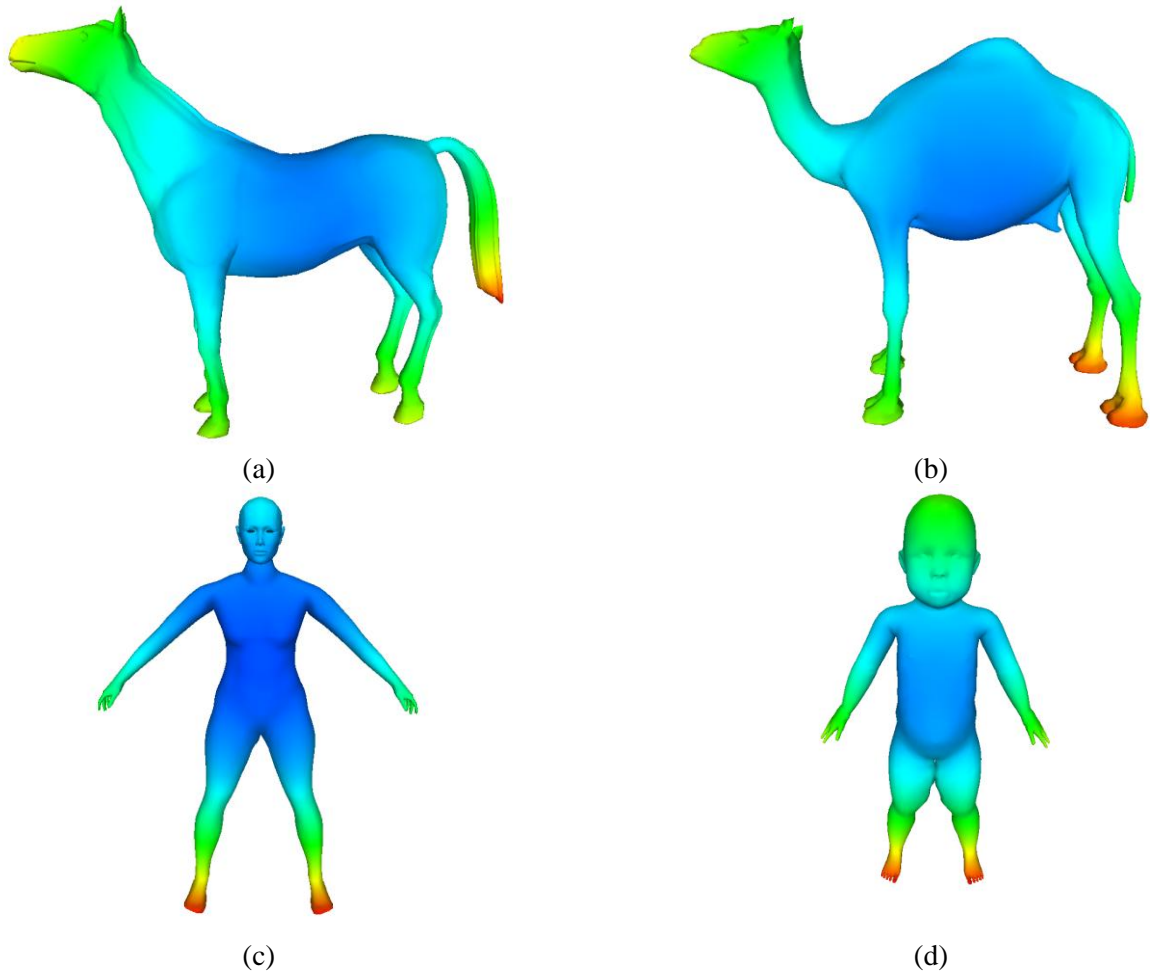


Figure 5-32. Average geodesic distance map. Horse (a), camel (b), woman (c), baby (d). Red color depicts high values and blue color low values of $|\Gamma_{\mathbf{p}}^M|$ correspondingly.

Definition 10. Given Dijkstra’s shortest path $\Gamma_{\mathbf{p}_1, \mathbf{p}_2}^M$ (Definition 7), we designate an average geodesic distance curve γ along $\Gamma_{\mathbf{p}_1, \mathbf{p}_2}^M$ between given vertices \mathbf{p}_1 and \mathbf{p}_2 such that $\forall \mathbf{v} \in \Gamma_{\mathbf{p}_1, \mathbf{p}_2}^M : \gamma(\mathbf{v}) = |\Gamma_{\mathbf{v}}^M|$.

Intuitively Definition 10 can be interpreted as follows. In each point $\mathbf{v} \in \Gamma_{\mathbf{p}_1, \mathbf{p}_2}^M$ we encounter along the path $\Gamma_{\mathbf{p}_1, \mathbf{p}_2}^M$ from \mathbf{p}_1 to \mathbf{p}_2 , we sample the average geodesic distance $\gamma(\mathbf{v})$ from \mathbf{v} to the rest vertices of the mesh.

Given two feature points of the animated mesh, we see that function γ is monotonous if \mathbf{p}_1 and \mathbf{p}_2 belong to the same semantic part of the object (i.e. \mathbf{p}_1 and \mathbf{p}_2 are located within the same limb of horse or camel). Function γ could be monotonously increasing, decreasing or non-monotonous depending on the choice of features \mathbf{p}_1 and \mathbf{p}_2 . In particular, function γ has a very important property of being non-monotonous with one global minima if features \mathbf{p}_1 and \mathbf{p}_2 belong to semantically different body parts. Indeed, the path $\Gamma_{\mathbf{p}_1, \mathbf{p}_2}^M$ for $\mathbf{p}_1, \mathbf{p}_2$ from distinct body parts always passes through the neighborhood of the mesh geodesic center (Pollack, Sharir et al. 1989) where γ reaches its minimum, as also reported by (Moenning 2005, Noyel, Angulo et al. 2011).

We used the property of monotonous/non-monotonous behaviour of function γ to improve significantly geodesic distortion term computation as detailed in **Algorithm 5-3**. An illustration of the influence of the described geodesic distortion term improvement technique that aids to effectively penalize obviously inconsistent assignment pairs (Figure 5-34).

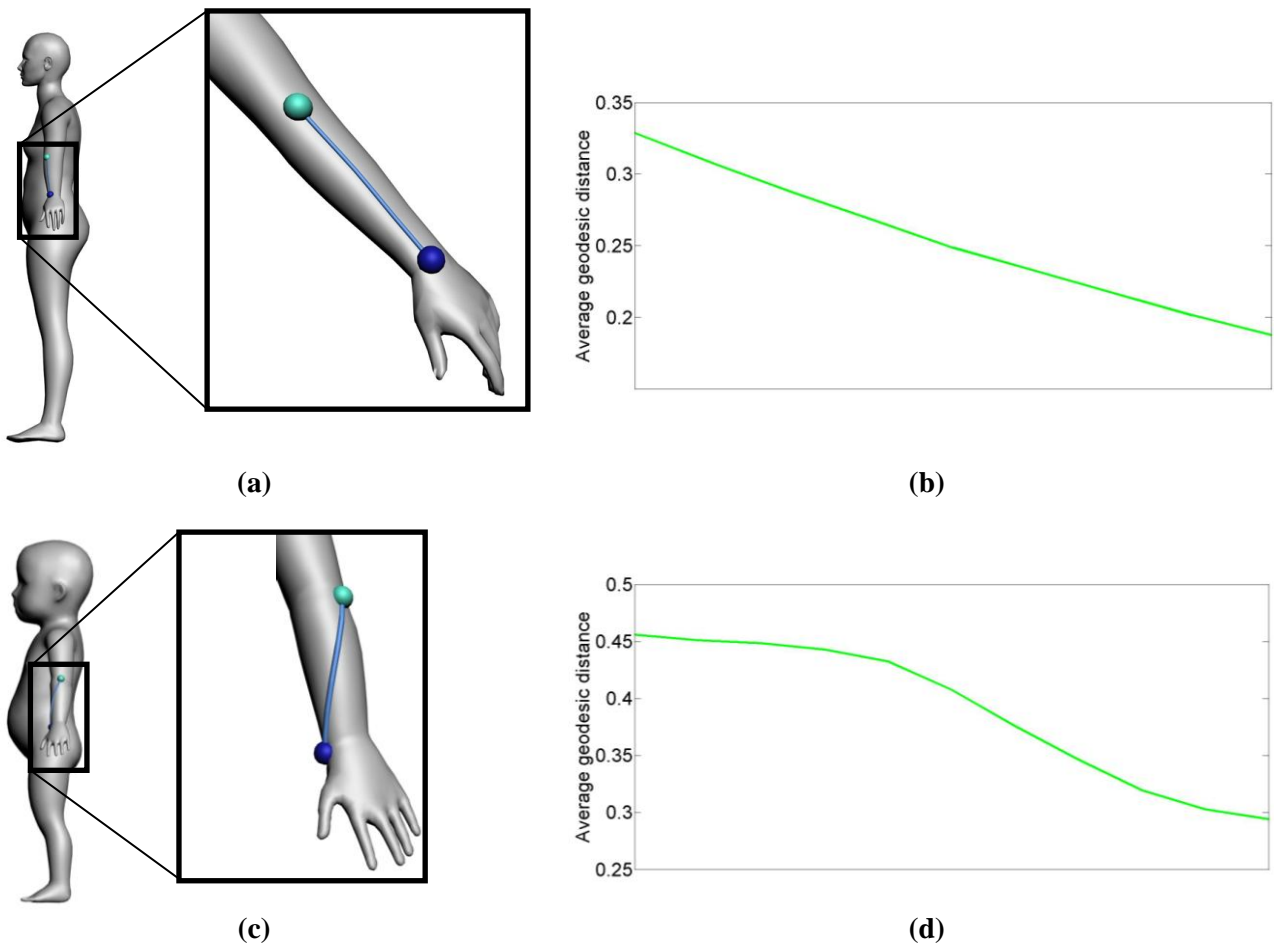


Figure 5-33. Geodesic paths (a), (c) on the woman and baby models and the corresponding change of average geodesic distance along the paths from the wrist to the elbow (b), (d).

Algorithm 5-3. Improved geodesic distortion term computation.

Input: Pair of assignments $a=(p_1, p_2)$, $b=(q_1, q_2)$, and corresponding geodesic curves $\gamma(\Gamma_{p_1, p_2}^M)$, $\gamma(\Gamma_{q_1, q_2}^M)$

Output: Improved geodesic distortion term θ_{ab}^{geod}

// \nearrow monotonously increasing function; \searrow - monotonously decreasing function

begin

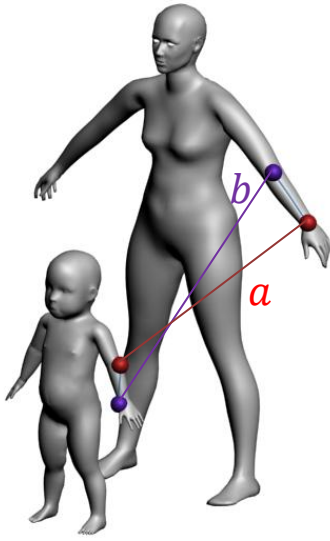
if ($\nearrow \gamma(\Gamma_{p_1, p_2}^M)$) **and** ($\nearrow \gamma(\Gamma_{q_1, q_2}^M)$) **or** ($\searrow \gamma(\Gamma_{p_1, p_2}^M)$) **and** ($\searrow \gamma(\Gamma_{q_1, q_2}^M)$)

$\theta_{ab}^{geod} \leftarrow \text{abs}(|\Gamma_{p_1, p_2}^M| - |\Gamma_{q_1, q_2}^M|)$

else

$\theta_{ab}^{geod} \leftarrow (+\infty)$

end



Geodesic distortion **before** the improvement:

$$\theta_{ab}^{geod} = 3.31$$

(assignments a and b are **compatible**)

Geodesic distortion **after** the improvement:

$$\theta_{ab}^{geod} = +\infty$$

(assignments a and b are **not compatible**)

Figure 5-34. Edge weights before and after introducing the average geodesic distance prior.

5.5.4 Experiments

In this section we present the results of feature correspondence using graph matching detailed previously in this chapter. We used bending cylinders, galloping horse/camel, walking woman/baby animations for the feature matching tests. In all of our experiments the graph matching algorithm produce a correct feature matching solution in less than few seconds. Table 5-2 indicates more detailed information on performance of feature graph matching. Experiments were performed on a workstation with 16GB of memory and Intel Core i7-2600 processor running at 3.40 GHz. The feature matching results are depicted in (Figure 5-35, Figure 5-36, Figure 5-37).

Data	#features on the source	#features on the target	#unmatched on the source	#unmatched on the target	# mismatch	Time
Cylinders	6	5	1	0	0	0.14s
Horse/Camel	19	24	0	5	0	0.79s
Woman/Baby	23	30	8	15	0	1.89s

Table 5-2. Feature matching results in bending cylinders, galloping horse/camel, walking woman/baby animations.

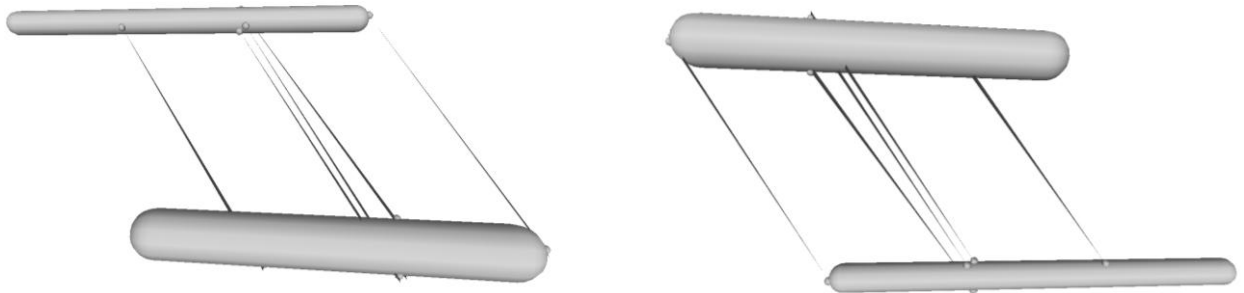


Figure 5-35. Matching result between feature of the cylinders animated meshes.

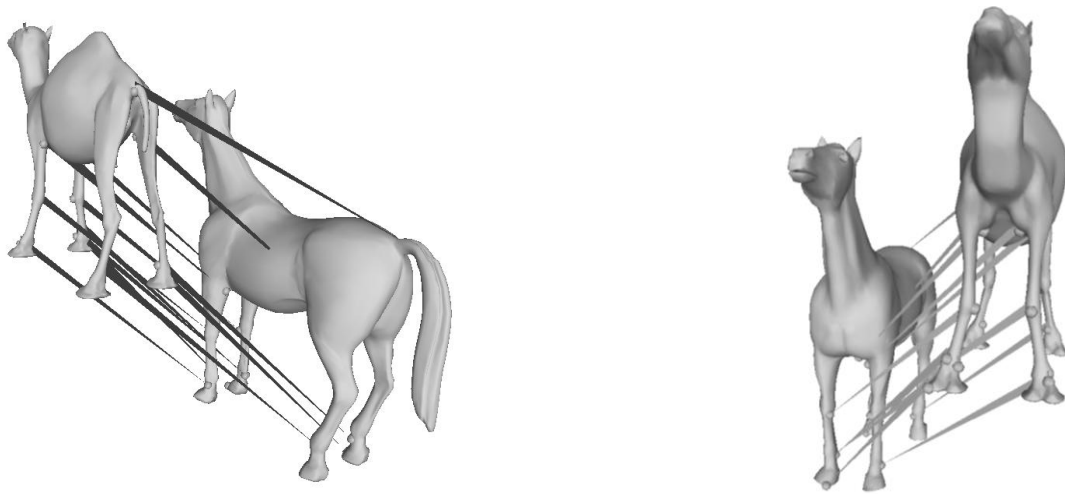


Figure 5-36. Feature matching result between the horse and camel.

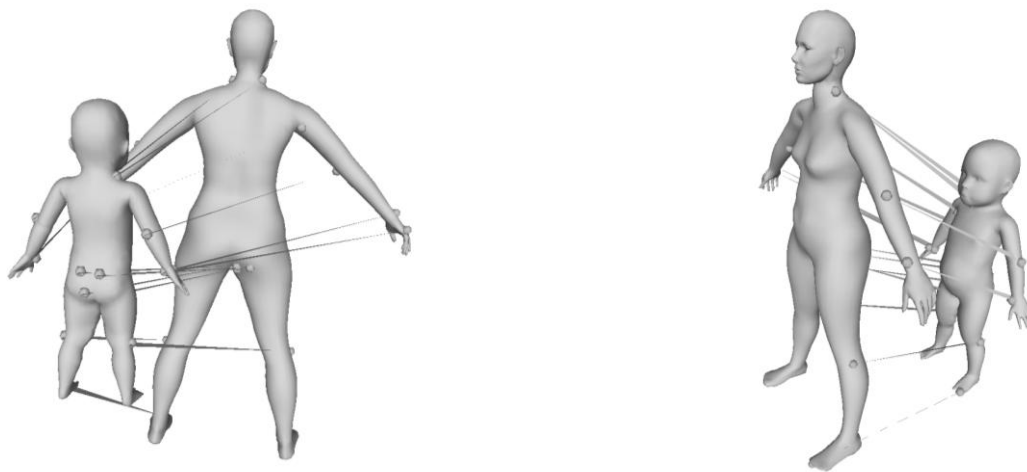


Figure 5-37. Matching of the features between the walking woman and baby animations.

5.6 Full matching

5.6.1 Spherical embedding

Once we have computed the matching among feature vertices, we propagate the computed correspondence to all points on the source mesh, which is the objective of the fine matching. The goal is to compute the one-to-one correspondence (i.e. bijective mapping) between every point⁷ of the source mesh and that of the target mesh with the feature constraint, i.e. the previously computed matching among the feature vertices is kept.

Methods combining the feature error, distortion (smoothness) error, and the data error could be adopted here (Allen, Curless et al. 2003) (see Section 3.1). Due to the high dimensionality of the solution space (number of vertices or sampled points multiplied by the degree of freedom, typically three), however, it is often unpractical to search for the solution in such settings. In particular, measuring the data error term requires considerable computation time, even with a data structure devoted to an efficient computation of the distance between the two surfaces.

In this thesis, we propose to compute the bijective mapping in the spherical parameterization, the parameterization of a genus-zero surface onto a spherical domain. Formally, the spherical parameterization ϕ of the mesh M is defined as:

$$\phi: M \rightarrow S^2, \text{ where } S^2 = \{x \in \mathbb{R}^3: \|x\| = 1\}.$$

Every point of the spherically parameterized mesh is located on the surface of a unit sphere centered at the origin. With the meshes embedded in the unit sphere, the problem of surface matching in the 3D space is simplified to that of matching in the 2D spherical domain. This not only reduces the dimensionality of the problem but also removes the need for the heavy computation of the data error term. In addition, there exist several methods (Saba, Yavneh et al. 2005, Praun and Hoppe 2003) to compute this parameterization efficiently.

Let M_{SRC} and M_{TRG} be the source and target meshes respectively; S_{SRC} and S_{TRG} are their spherical parameterization respectively. Also let $f_{M_{SRC} \rightarrow S_{SRC}}$ be the bijective mapping of M_{SRC} to S_{SRC} and $f_{M_{TRG} \rightarrow S_{TRG}}$ the bijective mapping of M_{TRG} to S_{TRG} . Then a bijective mapping between the source and the target meshes can be obtained by computing:

$$f_{M_{SRC} \rightarrow M_{TRG}} = f_{M_{SRC} \rightarrow S_{TRG}}^{-1} \circ f_{S_{SRC} \rightarrow S_{TRG}} \circ f_{M_{SRC} \rightarrow S_{SRC}} \quad (\text{see Figure 5-38})$$

The bijectivity of the composite function is guaranteed if each of the three functions involved is bijective. The mappings $f_{M_{SRC} \rightarrow S_{SRC}}$ and $f_{M_{TRG} \rightarrow S_{TRG}}$ we obtain from the spherical parameterization, which are both bijective. Thus we concentrate on the problem of finding $f_{S_{SRC} \rightarrow S_{TRG}}$ that is bijective while satisfying the aforementioned feature constraints.

⁷ Here, we distinguish an arbitrarily sampled *point* on the mesh surface from a *vertex* (point comprising the mesh).

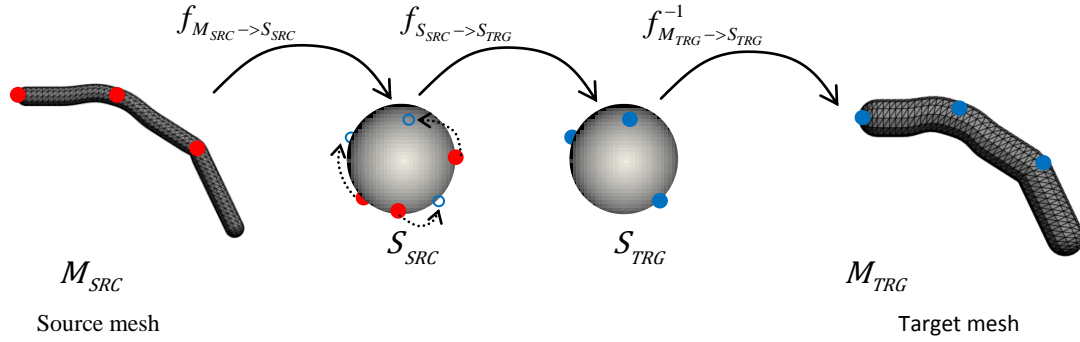


Figure 5-38. The bijective mapping between the source and target meshes using spherical parameterization. The source and target feature points are colored in red and blue respectively. For the sake of illustrational simplicity, only three feature points are shown on the meshes.

To this end, we develop a bijective warping method in the spherical domain. It takes as input the spherical mesh S_{SRC} and moves its vertices on the surface of the unit sphere such that the result mesh on the sphere is fold-over free, and its feature vertices are aligned with their corresponding counterparts of S_{TRG} . Similar in spirit to the work of (Seo and Cordier 2010), we compute this warping function as a sequence of warpings based on radial basis function; each warping step incrementally moves the source feature vertices to their counterpart on the target mesh S_{TRG} . We refer to the paper of Seo and Cordier (Seo and Cordier 2010) for the proof of the bijectivity and $C1$ -continuity properties of this approach.

Let $\{s_1, \dots, s_i, \dots, s_n\}$ and $\{t_1, \dots, t_i, \dots, t_n\}$ be the n feature points of S_{SRC} and S_{TRG} respectively. Since the mesh vertices are defined in the spherical domain, each of these point has two coordinates (θ, φ) which are the azimuth and elevation, respectively. After finding a good initial orientation of S_{SRC} that aligns its feature points to their counterparts in S_{TRG} as closely as possible (detailed description is given below), we compute the smooth warping of S_{SRC} that displaces s_i to their target positions t_i . However, computing the warping in a single step does not guarantee the bijectivity, in general. Our approach to the problem is to decompose the warping into m smaller ones; At each iterative warping step, a source feature point is moved toward its target along the shortest path between the two locations on the unit sphere (Figure 5-39). Given a feature point that we want to move from s_i to its target location t_i , with the warping, we first compute its $m-1$ intermediate positions $\{s_{i,1}, \dots, s_{i,j}, \dots, s_{i,m-1}\}$ by uniformly spacing along the shortest path between s_i and t_i . Then, we compute the warping by the *radial basis function* (as detailed below) that moves the feature points from their source positions $\{s_1, \dots, s_i, \dots, s_n\}$ to their first intermediate target positions $\{s_{1,1}, \dots, s_{i,1}, \dots, s_{n,1}\}$, then from $\{s_{1,1}, \dots, s_{i,1}, \dots, s_{n,1}\}$ to $\{s_{1,2}, \dots, s_{i,2}, \dots, s_{n,2}\}$, and so on (Figure 5-40). This process is repeated until the feature points reach their target positions $\{t_1, \dots, t_i, \dots, t_n\}$. Note that in order to guarantee the bijectivity, we require that $s_{i,j} \neq s_{k,j}$ ($i \neq k$) at all times.

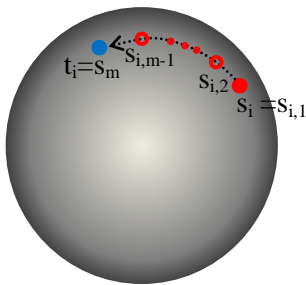


Figure 5-39. A feature point pair s_i and t_i in the spherical parameterization drive the iterative warping steps, by generating a series of intermediate positions $s_{i,2}, \dots, s_{i,m-1}$ along the geodesic path that connects them.

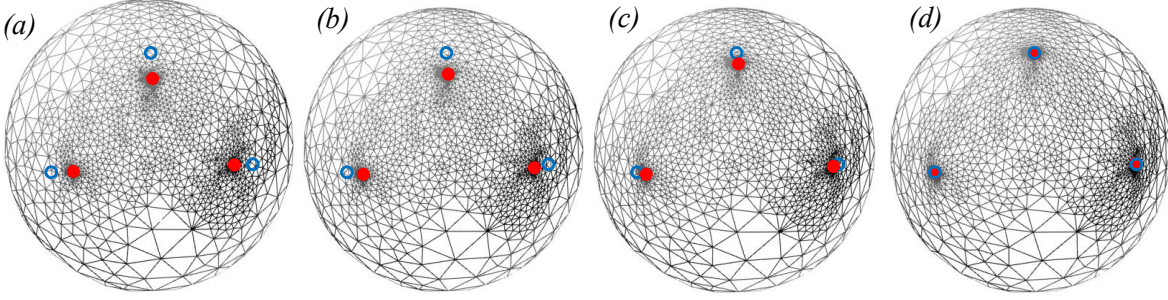


Figure 5-40. Warping of the mesh vertices to move the source feature points (shown in blue) to their target position (shown in red). Figures (a) and (b) are the spherical mesh before and after the warping respectively. Figures (b) and (c) are the intermediate steps of the warping.

5.6.2 Iterative warping

Initial alignment. Let S and T be matrices composed of 2×1 column vectors $\{s_1, \dots, s_i, \dots, s_n\}$ and $\{t_1, \dots, t_i, \dots, t_n\}$, respectively, i.e. $S = \begin{pmatrix} | & & | \\ s_1 & \cdots & s_n \\ | & & | \end{pmatrix}$ and $T = \begin{pmatrix} | & & | \\ t_1 & \cdots & t_n \\ | & & | \end{pmatrix}$. We wish to find a rigid transformation that optimally aligns the two vector sets in the least squares sense, i.e. we seek a rotation X such that

$$R = \underset{X}{\operatorname{argmin}} \|T - XS\|_F \text{ subject to } X \cdot X^T = I,$$

where $\|\cdot\|_F$ denotes the Frobenius norm. This problem is also known as orthogonal procrustes problem (Gower and Dijksterhuis 2004), for which a number of analytic solutions exist (Schönemann 1966, Zhang 2000, Sorkine 2009). Here we find R by using the singular value decomposition (SVD) of $M = S^T \cdot T$:

$$M = U \Sigma V^*,$$

where Σ is the scale matrix and $R = UV^*$ the rotation matrix, respectively.

Step size (Number of intermediate target positions). The smaller is the step size, the chance to have foldover becomes also smaller, but at the cost of heavier computation with the increased number of per-step RBF computation and evaluation. Thus, taking the largest step size that doesn't cause overlap in the warping would be ideal. In this thesis work, we start with 3 equally spaced intermediate target positions and subdivide the inter-target space by 2 if an overlap occurs during the warping. In theory, we repeat this subdivision until no overlap is found, but in practice, the initial spacing was sufficient in most cases. A good estimation of adaptive step size remains as future work.

Radial basis function. At each step of the iterative warping, we compute RBF functions by using the given source positions $\{s_{1,j}, \dots, s_{i,j}, \dots, s_{n,j}\}$ and the target positions $\{s_{1,j+1}, \dots, s_{i,j+1}, \dots, s_{n,j+1}\}$ of the feature points on the spherical mesh. When applied to s_i , the RBF functions Φ will compute its desirable displacement $s_{i,j+1} - s_{i,j}$, and every other vertex x , its appropriate displacement $\Phi(x)$. The displacement functions along the azimuth $\Phi_\theta: \mathbb{R}^2 \rightarrow \mathbb{R}$ and the elevation $\Phi_\varphi: \mathbb{R}^2 \rightarrow \mathbb{R}$ are defined as:

$$\Phi_\theta(x) = \sum_{i=1}^n a_{\theta,i} \cdot \rho(\|x - s_{i,j}\|),$$

$$\Phi_\varphi(x) = \sum_{i=1}^n a_{\varphi,i} \cdot \rho(\|x - s_{i,j}\|).$$

$s_{i,j}$ with $i=\{1,\dots,n\}$ are the centers of the radial basis functions. The value $\|x - s_{i,j}\|$ is the geodesic distance between the point x and the center $s_{i,j}$, that is, the shortest distance between the two points on the surface of the unit sphere. The coefficients $a_{\theta,i}$ and $a_{\varphi,i}$ are respectively computed by solving the following linear systems

$$\Phi_{\theta}(s_{i,j}) = \theta_{i,j} = \theta(s_{i,j+1} - s_{i,j})$$

and

$$\Phi_{\varphi}(s_{i,j}) = \varphi_{i,j} = \varphi(s_{i,j+1} - s_{i,j}).$$

$\theta_{i,j}$ and $\varphi_{i,j}$ are the displacements of the i^{th} feature point at step j along the azimuth and elevation, respectively. $\rho(r)$ with $r = \|x - s_{i,j}\|$ is the radial function; we use the thin plate spline: $\rho(r) = r^2 \ln(r)$.

The results of fine matching of two bending cylinders, galloping horse and camel, walking woman and baby are demonstrated in Figure 5-41. On average it takes less than 5 minutes to compute the spherical parameterization for each model and 2 minutes to establish the fine matching. The number of iterations for the horse/camel, woman/baby and the cylinders is about 10^5 and 10^4 correspondingly. The matching experiments were performed on Intel Core i7 (2.7GHz), 8Gb RAM workstation.

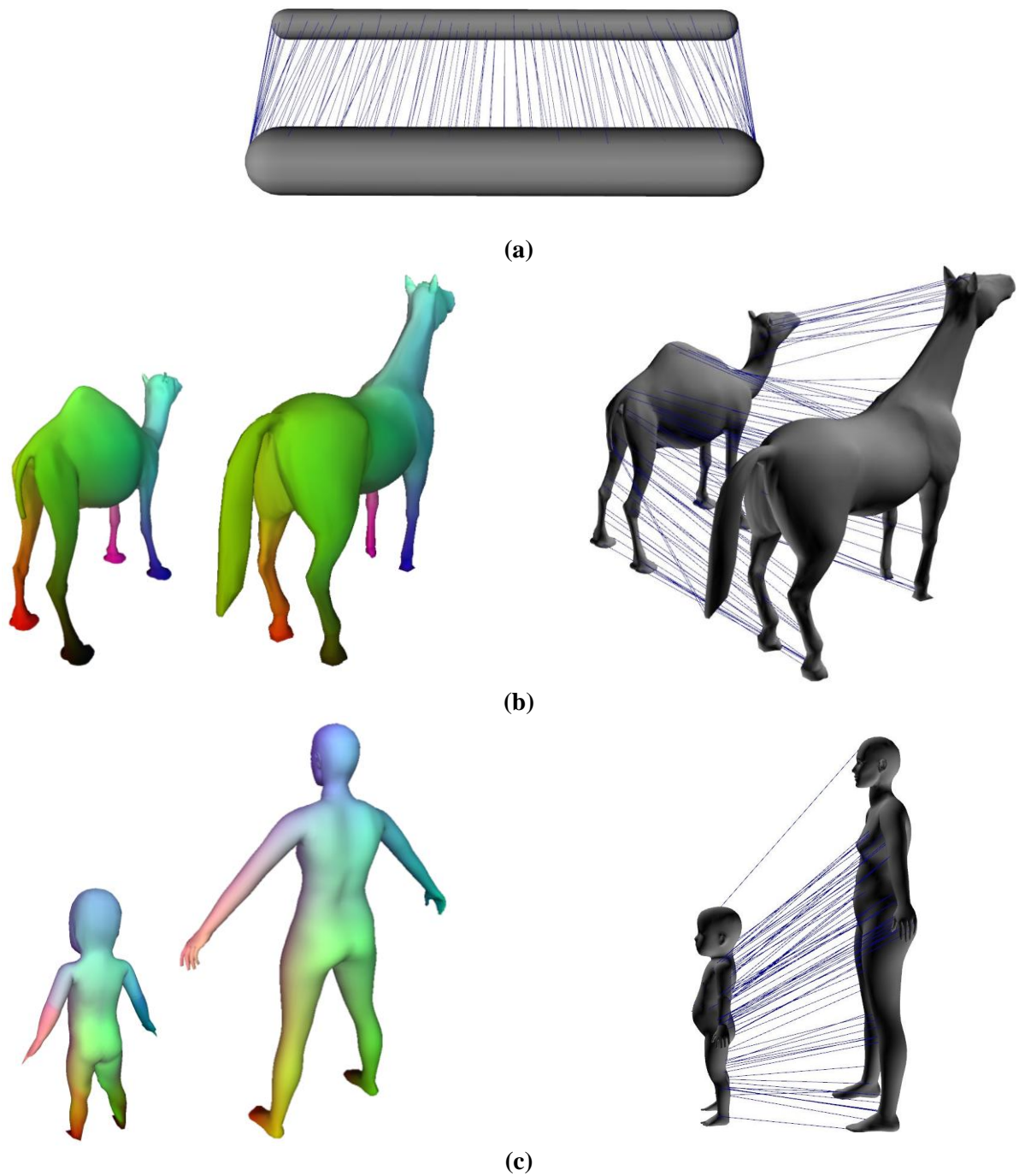


Figure 5-41. Fine matching between bending cylinders (a), galloping horse/camel (b) and walking woman/baby (c) animations. Subsets of matching pairs of vertices are depicted by lines. The dense correspondence is depicted in color such that the matching points on the source and target meshes share the same color

5.7 Conclusion

In this chapter we presented a complete framework for shape analysis and correspondence for animated meshes. The key insight we take advantage of in our work is that similarly deforming subjects carry a great amount of shape dynamics information that can be efficiently used for dynamic feature point description, similarity measure and correspondence computation of animated meshes.

Our method brings several valuable contributions. Differently from the existing works on shape analysis in computer graphics, we investigated a novel technique for a feature point signature on time-varying geometry represented in a form of animated meshes (Section 5.3). The introduced pioneer concept of dynamic feature point signature exploits all available movement and deformation available in the animated mesh. The new feature point signature is designed to capture unique dynamics and local deformation patterns of a point of the animated mesh. We use these dynamic point signatures for a robust graph-based dynamic feature point matching which estimates a coarse correspondence between animated meshes (Section 5.3). Finally we establish the fine-scale matching between animated mesh models guided by the dynamic feature points correspondences in spherical embedding (Section 4.6). We have demonstrated good and precise results of feature point matching based on the new dynamic point signature. Fine matching in spherical parameterization guided by feature correspondences has also shown promising results for similarly moving animated meshes.

Our deforming shape analysis algorithms assume semantical similarities between the source and target animated meshes with a fixed inter-frame mesh connectivity. In order to lessen the restriction on input animated meshes we will propose a new robust and fast matching approach in Chapter 5 which can be used for establishing inter-frame correspondence in animated meshes with a time-varying mesh structure.

Chapter 6 Case of animated meshes with changing mesh connectivity

6.1 Introduction

As established in Chapter 4 and Chapter 5, our frameworks of dynamic feature detection/description and feature-based shape correspondence are designed for the domain of animated meshes. By definition, an animated mesh is an ordered sequence of meshes with a fixed mesh connectivity and a priori known inter-frame vertex correspondences (Section 4.3). However, this is a relatively strong assumption which does not necessary hold for colossal diversities of dynamic geometry available, especially originated from real animation data acquisition.

In this chapter we address the problem of how to deal with deforming meshes with a changing mesh connectivity over time (Figure 6-1). We propose a fast and robust technique which can be potentially used to establish inter-frame correspondences in a time-varying deforming mesh, which allows it to be applicable to shape analysis (Chapter 4) and matching algorithms presented in Chapter 5.

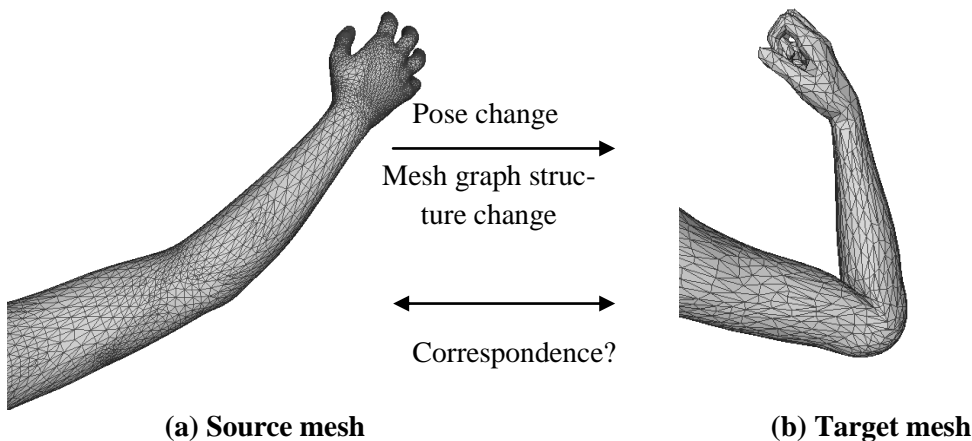


Figure 6-1. Mesh connectivity (mesh graph structure) is dissimilar in different postures (a, b) of the same subject. We relax a constraint on a fixed mesh connectivity in an animated mesh (Section 4.3) by introducing a method which can establish reliable vertex correspondences across the pose changes of the subject.

Our prime observation is that some geometric features are often persistent across pose changes and movements of subjects. Those persistent features allow us to define a geodesic coordinate system to locate any given point on a source and its correspondence on a target mesh. We develop our method for uniquely describing any given vertex on the shape, which is not necessarily geometrically significant. One of the main advantages of our method in comparison to existing shape matching algorithms is its fast computation time. This is possible because our method is optimally designed for using the minimum information for identifying point locations. We call our technique *landmark transfer with minimal graph* (LTMG). The method was initially developed both for

fast fine matching and coarse matching of “landmarks⁸”. Note that our non-rigid correspondence method is general and not limited to the inter-frame deforming mesh matching. The method can be successfully used in various non-rigid shape correspondence cases with moderate isometry constraints. In this chapter we demonstrate robust performance of our method for common non-rigid shape correspondence.

6.2 Outline of the method

Assumptions. Like many existing non-rigid correspondence methods, we expect that the meshes to be matched are approximately isometric. Isometry preservation is often the case in many real world shape deformations and movements such as motions of humans, animals and clothes.

We set the goal for any given landmark (arbitrary vertex) on the source mesh to find its meaningful correspondence on the target mesh. The different steps of our algorithm are illustrated in Figure.6-2. First, we build a graph G_F on the source mesh M_S , whose nodes are the set of automatically selected geometric feature points and the edges are composed of geodesic paths between the nodes Figure.6-2(a). Then, given a landmark, we build what we call the minimal graph G_M , a subgraph of G_F Figure.6-2(b). The graph G_M has three main properties: (1) it uniquely defines the landmark position, (2) it is as small as possible in terms of number of nodes and geodesic distances, (3) it is a unique subgraph of G_F , i.e. there is no other subgraph in G_F that matches with G_M .

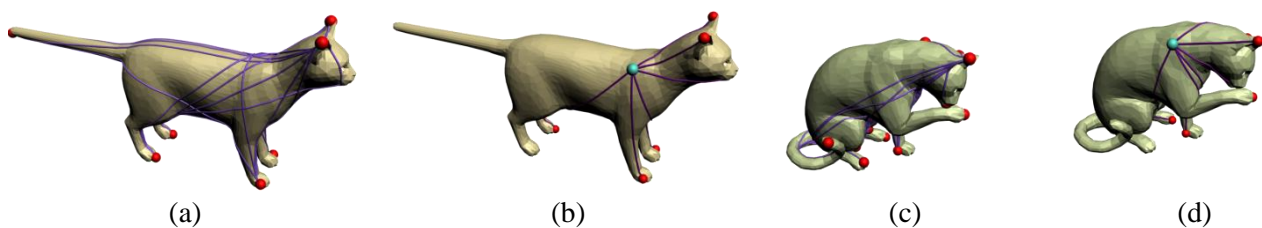


Figure.6-2. Overview of our approach. Extracted geometric feature points are marked with red spheres, and the landmarks as blue ones. (a) Geometric feature points are extracted on the source mesh, from which full graph G_F is computed (see Section 6.3.3). (b) Provided a landmark on the source mesh, minimal graph G_M for the landmark is constructed (see Section 6.3.4). (c) Similarly to the source mesh, geometric feature points are extracted, and the full graph \hat{G}_F is computed on the target. (d) A corresponding point is computed on the target mesh using \hat{G}_M , a partial matching of G_M on \hat{G}_F (Sections 6.4.2, 6.4.3).

Next, given a target mesh M_T , we select a set of points with the local shape signatures similar to the points from graph G_M . From these feature points we compute the graph \hat{G}_F by connecting the points which are within the maximum geodesic radius of G_M Figure.6-2(c). Then we use the approximate graph matching technique to find \hat{G}_M , a subgraph of \hat{G}_F , that best matches with G_M .

Finally, now that we have G_M matched with \hat{G}_F on the target mesh, we can find the corresponding landmark location on the target mesh by using \hat{G}_M Figure.6-2(d). This task would be made easier if the source and target meshes are perfectly isometric, since we can simply use the geodesic distances from each of the geometric feature points to be able to uniquely identify the landmark location. Unfortunately, the meshes are only approximately isometric and such a method may fail to estimate the landmark location reliably, especially when the deformation between the two meshes is large. We solve this problem by interpolating the updated geodesic distances on the target mesh in order to compensate changes in those that were induced due to non/roughly isometric deformation.

⁸In Chapter 6 we use a specific notion of landmark, which is essentially any point/vertex from a source to be matched on a target shape.

6.3 Graph construction on the source mesh

6.3.1 Geodesic distance computation

Since our method relies heavily on the geodesic distance, its accurate computation is crucial. Later in this work, geodesic distances are used to compute isocurves of the local descriptors on the surface (Section 6.3.2), as well as to compute geodesic paths between geometric feature points (Section 6.3.3). Throughout this work, we adopt the MMP method of exact geodesic computation proposed by (Mitchell, Mount, et al. 1987). The algorithm itself is very similar to Dijkstra’s approximation on the graph formed by vertices and edges of the mesh. This means that the surface of the mesh is regarded as locally planar on each face. As in Dijkstra’s algorithm we start from a source vertex v_S and compute the geodesic distance map in a region growing manner. Each edge in the graph representation of the mesh is subdivided into a set of segments by artificially adding vertices on the edge; on each Dijkstra’s step, when updating the geodesic map, a geodesic path is allowed to pass through these artificial vertices. When there is no edge partitioning, we get standard Dijkstra’s algorithm; the more partitioning vertices go through, the more precise is the geodesics computation. In the worst case the algorithm has time complexity $O(\log(N) N^2)$. Note that the partial computation is possible: we can stop computation when the path reaches certain distance or covers certain points on the surface of the mesh. This is an important point to reduce the computation time.

6.3.2 Feature point extraction

We use a local static shape descriptor to identify the geometric features. Assuming approximate isometry between the source and target shapes, we are interested in a descriptor invariant to isometry and insensitive to the mesh discretization as much as possible. We employ the intrinsic wave descriptor proposed by (Tevs, Berner et al. 2011) and further refine it so that it is more robust to changes in mesh sampling.

For each vertex x we compute a set of intrinsic geodesic isocurves of increasing the geodesic distance r_i from x with a fixed step Δr , by using the algorithm described in section 6.3.1. The length l_i of each curve is then normalized by $2\pi r_i$, the length of the geodesic isocurve on a flat surface. We sampled 16 isocurves as in (Tevs, Berner et al. 2011), resulting in the descriptor of a form $\mathbf{D}_x = (\frac{l_1}{2\pi r_1}, \frac{l_2}{2\pi r_2}, \dots, \frac{l_{16}}{2\pi r_{16}})^T$. We approximate l_i as a perimeter P_i of a polygon whose edges connect intersection points of the real isocurve with triangle edges on the mesh. Next we take the inverse of the Euclidean norm of \mathbf{D}_x in order to measure the geometric prominence (convexity/concavity) of vertex x :

$$\gamma(x) = \|\mathbf{D}_x\|_2^{-1}. \tag{6-1}$$

Convexity $\gamma(x)$ increases with growing "sharpness" of the shape in the neighborhood of x . Eventually γ comes up to infinitely large values for a vertex on the tip of an infinitely sharp, needle-like shape.

Having computed the convexity all over the whole of the mesh (Figure. 6-3(a)), we sort its values $\gamma(x)$ in a descending order and retain only the first $\alpha \cdot n$ vertices with the highest values of γ , with n being the number of vertices in the mesh. This gives us a set X_γ of most prominent vertices with respect to convexity. We normally set a user-defined parameter α with a value of 0.3. As can be seen from Figure. 6-3(b), the vertices from X_γ group around ‘tips’ of the mesh; we denote the number of these clusters as n_F .

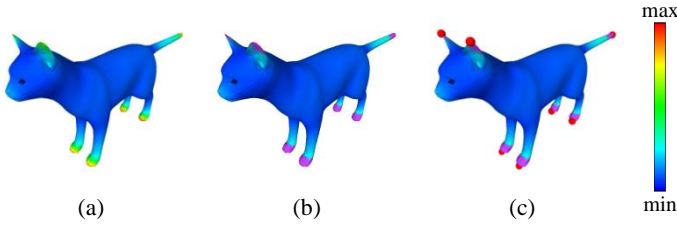


Figure. 6-3. Color-coded images of the convexity and geometric feature points on the mesh. (a) Visualization of the convexity field $\gamma(x)$ over the vertices of the mesh. (b) Set X_γ of vertices with highest convexity is shown in purple. (c) Extracted feature points, which are the ‘central’ points of the regions of high convexity, are depicted as red dots.

From these most prominent vertices X_γ on the mesh, we extract a set of feature points $V_F = \{f_i\}, i = 1..n_F$ in the following way. First, we assign vertices from X_γ to a set of clusters $L = \{L_i\}, i = 1..n_F$ according to their local shape descriptor similarity and geometrical proximity. We chose the most prominent vertex $\tilde{x} \in X_\gamma$ and add it to an initial cluster $L_0 = \{\tilde{x}\}$. Then, we grow L_0 around \tilde{x} according to the connectivity of vertices in L_0 ; the growing of the cluster stops when no more vertex x is encountered that is adjacent to L_0 and satisfies $|\gamma(\tilde{x}) - \gamma(x)| < \gamma'$, where γ' is a user-defined threshold. We repeat this process among those vertices that have not yet been labeled to construct subsequent clusters L_i until all vertices in X_γ have been assigned to a cluster. Second, in each of the clusters L_i we identify a vertex $f_i \in L_i$ whose average geodesic distance to all the other vertices in its cluster is maximal, in preference to center points of the cluster. The extracted set $\{f_i\}, i = 1..n_F$ represent the ‘tips’ of the mesh (Figure. 6-3(c)).

6.3.3 Construction of the full graph on the source mesh

Given the feature points $V_F = \{f_i\}, i = 1..n_F$ we proceed with the construction of the full graph $G_F = (V_F, E_F)$. Each f_i is connected by an edge $e \in E_F$ to all the others from V_F . So that, G_F forms a complete graph of n_F vertices. Let $\delta(v_i, v_j)$ be the geodesic distance between the vertices v_i and v_j . We label each edge $(f, f') \in E_F$ with the corresponding geodesic distance $\delta(f, f')$.

6.3.4 Minimal graph construction

Given a full graph on the source mesh, we build what we call minimal graph G_M , a subgraph of G_F . The graph G_M has two main properties: (1) it uniquely defines the landmark; i.e. position of a landmark can be uniquely identified by its geodesic distances to the nodes of G_M . (2) It is as small as possible in terms of the number of nodes and the geodesic distances it spans.

Given a landmark v , we build a minimal graph G_M by iteratively adding nodes from the feature point set $V_F = \{f_i\}, i = 1..n_F$ one by one, in an order of proximity. We repeat this process until either all the following conditions are satisfied, or all nodes in V_F are considered.

1. Position of v is uniquely defined by its geodesic distances to each node in G_M .
2. v is enclosed by the nodes of G_M .
3. G_M is a unique subgraph of G_F up to a symmetry.

Note that we cannot guarantee that G_M always meets all these conditions. In such case, G_M becomes equal to G_F . Algorithm 6-1, Algorithm 6-2 and Algorithm 6-3 summarize the procedure for the minimal graph construction.

Algorithm 6-1: MinimalGraphConstruction

Input: G_F : the full graph of the source mesh,
 v : a given landmark.
Init: $G_M = \emptyset, V_M = \emptyset$;
 $V_F \leftarrow$ all nodes of G_F sorted in an order of increasing geodesic distance from v ;
begin
 $n_{matching} \leftarrow \infty$ //Number of matchings of G_M to G_F ;
 $err_{geod} \leftarrow \infty$ // Geodesic error;
 $g_0 \leftarrow$ first node from V_F ;
 $V_M \leftarrow V_M \cup \{g_0\}$;
 $V_F \leftarrow V_F \setminus \{g_0\}$;
repeat
 $g \leftarrow$ fetch next node from V_F ;
 $V_M \leftarrow V_M \cup \{g\}$;
 $V_F \leftarrow V_F \setminus \{g\}$;
 $G_M \leftarrow$ a complete graph with V_M as nodes;
if (countMatching(G_M, G_F) < $n_{matching}$) AND
(localizationErr(v, G_M) < err_{geod})
 $err_{geod} \leftarrow$ localizationError(v, G_M);
 $n_{matching} \leftarrow$ countMatching(G_M, G_F);
else
 $V_M \leftarrow V_M \setminus \{g\}$;
endif
 $b_{enclosed} \leftarrow$ isEnclosedByNodes(v, G_M);
until ($n_{matching} == 1$ AND $err_{geod} < 2 \cdot \varepsilon$ AND
 $b_{enclosed} == \text{true}$) OR ($V_F == \emptyset$);
return G_M ;
end

Algorithm 6-2: localizationError(v, G_M)	Algorithm 6-3: isEnclosedByNodes(v, G_M)
<p>// Estimate the range of regions in which v can be localized in G_M. Input: G_M: the current minimal graph, v: a given landmark. Init: $U \leftarrow \emptyset$, $V_M \leftarrow$ all nodes of G_M; $\varepsilon \leftarrow$ a small value; begin $U \leftarrow \{v_u \mid \ \delta(v, g_i) - \delta(v_u, g_i)\ < \varepsilon, \forall g_i \in V_M\}$; $err \leftarrow$ the longest geodesic distance among $\{v_u\}$; return err; end</p>	<p>// Check if v is enclosed by nodes of G_M. Input: G_M: the current minimal graph, v: a given landmark. Init: $d \leftarrow$ a small value; begin $N_v \leftarrow \{p \in M_S \mid \ \delta(v, p)\ < d\}$; if $\exists p \in N_v: \delta(p, g_i) > \delta(v, g_i), \forall g_i \in V_M$ then return false; else return true; end</p>

Unique coordinates condition. Let $V_M = \{g_i\}, i = 1..n_M$ be the set of nodes of G_M . We first find the set U of all vertices v_u whose geodesic distances to g_i are of approximately equal length to those of v , as represented by:

$$\|\delta(v, g_i) - \delta(v_u, g_i)\| < \varepsilon \text{ for } \forall g_i \in V_M, \quad (6-2)$$

where ε is a distances tolerance of equal geodesic length. If the largest geodesic distance among the vertices in U is smaller than $2 \cdot \varepsilon$, we consider that G_M satisfies the unique coordinates condition, i.e. it can accurately locate v (see Figure. 6-4).

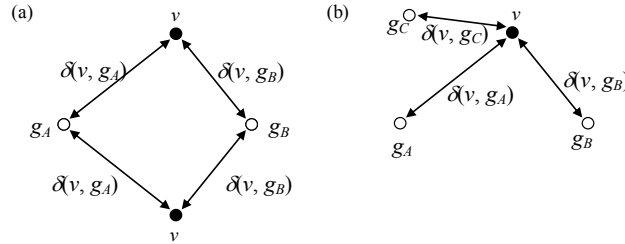


Figure. 6-4. Construction of the minimal graph. (a) By using two feature points (white dots), there are two possible position of landmark (black dot), thus the landmark is not uniquely defined. ε value from U is large. (b) With a minimal graph composed of three feature points, the landmark position is more unique (U is very localized and ε is small).

Enclose-by-nodes condition. The second condition requires v to be enclosed by the nodes of G_M , which makes the localization of v more robust to small changes of geodesic distances. In Figure. 6-5(a), feature points g_A, g_B and g_C are located on one (the left) side of the landmark v . When the geodesic distances $\delta(v, g_A), \delta(v, g_B)$ and $\delta(v, g_C)$ increase or decrease with the deformation, the estimated position of v will move to right or left, respectively. In Figure. 6-5(b), on the other hand, by using additional feature point g_D located on the other side of v , the distance changes influenced by $\delta(v, g_A), \delta(v, g_B)$ and $\delta(v, g_C)$ will counterbalance with the change of $\delta(v, g_D)$. This strategy assumes simultaneous increase or decrease of geodesic distances, which has been usually the case in our experiments.

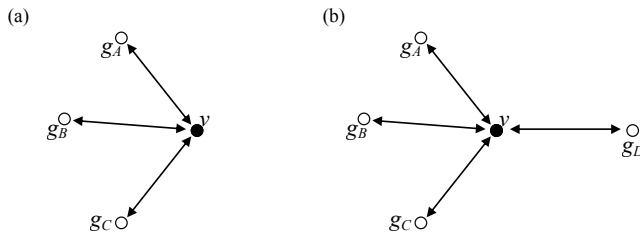


Figure. 6-5. (a), the landmark (dark dot) is not surrounded by feature points (white dots). In (b), by adding another feature point, the landmark is inside a convex hull; increases the confidence in the localization of the landmark.

The algorithm proceeds as follows. First, we compute a set N_v of all the vertices in the neighborhood (within certain geodesic distance) of v . If there exists a point $p \in N_v$ which is located further (with respect to v) to all the nodes of G_M , then G_M does not satisfy the enclose-by-nodes condition with respect to v .

Unique subgraph condition. Primary step of our minimal graph construction algorithm is to ensure that the landmark is defined uniquely on the source mesh. Several possible matching between G_M and G_F implies multiple matching between \hat{G}_M and \hat{G}_F , and therefore multiple transferred landmarks that are computed from each matching. In order to avoid such an ambiguity, we build G_M as a unique subgraph of G_F .

We initially tried to check the number of matching of the minimal graph with the full graph at each iteration, and stop growing the graph when we find only one matching. The graph matching algorithm we use is developed in spirit of Ullmann's tree-search subgraph isomorphism (Ullmann 1976), which we describe in (

Appendix B : Subgraph matching using Ullmann's Algorithm). However, in the presence of symmetry in the mesh, which is often the case, the minimal graph will always be equal to the full graph, which is undesirable. Thus, we slightly modify our initial algorithm and add vertices to the current minimal graph only when the resulting graph reduces the number of matching to the full graph. This means that the our method does not guaranty the uniqueness of the matching of the minimal graph to the full graph, permitting the symmetric ambiguity. Further discussions related to this aspect can be found in Section 6.5.5.

6.4 Landmark transfer via graph matching

6.4.1 Construction of the full graph \hat{G}_F on the target mesh

Similarly to the source, we first extract the feature points on the target mesh using the convexity values computed from the modified intrinsic wave descriptor (Section 6.3.2). These feature points constitute the nodes of \hat{G}_F , the full graph on the target mesh. To distinguish target mesh structures from the counterparts of the source, we use a ‘hat’ notation. Next, we compute the geodesic paths among them which serve as weighted edges of \hat{G}_F . We avoid computing all the geodesic paths by limiting ourselves to those geodesic paths on the target mesh whose length is smaller or equal to l_{max} , the longest geodesic distance in G_M . An explanation for this is that paths that exceed l_{max} will obviously not match with any path of the minimal graph G_M .

6.4.2 Matching the minimal graph to the full graph

Having computed \hat{G}_F , our goal now is to find a subgraph \hat{G}_M of \hat{G}_F , that best matches with G_M . In general, due to imperfect isometries in the real world data sets, full graphs might not be consistent across the given meshes. We handle this problem again by using a variant of Ullmann’s graph matching algorithm (Ullmann 1976) (see Appendix B for a detailed description), with partial matching. This time, while building a search tree of possible matching solutions we consider partial matching as well, i.e. we look for a subgraph of G_M which is isomorphic to some subgraph of \hat{G}_F . For each possible matching an error value is assigned, and the matching with the minimal error is chosen as the solution $\hat{G}_M=(\hat{V}_M, \hat{E}_M)$, which is then used to locate the landmark on the target mesh.

Note that instead of relying on modified Ullmann’s graph matching algorithm (Ullmann 1976), any inexact sub-graph matching approaches can be adopted such as (Torresani, Kolmogorov 2013). However, since the size of our graphs in most of the cases does not exceed ten nodes we decided to stick to the plain graph matching algorithm because there is no practical reason to use complex graph matching solutions, which might be interesting in the case of larger and less coherent graphs.

6.4.3 Landmark transfer

If the source mesh M_S and target mesh M_T are perfectly isometric, then we are able to uniquely identify the landmark location by using solely the geodesic distances from each of the nodes of \hat{G}_M . Let us denote a set of geodesic distances from a vertex $v \in M_S$ to the vertices from $V_M = \{g_i\}, i = 1.. \hat{n}_M$, as

$$\delta_{M_S}(v) = \left(\delta(v, g_1), \dots, \delta(v, g_{\hat{n}_M}) \right)^T, \quad (6-3)$$

and refer to it as feature point coordinates of v (FP-coordinates). Then, we must be able to uniquely determine the location of the transferred point \hat{v} on M_T that satisfies $\delta_{M_T}(\hat{v}) = \delta_{M_S}(v)$, where

$$\delta_{M_T}(\hat{v}) = \left(\delta(\hat{v}, \hat{g}_1), \dots, \delta(\hat{v}, \hat{g}_{\hat{n}_M}) \right)^T. \quad (6-4)$$

However, in practice, M_S and M_T are not isometric and in general case $\delta_{M_T}(\hat{v}) \neq \delta_{M_S}(v)$. This is partly due to the definition of the geodesic distance (Bose, Maheshwari et al. 2011), the shortest surface distance between the two points. As illustrated in Figure. 6-6, the shortest geodesic path between the two points of interest changes as the shape deforms. Along the bending of the cylinder, we observed up to 9% of change in the geodesic distances.

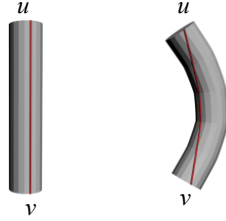


Figure. 6-6. A simple illustration of influence of pose change on the geodesic path between given points. The geodesic path as well as its distance between u and v change with the mesh deformation, from 100 to 90.7.

Our solution to the above problem is to modify the geodesic distances on the target mesh in a way that they become similar to those of the source mesh. Let $\hat{g}_i, \hat{g}_j, g_i, g_j$ be two feature points on the target mesh and their corresponding counterpart on the source mesh respectively. Due to the non-isometric deformation, the distances $\delta(\hat{g}_i, \hat{v})$ are different from $\delta(g_i, v)$, with v and \hat{v} being a vertex on the source mesh and its counterpart on the target mesh respectively. The idea is to modify the all geodesic distances from \hat{g}_i such that these geodesic distances become closer to those of the source mesh. That is, the distance $\delta(\hat{g}_i, \hat{g}_j)$ will become equal to $\delta(g_i, g_j)$. Similarly, the distance $\delta(\hat{g}_i, v)$ of vertex v in the close neighborhood of \hat{g}_j (i.e. $\delta(\hat{g}_i, v) \approx \delta(\hat{g}_i, \hat{g}_j)$) will become close to $\delta(g_i, g_j)$.

Computation of the feature point coordinates using inverse distance weighting (IDW). Let g_i be a vertex of the minimal graph on the source mesh and \hat{g}_i its counterpart on the target mesh. We compute the geodesic distance histogram of these two vertices. The geodesic distance histogram $H(g_i)$ describes the distribution of the geodesic distances between the vertex g_i and all the other vertices of the mesh M_S . As illustrated in Figure. 6-7, the histograms $H(g_i)$ and $H(\hat{g}_i)$ might be dissimilar, although g_i and \hat{g}_i are the same point on the shape. The main idea is to modify the geodesic distances of \hat{g}_i such that the histogram $H(\hat{g}_i)$ becomes similar to $H(g_i)$. This is done by using the inverse distance weighting method and the geodesic distances of the minimal graph vertices.

We define the interpolated geodesic distance $\delta_I(\hat{v}, \hat{g}_i)$ by means of inverse distance weighting:

$$\delta_I(\hat{v}, \hat{g}_i) = \sum_{j=1}^{\hat{n}_M} \frac{w_j(\hat{v}) \delta(g_j, g_i)}{\sum_{k=1}^{\hat{n}_M} w_k(\hat{v})}, \quad (6-5)$$

where $w_j(\hat{v}) = \frac{1}{\delta(\hat{v}, \hat{g}_j)^{p_j}}$.

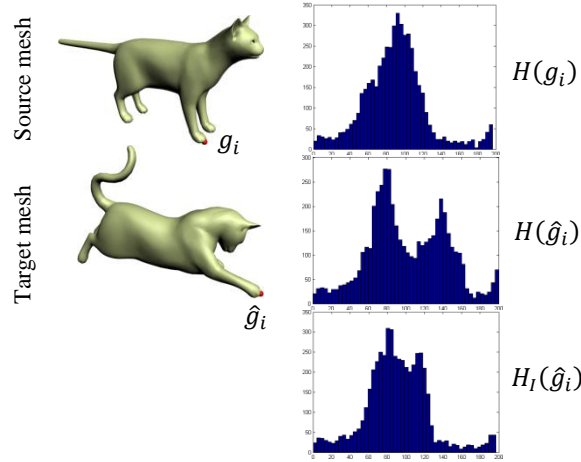


Figure. 6-7: $H(g_i)$ is the histogram of the feature point g_i on the source mesh, $H(\hat{g}_i)$ is the histogram of the corresponding vertex \hat{g}_i on the target mesh, $H_I(\hat{g}_i)$ is the histogram generated with the inverse distance weighting.

The value p_j is a positive real number, called the power parameter. \hat{n}_M is the number of vertices of the minimal graph. Each vertex of the minimal graph is assigned a different power parameter. Greater values of p_j assign greater influence of the vertex \hat{g}_j . The geodesic distance $\delta_I(\hat{v}, \hat{g}_i)$ is calculated with a weighted average of the geodesic distances between \hat{g}_i and other feature points on the source mesh. Intuitively speaking, as the vertex \hat{v} becomes closer to a feature point \hat{g}_i , its interpolated geodesic distance to \hat{g}_i becomes closer to $\delta(g_j, g_i)$.

Using Eq.(6-5), we compute the interpolated geodesic distance of \hat{g}_i to all the other vertices and generate the corresponding histogram $H_I(\hat{g}_i)$. An important step is to find the power parameters p_j for each minimal graph vertex \hat{g}_j so as to minimize the difference between $H_I(\hat{g}_i)$ and $H(g_i)$. We formulate this as a minimization problem where the unknown variables are the power parameters p_j and the cost function is

$$d(H_I(\hat{g}_i), H(g_i)), \quad (6-6)$$

where d is a metric to measure the distance between the two histograms. This minimization problem is computed for each minimal graph vertex \hat{g}_i separately.

One of the most common histogram metrics is the Earth Mover's distance (Rubner, Tomasi et al. 2000). In our implementation, we use a different version of the metric as follows. We compute a vector containing all the geodesic distances from g_i sorted in an increasing order. The same vector is calculated for \hat{g}_i . The distance between the two histograms is calculated as the norm of the difference of these two vectors. We assume that the vertex sampling on the source and target meshes is the same and the source and target meshes contain the same number of vertices.

To demonstrate the advantages of using the inverse distance weighting (IDW), we have compared the length of the geodesic paths before and after applying the IDW. Given a source and a target mesh whose correspondence is known, we have measured and compared the change of length of the geodesic paths between all pairs of vertices on the source mesh and their corresponding counterpart on the target. As shown in Figure. 6-8, the average of length variation and the standard deviation measured on the cat models is 10.91 and 2.87, respectively. After applying the IDW, they have been reduced to 3.9 and 1.11.

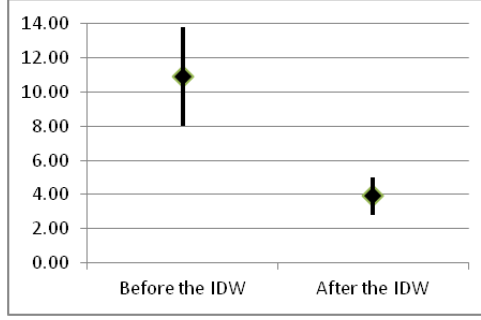


Figure. 6-8: The length variation of corresponding geodesic paths measured on the cat model, before and after applying the inverse distance weighting (IDW).

In Section 6.5.3, we further demonstrate the significantly improved performance of the landmark transfer with the use of IDW. These results clearly show that the IDW helps reducing the change of the geodesic distances caused by non-isometric deformation.

Landmark transfer using the FP-coordinates. Now that we have the interpolated geodesic distances on the target mesh, we proceed to the landmark transfer. Let v be a landmark on the source mesh; the goal is to compute the location of corresponding landmark \hat{v} on the target mesh. Note that \hat{v} is generally not a vertex on the mesh.

1. For each geometric feature points \hat{g}_i , we determine a set \mathbf{T}_i of all triangles which contain at least one vertex v_i whose geodesic distances $\delta_I(v_i, \hat{g}_i)$ are in the interval $\left[\frac{1}{2}\delta(v, g_i), \frac{3}{2}\delta(v, g_i)\right]$. The set of triangles that are common in all \mathbf{T}_i 's ($i=1\dots\hat{n}_M$) are considered for step 2. Needless to say, the process can be accelerated by limiting the subsequent range test for \hat{g}_{i+1} to those triangles in \mathbf{T}_i . The final pruned list of triangles $\mathbf{T} = \bigcap_{i=1}^{\hat{n}_M} \mathbf{T}_i$ is used for further processing.

2. For each triangle $t \in \mathbf{T}$, we compute a vertex \hat{v}_t such that its FP-coordinates are as close as possible to those of the landmark v on the source mesh. The FP-coordinates of the points inside t are interpolated from the FP-coordinates of the vertices of t using the barycentric coordinates. Let v_{t1}, v_{t2} and v_{t3} be the three vertices of the triangle t and $w_c, c=1, \dots, 3$ the barycentric coordinates of \hat{v}_t that need to be determined. The barycentric coordinates of \hat{v}_t such that its FP-coordinates are as close as possible to those of v are given by:

$$\begin{pmatrix} \delta_I(v_{t1}, \hat{g}_1) & \delta_I(v_{t2}, \hat{g}_1) & \delta_I(v_{t3}, \hat{g}_1) \\ \vdots & \vdots & \vdots \\ \delta_I(v_{t1}, \hat{g}_{\hat{n}_M}) & \delta_I(v_{t2}, \hat{g}_{\hat{n}_M}) & \delta_I(v_{t3}, \hat{g}_{\hat{n}_M}) \end{pmatrix} \begin{pmatrix} w_1 \\ w_2 \\ w_3 \end{pmatrix} = \begin{pmatrix} \delta(v, g_1) \\ \vdots \\ \delta(v, g_{\hat{n}_M}) \end{pmatrix}, \quad (6-7)$$

with $0 \leq w_c \leq 1$ for $c=1\dots 3$ and $\sum_{c=1}^3 w_c = 1$.

If the number of feature points are three ($\hat{n}_M=3$), we can compute the exact solution to the above equation. When $\hat{n}_M>3$, w_c 's are determined by taking the least square solution.

3. Finally, for each triangle $t \in \mathbf{T}$, we compute $\delta(\hat{v}_t)$, the FP-coordinates of \hat{v}_t by using the w_c 's we computed from Eq.(6-7) and choose the one that minimizes the distance error as defined by:

$$\hat{v} = \operatorname{argmin}_{\hat{v}_t} \left\| \delta(\hat{v}_t) - \begin{pmatrix} \delta(v, g_1) \\ \vdots \\ \delta(v, g_{\hat{n}_M}) \end{pmatrix} \right\|. \quad (6-8)$$

6.5 Results

In this section, we present results of experiments with the method described in the preceding sections. We implemented our algorithm using Matlab. All measurements were made on a Windows 7 Professional machine with 16GB of memory and Intel Core i7-2600 processor running at 3.40 GHz. We tested our method on the models of different mesh connectivity (Figure 6-9) from the Non-Rigid World Benchmark (Bronstein A., Bronstein M. et al. 2008), as well as on our own synthetic embossed plate models.

Figure 6-11 shows some of the results we obtained. Note that these models exhibit deformations which are only approximate isometries; also each family of objects have a mesh in an initial posture, which is labelled as a mesh in a rest posture (or source mesh). The landmarks have been chosen to be a set of 100 points evenly spaced over the surface using Poisson sampling. In order to avoid repetitive computation of the graph matching, the minimal graph is set to the full graph, so that, the graph matching is computed only once for the transfer of the 100 points. Compared to the minimal graph method, the computation time is about 2 to 3 times higher. We conducted a series of experiments and applied our algorithm to all the vertices in Poisson sampling sets. The quality of transfer is compared with the ground-truth correspondences from high-resolution Tosca models (Figure. 6-12), and with correspondences computed with existing methods (see Section 6.5.4).

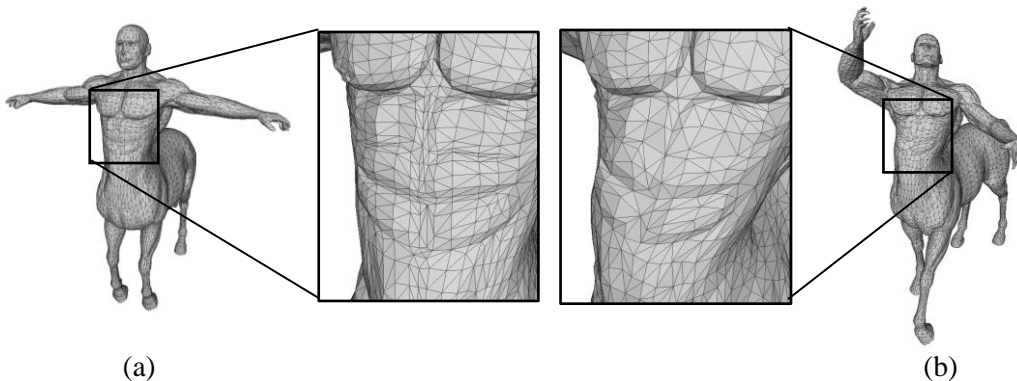


Figure 6-9. The models we used in our experiments have different number of vertices and mesh connectivity. (a) Centaur mesh comprised of 7K vertices. (b) Centaur mesh in different posture comprised of 5K of vertices.

6.5.1 Timing

In Table 6-1 an average computation time is shown, which was measured while transferring each of the landmarks; the time was measured and then averaged over landmark transfer to 10 cat models, 6 centaur models, 8 dog models, and 3 embossed plate models. We clearly see that the computation of the updated geodesic distances (see Section 6.4.3) is the most time-consuming task. However, an update of the geodesic distances according to the histograms (see Figure. 6-7) is required only once per each target mesh. That is, it does not matter how many landmarks are to be transferred from the source to the target (e.g. 10 or 103), the geodesics are updated only once. i.e. it makes our technique very efficient when working with a number of landmarks. For example, once the geodesic distances are updated, it takes only 256ms to transfer a landmark on the cat model (Table 6-1).

Data set	$ X $	$ T $	t_δ	t_{v_F}	t_{G_M}	$t_{v_F}+t_{\hat{G}_M}$	t_H
Cat	4K	9K	146ms	21ms	39ms	59ms	6.63s
Centaur	5K	10K	86ms	23ms	128ms	338ms	48.96s
Dog	5K	9.5K	104ms	20ms	33ms	39ms	5.98s
Embossed plate	1.5K	2.9K	19ms	7ms	85ms	1708ms	2.81s

Table 6-1: Average computation time. $|X|$ is the average number of vertices over all postures, and $|T|$ is the average number of triangles, t_δ is the average time needed to compute the geodesic distance matrix per each vertex, t_{v_F} is the average time needed to extract feature points, t_{G_M} is the average time needed to build a minimal graph, t_H is the average time for updating the geodesic distances; hat over a symbol refers to it the target mesh.

As shown in Table 6-1, the overall time of landmark transfer is just a matter of seconds; except for the centaur model. On the centaur our method shows rather a high computation time. The main reason is that this mesh has many more geometric feature points compared to other models (e.g. 15 feature points for the centaur vs. only 8 for the cat). Since t_H is a function of a number of vertices and geometric features, our technique works fast on the embossed plate, which also has many geometric features, but the number of vertices is much less compared to the centaur model. In general, the computation time is an advantage of our method. It takes about 1 minute to find full correspondence for the cat model (on Matlab platform). This has been possible because (1) the update of the geodesic distances has been made only once, and (2) full graph has been used in place of minimal graph for every vertex.

6.5.2 Robustness

Minimal graph plays one of the central roles in our landmark transfer algorithm; and naturally, the quality of transfer is correlated to the selection of G_M . In Figure. 6-10 (a, b) is shown a case when the landmark was picked at the base of a human neck, which is close to the geometric feature points on the head, breast and hands. With such settings our minimal graph construction algorithm gives a compact G_M . On the other hand, when the landmark is located far away from geometric feature points, as in Figure. 6-10 (c, d), G_M turns out to be ‘large’ in terms of the geodesic distances of the edges. A ‘small’ minimal graph is preferred in our algorithm. First reason for this is that the shorter the graph edges are, the less distortion and error is introduced for corresponding graph on the other isometric mesh. Second, when G_M is small, less geodesic computations are needed to find corresponding one on the target. Note that by configuring a maximum size and number of isocurves of the local shape descriptor, we can achieve detection of different number of feature points, according to our needs and mesh complexity. In our experiment, we were able to extract from just a few to dozens of feature points on the same human model.

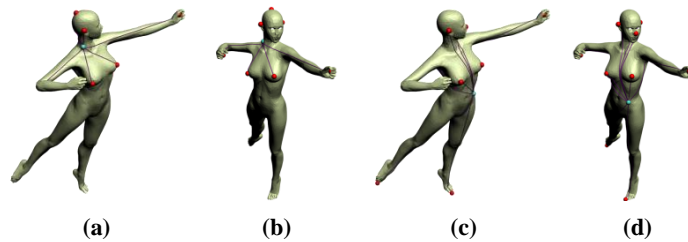


Figure. 6-10. Impact of the landmark location on the quality of transfer and performance. (a), (b) Landmark on the neck is closely surrounded by feature points. (c),(d) Landmark in the belly area has relatively large average distance to the feature points of the surface.

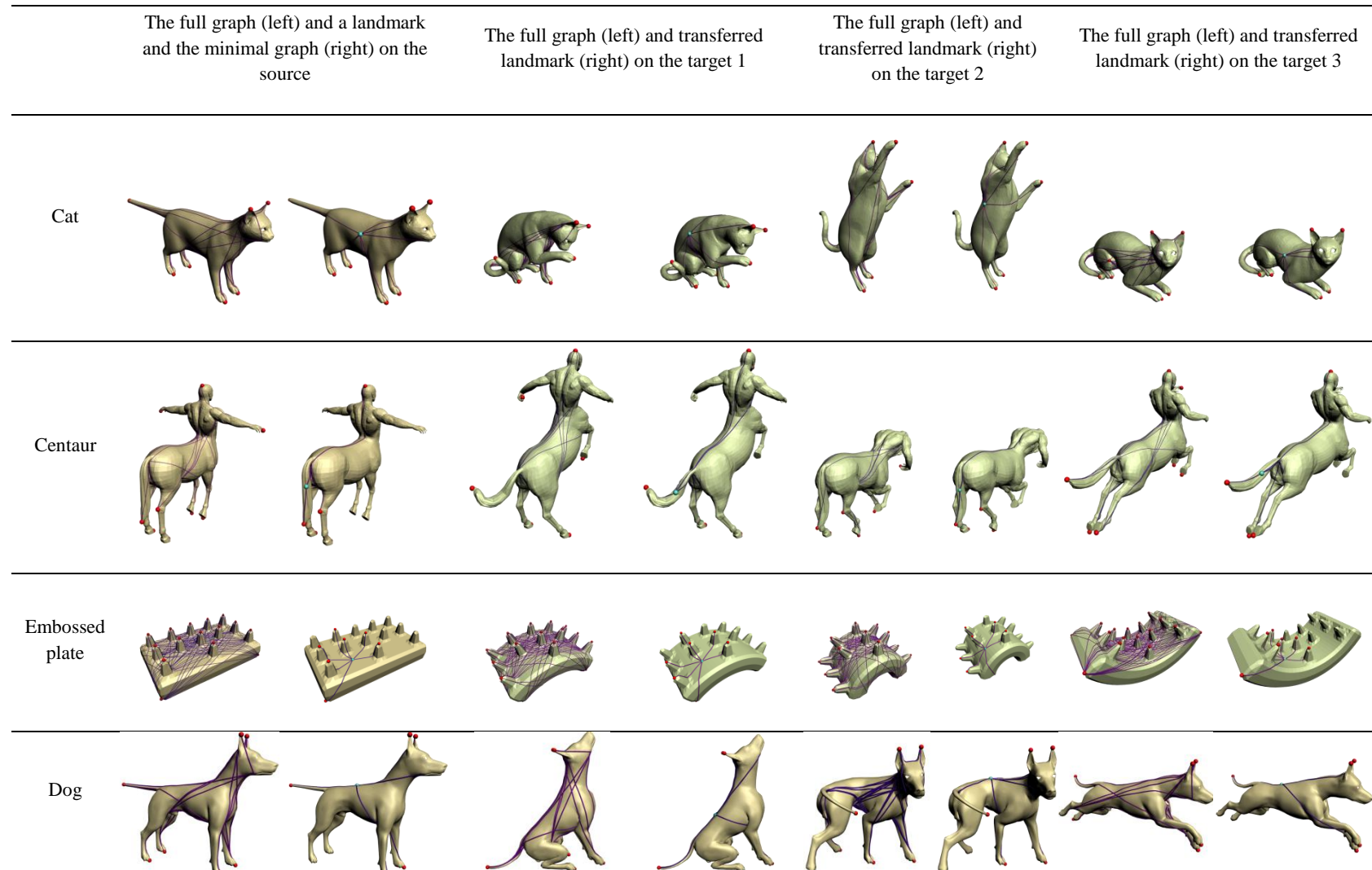


Figure 6-11. Results obtained from our landmark transfer technique. For each dataset, 3 target postures have been chosen. For each posture, full graph (left) and the minimal (right) is illustrated

In order to measure the quality of the results of landmark transfer, we perform cross-validations by using the Tosca high-resolution dataset as ground truth. We applied our technique to a mixed data set of different subjects in different postures. Our test cases evaluate the maximum and mean errors while transferring 100 Poisson sampled landmarks: on the cat models (Figure. 6-12(a)), for the Centaur models (Figure. 6-12(b)). The error of landmark transfer is measured as a geodesic distance deviation from the corresponding ground truth, further normalized by square root of the mesh surface area. Average error values for all data sets are evaluated as shown in Figure. 6-12(c). Due to imperfect isometries, the error values vary from one posture to another (clearly visible in Figure. 6-12(a,b)). (Be reminded that these models are only nearly isometric. For example, some of the cat postures show up to 30% of the geodesic distance change with respect to the rest posture. With the embossed plate, maximum of 40% of the geodesic changes can be observed.)

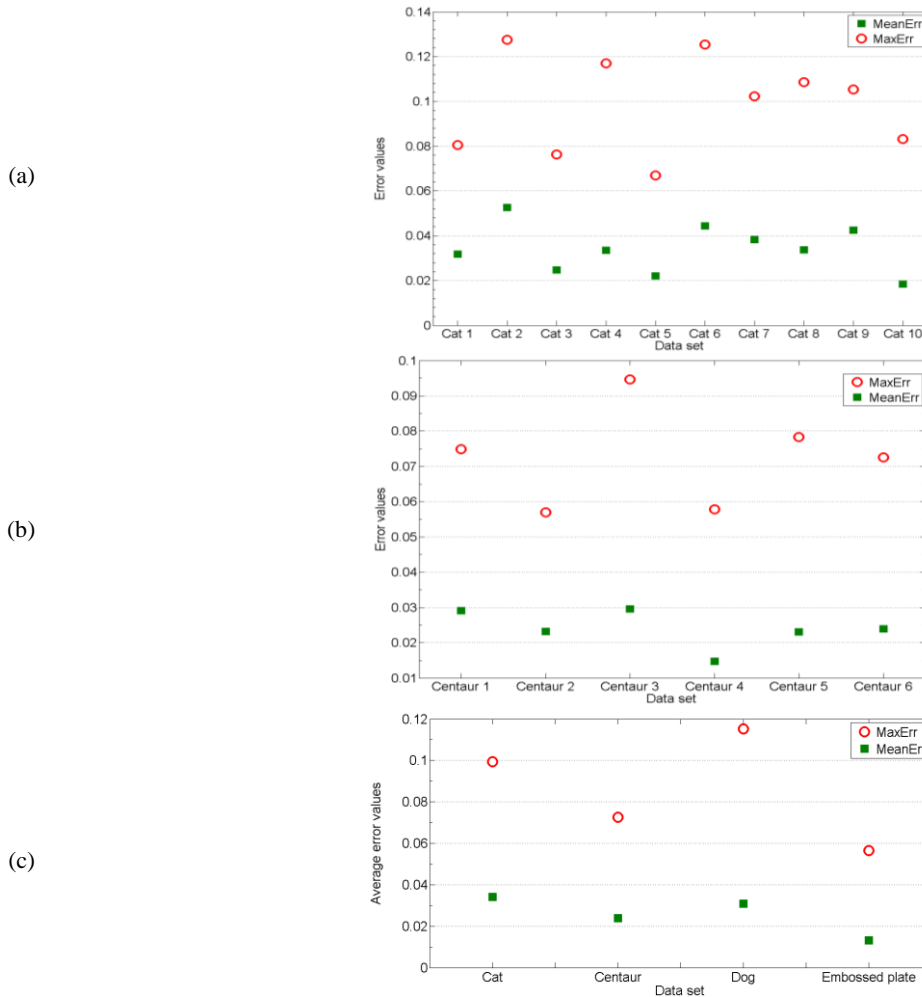


Figure. 6-12. Quality of landmark transfer with respect to the ground truth. We report mean and maximum error values for the (a) cat model and (b) centaur model.(c)Average mean and maximum error values are calculated for each data set.

As shown in Figure. 6-16, our method shows good quality of results on all the models. We can clearly see that the quality of landmark transfer depends on the landmark location with respect to the nodes of the minimal graph and degree of deformation in its neighborhood. In general, the best performance is obtained if the landmark location is close to the nodes of the minimal graph (tips of the limbs, tips of the breast). On the other hand, in the regions of highly non-isometric deformation the quality of transfer degrades (rear part and joints of humans, joints of animals). Note that we obtain a good quality of match on the embossed plate Figure. 6-16 (j) despite its high degree of non-isometric deformation. This is especially true on the top center part, which is contributable to the fact that landmarks are well-surrounded by many geometric feature points. Bottom part of the plate lacks feature points, which explains higher errors on it.

Experiments with genus-one model. We have tested landmark correspondences between two genus-one surfaces. Embossed plate model with a hole has been used, which has been synthetically generated and deformed. Our algorithm has shown a good accuracy in such settings as well Figure. 6-13. The average geodesic error with respect to ground truth is 0.009, and the maximum error 0.028.

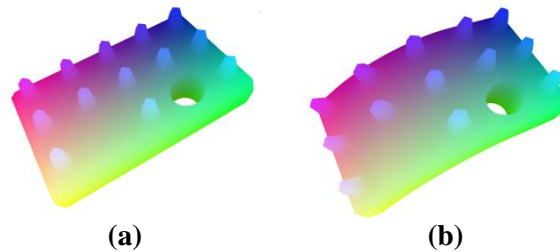


Figure. 6-13. Performance of our method on a genus-one plate model. (a)Each vertex in the source model is assigned with a color that corresponds to its position in a 3D color space. (b) On the target, the transferred locations are colored the same as their source vertices.

6.5.3 Inverse distance weighting scheme

As expected, the inverse distance weighting greatly improves the quality of the landmark transfer. In Figure. 6-14 color maps of the landmark transfer are presented for the cat and horse models. For the cat model, the maximum matching error is 0.17 without the IDW; however, when using the IDW it has been reduced to 0.08. For the horse model, maximum error has been reduced from 0.14 to 0.07 respectively. For these models, the matching quality is roughly two times better when using the IDW. More detailed comparison of the landmark transfer with the IDW and without the IDW is shown in Figure. 6-15, where the error plots of two landmark transfer with minimal graph (LTMG) implementations are shown. LTMG without the IDW yields approximately 50% correspondences exceeding the error value of 0.05, whereas with LTMG (with the IDW) this number is only 10% (which is better than the result obtained by Blended Intrinsic Map(Kim, Lipman et al. 2011) for the same error).

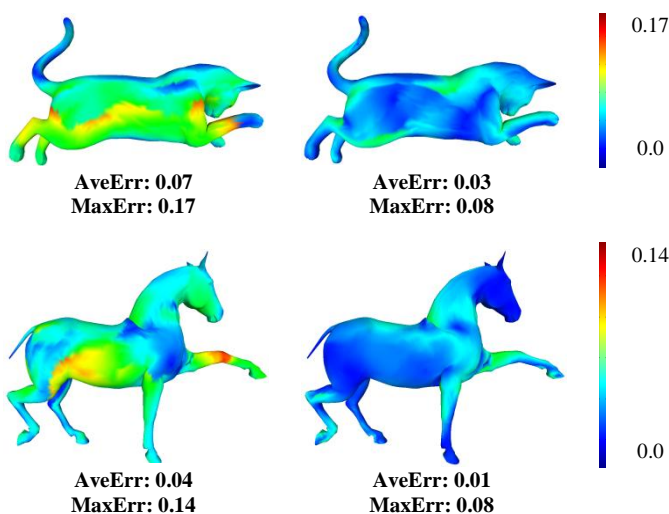


Figure. 6-14: Quality of landmark transfer without (left column) and with the IDW(right column) for the Cat1 (first row), and Horse7 (second row).

6.5.4 Comparison with existing methods

Our technique is tailored for the fast transfer of a sparse set of landmarks on a one-by-one basis. This makes it a bit difficult to perform fair comparisons with existing methods, which mostly focus on computing global optimal solution to the full correspondence. Nevertheless, we used our landmark transfer technique for the full correspondence, in order to make quantitative comparisons tractable. We note however that our landmark transfer finds the corresponding location independently for each vertex, and therefore it is not competitive in terms of computation time when it comes to the full correspondence problem.

For the comparison we have chosen two state-of-the-art techniques – Blended Intrinsic Maps (BIM) (Kim, Lipman et al. 2011) and Möbius Voting (MOB) (Lipman and Funkhouser 2009). Within each family of objects from the full Tosca dataset (11 cats, 9 dogs, 3 wolves, 8 horses, 6 centaurs, 4 gorillas, 39 human figures including one female and two male subjects), we arbitrarily selected a model as a source and computed full correspondences to the rest of the models using LTMG by treating each vertex on the source mesh as a landmark. The results of BIM benchmark and Möbius Voting were referred and reproduced, as presented in (Kim, Lipman et al. 2011). Comparative study of correspondence errors is illustrated in Figure. 6-15. Overall, LTMG and BIM show better accuracy than the Möbius Voting. LTMG shows comparable accuracy to Blended Maps. Compared to LTMG, BIM produces slightly larger number of correspondences in the error range of less than 0.03. However, in contrast to BIM, LTMG gives less outliers with errors higher than 0.04. Additionally, LTMG's plot is noticeably steeper and converges quickly to 100% of correspondences at the error value of 0.14 on the Tosca data set. On the contrary, BIM reaches 100% of correspondences only at the error value 0.25 on the same set.

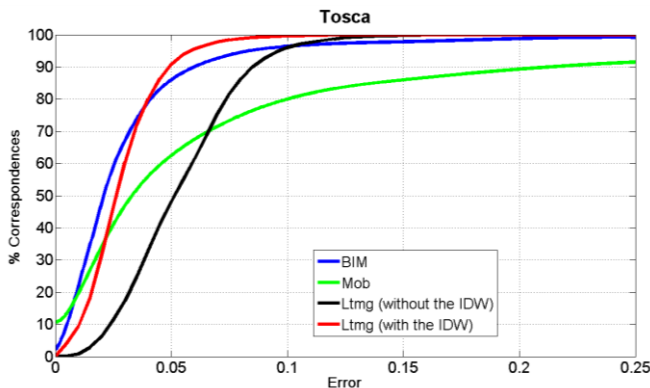


Figure. 6-15. Error plots from the BIM, MOB, LTMG (without IDW), LTMG (with IDW) methods on the full Tosca dataset. The x-axis represents the geodesic error and the y-axis the percentage of correspondences within the error from the ground truth. The IDW (red curve) shows a significant improvement on the performance of LTMG method (black curve).

Comparison with PLANSAC. We also compared our method to PLANSAC (Tevs, Berner et al. 2011) and its predecessor RANSAC (Tevs, Bokeloh et al. 2009). Provided by (Tevs, Berner et al. 2011) the average error score $E(f)$ for the centaur model computed with PLANSAC and RANSAC methods is 0.032 and 0.113 respectively. With the LTMG method applied to the same data, we observe an average matching error of 0.027. This makes our method comparable to PLANSAC matching method, and actually better than RANSAC.

Note that Tevs and co-workers (Tevs, Berner et al. 2011) run their algorithm on Poisson sampled centaur model and provide accuracy results in ε -units, where ε is the minimum distance between two points in the discretization. Unfortunately the value of ε is not provided. That is why, in order to compare error values, we first needed to bring them to a common scale. For this reason, we also applied uniform Poisson sampling to the centaur model and obtained discretization with the maximal number of samples ~ 1000 , as in PLANSAC

settings. With this sampling, we have estimated the exact value of ε . Further normalization by the square root of the model's surface area has yielded directly comparable error values.

6.5.5 Limitations

The main limitation of our method is that it relies on the geometric features of the shape. If the shape does not have any prominent geometric points, our method is not applicable (for instance, our technique will not be able to give a result on a sphere model). The reason for this is that our technique relies on a local shape descriptor to extract feature points, which are then used as nodes of full and minimal graphs.

Apart from this, isometry between the source and target meshes is one of the main assumptions used in our landmark transfer. That is rather strong assumption, although it holds valid in many real-world situations of matching 3D scan data. When the meshes come from different objects, this assumption is violated and proposed method may not work well.

Handling the symmetry. In the presence of symmetry, the landmark transfer will propose only one of all possible solutions. This is related to the uniqueness condition of our minimal graph construction, which favors light computation in graph growing and graph matching, at the cost of permitting matching ambiguity, which is originated from the symmetry. Since our current implementation of minimal graph construction algorithm does not differentiate between the two symmetric minimal graphs given the same (graph-) matching error, sometimes the transferred landmark can be located at the mirror-reflection of the desired location of the transferred landmark. However, it would be easy to extend our method in a way that all possible transfers are proposed to the user. We can simply consider all matching of the minimal graph to the full graph on the target, and compute landmark transfer from each minimal graph. The user will then choose either one or all of them, depending on what s/he wants to have. Note that in our robustness tests, the matching (landmark position) error has been measured on one half of the meshes, by considering one location and its reflective symmetry as identical.

6.6 Conclusion

Isometry preserving deformations are frequently encountered in real life: articulated motions and majority of human movements. In Chapter 6 we presented a landmark transfer technique that efficiently computes vertex matching on a source (original posture) and target (posture change) meshes that are approximately isometric.

The key idea of our approach is to use the minimum amount of information in geodesic coordinates which is sufficient for locating any given point on a source shape and efficient computing its correspondence on a target shape (Sections 6.3-6.4).

The matching method detailed in this chapter brings several contributions:

1. The new idea of the minimal graph (Section 6.3), which characterizes location of any point on a shape and is used for shape matching with minimal computation expenses.
2. Identification of vertex locations using a newly defined geodesic coordinates (Section 6.4). In contrast to previous approaches, we do not rely solely on geodesic distances. Instead we develop a reliable method of updating geodesic distances, which compensates well the distance changes due to imperfect isometry and assures precise and consistent vertex correspondence.

Our method shows robust and precise matching result with a low computational time cost in a large number of experiments and different data sets (Section 6.5). Although, we demonstrate the effective performance of our matching method in cases of pose changes of the given subjects, it is possible to proceed in a similar way for establishing inter-frame correspondences of deforming mesh with a time-varying mesh connectivity, which we plan to carry out in future. Additionally, our method can be ideal for a sparse one-to-many shapes matching. For instance, given a set of sparse landmarks, our algorithm can find precise correspondences on a set of multiple meshes in a matter of seconds, avoiding abundant multiple full shape matching.

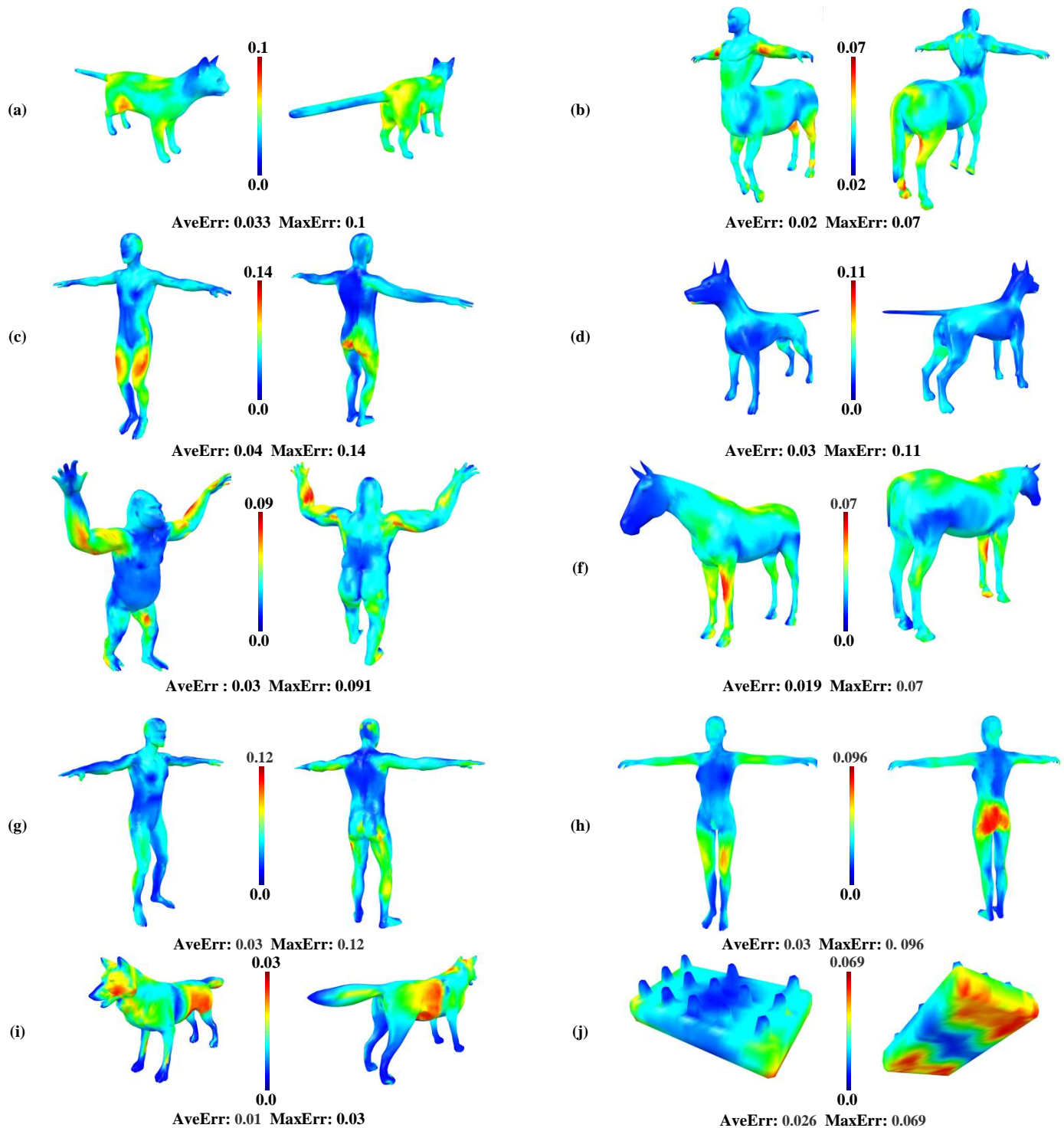


Figure 6-16. Quality of transferred landmark shown as color map. For each class of Tosca models (a-i) and synthetic embossed plate models (j) we show 2 figures, along with the average and maximum errors. The highest maximum error of landmark transfer could be observed on the models of David (c) (MaxErr: 0.14) and Michael (g) (MaxErr: 0.12). The lowest maximum error was obtained for the Wolf (i) (MaxErr: 0.03) and Embossed plate (j) (MaxErr: 0.069). We can clearly see that the quality of landmark transfer depends on the landmark location with respect to the nodes of the minimal graph and degree of deformation in its neighborhood. In general, the best performance is obtained if the landmark location is close to the nodes of the minimal graph (tips of the limbs, tips of the breast). On the other hand, in the regions of highly non-isometric deformation the quality of transfer degrades (rear part and joints of humans, joints of animals). For the embossed plate (j) we obtain good quality of match on the top center part because landmarks are well-surrounded by the graph nodes. Bottom part of the plate lacks feature points, which explains higher errors on it.

Chapter 7 Conclusion

In this thesis, we have been interested in investigating shape analysis of time-varying geometry (i.e. animated meshes) and have presented novel algorithms for the dynamic feature detection, feature description on animated meshes and their applications to shape correspondence. We paid a particular attention to the maximal use of dynamic motion properties in animated mesh sequences for dynamic feature point extraction and description. Based on the dynamic features, we proposed a new pipeline of the shape correspondence based on similarities of deformation properties of animated meshes rather than their purely static structures. On a number of example animated meshes of drastically different shapes we demonstrated robustness and efficiency of our surface deformation/motion-driven methods. Our approach is applicable to any deformations, skeletal (humans/animals) or non-skeletal (faces). In Section 7.1 we highlight the contributions of this dissertation and in Section 7.2 we present several interesting future research directions.

7.1 Contributions

In this dissertation, we have focused our research on establishing correspondence computation pipeline between animated meshes by exploiting their surface deformation characteristics. Our work brings the following prime contributions.

- We presented a new feature detection technique on animated mesh sequences. First we started with a local surface deformation characteristic scheme for animated meshes. Then we developed the core of the proposed dynamic feature extraction technique which is formed by the principles of the linear scale-space theory on animation's deformation characteristics. Our contributions include: introduction of a new spatio-temporal scale representation of the animated mesh's surface deformation, and an extension of the classical DoG (Difference of Gaussians) filter to spatio-temporal case of animated meshes. Our method is able to robustly and repeatably extract consistent sets of feature points over different deforming mesh surfaces. Validations and experiments on various types of data sets show consistent feature extraction results when the exhibited animations are identical, kinematically or semantically. Our approach has also shown robustness to spatial and temporal sampling of mesh animation.
- The main contribution of our work is a solid correspondence pipeline for animated meshes, featuring new dynamic feature descriptors. It consolidates the new dynamic feature detection, dynamic feature description, and sparse/dense point-to-point matching. The newly proposed dynamic point signature comprised of different motion modalities and deformation properties of animated mesh. It has been successfully adopted in efficient and precise *coarse* matching of dynamic feature points and consequently has driven robust *fine* matching between different animated meshes. Additionally, our method can help avoid symmetry confusion in matching of deforming meshes with the use of dynamic motion properties of the subject's motion (The majority of real-world human or animal motions are asymmetric).
- Finally, with an aim of finding inter-frame correspondence for animated meshes with the time varying mesh connectivity, we have developed an efficient and robust matching method for approximately isometric deformable shapes. The prime idea of the method is to use the minimal amount of

information to precisely locate a point location in geodesic coordinates on the source mesh and reconstruct its location on the target mesh. One of the major benefits of the method is a very light computational time of the matching method when it comes to the matching of a few number of selected points. Experiments on dense correspondence confirm that our technique shows a comparable performance with respect to the state of the art matching algorithms.

7.2 Future directions

We believe that the methods studied in this dissertation bring a number of promising research directions and interesting applications towards new contributions in analysis of time-varying geometry.

The outcome of the work conducted in scope of this dissertation suggests several new research paths.

- Given the developments we produced in the scope of this dissertation, one interesting research direction would be a statistical shape analysis of animated meshes. It is reasonable to pose a question on how existing shape analysis techniques based on statistical models (such as Anguelov, Srinivasan et al. 2005) can be adapted to incorporate dynamic data. Indeed, *statistical shape analysis* of animated mesh's shapes and corresponding deformations has a tremendous potential. One way to proceed is to set up a statistical model that captures both shape variations and deformation resulting from motions of instances of distinct animations in an animated mesh database. Within the low dimensional statistical model we can analyze the deformation properties involving different shape variations and different movements. The learnt animated mesh shape-deformation statistical model can be developed into techniques for the improvement of shape correspondence methods in spirit of how it was previously done in statistical atlases for static shapes. Additionally, machine learning algorithms can be applied to the full body time varying animation statistical model to enhance and contribute to the methods of human modelling and animation.
- We also consider improving the shape correspondence algorithms by capturing more mechanical properties of the deforming surface in an animated mesh. A substantial amount of research in computer graphics focuses on physic-based techniques. In real world, laws of physics govern motion and deformation of objects and might become an integral component of shape correspondence pipeline. Physic-based properties such as surface's strain and stress tensors directions (so far in this dissertation we have employed only magnitudes of strain tensors) can be eventually incorporated into the shape correspondence technique. Physical, mechanical properties of the deforming shapes might be further incorporated into dynamic feature vectors. One possible option can be to extract physical properties of the regions of interest on the source and compare extracted deformation tensor field directions to the ones estimated on the target animated mesh. Ultimately, the shape correspondence can be posed as a global optimization which compares and aligns deformation tensor fields on the surfaces of the source and target animated meshes.
- Alternatively, dynamic feature points which are equipped with shape correspondence of animated meshes can be employed in more pragmatic applications in medicine (i.e. deviations in movements of internal organs) and sports (performance and motion analysis of athlete's movements). For example, the comparison studies of dynamic feature points extracted from the heart movement data of a patient and a reference healthy heart can help clinicians to better understand and diagnose potential abnormalities.
- The principal idea of the geodesic graph-based surface representation from the landmark transfer algorithm could be potentially adopted for challenging inter-frame correspondence problems in time-varying geometry originating from optical sensors. Acquisition noise, holes etc. typically persist in such data sets, which make geodesic paths not completely reliable on deforming shapes that have

been captured. Therefore, after de-noising and assuming moderately small sizes of acquisition holes, we can proceed in a flowing way. First, construct a k nearest neighbourhood graph for the each point at each frame of the captured data. We consider setting k to a sufficiently large value to cover the acquisition holes. Then, given per-frame feature points and k -nn graph distances that approximate real geodesic paths, we can proceed in spirit of landmark transfer to establish initial inter-frame correspondences. Finally, in order to obtain reliable correspondences in entire input animation, we can formulate an optimisation problem that blends initial correspondence maps over all frames in a way that all inter-frame errors are minimized.

Finally, our dynamic feature detection technique can be applicable for a number of advantageous applications in computer animation field such as animated mesh simplification, optimal viewport selection, animation alignment and animation similarity (animated mesh retrieval).

- *Animated mesh simplification.* As it has been noted in earlier works on simplification of dynamic (deforming) meshes (Shamir, Bajaj et al. 2000, Kircher and Garland 2005), it is preferable to allocate bigger triangle budget for regions of high surface deformation while simplifying mostly rigid regions. Our algorithm could be adopted in these as it detects feature points that are exactly in deforming regions. Their spatial scales σ_k can be used to define regions around features where the mesh must keep denser sampling during simplification. For instance, the spatial scale of the feature points can be used to define regions where the mesh must be densely sampled during simplification. The temporal scale can also be used to dynamically determine the triangle budget around the feature point, when designing a time-varying simplification technique. A very small temporal scale implies either a short duration or a high speed of the animation, thus one may assign low priority to the feature point. In the same way, the region around a feature point with large temporal scale will be prioritized when allocating the triangle budget. Another use of the temporal scale is in the maintenance of the hierarchy. When transferring the previous frame's hierarchy to one better suited for the current frame in a time-critical fashion, the algorithm can use the temporal scale of a FP as a “counter” to determine whether to update or reuse the node corresponding to the region around the FP. By processing the nodes corresponding to the spatio-temporal feature points in an order of decreasing temporal scale, one can economize the time for the per-frame maintenance of the hierarchy while keeping the animation quality as much as possible.
- *Viewpoint selection.* With increasing advances in scanning and motion capture technologies animated mesh data becomes more and more available today. Thus it is very practical to have a tool for automatic viewpoint selection for the preview of the motion in animation repositories. The idea behind that is to let a user to quickly browse the animation data from the point that maximizes the visibility of mesh deformations. With such viewpoint selection, the user benefits from a better perception of the animation. One equally handy and straight forward way to automatically select optimal viewpoint is to compute the one which maximizes the number of visible feature points through the optimization. We note that our spatio-temporal feature points can simplify the selection of good viewpoint(s). For instance, the quality of a viewpoint could be defined as a function of the visibility of the spatio-temporal feature points in terms of the total number, temporal variability and the concavity of the projected feature region (as defined by the spatial and temporal scales), etc. Interested reader may refer to an optimization technique proposed in (Lee, Varshney et al. 2005) on saliency-based viewpoint selection for static meshes.
- *Animation alignment.* Another interesting application could be animated mesh alignment. Considering the consistency of the extracted feature points, their scales values can be employed for the temporal alignment. Given sets of features P and P' extracted from pair of similar animations, we consider corresponding sequences $\{(\sigma_1, \tau_1), \dots, (\sigma_n, \tau_n)\}, \{(\sigma'_1, \tau'_1), \dots, (\sigma'_m, \tau'_m)\}$ of spatio-temporal fea-

ture scales aligned along the time they were detected. Existing algorithms of sequence alignment such as (Gotoh 1990) can then be used to compute the temporal alignment between them. In addition to the spatial- and temporal- scales, more sophisticated feature descriptors can also be used to compose the sequences.

- *Animation similarity.* We can also think of extending the above mentioned animation alignment algorithm towards a measurement of animation similarity. From the feature sequence alignment map, we can sum up all penalty gaps i.e. some predefined costs for all features for which no match can be found. That cost function could serve as a distance metric between the animations and hence be a measure of dissimilarity/similarity. Note that an important by-product of the animation similarity is the animated mesh retrieval, which is particularly beneficial in emerging dynamic data repositories.

Chapter 8 Appendices

8.1 Appendix A. MOCAP Data Acquisition Process

In this appendix we briefly describe our motion capture acquisition process of facial animation which are involved in experiments in Chapter 3 and Chapter 4.

By means of our Mocap data acquisition process we aim to supply developers with real-world dynamic data sets in a form of animated meshes. This data is used in the new, shape analysis methods and all related techniques for deforming/animated mesh processing. At the current stage we focus on a certain part of human body, namely on human face. We are interested in a database of multi-subject animated meshes exhibiting intra-subject facial motions (expressions of emotions, lip movements, speaking, etc.), and coherent inter-subject facial motions (i.e. different subjects show exactly the same emotions, say exactly the same words etc). Among subjects for data acquisition there's no preference for gender proportion or age distribution. At the moment we have acquired the data from 6 distinct subjects.

The MOCAP system. Our system was custom-assembled of five Vicon T40 and of seven Vicon T40-S cameras. Such cameras are specifically tailored for marker motion capture and have a resolution of 4 megapixels, capture 10-bit gray scale using 2336 x 1728 pixels and can capture speeds of up to 2,000 frames per second. Entire set of twelve cameras is placed in the motion capture zone and forms a semi sphere around a subject (Figure 8-1). We configured the system to capture marker positions at 120-frame rate.

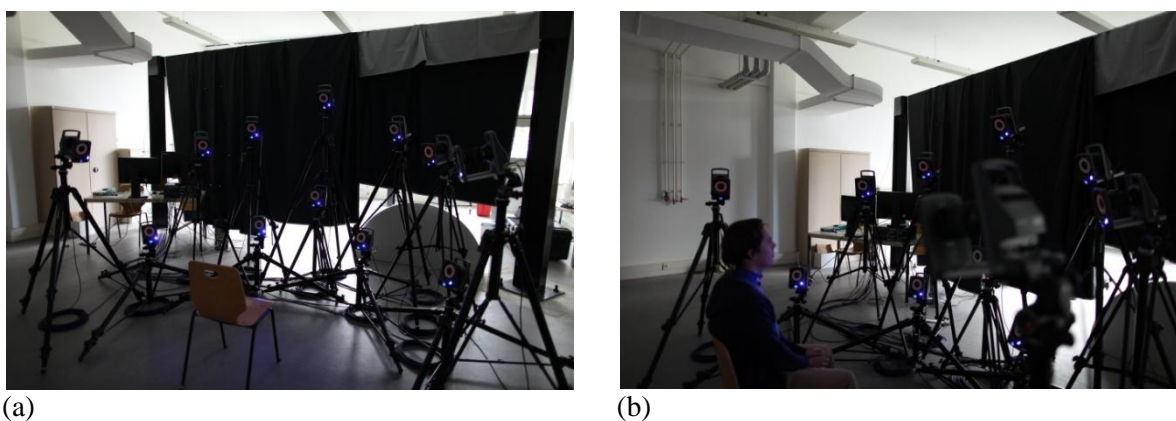


Figure 8-1. Vicon system installation (a) 12 cameras positioned in a semi sphere (b) subject of the motion capture is placed just in front of the system.

Data Acquisition. MOCAP session for data acquisition typically consists of the following stages: Set up markers, Capture marker trajectories, Data post-processing.

1. Set up markers. We estimated that for each subject we need from 120 to 200 of light reflective markers for robust data acquisition (may vary from one person to another). Currently we are using a set up with 160 markers (Figure 8-2 (a)). Entire surface of the face surface should be covered. Markers have to span all over

the face till the indicative boundaries defined by the hair, chin lines, etc. Ideally, any nearest 3 markers from the marker set should form a triangle which resembles the local face surface as much as possible; although it is extremely difficult to achieve in practice. We paid a lot of attention to the inter-marker distance: markers should be kept close enough to each other (0.8-1cm apart, depending on a subject and number of markers). Regions of high deformations (for instance, mouth area) should be covered by markers more densely; beside that we tried to place markers as regular as possible.

2. Capture markers trajectories. A person with markers is placed in front of Vicon system; then, the actor performs all the motions (normally motions are predefined and discussed before the session starts). Before the Mocap session, the participant shall make some exercises. One should be an actor, performing with exaggerated expressions. The Vicon cameras capture trajectories of the markers individually; the output trajectories data set is stored in one single binary file in .c3d format.

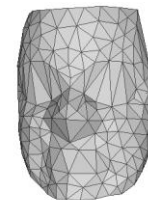
3. Data post-processing. After acquiring raw markers movement data, an engineer needs to post-process the data in order to construct an animated mesh. First, the engineer labels the trajectories if needed (during the motion capture some markers may disappear for a frame or two due to occlusions) with Vicon Blade software. Second, our software extracts the coordinates of each marker in every frame. As a result each frame is represented as a point cloud (Figure 8-2 (b)). Assuming the topology remains the same during the motion capture, we only need to triangulate only first frame for a subject (Figure 8-2 (c)). Finally, after transferring of the topology information to all point cloud frames we obtain a animated mesh sequence.



(a)



(b)



(c)

Figure 8-2. Data acquisition in MOCAP session (a) Actor with markers in place. (b) Point cloud acquired for each frame during the MOCAP session. Points represent marker locations. (c) Triangulated point cloud. While keeping the topology consistent over the frames we get an animated mesh.

8.2 Appendix B : Subgraph matching using Ullmann's Algorithm

Our subgraph matching method in Chapter 5 is similar in spirit to Ullmann's algorithm (Ullmann 1976). In the literature the subgraph matching problem is often called subgraph isomorphism. Given the source G_S and target G_T graphs, isomorphism is simply defined as a pair of injective mappings $f = (\alpha, \beta)$ between vertices and edges of G_S and G_T . In Ullmann's algorithm subgraph matching is determined by a tree-search enumeration (Ullmann 1976), i.e. by systematic generation of all possible matches between G_S and G_T . Consider the source and the target graphs $G_S = (V_S, E_S, \vartheta_S)$, $G_T = (V_T, E_T, \vartheta_T)$, $n = |V_S|$, $m = |V_T|$, where ϑ are node labels, A and B are weighted matrices of adjacency. A subgraph matching can be formally represented as a permutation matrix $M = [m_{ij}]$, $m_{ij} \in \{0, 1\}$, $i = 1 \dots n$, $j = 1 \dots m$. If the value of m_{ij} is equal to 1, it means that i th vertex of G_S is mapped to j th vertex of G_T . Two sequential left-multiplications of B by M , $M(M \cdot B)^T$ modify the target's graph adjacency matrix accordingly to the permutation matrix, in other words, the target's vertices are permuted according to M . Given $C \equiv M(M \cdot B)^T$, permutation matrix M defines a subgraph isomorphism of G_S to G_T , if $\forall i, j: A_{ij} \geq 0 \Rightarrow C_{ij} = A_{ij}$.

The valid permutation M has a following set of properties:

binary: M contains only 0 and 1;

injection: exactly one 1 in each row, and not more than one 1 in each column;

In order to support partial matches (i.e. only a subset of the source's vertices is mapped on the target) we modify the property set by removing the injection property and substituting it with a weaker condition: not more than one 1 in each row and column.

We use an iterative approach to find a permutation M which corresponds to valid subgraph matching. First, we initialize the permutation M^0 with all ones (all permutations are possible). Then, we prevent the mapping of the source vertex to the target vertex which has a smaller degree:

$$M_{ij}^0 = \begin{cases} 1, & \deg(v_T^j) \geq \deg(v_S^i) \\ 0, & \text{otherwise} \end{cases},$$

where $\deg(v)$ denotes a degree of a vertex.

When the initialization is done, we generate systematically all valid permutation matrices M^d by means of a depth-first tree search. M^0 is located in the root of a search tree; the tree node at level l is binded with a partial permutation matrix, which maps precisely first l vertices from G_S to G_T . For each next M^{d+1} we select a matching for $(l + 1)$ th vertex from the source and check whether the weights of the new matching pair of nodes are consistent. If corresponding weights are within a user-defined error threshold, we continue going down the search tree. If the weight constraints are violated, we prune the search branch and come back to the parent search node. When the generation of permutations is done, as an output $\{M_1, \dots, M_k\}$ we have a set of valid isomorphisms and a set of partial isomorphisms between G_S and G_T ; or in case when there is no valid isomorphism, the output is an empty set \emptyset .

References

- Aiger, D., et al. (2008). 4-points congruent sets for robust pairwise surface registration. *ACM Transactions on Graphics (TOG)*, ACM.
- Allen, B., Curless, B., & Popović, Z. (2002, July). Articulated body deformation from range scan data. In *ACM Transactions on Graphics (TOG)* (Vol. 21, No. 3, pp. 612-619). ACM.
- Allen, B., Curless, B., & Popović, Z. (2003, July). The space of human body shapes: reconstruction and parameterization from range scans. In *ACM Transactions on Graphics (TOG)* (Vol. 22, No. 3, pp. 587-594). ACM.
- Allen, B., Curless, B., Popović, Z., & Hertzmann, A. (2006, September). Learning a correlated model of identity and pose-dependent body shape variation for real-time synthesis. In *Proceedings of the 2006 ACM SIGGRAPH/Eurographics symposium on Computer animation* (pp. 147-156). Eurographics Association.
- Anguelov, D., et al. (2005). "The correlated correspondence algorithm for unsupervised registration of nonrigid surfaces." *Advances in neural information processing systems* **17**: 33-40.
- Arcila, R., et al. (2010). "A framework for motion-based mesh sequence segmentation."
- Arcila, R., et al. (2013). "Segmentation of temporal mesh sequences into rigidly moving components." *Graphical Models* **75**(1): 10-22.
- Kin-Chung Au, O., Tai, C. L., Cohen-Or, D., Zheng, Y., & Fu, H. (2010, May). Electors voting for fast automatic shape correspondence. In *Computer Graphics Forum* (Vol. 29, No. 2, pp. 645-654). Blackwell Publishing Ltd.
- Autodesk, I. "Autodesk Maya." from <http://www.autodesk.com/products/maya/overview>.
- Bartolini, G. (2006). "On Poincaré's Uniformization Theorem."
- Bay, H., et al. (2006). Surf: Speeded up robust features. *Computer Vision—ECCV 2006*, Springer: 404-417.
- Belongie, S., et al. (2000). Shape context: A new descriptor for shape matching and object recognition. NIPS.
- Bertsekas, D. P. (1999). *Nonlinear programming*.
- Besl, P. J., & McKay, N. D. (1992, April). Method for registration of 3-D shapes. In *Robotics-DL tentative* (pp. 586-606). International Society for Optics and Photonics.
- Biasotti, S., Marini, S., Spagnuolo, M., & Falcidieno, B. (2006). Sub-part correspondence by structural descriptors of 3D shapes. *Computer-Aided Design*, **38**(9), 1002-1019.
- Blanz, V., & Vetter, T. (1999, July). A morphable model for the synthesis of 3D faces. In *Proceedings of the 26th annual conference on Computer graphics and interactive techniques* (pp. 187-194). ACM Press/Addison-Wesley Publishing Co..
- Borg, I., & Groenen, P. J. (2005). *Modern multidimensional scaling: Theory and applications*. Springer Science & Business Media.
- Boykov, Y., Veksler, O., & Zabih, R. (2001). Fast approximate energy minimization via graph cuts. *Pattern Analysis and Machine Intelligence, IEEE Transactions on*, **23**(11), 1222-1239.
- Bronstein, A. M., Bronstein, M. M., & Kimmel, R. (2006). Generalized multidimensional scaling: a framework for isometry-invariant partial surface matching. *Proceedings of the National Academy of Sciences of the United States of America*, **103**(5), 1168-1172.
- Bronstein, A. M., Bronstein, M. M., Kimmel, R., Mahmoudi, M., & Sapiro, G. (2010). A Gromov-Hausdorff framework with diffusion geometry for topologically-robust non-rigid shape matching. *International Journal of Computer Vision*, **89**(2-3), 266-286.
- Bronstein, M. M. and I. Kokkinos (2010). Scale-invariant heat kernel signatures for non-rigid shape recognition. *Computer Vision and Pattern Recognition (CVPR), 2010 IEEE Conference on*, IEEE.

-
- Bulbul, A., et al. (2010). Saliency for animated meshes with material properties. Proceedings of the 7th Symposium on Applied Perception in Graphics and Visualization, ACM.
- Camplani, M. and L. Salgado (2012). Efficient spatio-temporal hole filling strategy for kinect depth maps. IS&T/SPIE Electronic Imaging, International Society for Optics and Photonics.
- Cao, C., et al. (2013). "Facewarehouse: a 3d facial expression database for visual computing."
- Carne, T. (2006). "Geometry and groups." Lecture notes, Cambridge University.
- Castellani, U., et al. (2008). Sparse points matching by combining 3D mesh saliency with statistical descriptors. Computer Graphics Forum, Wiley Online Library.
- Chen, M., Kanade, T., & Pomerleau, D. (2000). Bootstrap a statistical brain atlas. In *Applications of Computer Vision, 2000, Fifth IEEE Workshop on.* (pp. 114-119). IEEE.
- Chang, W., & Zwicker, M. (2008, July). Automatic registration for articulated shapes. In *Computer Graphics Forum* (Vol. 27, No. 5, pp. 1459-1468). Blackwell Publishing Ltd.
- Chardaire, P., & Sutter, A. (1995). A decomposition method for quadratic zero-one programming. *Management Science*, 41(4), 704-712.
- Cleveland, W. S. (1979). Robust locally weighted regression and smoothing scatterplots. *Journal of the American statistical association*, 74(368), 829-836.
- Cour, T., Srinivasan, P., & Shi, J. (2007). Balanced graph matching. *Advances in Neural Information Processing Systems*, 19, 313.
- Dalal, N. and B. Triggs (2005). Histograms of oriented gradients for human detection. *Computer Vision and Pattern Recognition, 2005. CVPR 2005. IEEE Computer Society Conference on*, IEEE.
- Dalal, N., et al. (2006). Human detection using oriented histograms of flow and appearance. *Computer Vision–ECCV 2006*, Springer: 428-441.
- Darom, T. and Y. Keller (2012). "Scale-invariant features for 3-D mesh models." *Image Processing, IEEE Transactions on* 21(5): 2758-2769.
- De Aguiar, E., et al. (2008). Automatic Conversion of Mesh Animations into Skeleton-based Animations. *Computer Graphics Forum*, Wiley Online Library.
- De Aguiar, E., Stoll, C., Theobalt, C., Ahmed, N., Seidel, H. P., & Thrun, S. (2008). Performance capture from sparse multi-view video. *ACM Transactions on Graphics (TOG)*, 27(3), 98.
- De Boor, C. (1978). A practical guide to splines.
- Dey, T. K., et al. (2010). Persistent Heat Signature for Pose-oblivious Matching of Incomplete Models. *Computer Graphics Forum*, Wiley Online Library.
- Dobrian, C. and F. Bevilacqua (2003). Gestural control of music: using the vicon 8 motion capture system. Proceedings of the 2003 conference on New interfaces for musical expression, National University of Singapore.
- Dollár, P., et al. (2005). Behavior recognition via sparse spatio-temporal features. *Visual Surveillance and Performance Evaluation of Tracking and Surveillance, 2005. 2nd Joint IEEE International Workshop on*, IEEE.
- Eilers, P. H., & Goeman, J. J. (2004). Enhancing scatterplots with smoothed densities. *Bioinformatics*, 20(5), 623-628.
- Elad, A., & Kimmel, R. (2003). On bending invariant signatures for surfaces. *Pattern Analysis and Machine Intelligence, IEEE Transactions on*, 25(10), 1285-1295.
- Elidan, J. D. D. T. G., & Koller, D. (2007). Using combinatorial optimization within max-product belief propagation. In *Advances in Neural Information Processing Systems 19: Proceedings of the 2006 Conference* (Vol. 19, p. 369). MIT Press.
- Faires, J. D., & Burden, R. (1998). *Numerical Methods*, Brooks. Cole, second ed., Pacific Grove, CA, USA.
- Fischler, M. A., & Bolles, R. C. (1981). Random sample consensus: a paradigm for model fitting with applications to image analysis and automated cartography. *Communications of the ACM*, 24(6), 381-395.

-
- Funkhouser, T., & Shilane, P. (2006, June). Partial matching of 3 D shapes with priority-driven search. In *ACM International Conference Proceeding Series*(Vol. 256, pp. 131-142).
- Gallagher, B. (2006). Matching structure and semantics: A survey on graph-based pattern matching. *AAAI FS*, 6, 45-53.
- Garland, M. and P. S. Heckbert (1997). Surface simplification using quadric error metrics. Proceedings of the 24th annual conference on Computer graphics and interactive techniques, ACM Press/Addison-Wesley Publishing Co.
- Gatzke, T., et al. (2005). Curvature maps for local shape comparison. Shape Modeling and Applications, 2005 International Conference, IEEE.
- Gelfand, N., et al. (2005). Robust global registration. Symposium on geometry processing.
- Gilles, B., Reveret, L., & Pai, D. K. (2010, December). Creating and Animating Subject-Specific Anatomical Models. In *Computer Graphics Forum* (Vol. 29, No. 8, pp. 2340-2351). Blackwell Publishing Ltd.
- GmbH, M. C. "Cinema 4D." from <http://www.maxon.net/>.
- Gower, J. C., & Dijksterhuis, G. B. (2004). *Procrustes problems* (Vol. 3). Oxford: Oxford University Press.
- Harris, C. and M. Stephens (1988). A combined corner and edge detector. Alvey vision conference, Manchester, UK.
- Hildreth, E. and D. Marr (1980). "Theory of edge detection." Proceedings of Royal Society of London **207**(187-217): 9.
- Huang, Q. X., Adams, B., Wicke, M., & Guibas, L. J. (2008, July). Non-Rigid Registration Under Isometric Deformations. In *Computer Graphics Forum* (Vol. 27, No. 5, pp. 1449-1457). Blackwell Publishing Ltd.
- Jain, V., et al. (2007). "Non-rigid spectral correspondence of triangle meshes." International Journal of Shape Modeling **13**(1): 101-124.
- Johnson, A. E. (1997). Spin-images: a representation for 3-D surface matching, Citeseer.
- Kim, V. G., et al. (2011). Blended intrinsic maps. ACM Transactions on Graphics (TOG), ACM.
- Klaser, A. and M. Marszalek (2008). "A spatio-temporal descriptor based on 3d-gradients."
- Komodakis, N., Paragios, N., & Tziritas, G. (2007, October). MRF optimization via dual decomposition: Message-passing revisited. In *Computer Vision, 2007. ICCV 2007. IEEE 11th International Conference on* (pp. 1-8). IEEE.
- Körtgen, M., et al. (2003). 3D shape matching with 3D shape contexts. The 7th central European seminar on computer graphics.
- Laptev, I. (2005). "On space-time interest points." International journal of computer vision **64**(2-3): 107-123.
- Laptev, I., et al. (2008). Learning realistic human actions from movies. Computer Vision and Pattern Recognition, 2008. CVPR 2008. IEEE Conference on, IEEE.
- Lee, C. H., et al. (2005). Mesh saliency. ACM Transactions on Graphics (TOG), ACM.
- Lee, T.-Y., et al. (2006). "Segmenting a deforming mesh into near-rigid components." The Visual Computer **22**(9-11): 729-739.
- Lempitsky, V., Rother, C., & Blake, A. (2007, October). Logcut-efficient graph cut optimization for markov random fields. In *Computer Vision, 2007. ICCV 2007. IEEE 11th International Conference on* (pp. 1-8). IEEE.
- Leordeanu, M., & Hebert, M. (2005, October). A spectral technique for correspondence problems using pairwise constraints. In *Computer Vision, 2005. ICCV 2005. Tenth IEEE International Conference on* (Vol. 2, pp. 1482-1489). IEEE.
- Li, H., et al. (2010). "Example-based facial rigging." ACM Transactions on Graphics (TOG) **29**(4): 32.
- Lindeberg, T. (1998). Feature detection with automatic scale selection. International journal of computer vision, **30**(2), 79-116.
- Lindeberg, T. (1993). Scale-space theory in computer vision, Springer.

-
- Lipman, Y. and T. Funkhouser (2009). Möbius voting for surface correspondence. *ACM Transactions on Graphics (TOG)*, ACM.
- Lowe, D. G. (2004). "Distinctive image features from scale-invariant keypoints." *International journal of computer vision* **60**(2): 91-110.
- Lucas, B. D. and T. Kanade (1981). An iterative image registration technique with an application to stereo vision. *IJCAI*.
- Maes, C., et al. (2010). Feature detection on 3D face surfaces for pose normalisation and recognition. *Biometrics: Theory Applications and Systems (BTAS)*, 2010 Fourth IEEE International Conference on, IEEE.
- Mahamud, S., Williams, L. R., Thornber, K. K., & Xu, K. (2003). Segmentation of multiple salient closed contours from real images. *Pattern Analysis and Machine Intelligence, IEEE Transactions on*, *25*(4), 433-444.
- Mamou, K., et al. (2006). A skinning prediction scheme for dynamic 3D mesh compression. *SPIE Optics+ Photonics*, International Society for Optics and Photonics.
- Mateus, D., et al. (2008). Articulated shape matching using Laplacian eigenfunctions and unsupervised point registration. *Computer Vision and Pattern Recognition, 2008. CVPR 2008. IEEE Conference on*, IEEE.
- F. Memoli, G. Sapiro, Comparing point clouds. In *Proc. of SGP*, pp. 32–40, 2004.
- Mian, A., et al. (2010). "On the repeatability and quality of keypoints for local feature-based 3d object retrieval from cluttered scenes." *International journal of computer vision* **89**(2-3): 348-361.
- Mikolajczyk, K. and C. Schmid (2004). "Scale & affine invariant interest point detectors." *International journal of computer vision* **60**(1): 63-86.
- Mikolajczyk, K., et al. (2005). "A comparison of affine region detectors." *International journal of computer vision* **65**(1-2): 43-72.
- Mitchell, J. S., Mount, D. M., & Papadimitriou, C. H. (1987). The discrete geodesic problem. *SIAM Journal on Computing*, *16*(4), 647-668.
- Moening, C. (2005). *Intrinsic point-based surface processing* (Doctoral dissertation, University of Cambridge).
- Noyel, G., Angulo, J., & Jeulin, D. (2011). Fast computation of all pairs of geodesic distances. *Image Analysis and Stereology*, *30*(2), 101-109.
- Ovsjanikov, M., et al. (2010). One point isometric matching with the heat kernel. *Computer Graphics Forum*, Wiley Online Library.
- Pauly, M., et al. (2003). Multi-scale Feature Extraction on Point-Sampled Surfaces. *Computer graphics forum*, Wiley Online Library.
- Petitjean, S. (2002). "A survey of methods for recovering quadrics in triangle meshes." *ACM Computing Surveys (CSUR)* **34**(2): 211-262.
- Plankers, R., Fua, P., & D'Apuzzo, N. (1999). Automated body modeling from video sequences. In *Modelling People, 1999. Proceedings. IEEE International Workshop on* (pp. 45-52). IEEE.
- Pollack, R., Sharir, M., & Rote, G. (1989). Computing the geodesic center of a simple polygon. *Discrete & Computational Geometry*, *4*(1), 611-626.
- Praun, E., & Hoppe, H. (2003, July). Spherical parametrization and remeshing. In *ACM Transactions on Graphics (TOG)* (Vol. 22, No. 3, pp. 340-349). ACM.
- Rabiner, L. (1989). "A tutorial on hidden Markov models and selected applications in speech recognition." *Proceedings of the IEEE* **77**(2): 257-286.
- Raviv, D., Dubrovina, A., & Kimmel, R. (2013). Hierarchical framework for shape correspondence. *Numer. Math. Theor. Meth. Appl*, *6*(1).
- Ruggeri, M. R., & Saupe, D. (2008, April). Isometry-invariant Matching of Point Set Surfaces. In *3DOR* (pp. 17-24).

-
- Saba, S., Yavneh, I., Gotsman, C., & Sheffer, A. (2005, June). Practical spherical embedding of manifold triangle meshes. In *Shape Modeling and Applications, 2005 International Conference* (pp. 256-265). IEEE.
- Sahillioğlu, Y. and Y. Yemez (2010). 3d shape correspondence by isometry-driven greedy optimization. *Computer Vision and Pattern Recognition (CVPR), 2010 IEEE Conference on*, IEEE.
- Sahillioğlu, Y. and Yemez, Y. (2012), Scale Normalization for Isometric Shape Matching. *Computer Graphics Forum*, 31: 2233–2240.
- Sattler, M., et al. (2005). Simple and efficient compression of animation sequences. *Proceedings of the 2005 ACM SIGGRAPH/Eurographics symposium on Computer animation*, ACM.
- Schlesinger, M. I., & Giginyak, V. V. (2007). Solution to structural recognition (MAX,+)-problems by their equivalent transformations. *Part, 1*, 3-15.
- Schönemann, P. H. (1966). A generalized solution of the orthogonal Procrustes problem. *Psychometrika*, 31(1), 1-10.
- Scott, G. L., & Longuet-Higgins, H. C. (1990, September). Feature grouping by'relocalisation'of eigenvectors of the proximity matrix. In *BMVC* (pp. 1-6).
- Scovanner, P., et al. (2007). A 3-dimensional sift descriptor and its application to action recognition. *Proceedings of the 15th international conference on Multimedia*, ACM.
- Seo, H., & Magnenat-Thalmann, N. (2003, April). An automatic modeling of human bodies from sizing parameters. In *Proceedings of the 2003 symposium on Interactive 3D graphics* (pp. 19-26). ACM.
- Seo, H., Yeo, Y. I., & Wohn, K. (2006). 3D body reconstruction from photos based on range scan. In *Technologies for e-learning and digital entertainment*(pp. 849-860). Springer Berlin Heidelberg.
- Seo, H., & Cordier, F. (2010, March). Constrained texture mapping using image warping. In *Computer Graphics Forum* (Vol. 29, No. 1, pp. 160-174). Blackwell Publishing Ltd.
- Shi, J., & Malik, J. (2000). Normalized cuts and image segmentation. *Pattern Analysis and Machine Intelligence, IEEE Transactions on*, 22(8), 888-905.
- Shor, N. Z., Kiwiel, K. C., & Ruszcayński, A. (1985). *Minimization methods for non-differentiable functions*. Springer-Verlag New York, Inc.
- Sipiran, I. and B. Bustos (2011). "Harris 3D: a robust extension of the Harris operator for interest point detection on 3D meshes." *The Visual Computer* 27(11): 963-976.
- Smyth, P. (1997). "Clustering sequences with hidden Markov models." *Advances in neural information processing systems*: 648-654.
- Sorkine, O. (2009). Least-squares rigid motion using svd. *Technical notes*, 120, 3.
- Spagnuolo, M., et al. (2012). "Affine-invariant photometric heat kernel signatures."
- Starck, J., & Hilton, A. (2007). Surface capture for performance-based animation. *Computer Graphics and Applications, IEEE*, 27(3), 21-31.
- Sumner, R. W. and J. Popović (2004). Deformation transfer for triangle meshes. *ACM Transactions on Graphics (TOG)*, ACM.
- Sun, J., et al. (2009). A Concise and Provably Informative Multi-Scale Signature Based on Heat Diffusion. *Computer Graphics Forum*, Wiley Online Library.
- Sundar, H., Silver, D., Gagvani, N., & Dickinson, S. (2003, May). Skeleton based shape matching and retrieval. In *Shape Modeling International, 2003* (pp. 130-139). IEEE.
- Tenenbaum, J. B., De Silva, V., & Langford, J. C. (2000). A global geometric framework for nonlinear dimensionality reduction. *Science*, 290(5500), 2319-2323.
- Tevs, A., Bokeloh, M., Wand, M., Schilling, A., & Seidel, H. P. (2009, June). Isometric registration of ambiguous and partial data. In *Computer Vision and Pattern Recognition, 2009. CVPR 2009. IEEE Conference on* (pp. 1185-1192). IEEE.

-
- Tevs, Berner et al. (2011). Intrinsic shape matching by planned landmark sampling. *Computer Graphics Forum*, Wiley Online Library.
- Tierny, J., Vandeborre, J. P., & Daoudi, M. (2009, March). Partial 3D shape retrieval by reeb pattern unfolding. In *Computer Graphics Forum* (Vol. 28, No. 1, pp. 41-55). Blackwell Publishing Ltd.
- Torr, P. H., & Zisserman, A. (2000). MLESAC: A new robust estimator with application to estimating image geometry. *Computer Vision and Image Understanding*, 78(1), 138-156.
- Torresani, L., Kolmogorov, V., & Rother, C. (2008). Feature correspondence via graph matching: Models and global optimization. In *Computer Vision–ECCV 2008* (pp. 596-609). Springer Berlin Heidelberg.
- Torresani, L., Kolmogorov, V., & Rother, C. (2013). A dual decomposition approach to feature correspondence. *Pattern Analysis and Machine Intelligence, IEEE Transactions on*, 35(2), 259-271.
- Tung, T., & Matsuyama, T. (2013). Invariant surface-based shape descriptor for dynamic surface encoding. In *Computer Vision–ACCV 2012* (pp. 486-499). Springer Berlin Heidelberg.
- Tuytelaars, T., & Mikolajczyk, K. (2008). Local invariant feature detectors: a survey. *Foundations and Trends® in Computer Graphics and Vision*, 3(3), 177-280.
- Tuzel, O., Subbarao, R., & Meer, P. (2005, October). Simultaneous multiple 3D motion estimation via mode finding on Lie groups. In *Computer Vision, 2005. ICCV 2005. Tenth IEEE International Conference on* (Vol. 1, pp. 18-25). IEEE.
- Ullmann, J. R. (1976). An algorithm for subgraph isomorphism. *Journal of the ACM (JACM)*, 23(1), 31-42.
- Valgaerts, L., et al. (2012). "Lightweight binocular facial performance capture under uncontrolled lighting." *ACM Trans. Graph.* 31(6): 187.
- Vlasic, D., Brand, M., Pfister, H., & Popović, J. (2005, July). Face transfer with multilinear models. In *ACM Transactions on Graphics (TOG)* (Vol. 24, No. 3, pp. 426-433). ACM.
- Vlasic, D., et al. (2007). Practical motion capture in everyday surroundings. *ACM Transactions on Graphics (TOG)*, ACM.
- Wang, C., Bronstein, M. M., Bronstein, A. M., & Paragios, N. (2012). Discrete minimum distortion correspondence problems for non-rigid shape matching. In *Scale Space and Variational Methods in Computer Vision* (pp. 580-591). Springer Berlin Heidelberg.
- Webb, J. and J. Ashley (2012). *Beginning Kinect Programming with the Microsoft Kinect SDK*, Apress.
- Weise, T., et al. (2011). "Realtime performance-based facial animation." *ACM Transactions on Graphics (TOG)* 30(4): 77.
- Weise, T., et al. (2009). Face/off: Live facial puppetry. *Proceedings of the 2009 ACM SIGGRAPH/Eurographics Symposium on Computer animation*, ACM.
- Tai, Y. W., & Park, I. K. (2014). Accurate and real-time depth video acquisition using Kinect–stereo camera fusion. *Optical Engineering*, 53(4), 043110-043110.
- Willems, G., et al. (2008). An efficient dense and scale-invariant spatio-temporal interest point detector. *Computer Vision–ECCV 2008*, Springer: 650-663.
- Zaharescu, A., et al. (2009). Surface feature detection and description with applications to mesh matching. *Computer Vision and Pattern Recognition, 2009. CVPR 2009. IEEE Conference on*, IEEE.
- Zelinka, S. and M. Garland (2004). Similarity-based surface modelling using geodesic fans. *Proceedings of the 2004 Eurographics/ACM SIGGRAPH symposium on Geometry processing*, ACM.
- Zhang, H., Sheffer, A., Cohen-Or, D., Zhou, Q., Van Kaick, O., & Tagliasacchi, A. (2008, July). Deformation-Driven Shape Correspondence. In *Computer Graphics Forum* (Vol. 27, No. 5, pp. 1431-1439). Blackwell Publishing Ltd.
- Zhang, Z. (2000). A flexible new technique for camera calibration. *Pattern Analysis and Machine Intelligence, IEEE Transactions on*, 22(11), 1330-1334.

Zhu, C., Byrd, R. H., Lu, P., & Nocedal, J. (1997). Algorithm 778: L-BFGS-B: Fortran subroutines for large-scale bound-constrained optimization. *ACM Transactions on Mathematical Software (TOMS)*, 23(4), 550-560.